Durham E-Theses

Modelling and characterization of supported catalytic centres

Bell, Gillian

How to cite:

Bell, Gillian (1994) *Modelling and characterization of supported catalytic centres*, Durham theses, Durham University. Available at Durham E-Theses Online: http://etheses.dur.ac.uk/5815/

Use policy

MODELLING AND CHARACTERIZATION OF SUPPORTED

CATALYTIC CENTRES

by

Gillian Bell   B.Sc. (Nottingham),   M.Sc. (Dunelm)

A thesis submitted to the University of Durham
for the degree of Doctor of Philosophy

July 1994

1

28 SEP 1995

Declaration

The work in this thesis was carried out in the Univerity of
Durham between October 1988 and November 1992. It has not
been submitted, either wholly or in part, for a degree in
this or any other University and is the original work of the
author except where acknowledged by reference.

Acknowledgements

I wish to express my appreciation to my supervisor Dr. M. Kilner for all his help, advice and encouragement during this period of study and during the writing of this thesis.

I am also grateful to Dr. J.P.S. Badyal for his help and advice with the XPS and mass spectral experiments, and to the members of the departmental technical staff and lab. 115 for their assistance throughout this period of study. I would also like to thank Mr. A. Coulthard for his help with the production of this thesis.

G. Bell

July 1994

Modelling and Characterization of Supported Catalytic Centres
Abstract

A series of aluminia and titania promoted, silica-supported chromium (III) acetate catalysts were characterized using X-ray photoelectron spectroscopy (XPS) prior to, and after, activation in oxygen at 780°C. The results indicated that Cr (VI) was formed in each case as a result of the activation process. Increased promoter metal binding energies implied an interaction between the promoter and silica support. It is proposed that there is insertion of aluminium and titanium atoms into the silica network, which leads to formation of surface silicates. A qualitative measure of the metal dispersions has been made using the XPS results. In general, the chromium dispersion fell on activation, but the greatest decline was seen with the lowest chromium loading (0.5% Cr). Promoter metal dispersion was unchanged on activation, except in the case of the highest titanium loading (4.35% Ti), where small titania clusters are formed.

Mass spectral analysis of the gases evolved during thermal decomposition in argon led to a mechanism being proposed for the decomposition of the acetate precursor. The first step is dehydration of the silica support, which is followed by decompositon of acetate ligands to form an intermediate, which was thought to be a carbonate, and the final stage is the decomposition of this intermediate to chromium (III) oxide for the unpromoted catalysts. Where a promoter is present a structural and electronic interaction between the chromium complex and the promoter is proposed, which leads to formation of mixed surface oxides of perovskite ($M^{II}Ti^{IV}O_3$) or spinel ($M^{II}Al_2^{III}O_4$) structure, where M = Cr.

For activation under oxygen the pattern of decomposition was much simpler. Studies of the promoted catalysts showed the oxidation to occur in two stages. It was not clear which chromium species were present after the first step, but the second step led to the formation of chromium (VI) oxide for all catalysts.

Modelling of the adsorption sites on metal surfaces has also been undertaken with a series of triosmium carbonyl complexes containing ligands derived from aniline, phenol, pyrrole, furan, thiophene and benzene. These complexes have been characterized using Fourier Transform Infra Red spectroscopy and their vibrational spectra assigned in full. The usefulness of these complexes as models, and in the assignment of vibrational spectra of adsorbates on metal surfaces, is discussed.

4

A List of Acronyms Used in the Text

AES	Auger Electron Spectroscopy
ARUPS	Angle Resolved Ultraviolet Photoelectron Spectroscopy
CP/MAS	Cross Polarisation/Magic Angle Spinning (in NMR)
DRS	Diffuse Reflectance Spectroscopy
DTA	Differential Thermal Analysis
DTG	Differential Thermogravimetry
EDAX	Energy Dispersive X-ray Spectroscopy
EELS	Electron Energy Loss Spectroscopy
EGA	Evolved Gas Analysis
EPR	Electron Paramagnetic Resonance Spectroscopy
ESCA	Electron Spectroscopy for Chemical Analysis (now XPS)
ESR	Electron Spin Resonance Spectroscopy
EXAFS	Extended X-ray Absorption Fine Structure
FTIR	Fourier Transform Infra Red Spectroscopy
HREELS	High Resolution Electron Energy Loss Spectroscopy
LEED	Low Energy Electron Diffraction
MS	Mass Spectroscopy
NEXAFS	Near-Edge X-ray Absorption Fine Structure
NMR	Nuclear Magnetic Resonance Spectroscopy
QMS	Quadrupole Mass Spectroscopy
RAIRS	Reflection-Absorption Infra Red Spectroscopy
SEM	Scanning Electron Microscopy
SIMS	Secondary Ion Mass Spectrometry
TDS	Thermal Desoprtion Spectroscopy
TEM	Transmission Electron Microscopy
TG	Thermogravimetry
TGA	Thermogravimetric Analysis
TPD	Temperature Programmed Desorption
TPR	Temperature Programmed Reduction
UHV	Ultra High Vacuum
XANES	X-ray Absorption Near-Edge Structure
XPS	X-ray Photoelectron Spectroscopy (ESCA)
XRD	X-Ray Diffraction

CONTENTS

PREFACE

The work in this thesis is divided into two parts, the first being devoted to the characterization of supported catalytic centres (Chapters 1, 2, 3) and the second to the modelling of adsorption sites on metal surfaces using well-characterized organometallic cluster complexes (Chapter 4).

Chromium (VI) oxide supported on silica is the Phillips catalyst which is important industrially for the polymerization of ethylene. The catalytic activity is promoted by addition of Ti^{4+} or Al^{3+}, generally as the oxides. Whilst the polymerization reaction is well studied there are fewer investigations of the catalyst itself. It is these promoted systems which are the focus of this study.

A review of the surface chemistry of silica and silica-supported titania and chromium oxides is contained in Chapter 1. Chapter 2 contains the results of X-ray photoelectron spectroscopic investigations of a series of silica-supported chromium catalysts, promoted by titania and alumina, which have been previously activated by heating in oxygen at 780°C. This technique presents a picture of the changes in surface chemistry which have occurred as a result of activation, in particular changes in metal oxidation state and dispersion.

The thermal decomposition which occurs when the catalysts are heated in inert gas (argon) and when activated in oxygen has been studied using evolved gas analysis with mass spectrometry. A mechanism of decomposition was proposed and the results are contained in Chapter 3.

Chapter 4 presents the characterization of a set of triosmium carbonyl complexes containing ligands derived from pyrrole, thiophene, furan, aniline, phenol and benzene. Fourier Transform Infra Red spectra of the complexes have been obtained and the vibrational modes assigned. The chemistry of the same ligands as adsorbates on metal surfaces is considered, together with the suitability of the organometallic complexes as models for the adsorbate-surface bonding and their role in assisting the assignment of vibrational spectra of the surface species.

1

CHAPTER 1

Transition Metal Oxides Supported on Silica:

A Review of Silica-supported Titanium and Chromium Oxides

1 Introduction

Metal oxides are important catalysts in organic synthesis and in the chemical industry. Catalytic cracking, isomerization of hydrocarbons, alkylations of alkanes and aromatics with olefins, polymerization of olefins and partial oxidation of hydrocarbons are among the reactions carried out over metal oxide catalysts [1,2].

There are a number of reasons for using supported oxides, including the increased surface area and the fact that the support can reduce sintering. Sometimes the support is used as a heat conduction medium, which may be important in oxidation reactions which have large heats of reaction. In a number of systems the support provides a template for the oxide to form in a certain desired morphology, such as the exposure of one predominant plane eg., V_2O_5 on TiO_2.

A supported catalyst consists of an active component dispersed on a support with a highly specific surface [6]. The active component can be in one of four forms: (i) it retains its chemical identity as a separate crystalline or amorphous phase, (ii) it forms a new stoichiometric compound with the support, (iii) it disperses in the support to form a solid solution, or (iv) it can form a monolayer. A monolayer dispersion is common - many oxides and salts disperse spontaneously onto the support surface to give a monolayer or submonolayer, as this is the thermodynamically stable form.

Silica is used as a support because it is relatively inert: interaction with the immobilized species is generally weak [4,7]. In this sense, silica acts mainly as a dispersant, without altering the activity of the deposited material. This property may be desirable in certain cases, but is connected with a fairly weak bonding between silica and the dispersed species. As a consequence, a high tendency for thermal aggregation of the immobilized compound is frequently observed. However, it is important to recognise that silica can form a silicate with many oxides, especially those of the first transition series. Their formation is often thermodynamically favourable but kinetically limited, and thus high temperature calcination leads to their production.

In order to tailor and improve catalysts for new processes (such as production of speciality chemicals) it is necessary to control, and hence to understand, the surface properties of metal oxides [11]. Whilst much has been learned concerning the chemical nature of surface oxides (types of bonding), both within the surface oxides and to substrates, and of the valence of surface species, comparatively little work has been done on the physical structure of the surface phase and the role of the

3

underlying support on the surface structure [8]. The effects of changing variables such as support phase and composition, preparation temperature and environment, and surface oxide loading, on the catalytic properties of the systems need to be studied. The structure of the support may influence the structure of the oxide on the surface and there is varying extent of oxide interaction with the support. A better understanding of this influence is needed, especially where the support may itself be a catalyst for some reactions.

One of the reasons for the slower progress towards understanding catalysis on supported oxides compared to supported metals arises from the difficulty of preparing well-dispersed oxides and from the lack of a reliable method of measuring the dispersion, similar to hydrogen chemisorption for metals [9]. The support plays an important role in the dispersion of the metal oxide [10], which leads to ambiguity in the separate role of the carrier from the effect of the active phase particle size [2]. As a result there is interest in studying the use of supported oxides on high surface area carriers. To fully understand the effect of a supported oxide carrier on an active phase, the chemical state and the dispersion must be known.

The incipient wetness impregnation technique often leads to weak active phase-support interactions and hence to poor oxide particle dispersions, although more complex interactions between the ions and the carrier may occur simultaneously [12]. The ion exchange method frequently leads to high and homogenous dispersions but also to low metallic contents. Deposition-precipitation of metal precursors on supports when accompanied by adsorption is recognised to give high and homogeneous dispersion even at high metallic contents [13].

Characterization of the molecular structure of supported metal oxides is complicated since the supported oxide phase can simultaneously possess several different molecular structures, as well as chemical states. Techniques which can provide detailed information about the molecular structure must be capable of discriminating between these different states. EXAFS, XANES, FTIR, Raman and solid state nmr can provide such detailed molecular information [3,5]. However, many *in situ* Raman studies take place under ambient conditions, i.e. moisture is present on the surface. The influence of hydration/dehydration remains a source of confusion. Drastic changes in spectra and structural changes occur on dehydration, which are not just loss of water from the surface [3].

Despite the problems of characterization, a large body of work exists in the literature. Below is a review of the work carried out on silica supported chromium and titania oxides, which is important with regard to the experimental work

4

which follows on the Phillips catalyst (chromium/silica) and its promotion with titania.

2 Silica

There are a number of amorphous forms of silica which have no crystalline structure:

Vitreous   - silica glass

Colloidal (sols) - the dispersion of silica particles in water

Silica gel   - a 3D network of aggregated SiO_2 particles of colloidal dimensions (3-100nm). The pores are filled with the medium in which the gel is prepared (usually water). Removal of this medium leads to aerogels.

Precipitated   - a powder obtained by coagulation of SiO_2 particles from an aqueous medium under the influence of high salt concentrations.

Fumed (aerosils) - produced by a vapour phase process, the flame hydrolysis of silicon tetrahalides [14]. Cab-o-sil, a commonly used catalyst support is a fumed silica.

The bulk of the silica structure is composed of siloxane Si-O-Si bonds, whereas at the surface silanol bonds Si-OH are formed, together with physisorbed water [15].

Figure 1.1 Silica siloxane and silanol bonds

Siloxane   Silanol
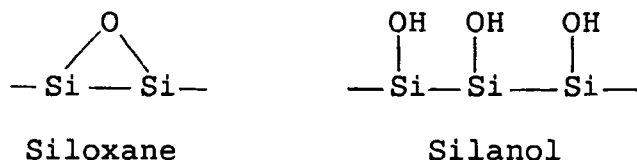
The surface chemistry and reactivity of silica are mainly determined by its surface OH groups. These groups are most important for the attachment of transition metal oxides, the siloxane bridges being much less reactive [16]. The surface silanol groups are found to have a pKa value of between 4 and 7, depending on the method of measurement [17], indicating that silanol groups show weak acidic or nearly neutral behaviour [18].

Kiselev discovered the surface OH groups on silica in 1936 [19] and since then there have been many studies on the quantification of the silanol number (a_{OH}, the number of OH groups per nm²) and on the assignment of different OH

groups. A theoretical model of the (111) surface of β-crystobalite obtained a value of 4.55 for a_{OH} [20]. Zhuravlev obtained a figure of 4.9 OH/nm² after evacuation at 200°C for over 100 different types of amorphous silica [21,22], and found that a_{OH} is a physicochemical constant for a fully hydroxylated surface.

It was calculated using ^{1}H decoupled/MAS NMR that the number of OH/nm² varies from 7.7-17.0 [23]. This is greater than the theoretical value, implying that the internal surface is accessible to water molecules only. Higher values were obtained in this study because nmr takes into account all the OH groups present in the sample, i.e. both surface OH and internal OH groups which are structural water or OH groups inside silica particles and are inaccessible to small molecules such as MeOH or D_2.

2.3 The Effect of Thermal Treatment on Silica Surface Chemistry

Thermal treatment of silica at 473K removes physisorbed water but hardly affects the surface silanol groups [24]. At elevated temperatures the progressive elimination of water between neighbouring silanol groups takes place and the OH concentration falls to 1 OH/nm² by dehydroxylation at 1073K, when only isolated, free Si-OH groups are observed [25]. Some OH groups are retained even after heating at 1273K: a_{OH} has been determined as 0.65 (1173K) and 0.4 (1273K) OH/nm² [26]. Complete dehydroxylation requires even higher temperatures. The density as a function of temperature is shown in Table 1.1, and it does not depend significantly on the type of silica.

Table 1.1 The total number of hydroxyl groups (a_{OH}) on the silica gel surface

Temperature/K	a_{OH}/OH nm^{-2}
373	5.0
473	4.7
573	3.4
673	2.2
773	1.8
873	1.6
973	1.1
1073	1.0

The initial number of surface OH groups may vary with origin or the nature of the silica being studied but an estimation of their population can be obtained from studies of the thermal desorption of water and from surface reactions involving D_2, D_2O, Grignard reagents, halogen-containing compounds, e.g. $AlCl_3$ and $SiCl_4$, and B_2H_6 [27,28-

46]. Such experiments also indicate that silica surfaces
dehydroxylated below 773K have OH groups sufficiently close
together to interact bimolecularly with the reagents used,
even in cases where adjacent OH groups are known not to
hydrogen bond because their separation is greater than
0.31nm [47]. This tendency diminishes with Aerosil or Cab-O-
Sil. Price and Hensley [48] found for stoichiometric
reaction of $AlCl_3$ and $SiCl_4$ that 90% OH groups are paired
(geminal or vicinal pairs) below 870K on silica gels. With
Aerosil or Cab-O-Sil pretreated at 623K this value falls to
61%. 55% was indicated for Aerosils dried at 573-775K
reacting with chloromethylsilanes [49]. Hydrogen exchange
reactions with D_2O indicated a higher reactivity for geminal
pairs than single silanols, but the most reactive groups
were hydrogen bonded vicinal pairs [50]. The different
arrangements of surface OH groups on the silica surface are
shown in Figure 1.2.

*Figure 1.2 The types of OH groups on the silica surface*

```
   H        H   H          H.    .H       H          H
   |        |   |           \   /         |          |
   O        O   O          O     O        O   O—H---O     O—H
   |         \ /           |     |         \ /         \ /
   Si        Si           Si    Si         Si          Si
  /|\       / \          /|\   /|\        / \         / \
```

| Isolated | Geminal | Hydrogen-bonded vicinal | Hydrogen-bonded geminal |
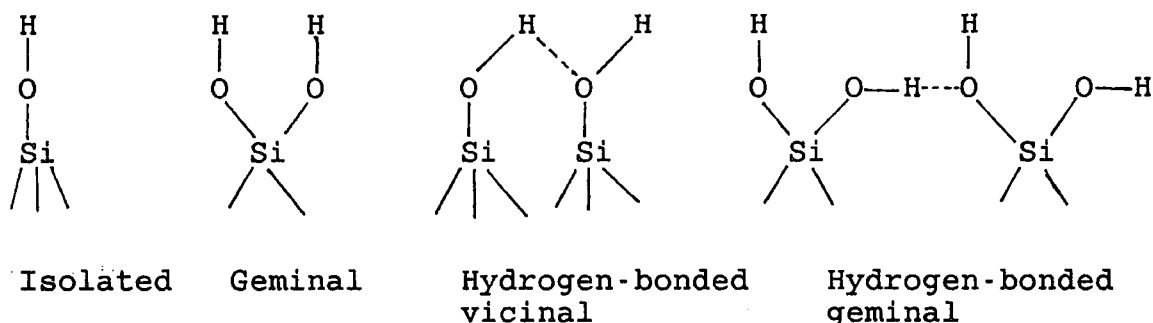
Line narrowing studies of ^1H nmr signals demonstrate that
the protons associated with the silanols migrate from oxygen
atom to oxygen atom [51]. This proton hopping increases with
temperature, the average hopping frequency being estimated
at 10^4 s^{-1} at 773K. The use of multiple pulse experiments
[52] established a H-H distance of >0.4nm on a silica gel
calcined at 773K, the result not excluding the presence of
geminal pairs.

2.4 Infrared Spectroscopic Studies of Silica

Because of the insulating nature of silica UHV techniques
have had limited use in providing understanding of the OH
group chemistry [53] and IR spectroscopy has been most
widely used to study the types of OH groups present on the
surface. Silica surfaces contain a variety of terminal
silanol groups, some of which are isolated single or
geminal, whereas others of either of the above types are
involved in hydrogen bonding or are perturbed due to
interparticle contact [54-56]. Differences between Cabosil
(fumed silica) and precipitated silica can be observed for

example, by IR spectroscopy [53]. For example, structure is seen in the O-H stretching region for the initial Cabosil sample (3747, 3660 and 3520 cm^{-1}), whereas a broad absorption between 3800 and 3000cm^{-1} was observed for precipitated silica.

*Figure 1.3* The IR spectra of fumed and precipitated silica

FUMED SILICA   PRECIPITATED SILICA
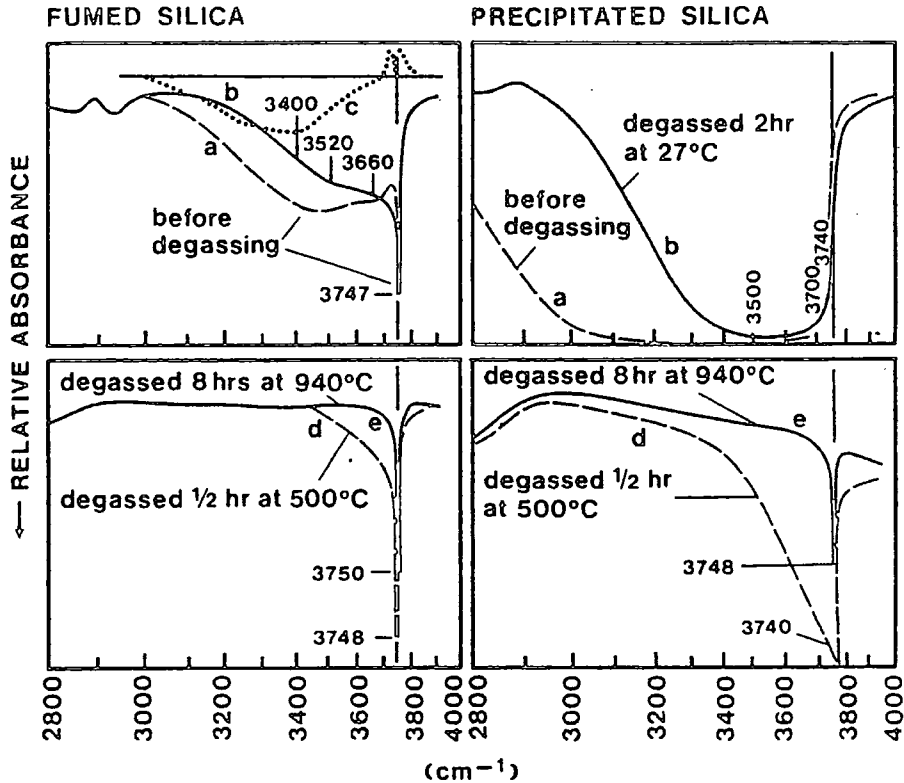
a) before degassing
b) after degassing for 3h at 30°C
c) difference between a) and b)
d) degassed 30min at 500°C *in vacuo*
e) degassed 8.5hr at 940°C *in vacuo*

Evacuation at room temperature leads to loss of absorption in the region 3500cm^{-1} for both samples, and the band at 1625 cm^{-1} (a bending mode) is identified as due to weakly physisorbed molecular water. As the temperature is raised the band at 3520 cm^{-1} is first removed and this is followed by a gradual reduction in intensity at 3660 cm^{-1} until it appears only as a tail on the 3747 cm^{-1} band. Only after heating to over 900°C do the two surfaces give indentical IR spectra.

Gravimetric results on the adsorption and desorption of water are shown in Figure 1.4 [53]

Figure 1.4 *Dehydration-rehydration of silica*
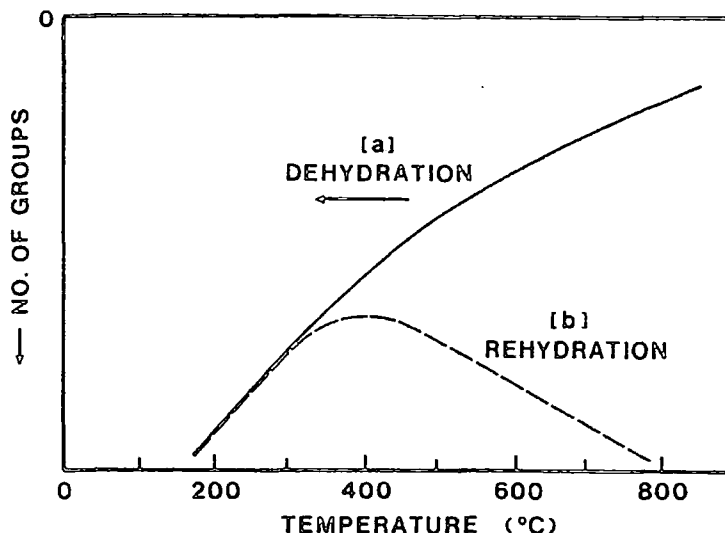
a) loss of surface silanol groups on heating
b) OH groups which can be reformed after preheating to the temperature indicated

After molecular water is removed from the surface (<160°C) there is a slow loss of weight which corresponds to the removal of the 3660 cm^{-1} IR band [53]. This band can be attributed to OH groups which are hydrogen bonded and removed as water during thermal dehydroxylation. At 900°C approximately 1 OH/nm^2 remains which corresponds to the extremely sharp 3747 cm^{-1} band, and is attributed to a "freely vibrating" OH group completely unperturbed by its environment. Its intensity changes very little during the removal of physisorbed water and it can be concluded that the physisorbed water does not sit on this group at low coverage.

Upto 450°C, the dehydration of the surface OH groups is completely reversible. Above this temperature the dehydration becomes progressively more irreversible. Above 800°C the dehydration is irreversible.

Scheme 1   The effects of temperature on the dehydration-rehydration of the silica surface

Δ

< 400°C   reversible
> 800°C   irreversible

$+ \quad H_2O \uparrow$

$+ \quad H_2O \uparrow$
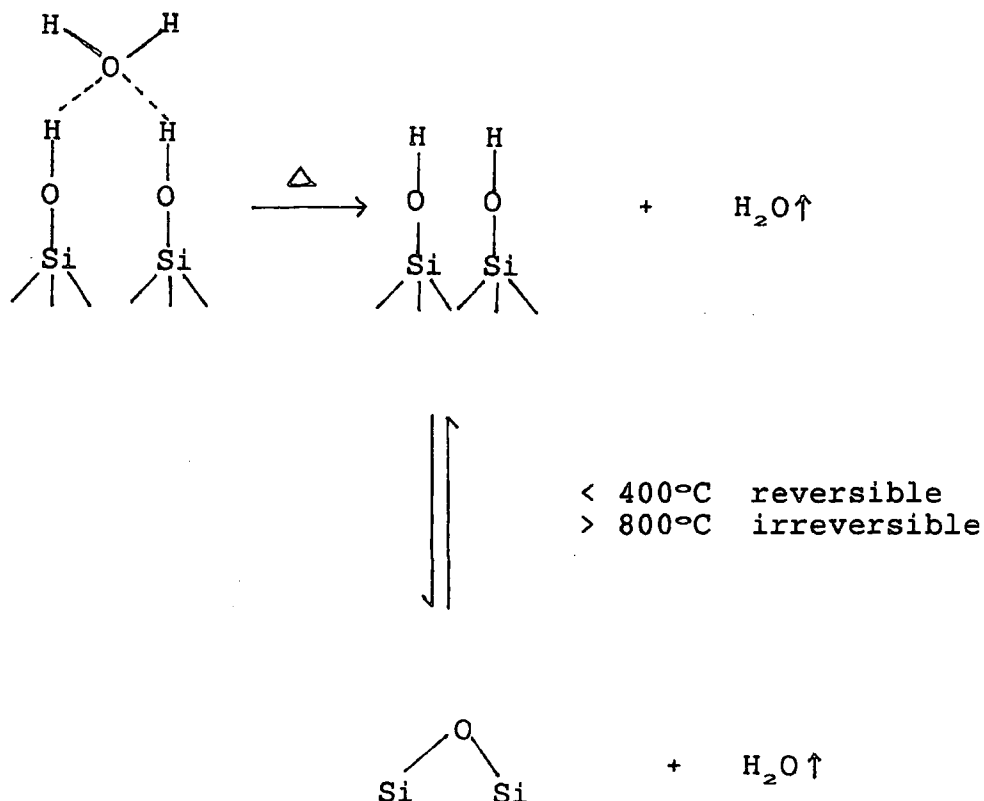
Van Rosmalen and Mol [50] reported four bands present in the OH stretching region for dry silica gels heated at 873K. The different types of OH grouping are shown in Figure 1.2 above.

v_a	(isolated, single OH)	3749
v_b	(very weakly coupled symmetric/ antisymmetric geminal pairs)	3742
v_c	(H-bonded vicinal pair)	3600
v_d	(silanol of a vicinal pair)	3720 cm^{-1}

There is considerable dispute over the assignment of IR frequencies. Hair and Hertl [57] suggest that the band at 3747 cm^{-1} is due to single OH groups (v_a) while bands at 3751 and 3743 cm^{-1} are due to geminal OH groups (v_b). Ghiotti et al [58] observed a sharp band at 3748 cm^{-1} for highly dehydroxylated Aerosil silica (1.5 OH/nm^2), assigned to v_a and bands at 3540 and 3720 cm^{-1} for fully hydroxylated Aerosil silca corresponding to v_c and v_d respectively. In addition, bands at 3680 and 3450 cm^{-1} were observed. Band splitting at 3750 cm^{-1} has been contested [59-62] with

authors finding no splitting or no distinct shoulder. On
silica surfaces pretreated above 473K isolated, geminal and
vicinal groups are obviously present . The two modes v_a and
v_b are observed between 3742 and 3751 cm^{-1}, with the band
from the hydrogen bonded vicinal pair (v_c) absorbing at 3540
- 3600 cm^{-1} [49,50,58,63,64]. The band between 3640 and 3660
cm^{-1} is ascribed to inaccessible internal hydroxyl groups,
since this broad band exhibits no isotope shift on H-D
exchange with D_2O.

Morrow and McFarlan [65] have used FTIR spectroscopy to
study the vibrational modes associated with free (isolated)
silanol groups on an aerosil and a precipitated silica,
activated in vacuum in the temperature range 450-800°C.
Activation at 450°C removes virtually all the hydrogen-
bonded silanols [54-56,66-69]. Spectra were obtained at 22
and -191°C and are shown in Figures 1.5 - 1.8.

Figure 1.5 Infrared spectra of aerosil and precipitated
silicas activated at 800°C

Aerosil silica
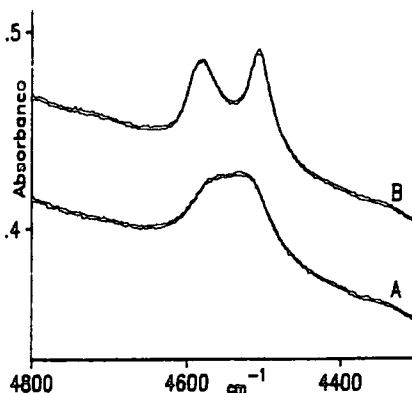
Precipitated silica
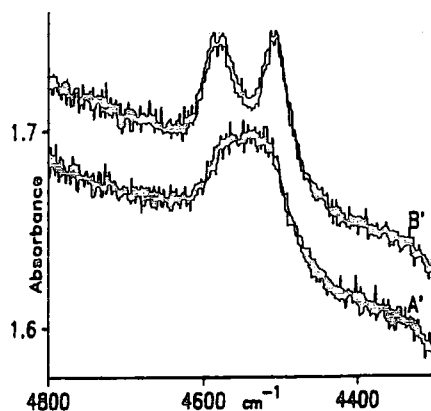
Spectrum obtained at 22°C (A and A')
Spectrum obtained at -191°C (B and B')

Figure 1.6 IR spectra of aerosil and precipitated silica at
-191°C after activation at 450, 800 or 1000°C
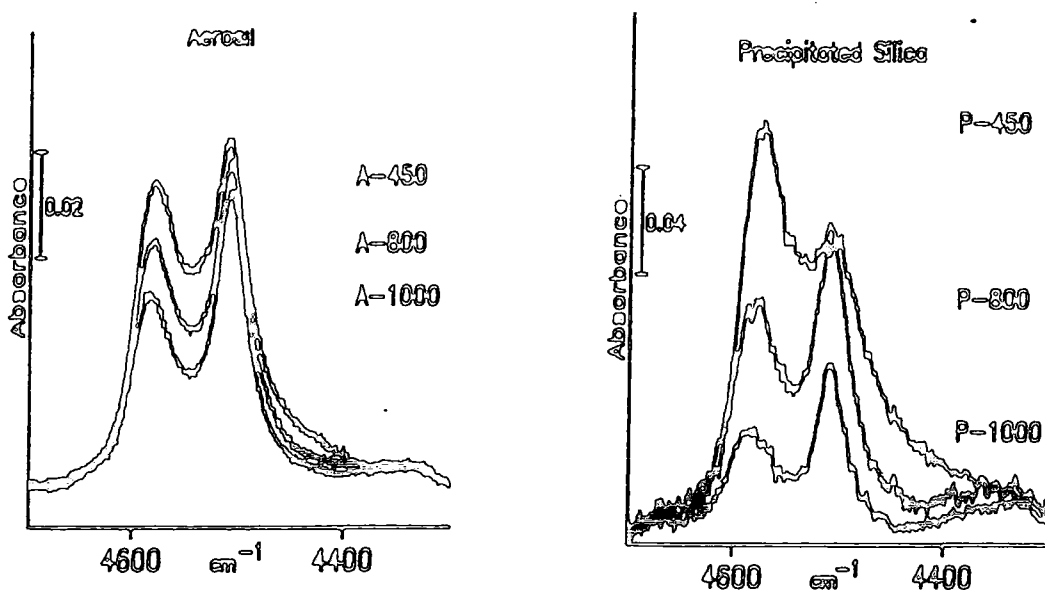
Figure 1.7 IR spectra of aerosil and precipitated silica at
22°C after activation at 450, 600 or 800°C
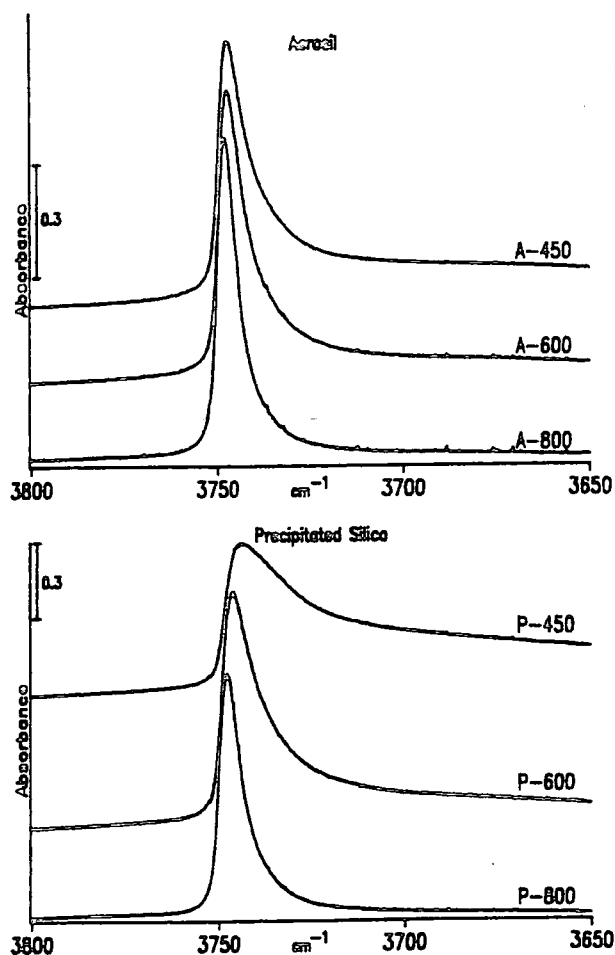
Figure 1.8 IR spectra of the same samples after cooling to
-191 °C
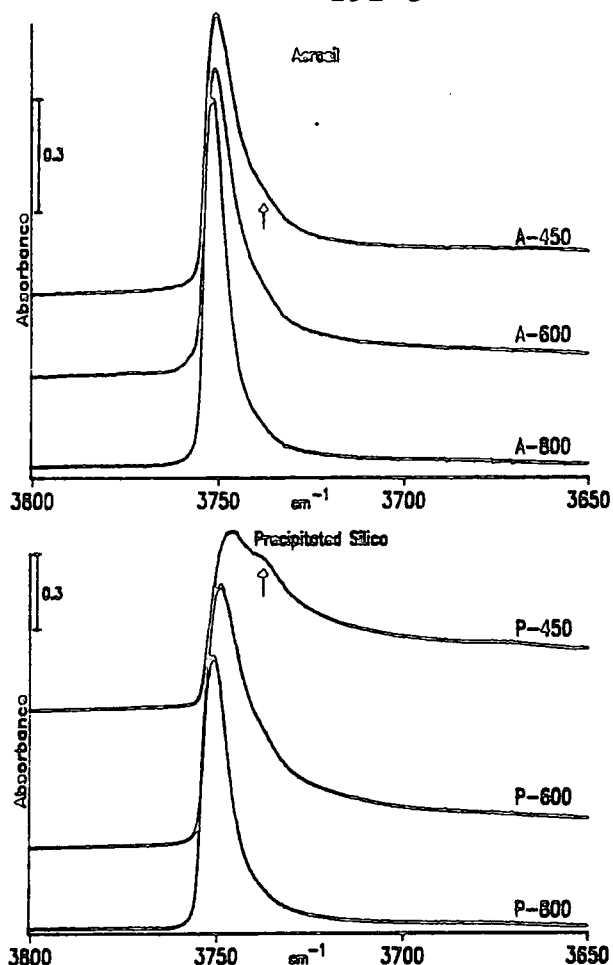
(i) 5000-4000cm^{-1} spectral region

A broad peak centred near 4550cm^{-1} is observed for both aerosil and precipitated silicas at 22°C (Figure 1.5). On cooling to -191°C a well resolved doublet having maxima at 4580 and 4510cm^{-1} was observed. Figure 1.6 shows the spectra of both silicas at -191°C after vacuum activation at 450, 800 or 1000°C and it is apparent that the intensity of the 4510cm^{-1} peak decreases much faster than as the activation temperature is raised, with the change being much more pronounced for precipitated silica. After 1000°C activation the spectra for both silicas are similar.

(ii) 4000-3000cm^{-1} spectral region

In the 4000-3000cm^{-1} region the bands were assigned as follows at 22°C:

3720	H-bonded pairs or chains of silanols
3520	" "
3650 cm^{-1}	Silanols perturbed by interparticle contact

After activation at 450°C these bands have largely disappeared leaving a relatively sharp but asymmetric peak near 3745cm^{-1} (Figure 1.7). This band has been attributed to isolated, non-interacting silanol groups. On cooling to -191°C a distinct shoulder emerges near 3738cm^{-1} (Figure 1.8) for both silicas activated at 450°C. This disappears in the spectra of the 800°c activated samples but is still evident in the spectrum of the precipitated silica activated at 600°C.

On cooling, the 3745cm^{-1} peak mimics that of the 4550cm^{-1} peak in the combination band region, demonstrating that they are probably closely related. The intensity of the 3738cm^{-1} shoulder closely follows that of the 4580cm^{-1} band.

A peak observed at 980cm^{-1} is known to be due to the silicon-oxygen stretching mode of isolated silanol groups [56,70-74]. Interestingly, the use of CO as a probe molecule with samples activated at 450°C leads to the observation of loss of vibrational modes at 840 and 760cm^{-1} and growth of a new feature at 870cm^{-1}. H/D exchange at 22°C of the activated samples led to an observed replacement of the Si-OH 840/760cm^{-1} pair by a single band at 610cm^{-1} (Figures 1.10, 1.11).

Figure 1.9 *IR spectra of aerosil silica following addition of carbon monoxide*
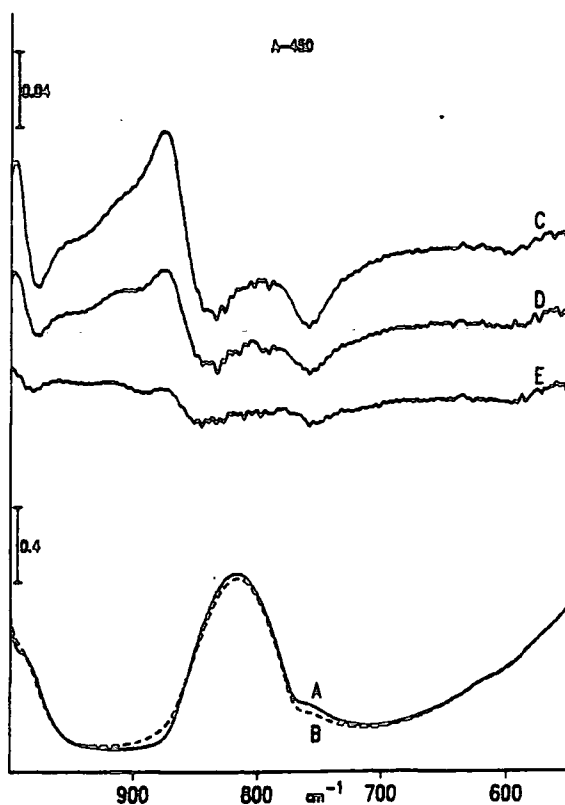
A Activated at 450°C, 0.84 Torr helium at -191°C
B After evacuation of A followed by addition of 2.03 Torr CO
at -191°C
C Difference spectrum B - A
D and E Difference spectra where the equilibrium pressure of
CO was 0.52 and 0.1 Torr respectively

Figure 1.10 *IR spectra of precipitated silica following*
addition of carbon monoxide
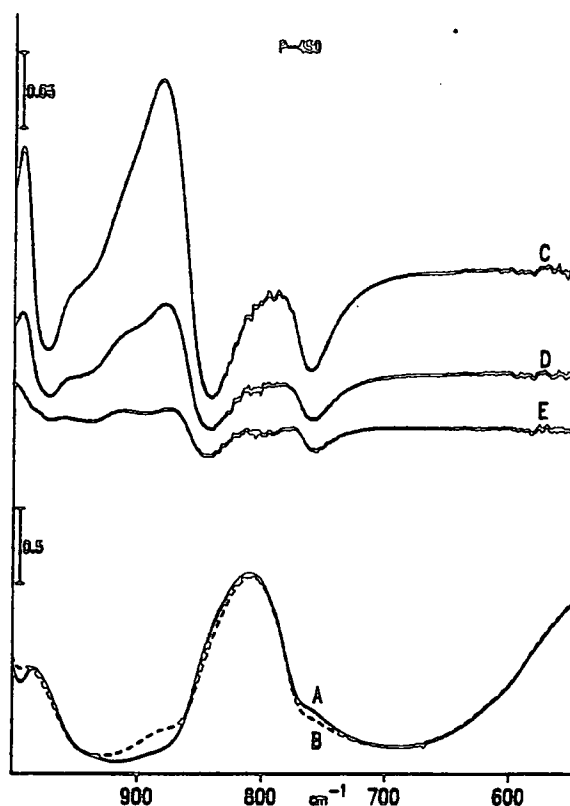
A Activated at 450°C, 0.50 Torr helium at -191°C
B After evacuation of A followed by addition of 0.53 Torr CO
at -191°C
C Difference spectrum B - A
D and E Difference spectra where the equilibrium pressure of
CO was 0.07 and 0.02 Torr respectively

The 840 and 760 cm^{-1} bands cannot be assigned to SiOH
angle deformation modes of a single surface species because
their relative intensity changes with activation temperature
and similar changes are observed for absorptions at
3740/3750 and 4580/4510 cm^{-1} for both silicas. Considering
these changes in relative intensity as a function of the
activation temperature the bands at 4510, 3750 and 760 cm^{-1}
can be attributed to a unique surface silanol species (I)

whereas 4580, 3740 and 840 cm^{-1} are due to a second different silanol species (II) [65].

The OH stretching band becomes progressively more symmetric at higher temperatures of activation and at 1000°C the silanol band is entirely due to species I, attributed to isolated single silanols as these are the last to be eliminated [16,54-56,66-69,75]. Species II is a minority species which is preferentially eliminated as the temperature of activation is raised. Species II was initially thought to be geminal silanols Si(OH)$_2$ as theoretical calculations have shown that the vibrational modes of this species are expected to be very close to isolated single silanols [76]. Also of relevance, the v(OH) frequencies of Me$_3$SiOH and Me$_2$Si(OH)$_2$ differ from each other by only 2 cm^{-1} [77,78]. A summary of the spectral assignments is given in Table 1.3.

Table 1.2 Observed frequencies and assignments for isolated surface silanol species at -191°C

observed, cm^{-1}	assignment
610	δ(Si-O-D) of I/II
760	δ(Si-O-H) of I
840	δ(Si-O-H) of II
960	v(Si-OD) of I/II
980	v(Si-OH) of I/II
2756	v(SiO-D) of II
2763	v(SiO-H) of I
2850	τ(SiOD) + v(SiO-D) of I/II
3370	δ(Si-O-D) + v(SiO-D) of I/II
3740	v(SiO-H) of II
3750	v(SiO-H) of I
3870	τ(SiOH) + v(SiO-H) of I/II
4510	δ(Si-O-H) + v(SiO-H) of I
4580	δ(Si-O-H) + v(SiO-H) of II

The far infra red studies of Hoffmann and Knozinger [75] showed two broad bands centred around 148 and 127 cm^{-1} (Figure 1.11). The isotopic ratios of the band positions on deuteration prove that the modes have to be described as torsional motions of OH groups with respect to the Si-O bond. It is likely that they are related to geminal and single free OH groups respectively. Very weak absorption signals below 150 cm^{-1} could only be manifested by spectral subtraction.

<u>*Figure   1.11*</u> *Far IR spectra of undeuterated and deuterated*
silica activated at 600, 900 and 1100°C
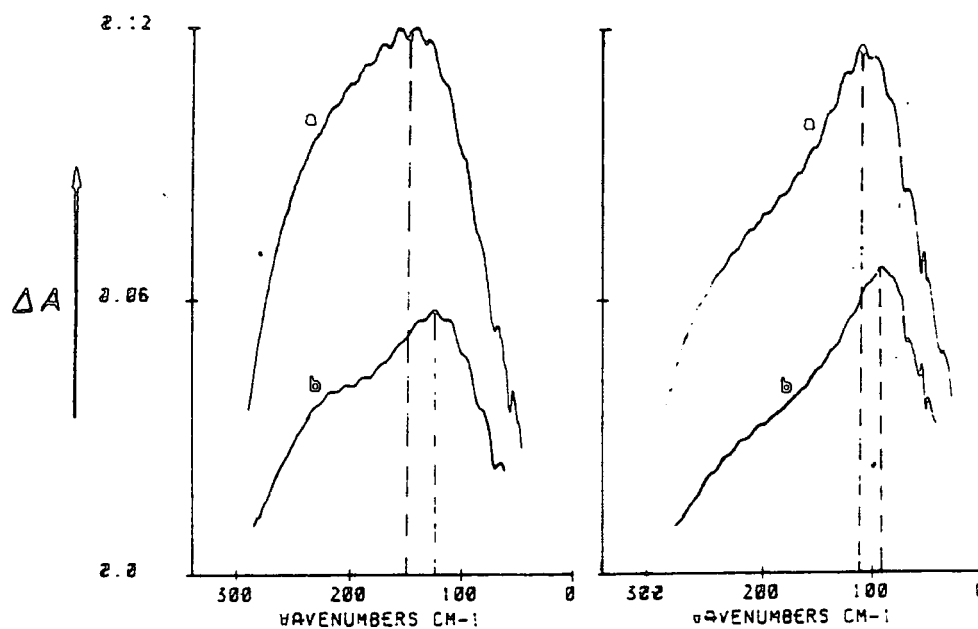
a   Spectrum obtained at 600°C - spectrum obtained at 900°C
b   Spectrum obtained at 900°C - spectrum obtained at 1100°C

2.5 NMR studies of silica

Several ^{29}Si NMR studies have indicated that the ratio of
geminal   to   single   isolated   silanols   does   not   vary
significantly according to the type of silica or with the
temperature of activation under vacuum [79-83]. For all
types of silica activated upto 800°C a ^{29}Si NMR signal, due
to geminal [Si(OH)$_2$], was detected at all temperatures [84].
Maciel   and   Sindorf   [81] used ^{29}Si CP/MAS   NMR   to study
silica   gel   at various stages of dehydration upto 1100°C.
Spectra are shown in Figures 1.12 - 1.16.

17
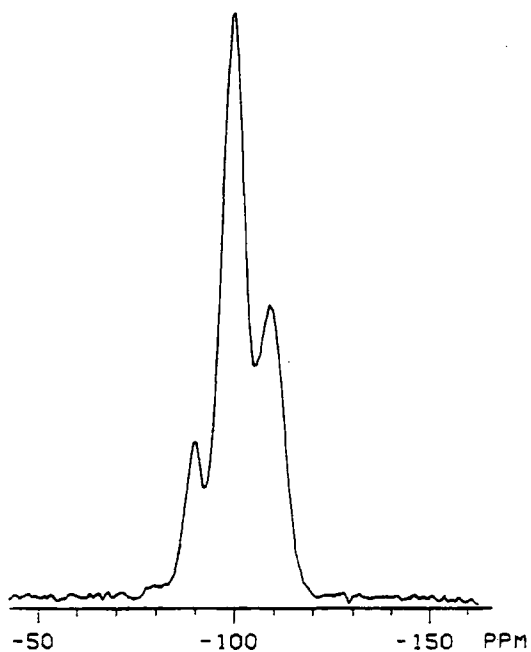
-89ppm   assigned to geminal hydroxyl silanol sites
-100ppm   assigned to single hydroxyl silanol sites
-109ppm   assigned to surface silicons of the type: $(SiO)_4 Si^{*}$

Figure 1.13 ^{29}Si CP/MAS NMR spectra of silica gel dehydrated
at 209-567°C

18
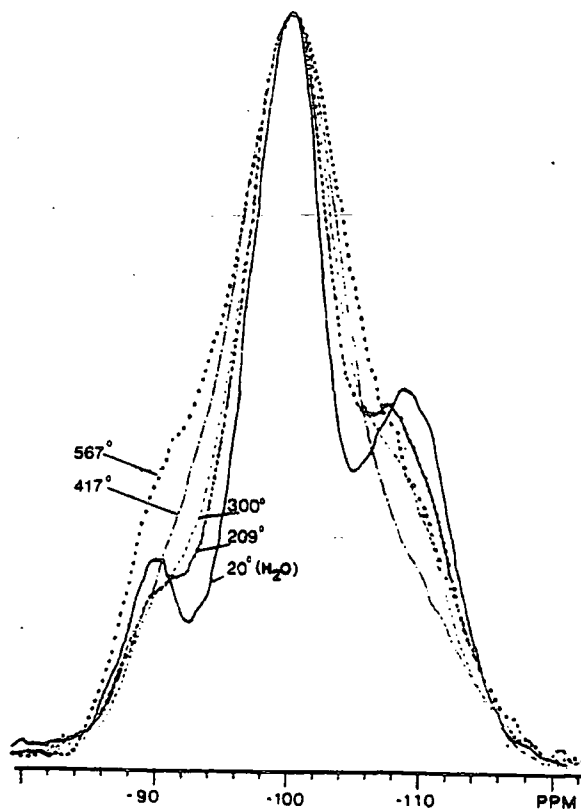
Figure 1.14 *^{29}Si CP/MAS NMR spectra of silica gel dehydrated at 650-800°C*
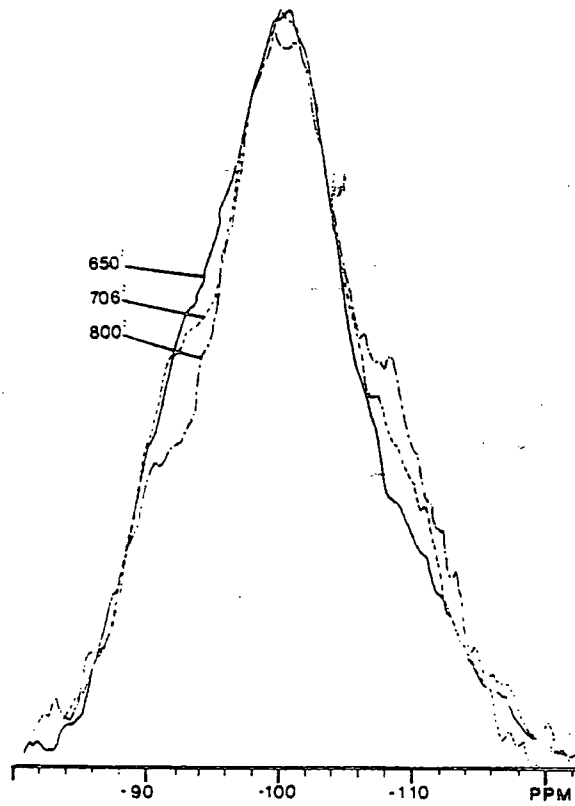
Figure 1.15 *Plot of fractional population of geminal sites measured for dehydrated and rehydrated samples vs. dehydration temperature*
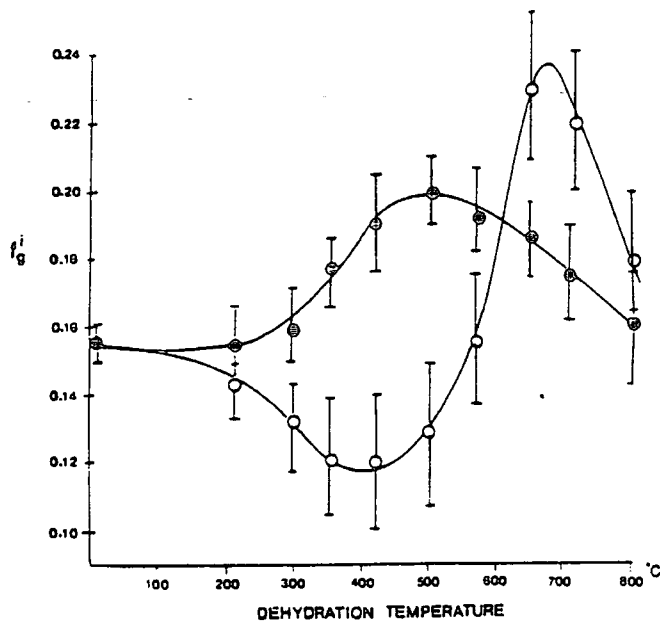
Figure 1.16 *Estimated fractions of original single-hydroxyl and geminal-hydroxyl sites remaining vs. dehydration temperature*
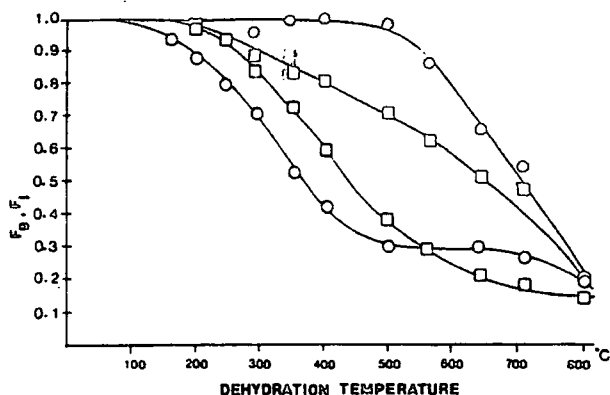
O geminal sites after dehydration
O geminal sites following rehydration
□ single sites after dehydration
□ single sites following rehydration

At 20°C, f_g the fraction of geminal sites, is 15.5%, the majority of the surface silanols being single isolated Si-OH species, and the fraction decreases to 12% at 350-400°C (Figure 1.15). Above 400°c there is a sharp increase in the relative population of geminal sites which reaches a maximum of 24% at 650°C before decreasing again at higher temperatures. Figure 1.16 shows that from 200-500°C condensation occurs preferentially for geminal hydroxyl sites, whilst from 500-700°C the geminal population remains essentially constant. This has been confirmed by DTG [85].

The behaviour of the single and geminal OH sites follows that for the overall OH population and therefore a chemical equilibrium which is independent of the total number of OH groups at the silica surface is established.

Leonardelli *et al* [23] found the fraction of geminal sites remains constant for all samples studied. This was generalized to all amorphous silica exposed to water whatever treatment they have undergone. It seems possible that a proportionality could exist between the number of single and geminal OH sites in these samples and IR indicates that there is no difference between single and geminal OH sites in their behaviour when water molecules are adsorbed [76]. It was calculated that 30% of the OH groups in amorphous silica are present as geminal groups; the remaining 70% could be single or vicinal OH groups. This population of geminal groups has already been found on a deactivated silica gel at 25°C [81].

20

2.6 Effects of porosity on the reactivity and distribution of surface hydroxyl groups

Van der Voort *et al* [85,86] have studied the effect of porosity on the distribution and reactivity of OH groups on the surface of silica gel. Three types of silica gel with different pore distributions were used and the quantitative distribution of the isolated and hydrogen-bonded OH groups on the surface were calculated. Their reactivity was studied by chemical modification with trichlorosilane (TCS), probed by titrimetric determination and FTIR with photoacoustic detection.

A decline in the number of hydrogen-bridged OH groups with an increase of isolated ones was observed as a function of increasing temperature. The increase in isolated OH groups is caused by the random condensation of hydrogen-bonded OH groups. This is consistent with the condensation reaction:

$$\text{(I)}$$
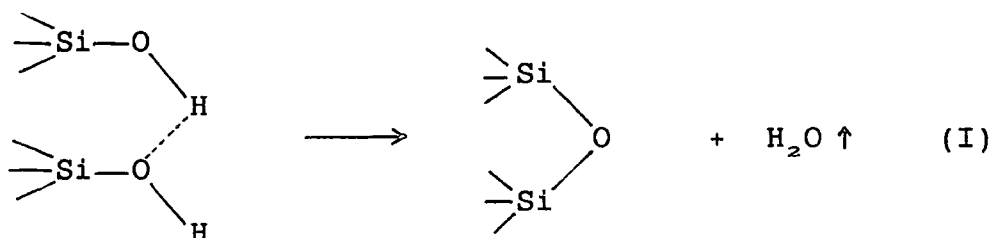
A recent study noticed a contribution from the condensation of geminal OH groups [86]:

$$\text{(II)}$$
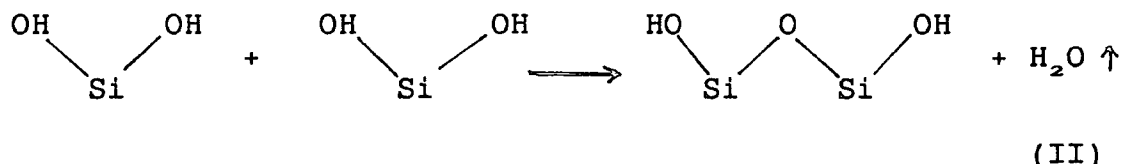
It was found that fewer hydrogen-bonded OH groups remain after high temperature degassing of silicas with smaller pore radii. Reaction I proceeds at lower temperatures for silicas with smaller pore volumes, which was explained by the perturbation degree: the greater the pore radius, the greater the intersilanol distance and the more "isolated character" the hydrogen-bonded silanols have. Isolated silanols only condense with difficulty.

TCS does not react exclusively with free hydroxyl groups [63] but reactivity of bridged OH groups was found to be low. There is total conversion of free OH groups after 17 hours for all samples, which indicates that porosity has no straightforward effect on the reactivity of free OH. This is understandable since isolated OH groups are not affected by their environment. Bridged OH groups are affected by the pore radius of the material used. Small pore radii leads to

less reactivity towards TCS and only the gel of lowest pore size was able to influence reactivity.

Reaction with hydrogen-bonded hydroxyl groups occurs only in the low pretreatment temperature region (there are no hydrogen-bonded OH groups at high temperature). The pretreatment temperature had a great impact on reactivity towards isolated and hydrogen-bonded OH. (At low temperatures TCS reacts predominantly with hydrogen-bonded OH; exclusively with isolated OH at high temperatures).

2.7 X-ray Photoelectron Studies of silica surfaces

Legrand *et al* [83] have reviewed studies of silica using XPS. Figures 1.17 - 1.19 show their results for aerosil (A) and silica gels (P and G).

Figure 1.17 C 1s spectra for aerosil and silica gel samples
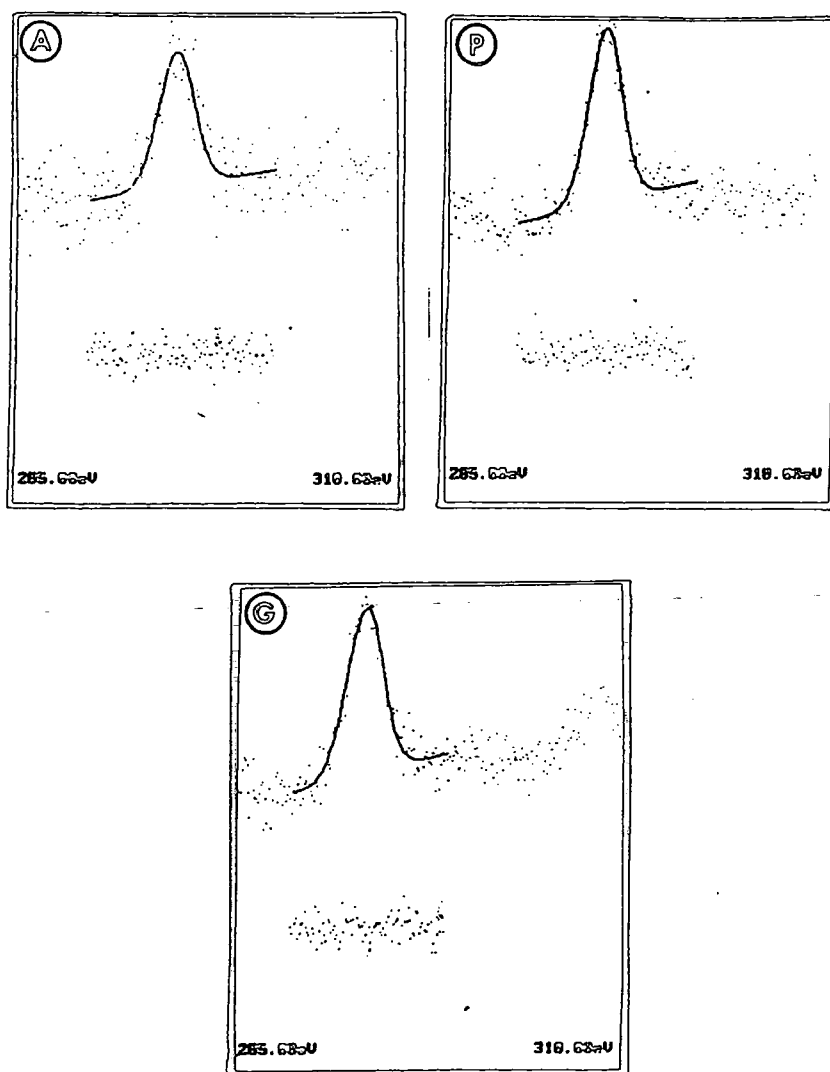
Figure 1.18 *Si 2p spectra for aerosil and silica gel samples*

23
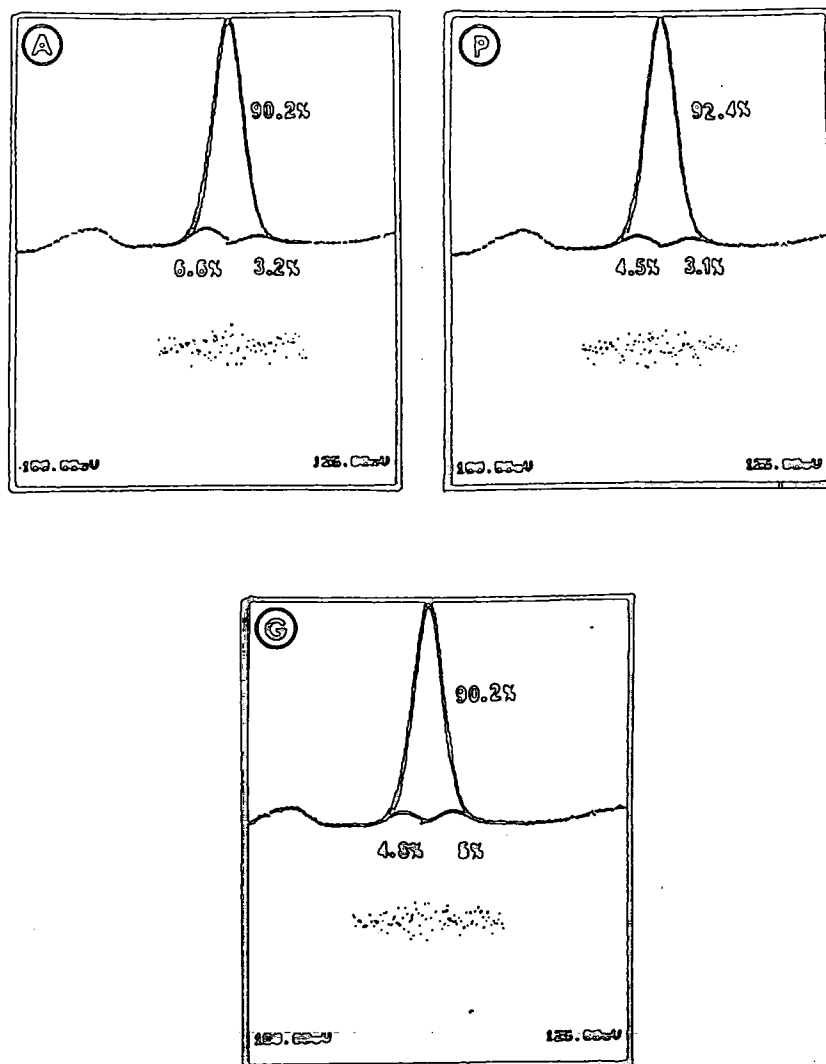
Figure 1.19 _O 1s spectra for aerosil and silica gel samples_
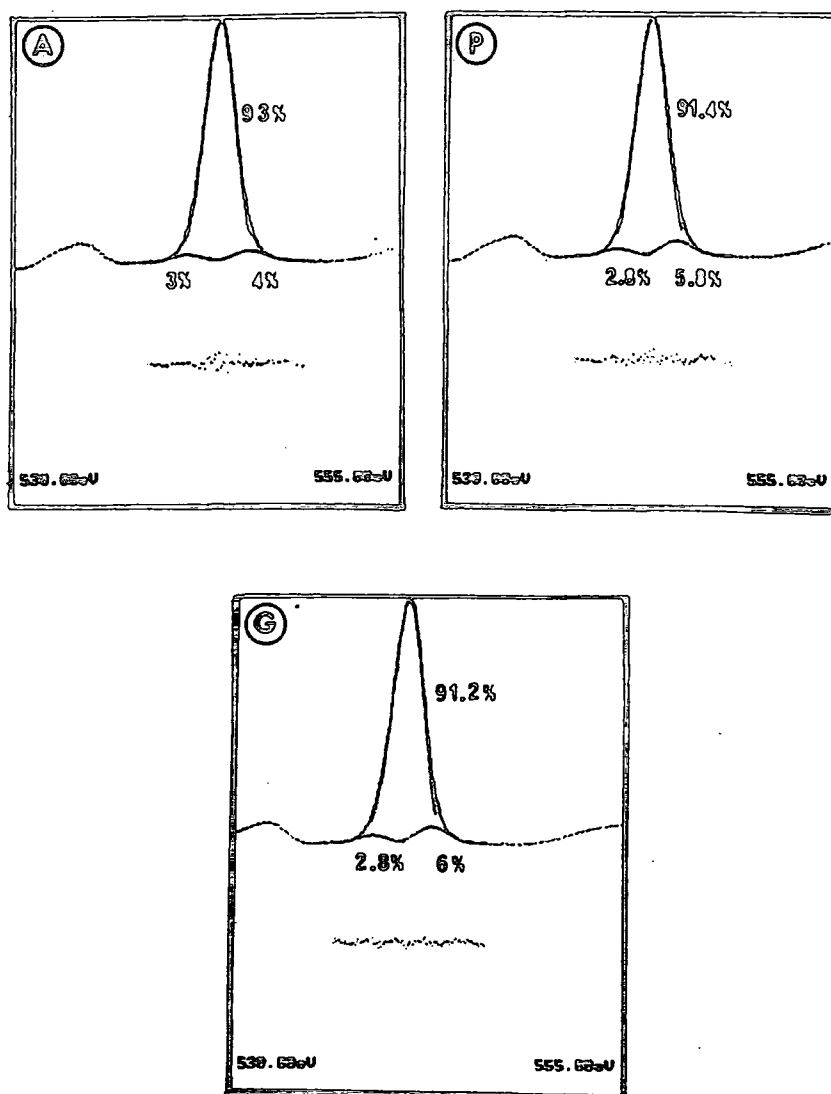
Analysis of the O_{1s} and Si_{2p} spectra reveals the presence of three components:
(i) Si-O-Si binding energies of O_{1s} 532.3eV, Si_{2p} 103eV
(ii) Binding energies of O_{1s} 534eV, Si_{2p} 104.7eV attributed to silanols
(iii) Binding energies of O_{1s} 530.5eV, Si_{2p} 101.7eV assigned to oxygen and silicon atoms respectively having an increased electron density. This may result from the presence of silanolate functions or the formation of Si-O* radicals from ion bombardment . In the case of silicas it can be equally understood that an unsymmetric bond stretching of a siloxane bridge (Si-O-Si) will bring about the same effect. Also, where silicas are non-stoichiometric (oxygen

deficient) the peaks will be driven to lower binding energy.

Table 1.4 Percentage contributions of the Si-O components to the O 1s and Si 2p peaks

	Si-O--Si or Si---Si		Si-O-Si		Si-OH	
	Si 2p	O 1s	Si 2p	O 1s	Si 2p	O 1s
A	6.6	2.9	90.2	93.0	3.2	4.1
P	4.5	2.8	92.4	91.4	3.1	5.8
G	4.8	2.8	90.4	91.2	5.0	6.0

The results in Table 1.4 show that the surface layers are essentially composed of silanol groups but also oxygen deficient (non-stoichiometric) sites and strained siloxane bridges.

3 Silica supported titania

3.1 Introduction

Titania supported on silica is of considerable interest both as a catalyst and as a support. Titanium in TiO_2/SiO_2 can catalyse oxidation reactions such as that of CO and photooxidation of methane [88,89]. It also oxidises carbonaceous compounds deposited on its surface during the decomposition of chlorinated organics and maintains its catalytic activity [90]. The mixed oxides are very promising model systems as a support for metal catalyst preparations and investigation of Strong Metal-Support Interaction (SMSI) phenomena because at low TiO_2 concentration Ti ions may be considered as isolated and immobilized in the silica matrix [91]. Its SMSI characteristics [92] give it a higher catalytic activity than unmodified silica supported transition metal ions [93] and it has been shown that titania-silica exhibits SMSI behaviour for supported iridium and nickel [94-96]. Titanium ions on the silica surface increase the dispersion of cobalt and give increased relative yields of hydrocarbons and ethanol during CO hydrogenation [3].

3.2 Preparation

The titania-silica systems can be prepared using liquid impregnation, vapour phase deposition, which deposits titania on the silica surface, or by coprecipitation of two precursors [98-102]. This latter method appears to give

catalysts with the mechanical properties of silica and the chemical properties of the active support titania. A complication is that mixed oxides i.e. those samples prepared by coprecipitation, often develop acidic properties, becoming more acidic than silica-aluminas [103], and the acidic support can also interact with the metal [104,105], which can be undesirable in certain cases. The catalytic activity has been correlated with the surface acidity [106].

3.3 SiO_2/TiO_2 Cogels

Cogels have been prepared by coprecipitation using (i) $TiCl_4$ and $SiCl_4$ mixtures in methanol solution and addition of NH_4OH [96], (ii) from Na_2SiO_3 and $TiCl_4$ [107], (iii) from titanium (IV) isopropoxide and ethyl silicate in ethanol solution [108] and (iv) from $Ti(NO_3)_4$ and $Si(OEt)_4$, precipitated from acid solution by addition of aqueous ammonia [91].

A study by Ko et al [96] used samples with compositions from 0-100% TiO_2. Pure titania crystallized as anatase, the rest of the samples being amorphous after calcination, according to XRD studies. Imamura et al [108] found anatase-like diffraction peaks for 75:25 $TiO_2:SiO_2$ samples, with no diffraction peaks at lower titania contents. TEM showed that 50:50 $TiO_2:SiO_2$ samples had mainly anatase structure, although a weak pattern due to rutile was also observed. A mean particle size of 90A for TiO_2 was obtained from TEM. No crystallized TiO_2 was visible in a 30% TiO_2 sample. SEM suggested that the two oxides were distributed homogeneously in mixed oxides.

3.3.1 The acid strength and acidity of SiO_2/TiO_2 cogels

The acid strength has been determined with six Hammett indicators and the acidity measured by n-butyl amine titration. It was found that the mixed oxides have greater surface acidity and greater acid strength than either of the pure components [107]. This is consistent with the hypothesis of Tanabe [109], that acidity is produced by a charge imbalance resulting from the difference in the coordination states of Ti^{4+} and Si^{4+}. The generation of acid sites on TiO_2/SiO_2 prepared from ethylorthosilicate and $TiCl_4$ was reported by Itoh et al [111]. Results also suggest that the relative concentrations of Bronsted and Lewis sites vary with the composition of these mixed oxides. Stronger sites are present on powders having Ti:Si ratios of 25:75, in agreement with Odenbrand et al [107].

In Odenbrand's study of mixed oxide systems the acidity was characterised by TPD of adsorbed ammonia and by IR studies of various probe molecules such as pivalonitrile (PN), pyridine, ammonia and n-butylamine [107]. The spectra

of PN adsorbed on samples with 25-99% TiO$_2$ contain both the features of PN adsorbed on the silanol groups (absorption band at 2245cm^{-1}), easily desorbed by evacuation at room temperature, and on Ti^{4+} groups of titania (absorption band at 2285cm^{-1}), resistant to evacuation at room temperature (Figure 1.20).

Figure 1.20 FTIR spectra of pivalonitrile adsorbed on SiO$_2$ (A), 50% TiO$_2$/SiO$_2$ (F) and TiO$_2$ (K) (vCN region)
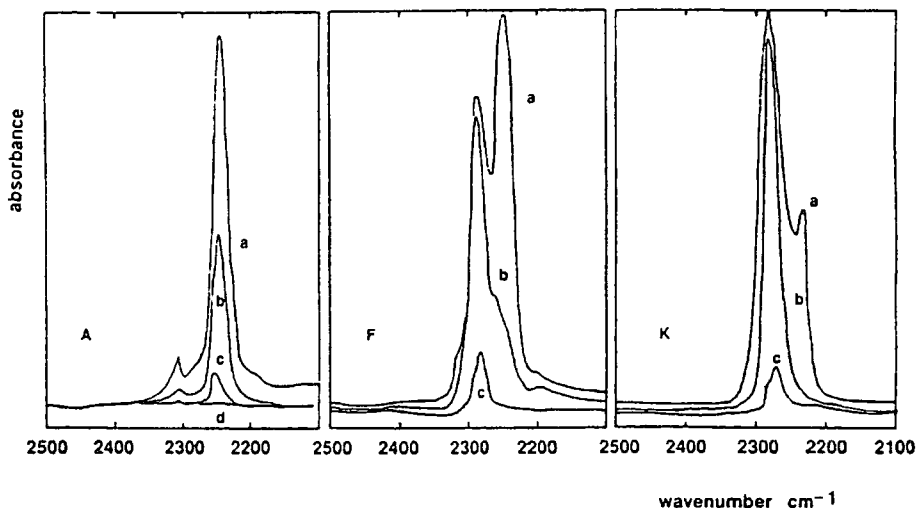
A a) 0.1 Torr PN vapour, b) evacuation at room temperature 5 mins., c) 15mins, d) 30mins
F and K a) 0.1 Torr PN vapour, b) under evacuation at room temperature for 30mins, c) evacuation at 167°C for 30 mins

These features have different relative intensities dependent on the SiO$_2$/TiO$_2$ ratio. At very low coverages on 10% TiO$_2$ a further component is observed at 2308cm^{-1}, more stable to evacuation. On the basis of both the very strong shift of the v(CN) band and its strong stability to evacuation, this species must be coordinated to very strong Lewis sites. Though few in number these sites are extremely strong and characterise this sample as one of the most acidic solids as far as the strength of acid sites is concerned. This result accords with those arising from CO adsorption [98].

PN adsorption can also be used to check the Bronsted acidity of solids through the measure of the shift of the v(OH) band of acidic OH groups. These bands are centred near 3350cm^{-1} on silica, near 3300cm^{-1} on the sample with 10mol% titania, while on samples containing more titania they shift to higher frequencies, at ca. 3340cm^{-1}. This indicates that the surface Bronsted sites are stronger in the 10mol% titania sample than in silica alone, and are definitely

weaker in samples with high titania contents.

The results concerning pyridine adsorption confirm the above data and show: (i) Lewis sites are associated with Ti^{4+} cations present on the surface of titania and all titania-containing materials; (ii) very weakly acidic silanol groups predominate on the surface of silica together with a few stronger Bronsted sites; (iii) relatively stronger Bronsted acidic silanol groups are present on the samples containing both silica and titania (these sites hydrogen bond pyridine strongly but are not able to protonate it), and (iv) these stronger sites are present in relatively large amounts on the sample containing 10% TiO_2, where silica-containing Ti^{4+} ions are more predominant than on samples with 50-99.5% TiO_2 contents, where silica covers bulk titania. This implies that these more acidic silanols are associated with the phase consisting of a saturated solid solution of titania in silica. Thus at lower titania contents a substitutional solid solution of titania in silica is the predominant phase. With greater titania content silica covers the anatase phase producing silica supported on titania. Analogous results were obtained using ammonia as the basic probe molecule. Figure 1.21 shows the distribution of acid strength for the TiO_2/SiO_2 samples.

Figure 1.21 *The distribution of acid strength for mixed*
TiO_2/SiO_2 catalysts derived from TPD curves in
the region 150-400°C
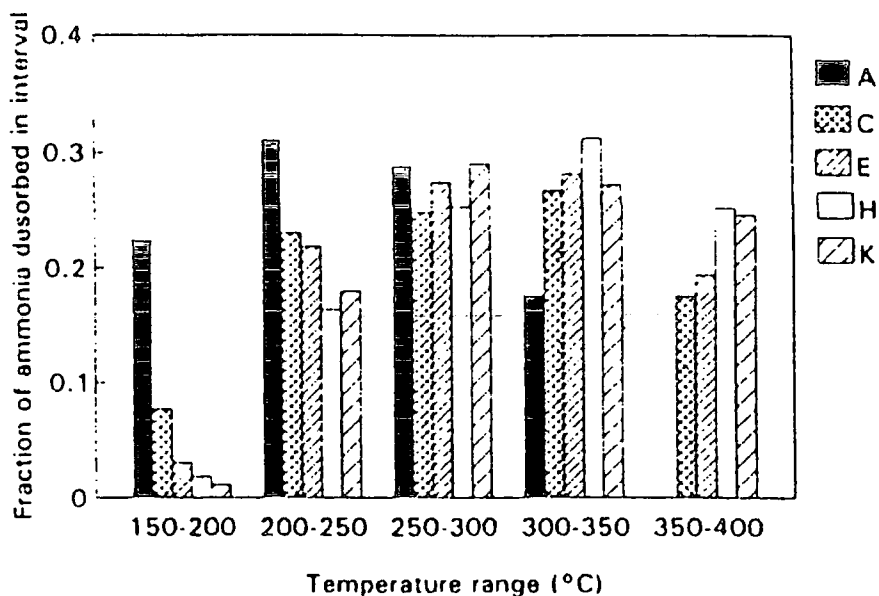
A SiO_2
C 10% TiO_2/SiO_2
E 50% TiO_2/SiO_2
H 90% TiO_2/SiO_2
K TiO_2

At lower titania contents there are two types of Lewis acid site. The very strong sites are Ti^{4+} ions in an incomplete tetrahedral coordination exposed at the surface. FTIR [98] has detected T_d substituted Ti^{4+} in the silica phase. The number of such sites is probably very small due to the small solubility of Ti^{4+} in the silica framework. The amount is expected to decrease along the with the decrease in the amount of silica. These sites are not seen on anatase or rutile because titanium is in an octahedral coordination here.

Imamura et al [18] found no clear evidence for Lewis acid sites in an IR study of pyridine adsorption where bands at 1447, 1490 and $1540cm^{-1}$ were seen for samples containing 75, 50 and 25% TiO_2. The absorption band at $1447cm^{-1}$ arises from pyridine coordinated to a Lewis acid site or physically adsorbed through hydrogen bonding. Pyridine coordinated to Lewis sites and pyridinium coordinated to Bronsted sites gave rise to $1490cm^{-1}$, and the $1540cm^{-1}$ absorption is due to a ring vibration of the pyridinium ion on Bronsted sites.The number of acid sites was found to reach a maximum at a TiO_2 content of 60% (Figure 1.22). Interaction between silica and titania is necessary for the production of acid sites and their strength depends on the titanium content and the grain size, in agreement with Nishikawa et al [112] who reported that decreasing the particle size of titania resulted in charge imbalance produced acid sites are produced even in the absence of silica.

Figure 1.22 *The number of acid sites per unit surface Ti atom.*
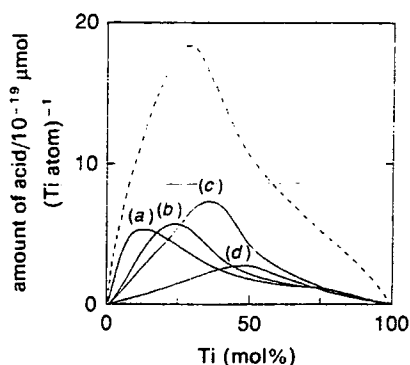
The acid sites were sorted according to their acid strength:
a) $1.5 < H_o < 3.3$, b) $-3.0 < H_o < 1.5$, c) $-5.6 < H_o < -3.0$
d) $-8.2 < H_o < -5.6$
---- $H_o < 3.3$

For both Lewis and Bronsted sites the ability of the sites to accommodate electrons is important in determining

the acid strength. With high TiO_2 contents and large grain sizes electrons donated by bases or protons can be easily accommodated since the band gap between the valence and conduction bands is relatively small (for a particle size of 200A) and hence strong acidity is exhibited (Figure 1.23). For low TiO_2 contents there are mainly weak acid sites due to the low electron accepting (withdrawing) ability of the small grains. The maximum number of strongest acid sites was found at 50mol% TiO_2 where there is a balance between the number of acid sites produced and the effect of TiO_2 grain size.

Figure 1.23 Energy level diagram showing the dependence of band gap on particle size
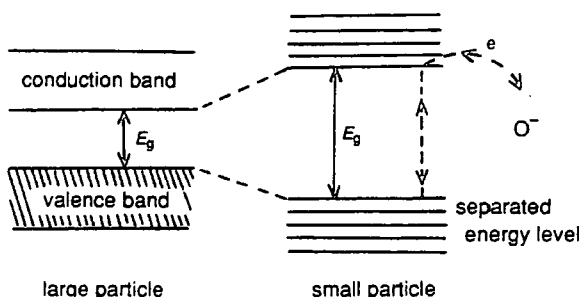
All silica-titanias remain weak Bronsted acid solids, being unable to protonate a relatively weak base such as pyridine and stronger bases such as ammonia. High acidity reported by previous authors [96,103,106,113] can therefore be attributed mostly to Lewis acid strength. These are similar to the findings of Kataoka and Dumesic [96,98,111,114].

3.3.2 Structural studies

Odenbrand *et al* [98] studied the structural properties of a series of coprecipitated catalysts containing 0-100% TiO_2. These samples were found to be micro, meso and macroporous. All these textural quantities decrese with the addition of titania to silica. The macroporosity reaches its maximum value at 50mol% TiO_2.

The increasing binding energy of Ti $2p_{3/2}$ when silica is incorporated and the decreasing Si 2p binding energy in the XPS spectra indicate clearly that there is an electronic interaction between titania and silica (Table 1.5) [108].

Table 1.5 XPS analysis of titania/silica

Ti (mol%)	Si (mol%)	E_b/eV		
		Ti $2p_{3/2}$	Si $2p_{1/2}$	O $1s_{1/2}$
0	100	—	104.4	534.0
5	95	459.5	104.5	533.5
10	90	459.7	103.6	533.2
20	80	459.5	103.4	533.1
30	70	459.5	103.3	531.8[a] 533.0
40	60	459.5	103.0	531.4[a] 532.9
50	50	459.3	102.7	531.3[a] 532.5
60	40	459.3	102.7	529.9 532.2
75	25	459.1	102.6	529.8 532.2[a]
100	0	458.7	—	529.9

[a] Shoulder peak.

At low titanium concentrations (<10wt% TiO_2) the titanium surface atomic concentration is the same as in the bulk; at higher loadings it is lower than expected- a surface enrichment with silicon is observed [91]. It was concluded that silica concentrates on the surface of titania particles. The measured Si 2p/Ti $2p_{3/2}$ intensity ratio is equal to the calculated one, indicating monolayer distribution.

At low (<10wt%) TiO_2 concentrations qualitative analysis shows a homogeneous distribution of Ti^{4+} in the oxide matrix - a solid solution of Ti in silica. High Ti $2p_{3/2}$ binding energies probably indicate the insertion of Ti^{4+} ions into tetrahedral sites of the silica framework as in silica-titania glasses [115] and titanium silicate [116]. O 1s and Si 2p lines gradually shift to lower binding energy reflecting substitution of silicon atoms by less electronegative and more polarizable titanium atoms in the silica lattice. The dramatic changes in the O 1s, O KLL and Ti $2p_{3/2}$ spectra reflect the formation of a two phase system, containing both titania-rich and silica-rich-titania solid solutions.

The Si 2p binding energy is rather low and the value of $\propto'$-Si (Auger parameter) is high for these samples which are titania rich. Odenbrand showed that silicon tends to substitute titanium cations in the near-surface region of titania [98]. In this case the low Si 2p binding energy observed in high titania content samples might be explained by the formation of a new silica-titania compound. The surface of the titania particles is coated by a monolayer of a new titanium silicate compound.

The observed changes in the XPS spectra can be attributed to a decrease in the effective positive charge on the silica atoms due to the formation of Ti-O-Si bonds. The significant shift in the Si Auger parameter implies dramatic changes in

the coordination of silicon atoms; such as octahedral coordination of silicon in the titania matrix.

3.4 Impregnated TiO$_2$/SiO$_2$ Catalysts

3.4.1 Structural studies

A 7wt% TiO$_2$-SiO$_2$ catalyst was prepared using the impregnation method, by the reaction of a Ti(IV) alkoxide with the surface hydroxyl groups of silica [117]. A physical mixture of 7wt% TiO$_2$ and 93wt% SiO$_2$ was made for comparison. XRD revealed anatase and rutile peaks in the mixture but no crystalline titania in the impregnated sample. Electron microscopy showed the presence of spherical and porous particles in the impregnated sample and EDAX implied a homogeneous distribution of titania at the spatial resolution of the analysis (0.1µm). Reichmann and Bell [118] reported the formation of anatase with crystallite sizes of 7-8µm for similarly prepared material containing 25wt% TiO$_2$. XRD of a 19.9wt% TiO$_2$ catalyst corresponding to one monolayer of surface phase oxide showed no bulk titania peaks, and ATEM confirmed a homogeneous distribution of titanium concentrated over the silica substrate [95]. It is believed that the deposited titania is well dispersed as a surface phase oxide. UV-VIS reflectance spectroscopy supports the high dispersion of titania on silica; the absorption edge of TiO$_2$/SiO$_2$ is shifted towards lower wavelengths and becomes spread over a wider energy range compared to the mixture and titania alone (Figure 1.24).

Figure 1.24 Diffuse reflectance spectra of (a) TiO$_2$/SiO$_2$, (b) TiO$_2$ + SiO$_2$ and (c) pure TiO$_2$
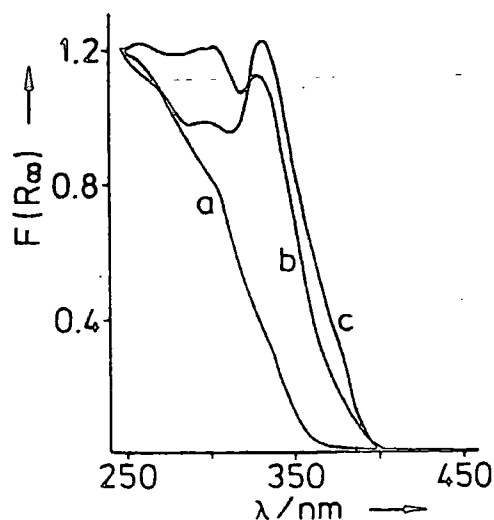
XPS studies also gave information on the dispersion of titania on silica and it was found that the amount of titanium detectable in the physical mixture was significantly less than for the impregnated sample though the wt% was the same. This implies a high dispersion of titania on silica. It was estimated that the Ti/Si ratio is 1/76 in the physical mixture but the experimental value for the impregnated sample is 1/2 [117].

Table 1.6 *XPS data for the TiO_2/SiO_2 catalyst and the physical mixture*

	O (1s)	Ti (2p)	Si (2p)	Ti/Si
TiO_2/SiO_2	69.7	1.3	28.9	1/22
$TiO_2 + SiO_2$	65.3	0.5	34.2	1/67

Tanabe and co-workers also undertook EXAFS/XANES studies of impregnated titania/silica catalysts prepared as above, and containing 7.4, 10.5 and 13.6wt% TiO_2 [119]. Their results are shown in Figure 1.25.

Figure 1.25 *Near-edge structure of titanium-containing samples on the Ti K-edge*
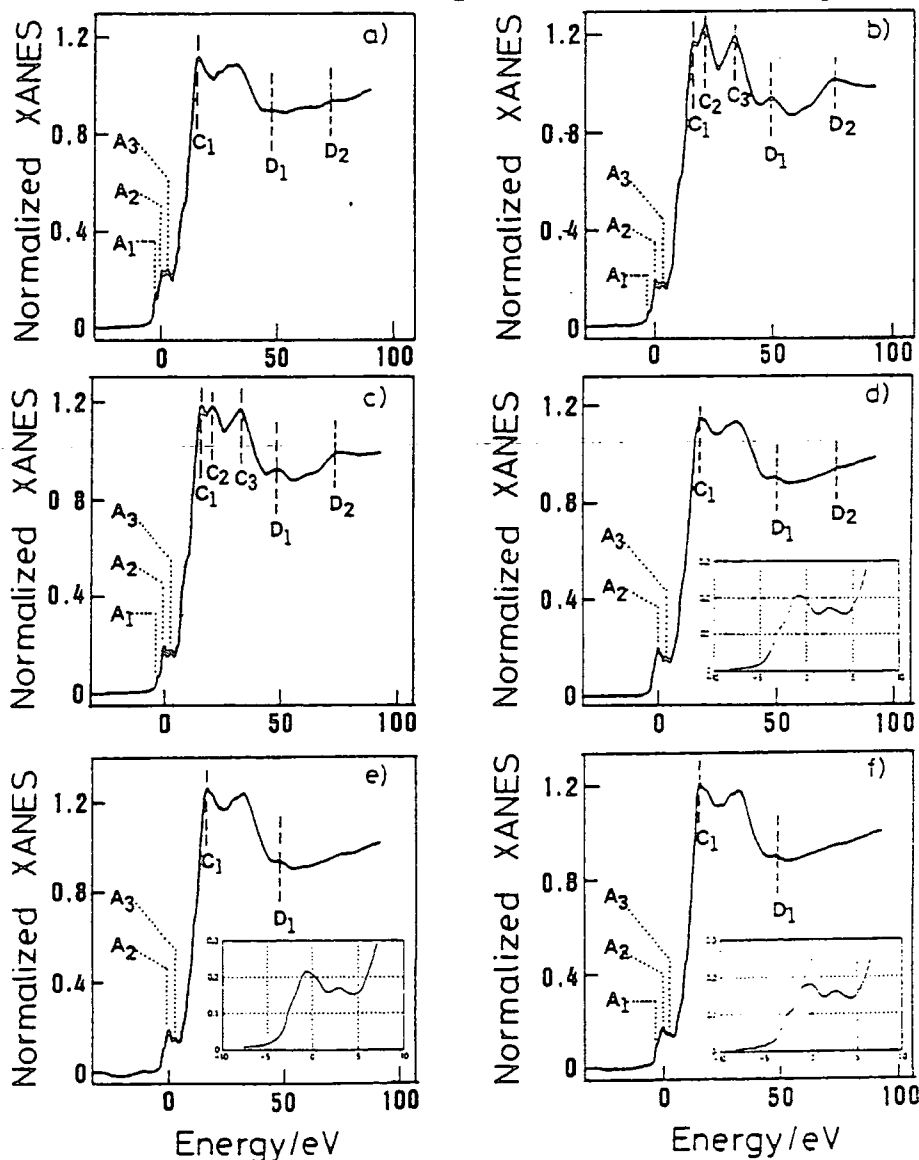
a) Anatase   b) Rutile   c) TiO_2 prepared from calcining $Ti(OPr)_4$ d) 7.4% TiO_2/SiO_2 e) 10.5% TiO_2/SiO_2 f) 13.6% TiO_2/SiO_2

The intensity of the 1s-3d transition was chosen as a good measure to evaluate the coordination environment of the titanium atoms. As the intensity of this peak is not considerable, a Ti tetrahedral structure was thought unlikely. The A_2 peak was intense in the lower weight samples but weaker in the 13.6wt% sample, indicating that the great distortion from octahedral coordination may occur at the earlier deposition stage. At the higher weight % such distortion vanishes and points to an octahedral structure. This implies that the TiO_x species on silica tends to be a TiO_6 octahedron. The main absorption peaks C_1, C_2 and C_3 are assigned to 1s-np dipole transitions and resemble those of anatase. It was therefore tentatively proposed that an anatase-like local structure of TiO_x is formed selectively on silica. From the peaks appearing in the range 2-3 and 3-4A, two types of configuration of Ti-Ti were proposed, as shown in Figure 1.26.

Figure 1.26 *Possible adjacent Ti-Ti configurations in TiO_2*
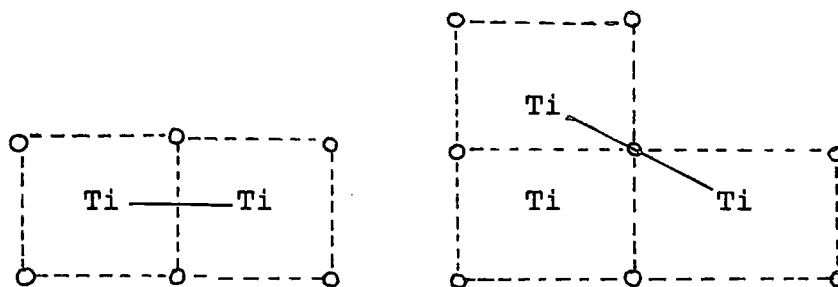
O = oxygen atoms

One configuration is located in the adjacent edge-shared octahedrons (shorter distance) and the other is in the corner-shared octahedrons (at longer distances). These results suggest that the surface species have the anatase-like structure in the short range order and that the crystalline growth is not complete. This deduction is also supported by the results of XRD; the diffraction patterns are detectable only for the 13.6wt% sample. The formation of the precursor amorphous state directing toward anatase phase starts at a small amount of titanium.

Srinivasan *et al* [120] found that crystalline titania was formed after calcination of impregnated catalysts in dry air. Laser Raman spectroscopy identifies the crystalline phase as TiO_2(brookite) at low Ti loadings (<10wt%) and TiO_2(anatase) at higher weight loadings. The formation of

crystalline titania at loadings very much less than the monolayer capacity expected from BET surface area measurements (a monolayer would be 29wt% in this study) implies that the silica surface is unable to stabilize the dispersed metal oxide, behaviour in contrast to other supports such as alumina, where monolayer dispersions are reported [121,122]. In other work [123,124] near-monolayer dispersions of titania are reported. Differences in the ability of silica to stabilize monolayer dispersions of titania in these studies may be due to the specific precursors used in the work and the possible influence of alkaline materials in modifying the silica surface and stabilizing the deposited titania. It should also be noted that it is difficult to detect crystalline titania with XRD since at low loadings the small size of the oxide crystals causes significant line broadening. The absence of lines from the crystalline phase does not rule out the presence of small particles of crystalline oxide.

Titania was dispersed via an alkoxide on Cabosil in a study by Srinivasan et al [120] and also on nonporous silica spheres by the method of Stober and Fink [125]. TEM studies, analysed by EDS, showed that the nonporous silica was coated uniformly with titania and had a wt% of 0.6 where the theoretical monolayer capacity is 1.7%. The 2.8wt% Cabosil sample also showed a uniform coating of titania but the images were obtained at lower magnification due to the excessive charging of fumed silica. On Cabosil crystalline titania (anatase) appears at higher loadings of titania (>3wt%) which implies that the monolayer capacity has been exceeded. A monolayer has been established as 2.8wt%, only 7% of the theoretical monolayer capacity based on BET surface area measurements.

Raman spectroscopy was used to determine the nature of the dispersed titanium species. The samples had to be heated to 973K in dry air to reduce fluorescence. On the spheres there was no evidence for a dispersed titania phase, probably due to the low loading. The absence of bands due to crystalline titania agrees with TEM. The Raman spectra are shown in Figures 1.27 and 1.28.

Figure 1.27 *Raman spectrum of titania-coated silica spheres after heating in dry air at 973K.*
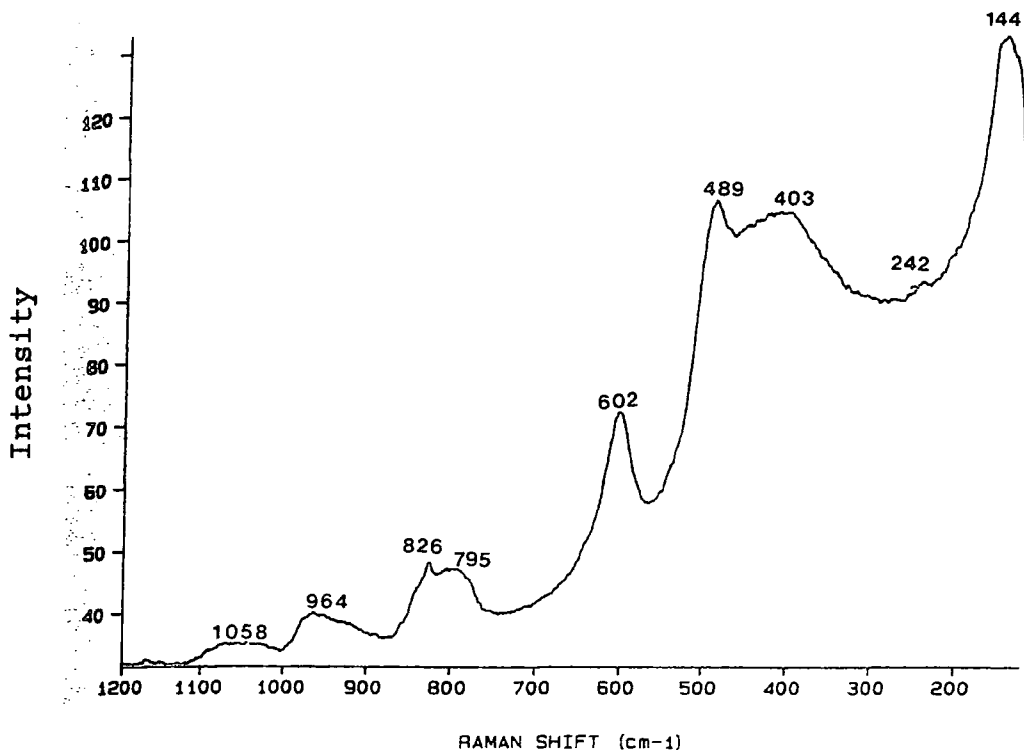
Figure 1.28 *Raman spectra of Cabosil silica having 0-3wt% TiO_2 having been heated in dry air at 973K*
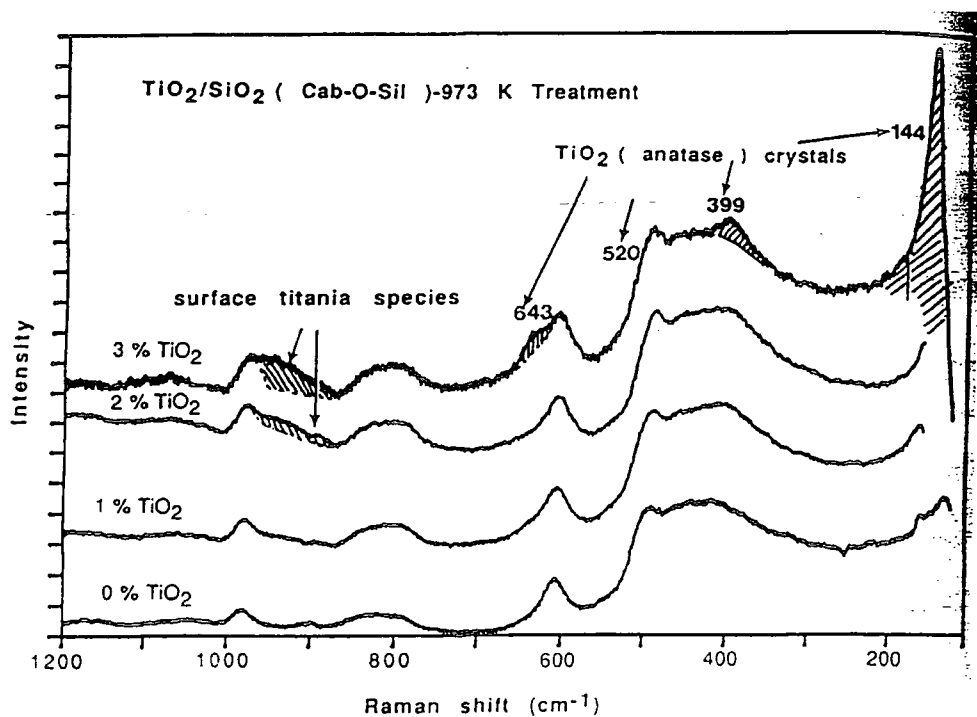
Biaglow *et al* [126] supported titania (anatase) on Cabosil and nonporous spherical silica particles (prepared by the method of Stober and Fink [125]) by impregnation with a THF solution of Ti(IV) t-butoxide and subsequent calcining. Titania was found to cover the silica uniformly with no bulk forms observed using either Raman spectroscopy or TEM. There is a greater fractional coverage of the spheres than on Cabosil (1wt% TiO_2 vs 4wt% for a theoretical monolayer on the nonporous spheres compared with 3wt% and 29wt% for Cabosil).

TPD and TGA studies of the desorption of the probe molecule 2-propanol from the catalysts showed that upon evacuation a significant amount remained on the surface, with a fraction of this reacting to form propene and water. The 2-propanol associated with titania can be distinguished from that on silica, where there is only a very weak interaction. The coverage of 2-propanol was found to be approximately proportional to the titania surface area. For titania on the model spheres the total amount of 2-propanol adsorbed was 3.9×10^{18} molecules/m², whilst for Cabosil the value was 6.1×10^{18}. The higher coverage on the Cabosil sample was probably due to the higher titania surface density on the model spheres.

4 Silica-supported chromium oxides

4.1 Introduction

Supported chromium oxide catalysts are known to possess excellent activity for the hydrogenation and dehydrogenation reactions of hydrocarbons, the dehydrocyclization of alkanes and the polymerization of olefins [127]. The catalytic properties of these systems are due to surface chromium oxide species and not bulk oxides such as crystalline CrO_3 [128].

Chromium oxide supported on silica is the Phillips ethylene polymerisation catalyst and is prepared by impregnating a chromium compound, most commonly CrO_3, onto wide pore silica and then calcining in oxygen to activate the catalyst. The chromium content, nature of the support and pretreatment conditions strongly affect the structure and the properties of the catalyst [129].

4.2 Silica-supported chromium (VI) oxide

Bulk chromium VI oxide begins to decompose above 200°C in air to give oxygen and chromium III oxide, but a certain amount is stabilized on silica even upto 900°C [130]. This is due to the formation of a surface chromate or perhaps dichromate ester in which each chromium atom is directly linked to the support [131]. The structures are shown in

Figure 1.29

Figure 1.29 *The structure of chromate and dichromate species*

chromate   dichromate
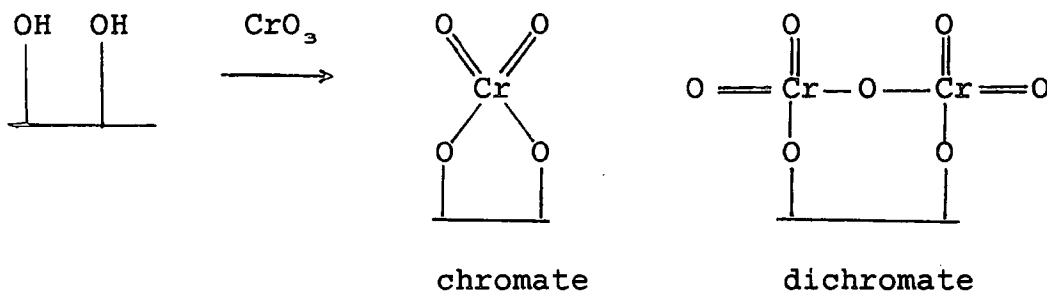
Evidence has been put forward, from studies using Raman spectroscopy [132,137-139], for trimeric and tetrameric chromate structures also being present on the silica surface. There is still considerable debate over the exact nature of the chromium species obtained.

Zecchina *et al* [129] calculated, by extrapolation from a series of silica-supported chromium catalysts prepared by the impregnation method, that the total coverage of the silica surface of their samples would be reached by a chromium loading of 10wt%, i.e. by a chromium surface density of 4.5 atoms/100Å^2. This is near to the value normally accepted for the surface density of silicon atoms in silica [150]. The ratio Cr:surface Si is approximately one. This value can be accounted for by dichromate formation (for chromates the value would be 0.5). The authors therefore concluded that chromium VI oxide binds to the silica surface mainly as dichromate in the 0-5wt% range, chromates representing a minor component. For higher chromium loadings binding stops and Cr_2O_3 crystallites are formed. The preference for dichromate was accounted for by structural reasons - there is less strain in dichromate and good geometrical fit between dichromate and silica moieties [150-155].

The 'reverse' experiments have been carried out which strip the chromium species from the surface and leave behind one OH group for each point of attachment to the surface. Determining the number of these groups should reveal the type of chromium species present. McDaniel [160] prepared CrO_3/SiO_2 catalysts, calcined between 400 and 900°C, and then treated with HCl gas, which strips off the Cr(VI) as CrO_2Cl_2 vapour.

In order to determine the nature of the chromium species it needs to be known whether chromium selectively occupies certain surface sites, those which would otherwise be hydroxylated, or condensed or 'paired', or whether the occupation of sites is random. There are three models for

the occupation of sites, as shown below.

1 Selective occupation of hydroxylated sites

$\triangle OH/Cr$

0
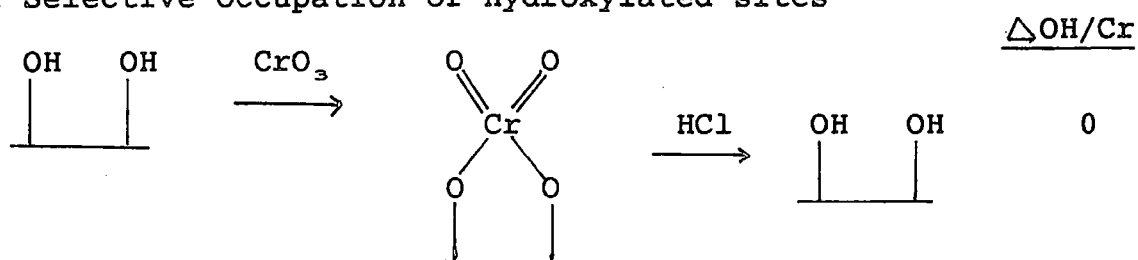
2 Selective occupation of easily condensable sites

2
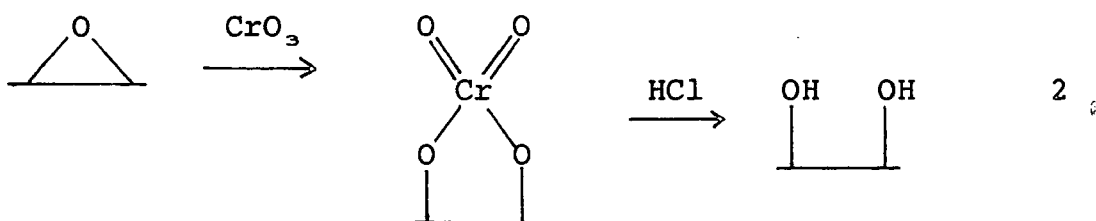
3 Random occupation of sites

2(1-F)
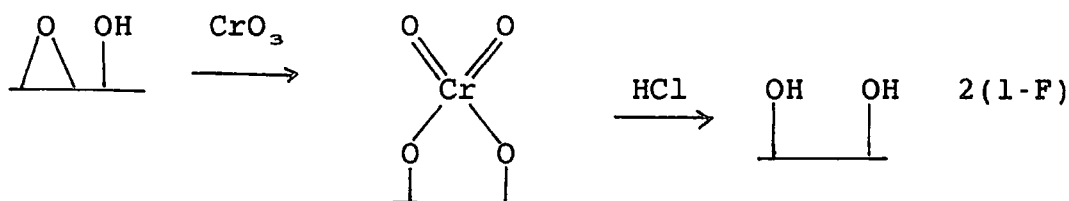
OH = hydroxyl population
Cr = chromium loading
F = function of number of sites hydroxylated on silica

In all cases the slope of the plot of the number of OH groups/nm² versus the amount of Cr(VI) stripped off is closer to that expected for chromate than dichromate. There is the possibility of a small contribution from dichromate.

4.2.1 Raman spectroscopic studies of CrO_3/SiO_2

The behaviour of CrO_3 in aqueous solution has been widely studied [133-136] and it was found that the species vary as a function of pH and concentration of Cr(VI). At low concentrations and in basic conditions CrO_4^{2-} dominates, while at high concentrations and mild acidic conditions $Cr_2O_7^{2-}$ dominates [133]. In highly concentrated solutions and acid conditions $Cr_3O_{10}^{2-}$ and $Cr_4O_{13}^{2-}$ are also found [136].

Aqueous impregnation processes hydroxylate the silica

39

surface by hydrolyzing Si-O-Si bonds. These OH groups are able to solvate the protons associated with the anionic species and therefore Wachs and Hardcastle [137] argue that the structures of the chromium oxide species on the hydroxylated silica surface should not be very different from the species present in solution. Raman spectroscopy has revealed monomers, dimers, trimers and tetramers are present on the silica surface under hydrated conditions.

Five bands due to a surface chromium species were observed in a laser Raman spectrum of a 4wt% CrO_3/SiO_2 catalyst and assigned as follows:

963   v_{asym} terminal CrO_4
902   v_{sym} terminal CrO_4
844   v_{sym} nonterminal CrO_4
370   bending mode terminal CrO_4
217cm^{-1} bending mode Cr-O-Cr

This is consistent with the presence of surface tetrachromate $[Cr_4O_{13}]_{ads}$ and Cr_2O_3 crystallites (band at 543cm^{-1}). A band at 989cm^{-1} is due to partial dehydration of the surface chromium oxide species by the laser beam.

Wachs et al [132,138,139] have also used in situ Raman spectroscopy to study these catalysts under dehydrated conditions (Figure 1.30). Catalysts were prepared using an incipient wetness impregnation with an aqueous solution of $Cr(NO_3)_3.9H_2O$, with subsequent calcination at 773K.

Figure 1.30 In situ Raman spectra of CrO_3/SiO_2 catalysts as a function of chromium oxide content
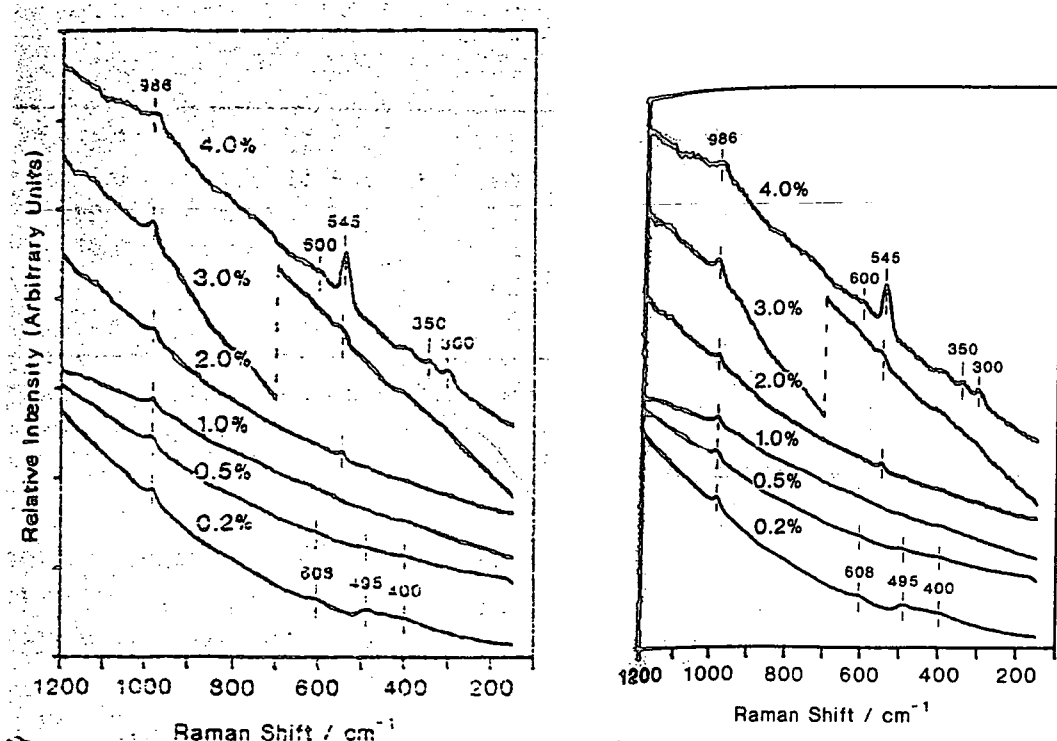
The 986cm^{-1} band is assigned to the symmetric Cr=O stretch of a highly distorted, tetrahedrally coordinated monomeric surface chromium oxide, i.e. the chromate. It is the only band due to dehydrated chromium oxide which is present irrespective of the CrO$_3$ content.

The absence of characteristic Raman features due to the bending mode of the Cr-O-Cr linkage at 210-230cm^{-1} indicates that the surface chromium oxide species appears to be isolated on silica.

The asymmetric stretching mode of the chromate should occur at higher wavenumbers than the symmetric mode but is not observed because of its weaker intensity and the strong background (fluorescence) of the catalyst. The absence of bands due to polymeric chromium oxide species indicates that they are not stable on silica under dehydrated conditions and they convert to a highly distorted monochromate species. Scheme 2 shows a model for the hydrated and dehydrated states on the silica surface.

<u>*Scheme 2*</u> *2-D model of surface chromium oxide species on the silica surface*

Hydrated states   (n = 1,2)
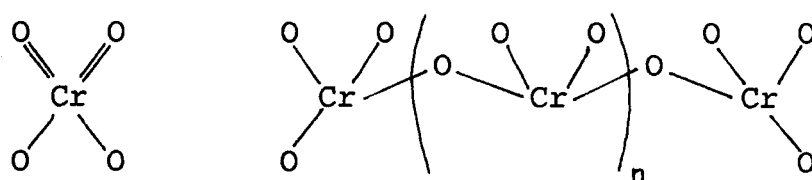
Dehydrated states
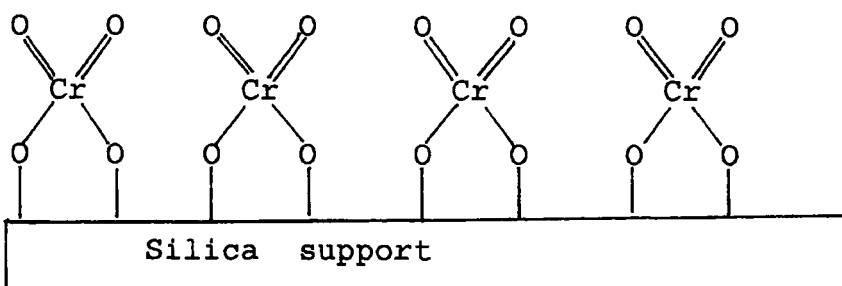
Dehydration removes water molecules from the silica surface and chromium species become bound to the surface

through an oxygen bridge (Cr-O-Si). Exposing the dehydrated samples to water results in reappearance of the polymeric species.

When the CrO_3 loading is at least 2% crystalline Cr_2O_3 was observed (band at $545cm^{-1}$) [132]. Its intensity was seen to increase with increasing chromium content where bands at 600, 350 and $300cm^{-1}$ were also attributed to Cr_2O_3.

4.2.2 Diffuse reflectance and UV-Visible reflectance spectroscopic studies of CrO_3/SiO_2

UV-vis reflectance spectroscopy of a 0.5wt% catalyst prepared by aqueous impregnation with CrO_3 showed bands at 21,700, 28,500 and $39,000cm^{-1}$, a shoulder at $26,000cm^{-1}$ and a small band at $14,000cm^{-1}$ [174]. The $21,000cm^{-1}$ band is typical of dichromate (by comparison with reference compounds) and the relative intensity agrees with a dichromate only surface phase. The bands at 28,500, 39,000 and $26,000cm^{-1}$ can be assigned to chromates and dichromates. The $14,000cm^{-1}$ band must be due to chromium in a lower oxidation state than 6+, probably 5+.

Reflectance spectra have shown evidence for both chromate and dichromate species [129,142-144]. DR spectra of 0.5 mole% catalysts show bands at 290, 360, 465 and 600nm. As loading increased the band at 290nm shifts to 310nm. At 10mole% loading the absorptions below 500nm are typical of chromate (Cr^{6+}-O) species, whereas Cr^{3+}-O species such as Cr_2O_3 are known to give absorptions above 600nm [145].

CrO_4^{2-} is characterised by four charge transfer transitions [146]:

I	$^1A_1$	$\longrightarrow$	$^1T_1$		429-459nm
II	$^1A_1$	$\longrightarrow$	$^1T_2$	($^1t_1 \longrightarrow 2e$)	360-375nm
III	$^1A_1$	$\longrightarrow$	$^1T_2$	($^1t_1 \longrightarrow 7t_2$)	270-330nm
IV	$^1A_1$	$\longrightarrow$	$^1T_2$	($6t_2 \longrightarrow 2e$)	257-263nm

It was concluded that 0.5mole% loading lead to the formation of surface chromates. The weak absorption at 600nm implies the coexistence of Cr^{3+}-O species. The chromates seem to be anchored onto weakly (SiO_2) and strongly (Cr^{3+}-O) polarizing surfaces.

At higher loadings the 290nm band shifts to 310nm and the 360, 465nm, and the Cr_2O_3 absorptions above 600nm, develop considerably. The low energy shift of transition III suggests the remaining chromates are dominantly anchored onto the highly polarizing surfaces of Cr^{3+}-O which can be correlated with the formation of bulk Cr_2O_3 indicated by XRD.

Weckhuysen *et al* [144] recorded the DRS spectra of 0.1-0.8wt% CrO_3/SiO_2 catalysts prepared by the incipient wetness method with CrO_3. Deconvolution of the spectrum obtained for the 0.2wt% Cr sample is shown in Figure 1.31.

Figure 1.31 Deconvolution of the DRS spectrum of 0.2wt% Cr/SiO_2
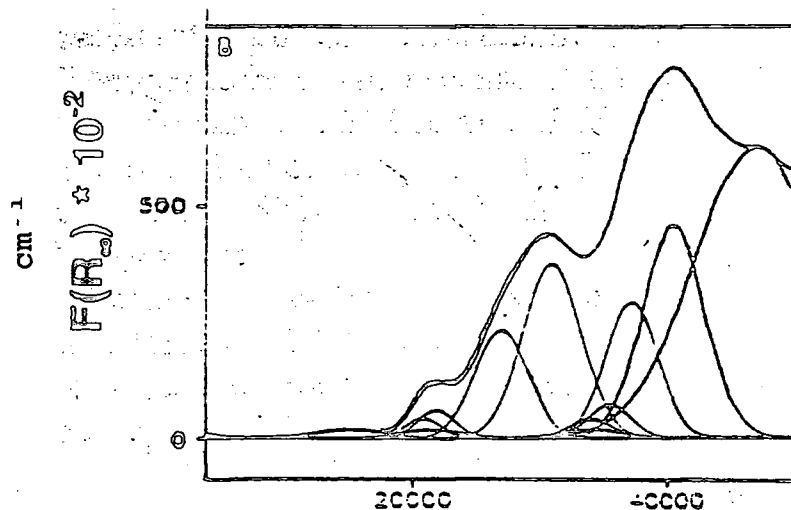
Four $O^{2-} \longrightarrow Cr^{6+}$ charge transfer bands at 15,500, 22,000, 30,500 and 40,500cm^{-1} and a shoulder at 27,000cm^{-1} are visible. After deconvolution eleven bands were resolved. Three weak bands at 15,500, 21,500 and 33,900cm^{-1} with equal width and intensity are ascribed to octahedral Cr^{3+} in accordance with the literature [147]. The remaining eight bands were assigned to chromate (21,000, 27,000, 34,000 and 37,300cm^{-1}) and dichromate (22,000, 31,000, 35,500 and 40,700cm^{-1}). The blue shift of the dichromate with respect to the chromate bands is in accordance with solution spectra and literature data [148,149].

4.2.3 Luminescence spectroscopic studies of CrO_3/SiO_2

Luminescence was observed at 4.2K on samples prepared by impregnating silica with an aqueous solution of $NH_4Cr_2O_7$, giving a loading of 5wt% of a monolayer [156]. The samples were calcined in air and kept away from air when cooling to prevent water adsorption. The luminescence spectra are shown in Figure 1.32.

Figure 1.32 *Emission (EM) and excitation (EX) spectra of the luminescence of Cr/SiO$_2$ at 4.2K*
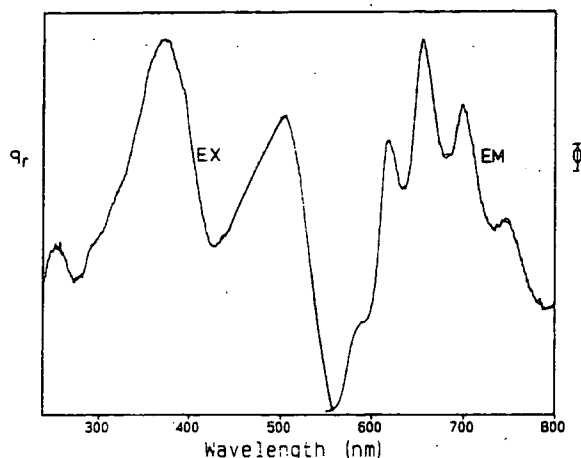
The luminescence was ascribed to charge-transfer transitions involving one kind of oxo-Cr(VI) species in which the metal is four coordinate. There are only a limited number of chromium compounds which are known to be luminescent [157]. The first absorbance band at 500nm is at a longer wavelength than only slightly distorted CrO$_4^{2-}$ which is tetrahedral in CaCrO$_4$ (450nm). There is better agreement with oxo chromium compounds with less cubic symmetry like K$_2$Cr$_2$O$_7$ which implies that the luminescent species has a distorted tetrahedral symmetry. The vibrational structure in the emission spectrum and the anomalously long decay time suggest that the excited state is localized in a short Cr-O bond, shorter than those in the tetrahedral CrO$_4^{2-}$ ion [158]. It was therefore proposed that the luminescent species is a monomeric four coordinate oxo-Cr(VI) species with two short Cr-O bonds. Its existance on silica has been suggested before [159,160]. Following a general trend for dehydrated silica supported oxo catalysts at low loadings only monomeric species are expected [161,162].

The most that can be concluded from such experiments is that CrO$_3$ attaches initially to the hydrated surface as chromate. There is a basic uncertainty in all these experiments because correct interpretation depends on knowing what sites are occupied and how this affects later dehydration of the silica.

4.2.4 TPR, EPR and SIMS studies of CrO$_3$/SiO$_2$

Ellison *et al* [163] studied a series of 0.6-2.55% CrO$_3$/SiO$_2$ catalysts using TPR. The resolved peaks could be classified in four categories:

Table 1.7 Components of the CrO3/SiO2 catalysts identified by TPR

peak type	Tm range /°C
Cr_A	355 - 365
Cr_B	395 - 405
Cr_C	450 - 480
Cr_D	505 - 515

For comparison:

sample	peak maximum/°C
CrO_3	400 - 420
Na_2CrO_4	540 - 560
$Na_2Cr_2O_7$	640 - 660

Cr_C (450-480°C) was the most abundant surface species and in most cases a low temperature component was also detected - Cr_A or Cr_B. Cr_A tended to be present only after low temperature activation, whilst Cr_B persisted at higher temperatures. Cr_D, a high temperature species, was detected for all. Stepwise reduction of a single species is rejected because the number of different species formed depends on the Cr loading. Upto 1% Cr and with an activation temperature <700°C Cr_C and Cr_D only are present. When the activation temperature is 700°C a small amount of the more easily reduced Cr_B was produced, possibly representing CrO_3 aggregates or polychromates on the surface. Cr_C and Cr_D may be chromate- or dichromate-like surface species. Thus at Cr loadings less than or equal to 1% the most abundant species is chromate, with 5% dichromate, with aggregates at higher activation temperatures. Increasing the chromium loading led to an increase in the surface dichromate and an increase in the degree of aggregation (Cr_B = aggregates of CrO_3). An increase in the activation temperature also causes an increase in the aggregation. Commercial 1% catalysts were found to have a higher proportion of aggregated chromium species.

EPR detects a phase resonance, indicating the presence of an oxidation state lower than 6+. The double signal means the species exists in two different environments, possibly in different states of dispersion. The signal has been attributed to mixed-valence Cr^{6+}/Cr^{3+} species [164]. Figure 1.33 depicts a typical EPR spectrum for the catalysts.

Figure 1.33 A typical EPR spectrum of a Cr/SiO$_2$ catalyst sample
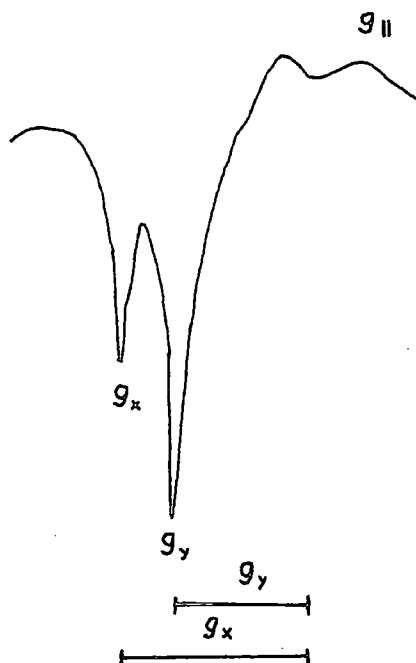
After all activation steps g was observed but g_x was detected only when the activation temperature was greater than 500°C. As it increases the interaction between the support and the chromium species increases [130] and g_x could indicate the presence of extensive Cr-SiO$_2$ interaction, i.e. a surface species. At higher activation temperatures the silica surface is dehydroxylated leading to a more dispersed chromium species [165]. The two resonances could arise from mixed valence states in different states of dispersion, possibly surface species and aggregates.

At concentrations as low as 0.5wt% considerable clumping or clustering of the supported chromium oxide predominate [143]. No adsorption takes place on silica and chromium simply matts or clogs the surface during during sample preparation to form spread-out and relatively thin clusters, a process aided by the redistribution of chromium occurring for the higher chromium loadings on calcination. The less exposed the silica surface the more extensive but 'thinner' the chromium clusters. This is shown in Figure 1.34.

Figure 1.34 *A schematic representation of chromium clusters on the silica surface*
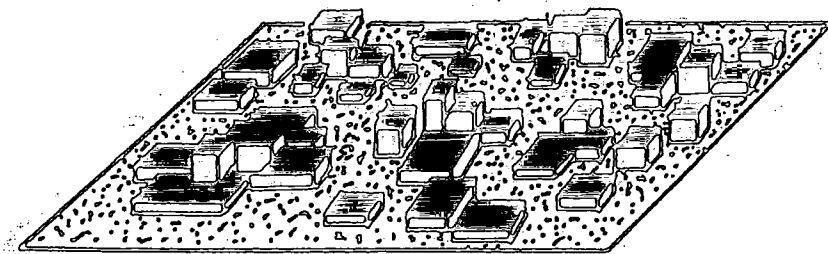
SIMS spectra of a series of 1-18wt% Cr catalysts show that the sizes of Cr and Cr-Si clusters released from the catalyst surfaces are consistently larger for chromium/silica samples than chromium/alumina [164]. Data may indicate that the chromium oxide cluster surface is more extensive on silica or that the long-range interaction of the support with the chromium surface is larger in the case of alumina. Fragment ratio data show that in general for Cr-SiO$_2$ the ratios are consistent regardless of chromium loading as though the surface texture of each Cr-SiO$_2$ is similar. ESR spectra support SIMS data that clustering of chromium species occurs even at 1wt% loading: β_2 esr appears at a lower temperature for Cr-SiO$_2$ and decomposes at a lower temperature to give the normal β_3 resonance characteristic of Cr(III) clusters. The resonance behaviour above 400°C is very similar for all chromium loadings implying the close similarity of cluster types.

DTA shows that on calcination in air more chromium oxide sublimes from silica than alumina. The chromium oxide is spread out on the surface so that the texture, environment and therefore the properties of the chromium oxides are similar.

A modification of textural parameters can be expected as the formation of crystalline CrO$_3$, when occurring inside the pore system, can cause pore blockage [166]. The texture of the catalysts was characterized as a function of the chromium loading at a chromium loading of 10wt% pores with radii less than 22nm are plugged. Approximately 25% of the overall pore volume is represented by pores with a radius of 22nm. The rsult of this plugging is to lead to an increase in the mean pore radius.

As expected the BET surface area and the integral pore volume decrease with increased chromium loading but there is a small increase in the porosity with loading (slight maximum at 5-6wt%), implying that the texture of the silica

is at least partly replaced by the texture of the crystalline CrO_3.

4.3 Silica-supported Cr_2O_3

The appearance of Cr_2O_3 particles in CrO_3/SiO_2 catalyst samples, where the chromium loading is >2wt%, is due to the low surface concentration of reactive OH groups on silica and their surface chemistry [137,140,141]. This has been studied by Knozinger and co-workers [142] who prepared catalysts by impregnating silica with $Cr(NO_3)_3.9H_2O$ and CrO_3, and coating with a $Cr_2O_3.5H_2O$ gel, followed by calcination at 600°C. The calcined catalysts were examined by XRD (for bulk phases) and DRS (for Cr-O species). The results are similar irrespective of the parent compound. The diffractograms and spectra obtained are shown in Figures 1.35 and 1.36.

Figure 1.35 XRD powder diffractograms for variously loaded Cr(VI)/SiO₂ catalysts
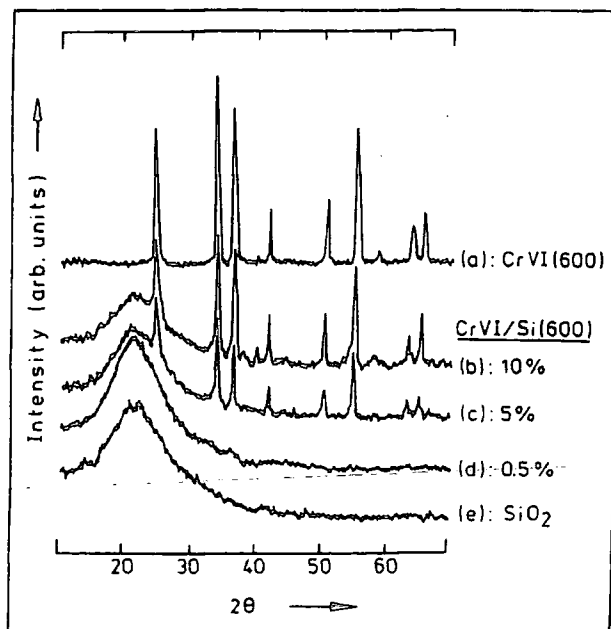
Figure 1.36 DR spectra of variously loaded Cr(VI)/SiO2 catalysts
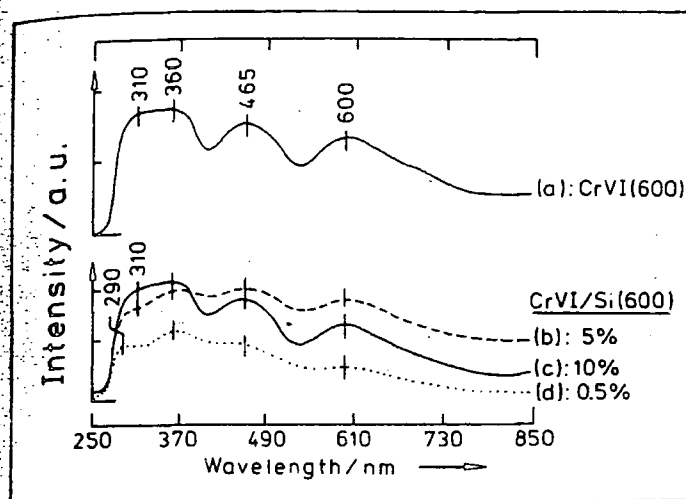
For 5 and 10 mol% CrO_3/SiO_2 catalysts Cr_2O_3 was the sole detectable bulk phase and the interaction between the parent compound and the silica surface weakens markedly for loadings greater than 0.5mole%, irrespective of the parent compound. As the loading increased the Cr-O species produced tend to polymerise leading finally to bulk Cr_2O_3.

Knozinger *et al* [167] have also characterized catalysts with 0.5, 5 and 10mol% loadings of Cr_2O_3 on silica using nitrogen adsorption at 77K. The catalysts were prepared by impregnation of Aerosil silica with CrO_3 and $Cr(NO_3)_3.9H_2O$ and also by coating the silica with the nitrate precursor. Calcination at 873K followed. The nitrogen adsorption isotherms were analysed using the BET and a$_e$ methods and the results showed the Cr_2O_3 surface area was significantly less than that for silica alone, indicating a poor dispersion on the silica and leading to surfaces dominated by the chemistry of the support. The total pore volume was found to decrease sharply as the chromia loading was increased - at 10mole% it drops to 43% of the initial value for pure silica at 873K. This may infer an effective pore blocking caused by 3-D chromia. These results are independent of preparation method. XRD [145], TEM [168] and electronic spectra [142] - bands at 296, 370, 465 and 600nm - are confirmation of the presence of chromia particles.

The poor dispersion irrespective of the different precursors and the preparation method is surprising. The isoelectric point of silica is pH 2 [169]. Thus silica should preferentially adsorb cationic species such as $[Cr(H_2O)_5(OH)]^{2+}$ from the nitrate solution [133], while $Cr_2O_7^{2-}$ should not interact with the surface. The cation exchange capacity of silica is typically very low unless the

solution pH is greater than 8-9 [170] so one can assume in the present case that adsorption is very limited due to the low cation exchange capacity, or negligible due to the surface polarizaton. Thus only a small percentage of the total precursors can be stabilized in high dispersions, the majority being decomposed during calcination to give Cr_2O_3 crystallites. The surface and interface free energies and the high Tammann temperature of chromia obviously do not allow surface spreading of Cr_2O_3 across the silica surface.

4.4 Cr/SiO₂ catalysts prepared from allyl and oxychloride precursors

Iwasawa *et al* [171] have prepared fixed 'paired' chromium catalysts by reaction of $Cr_2(\eta^3 C_3H_5)_4$ with the hydroxyls of silica at 273K, giving a chromium loading of 0.52wt%. This route is shown in Scheme 3.

Scheme 3 Preparation route from the allyl precursor

SiO_2

+

$Cr_2(\eta^3C_3H_5)_4$

$\xrightarrow{273K}$

$$
\begin{array}{cc}
C_3H_5 & C_3H_5 \\
| & | \\
Cr^{2+} & Cr^{2+} \\
| & | \\
O & O \\
| & |
\end{array}
$$

(I)

$$
\begin{array}{cc}
Cr^{2+} & Cr^{2+} \\
| & | \\
O & O \\
| & | \\
\end{array}
$$

$\xrightarrow{823K,\ O_2}$

$$
\begin{array}{cc}
O & O \\
\| & \| \\
O\!=\!Cr\!-\!o\!-\!Cr\!=\!O \\
| & | \\
O & O \\
| & |
\end{array}
$$

$$
\begin{array}{ccc}
Cr^{2+}\!-\!O\!-\!Cr^{2+} \\
| \qquad\qquad | \\
O \qquad\qquad O \\
| \qquad\qquad |
\end{array}
$$

$\xleftarrow{860K,\ H_2}$ $\xrightarrow{773K,\ O_2}$
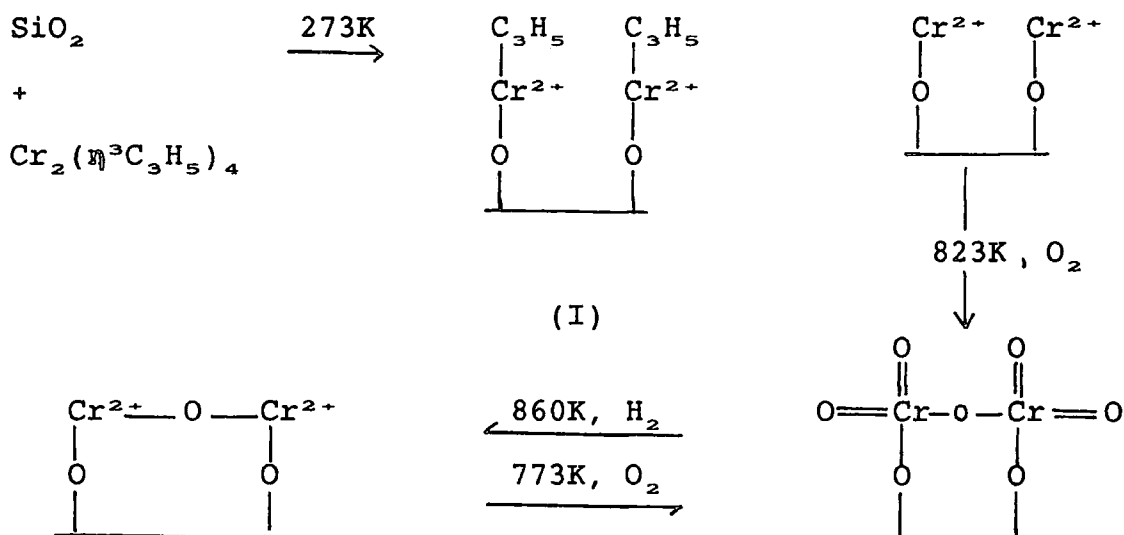
Surface structures were characterized spectroscopically (IR, UV diffuse reflectance, esr and photoluminescence), volumetrically and by temperature programmed hydrogenolysis (TPH). The latter technique applied to structure 1 showed a sharp desorption peak due to propene at 690K, implying that the surface species on silica were uniformly distributed. A peak at 553nm in the UV diffuse reflectance spectrum was assigned to a $A_{2u} \longleftarrow A_{1g}$ transition, from which a Cr^{2+}═ Cr^{2+} bond length of 222pm could be estimated.

Nishimura and Thomas grafted Cr (VI) onto the OH groups of silica using CrO_2Cl_2 vapour [130,160,172,173], producing better defined chromium sites on a 0.63wt% Cr catalyst. FTIR spectra showed that CrO_2Cl_2 is chemisorbed onto isolated OH

groups, selectively reacting with vicinal groups at room temperature to bind to the silica surface (bands at 3720 and $3600cm^{-1}$ disappear). The more uniform environment of the chromium atoms improved four fold the activity of the sample for ethylene polymerization.

REFERENCES

[1] B.C. Gates, J.R. Katzer and G.C.A. Schuit, *Chemistry of Catalytic Processes*, McGraw-Hill, New York, 1979

[2] M.A. Stranwick, M. Houalla and D.M. Hercules, *J. Catal.*, 106, 362, 1987

[3] M.A. Vuurman and I.E. Wachs, *J. Phys. Chem.*, 96, 5008, 1992

[4] O. Clause, L. Bonneviot, M. Che and H. Dexpert, *J. Catal.*, 130, 21, 1991

[5] H.H. Kung, *Transition Metal Oxides: Surface Chemistry and Catalysis*, Elsevier, Amsterdam, 1989

[6] Y-C. Xie and Y-Q. Tang, *Adv. Catal.*, 37, 1, 1990

[7] M. Schraml-Marth, A. Wokaun, M. Pohl and H-L. Krauss, *J. Chem. Soc. Faraday Trans.*, 87, 2635, 1991

[8] J. Datka, A.M. Turek, J.M. Jehng and I.E. Wachs, *J. Catal.*, 135, 186, 1992

[9] M. Che, C. Louis and J.M. Tatibouet, *Polyhedron*, 5, 123, 1986

[10] M. Niwa, Y. Matsuoka and Y. Murakami, *J. Phys. Chem.*, 91, 4519, 1987

[11] N. Cardona-Martinez and J.A. Dumescic, *J. Catal.*, 125, 427, 1990

[12] L. Bonneviot, O. Clause, M. Che, A. Manceau, A. Decarreau, F. Villain, D. Bazin and H. Dexpert, *Physica B*, 158, 43, 1989

[13] J.T. Richardson, R.J. Dubus, J.G. Crump, P. Desai, U. Osterwalder and T.S. Cale, in *Preparation of Catalysts II*, ed. B. Delmon, Elsevier, Amsterdam, 1979

[14] *Kirk Othmer Encyclopaedia of Chemical Technology*, Wiley Interscience, New York, 3rd edn.,1982, v. 20, p. 748

[15] Y. Iwasawa, *Tailored Metal Catalysts*, Reidel, Dordrecht, 1986

[16] B.A. Morrow and I.A. Cody, *J. Phys. Chem.*, 80, 1995, 1980

[17] H.A. Bebesi and B.H.C. Winquist, *Adv. Catal.*, 27, 98, 1978

[18] Y. Iwasawa, *Adv. Catal.*, 35, 187, 1987

[19] A.V. Kiselev, *Kollodn. Zh.*, 2, 17, 1937

[20] J.H. De Boer and J.M. Vleeskins, *Proc. K. Ned. Akad. Wet., Ser. B*, 61, 85, 1958

[21] V.Ya. Davidov, A.V. Kiselev and L.T. Zhuravlev, *Trans. Faraday Soc.*, 60, 2254, 1964

[22] L.T. Zhuravlev, *Langmuir*, 3, 316, 1987

[23] S. Leonardelli, L. Facchini, C. Fretigny, P. Tougne and A.P. Legrand, *J. Am. Chem. Soc.*, 114, 6412, 1992

[24] R.S. McDonald, *J. Phys. Chem.*, 62, 1168, 1958

[25] B.E. Wagner, J.N. Helbert and E.H. Poindexter, *Surf. Sci.*, 67, 251, 1977

[26] G. Curthoys, V.Ya. Davydov and A. V. Kiselev, *J. Colloid Interface Sci.*, 48, 58, 1974

[27] H.P. Boehm, *Adv. Catal.*, 16, 179, 1966

[28] W.K. Hall, H. P. Leftin, F.J. Cheselske and D.E. O'Reilly, *J. Catal.*, 2, 506, 1963

[29] F.J. Cheselske, W.K. Hall and W.E. Wallace, *J. Phys. Chem.*, 63, 505, 1959

[30] R.G. Haldeman and P.H. Emmett, *J. Am. Chem. Soc.*, 78, 2917, 1956

[31] V. Ya. Davydov, A.V. Kiselev, S.A. Kiselev and V.O.V. Polotnyuk, *J. Colloid Interface Sci.*, 74, 378, 1980

[32] H.P. Boehm and R. Sappok, *Z. anorg. allg. Chem.*, 365, 152, 1960

[33] V.M. Burmudez, *J. Phys. Chem.*, 75, 3249, 1971

[34] J.J. Fripiat and J. Uytterhoeven, *J. Phys. Chem.*, 66, 800, 1962

[35] A.H. Boonstra and C.A.H.A. Mutsaers, *J. Phys. Chem.*, 79, 1694, 1975

[36] M.L. Hair, *J. Colloid Interface Sci.*, 60, 154, 1977

[37] C.G. Armistead, A.J. Tyler, F.H. Hambleton, S.A. Mitchell and J.A. Hockey, *J. Phys. Chem.*, 73, 3947, 1969

[38] K.H. Rhee and M.R. Basila, *J. Catal.*, 10, 243, 1968

[39] M.L. Hair and W. Hertle, *J. Phys. Chem.*, 77, 2070, 1973

[40] J.K. Lee and S.W. Weller, *Anal. Chem.*, 30, 1057, 1958

[41] R.J. Peglar, F.H. Hambleton and J.A. Hockey, *J. Catal.*, 20, 309, 1971

[42] M. Lieflander and W. Stober, *Z. Naturforsch.*, 156, 411, 1960

[43] M. Sato, T. Kanbayashi, N. Kobayashi and Y. Shima, *J. Catal.*, 7, 342, 1967

[44] D.J.C. Yates, G.W. Dembinski, W.R. Kroll and J.J. Elliot, *J. Phys. Chem.*, 73, 911, 1969

[45] H.G. Weiss, J.A. Knight and J. Shapirs, *J. Am. Chem. Soc.*, 81, 1823, 1959

[46] W. Hertle, *J. Phys. Chem.*, 72, 1248, 1968

[47] G.C. Pimenten and A.L.McClellan, *The Hydrogen Bond*, Freeman, San Fransisco, 1960

[48] J.B. Peri and A.L. Hensley, *J. Phys. Chem.*, 72, 2926, 1968

[49] J.B. Peri and A.L. Hensley, *J. Phys. Chem.*, 70, 3168, 1966

[50] A.J. Van Rosmalen and J.C. Mol, *J. Phys. Chem.*, 82, 2748, 1978

[51] W.K. Hall, *Acc. Chem. Res.*, 8, 257, 1975

[52] L.B. Schreiber and R.W. Vaughan, *J. Catal.*, 40, 226, 1975

[53] M.L. Hair, *Vibrational Spectroscopy for Adsorbed Species*, American Chemical society, Washington, 1980

[54] A.V. Kiselev and V.I. Lygin, *Infrared Spectra of Surface Compounds*, Wiley, New York, 1975

[55] M.L. Hair, *Infrared Spectroscopy in Surface Chemistry*, Marcel Dekker, New York, 1967

[56] B.A. Morrow, *Stud. Surf. Sci. Catal.*, 57A, A161, 1990

[57] M.L. Hair and W. Hertle, *J. Phys. Chem.*, 73, 2372, 1969

[58] G. Ghiotti, E. Garrone, C. Morterra and F. Boccuzi, *J. Phys. Chem.*, 83, 2863, 1979

[59] F.H. Van Cauwelaert, P.A. Jacobs and J.B. Uytterhoeven, *J. Phys. Chem.*, 76, 1434, 1972

[60] J.A. Hockey, *J. Phys. Chem.*, 74, 2570, 1970

[61] B.A. Morrow and I.A. Cody, *J. Phys. Chem.*, 77, 1465, 1973

[62] K. Klier, J.H. Shen and A.C. Zettlemoyer, *J. Phys. Chem.*, 77, 1458, 1973

[63] V.Ya. Davydov, L.T. Zhuravlev and A.V. Kiselev, *Zh. Fiz. Khim.*, 38, 2047, 1964

[64] F.H. Van Cauwelaert, F. Vermoortele and J.B. Uytterhoeven, *Discuss. Faraday Soc.*, 52, 66, 1971

[65] B.A. Morrow and A.J. McFarlan, *J. Phys. Chem.*, 96, 1395, 1992

[66] B.A. Morrow and A.J. McFarlan, *J. Non-Cryst. Solids*, 120, 61, 1990

[67] B.A. Morrow and A.J. McFarlan, *Langmuir*, 7, 1695, 1991

[68] A. Burneau, O. Barres, J.P. Gallas and J.C. Lavalley, *Langmuir*, 6, 1364, 1990

[69] A. Burneau, O. Barres, J.P. Gallas and J.C. Lavalley, *Langmuir*, 7, 1235, 1991

[70] F. Boccuzzi, S. Coluccia, G. Ghiotti, C. Morterra and A. Zecchina, *J. Phys. Chem.*, 82, 1298, 1978

[71] C.A. Murray and T.J. Greytak, *Phys. Rev. B*, 20, 3368, 1979

[72] A. Burneau, O. Barres, J.P. Gallas and J.C. Lavalley, *Proc. Int. Workshop FTIR Spectrosc.*, ed. E.F. Vansant, University of Antwerp, 1990

[73] F.J. Heilweil, M.P. Casassa, R.R. Cavanaugh and J.C. Stephenson, *J. Phys. Chem.*, 82, 5216, 1985

[74] B.A. Morrow and R.A. McFarlane, *J. Phys. Chem.*, 90, 3192, 1986

[75] P. Hoffmann and E. Knozinger, *Surf. Sci.*, 188, 181, 1987

[76] J. Sauer and K.P. Schroder, *Z. Phys. Chem., Leipzig*, 266, 379, 1985

[77] R. West and R.H. Baney, *J. Am. Chem. Soc.*, 81, 6145, 1959

[78] G.I. Harris, *J. Chem. Soc.*, 5978, 1963

[79] C.P. Tripp and M.L. Hair, *Langmuir*, 7, 923, 1991

[80] G.E. Maciel and D. W. Sindorf, *J. Am. Chem. Soc.*, 102, 7606, 1980

[81] G.E. Maciel and D. W. Sindorf, *J. Am. Chem. Soc.*, 105, 7606, 1980

[82] G.E. Maciel and D. W. Sindorf, *J. Phys. Chem.*, 86, 5208, 1982

[83] A.P. Legrand, H. Hommel, A. Tuel, A. Vidal, H. Balard, E. Papirer, P.Levitz, M. Czernichowski, R. Erre, H. van Damme, J.P. Gallas, J.F. Hemidy, J.C. Lavalley, O. Barres, A. Burneau and Y. Grillet, *Adv. Colloid Interface Sci.*, 33, 91, 1990

[84] B.A. Morrow and I.D. Gay, *J. Phys. Chem.*, 92, 5569, 1988

[85] P. van der Voort, I. Gillis-D'Hamers, K.C. Vrancken and E.F. Vansant, *J. Chem. Soc. Faraday Trans.*, 87, 3899, 1991

[86] P. van der Voort, I. Gillis-D'Hamers, and E. Vansant, *J. Chem. Soc. Faraday Trans.*, 86, 3751, 1990

[87] P. Fink, H. Hartmut and G. Rudakoff, *Wiss. Ztschr. FSU*,

Naturwiss. R., 36, 581, 1987
[88] Y. Onishi and T. Hamamura, *Bull. Chem. Soc. Jpn.*, 43, 996, 1970
[89] K.R. Thampi, J. Kiwi and M. Gratzel, *Catal. Lett.*, 1, 109, 1988
[90] S.M. Mukhopadhyay and S.H. Garofalini, *J. Non-Cryst. Solids*, 126, 202, 1990
[91] A.Yu. Stakheev, E.S. Shpiro and J. Apijok, *J. Phys. Chem.*, 97, 5668, 1993
[92] S.J. Tauster, S.C. Fung and R.L. Garten, *J. Am. Chem. Soc.*, 100, 170, 1978
[93] J.S. Rieck and A.T. Bell, *J. Catal.*, 99, 262, 1986
[94] L.L. Murrell and D.J.C. Yates, *Stud. Surf. Sci. Catal.*, 7, 1470, 1981
[95] E.I. Ko and N.J. Wagner, *J. Chem. Soc. Chem. Commun.*, 1274, 1984
[96] E.I. Ko, J-P. Chen and J.G. Weissman, *J. Catal.*, 105, 511, 1987
[97] A.S. Lisitsyn, A.V. Golovin, V.I. Kuznetsov and Yu.I. Yermakov, *J. Catal.*, 95, 527, 1985
[98] C.U.I. Odenbrand, S.L.T. Andersson, L.A.N. Andersson, J.G.M. Brandin and G. Busca, *J. Catal.*, 125, 541, 1990
[99] H.A. Benesi and B.H.C. Winquist, in *Advances in Catalysis*, eds. D.D. Eley, H. Pines and P.B. Weisz, Academic Press, New York, 1978
[100] J. Haber, in *Catalysis, Science and Technology*, eds. J.R. Anderson and M. Boudart, Springer-Verlag, Berlin, 1981, v. 2
[101] G. Ramis, G. Busca, V. Lorenzelli, P.F. Rossi, M. Bensitel, O. Saur and J.C. Lavalley, in *Proc. 9th Int. Congr. Catal.*, Calgary, 1988
[102] G. Busca, H. Saussey, O. Saur, J.C. Lavalley and V. Lorenzelli, *Appl. Catal.*, 14, 245, 1985
[103] K. Shibata, T. Kiyoura, T. Kitagawa, T. Sumiyoshi and K. Tanabe, *Bull. Chem, Soc. Jpn.*, 46, 2985, 1973
[104] K. Tanabe, *Solid Acids and Bases*, Academic Press, New York, 1970
[105] K. Tanabe, in *Catalysis, Science and Technology*, eds. J.R. Anderson and M. Boudart, Springer-Verlag, Berlin, 1981, v. 2, ch. 5
[106] M. Niwa, M. Sago, H. Ando and Y. Murakami, *J. Catal.*, 69, 69, 1981
[107] C.U.I. Odenbrand, J.G.M. Brandin and G. Busca, *J. Catal.*, 135, 505, 1992
[108] S. Imamura, S. Ishida, H. Tarumoto, Y. Saito and T. Ito, *J. Chem. Soc. Faraday Trans.*, 89, 757, 1993
[109] K. Tanabe, T. Sumiyoshi, K. Shibata, T. Kiyoura and J. Kitagawa, *Bull. Chem. Soc. Jpn.*, 47, 1064, 1974
[110] H.H. Kung, *J. Solid State Chem.*, 51, 191, 1984
[111] M. Itoh, H. Hattori and K. Tanabe, *J. Catal.*, 35, 225, 1974
[112] K. Nishikawa, N. Kakuta, A. Ueno and H. Nakabayashi, *J. Catal.*, 118, 498, 1989
[113] S. Imamura, H. Tarumoto and S. Ishida, *Ind. Chem. Eng.*

Res., 28, 1449, 1989

[114] T. Kataoka and J.A. Dumesic, *J. Catal.*, 112, 66, 1988

[115] M.F. Brest and R.A. Condrate, *J. Mater. Sci. Lett.*, 4, 994, 1985

[116] M.R. Boccuti, K.M. Rao, A. Zecchina, G. Leofanti and G. Petrini, *Stud. Surf. Sci. Catal.*, 48, 133, 1984

[117] A. Fernandez, J. Leyrer, A.R. Gonzalez-Elipe , G. Munuera and H. knozinger, *J. Catal.*, 112, 489, 1988

[118] M.G. Reichmann and A.T. Bell, *Langmuir*, 3, 111, 1987

[119] T.M. Salama, T. Tamaka, T. Yamaguchi and K. Tanabe, *Surf. Sci. Lett.*, 227, L100, 1990

[120] S. Srinivasan, A.K. Dayte, M. Hampden-Smith, I.E. Wachs, G. Deo, J.M. Jehng, A.M. turek and C.H.F. Peden, *J. Catal.*, 131, 260, 1991

[121] F.D. Hardcastle and I.E. Wachs, *Proc. 9th Int. Congr. Catal.*, Calgary, 1988

[122] I.E. Wachs, *Chem. Eng. Sci.*, 45, 2561, 1990

[123] M.P. McDaniel, M.B. Welch and J. Dreiling, *J. Catal.*, 82, 118, 1983

[124] E.T.C. Vogt, A. Boot, A.J. van Dillen, J.W. Geus, F.J.J.G. Jansses and F.M.G. van den Kerkhof, *J. Catal.*, 114, 313, 1988

[125] W. Stober, A. Fink and E. Bohn, *J. Colloid Interf. Sci.*, 26, 62, 1968

[126] A.I. Biaglow, R.J. Gorte, S. Srinivasan and A.K. Dayte, *Catal. Lett.*, 13, 313, 1992

[127] C.L. Thomas, *Catalytic Processes and Proven Catalysis*, Academic Press, New York, 1970

[128] M.P. McDaniel, *J. Catal.*, 76, 17, 1982

[129] A. Zecchina, E. Garrone, G. Ghiotti, C. Morterra and E. Borello, *J. Phys. Chem.*, 79, 966, 1975

[130] M.P. McDaniel, *Adv. Catal.*, 33, 47, 1985

[131] J.P. Hogan, *J. Polym. Sci. A-1*, 8, 2637, 1970

[132] D.S. Kim, J-M. Tatibouet and I.E. Wachs, *J. Catal.*, 136, 209, 1992

[133] C.F. Baes and R.E. Mesmer, *The Hydrolysis of Cations*, Wiley, New York, 1986

[134] G. Michel and R. Machiroux, *J. Raman Spectrosc.*, 14, 22, 1988; 17, 79, 1986

[135] M.A. Vuurman, D.J. Stufkens, A. Oskam, J.A. Moulijn and F. Kapteijn, *J. Mol. Catal.*, 60, 83, 1990

[136] G. Michel and R. Cahay, *J. Raman Spectrosc.*, 17, 4, 1986

[137] F. D. Hardcastle and I.E. Wachs, *J. Mol. Catal.*, 46, 173, 1988

[138] M.A. Vuurman, I.E. Wachs, D.J. Stufkens and A. Oskam, *J. Mol. Catal.*, 80, 209, 1993

[139] D.S. Kim and I.E. Wachs, *J. Catal.*, 142, 166, 1993

[140] M.P. McDaniel and M.M. Johnson, *J. Catal.*, 101, 446, 1986

[141] R. Merryfield. M.P. McDaniel and G. Parks, *J. Catal.*, 77, 348, 1982

[142] N.E. Fouad, H. Knozinger, M.I. Zaki and S.A.A. Mansour, *Z. Phys. Chem.*, 171, 75, 1991

[143] C. Groeneveld, P.P.M.M. Wittgen, A.M. van Kersbergen, P.L.M. Mestrom, C.E. Nuijten and G.C.A. Schuit, *J. Catal.*, 59, 153, 1979

[144] B.M. Weckhuysen, L.M. de Ridder and R.A. Schoonheydt, *J. Phys. Chem.*, 97, 4756, 1993

[145] M.I. Zaki, N.E. Fouad, J. Leyrer and H. Knozinger, *Appl. Catal.*, 21, 359, 1986

[146] Z.G. Szabo, K. Kamaras, Sz. Szebeni and I. Ruff, *Spectrochim. Acta*, 34A, 607, 1978

[147] A.B.P. Lever, *Inorganic Electronic Spectroscopy*, Elsevier, amsterdam, 2nd edn., 1984

[148] V. Miskowski, H.B. Gray and C.J. Ballhausen, *J. Mol. Phys.*, 28, 729, 1974

[149] M. Sieslak-Golonka, *Coord. Chem. Rev.*, 109, 223, 1991

[150] J.B. Peri and A.L. Hensley, *J. Phys. Chem.*, 72, 2926, 1968

[151] C. Mortera and M.J.D. Low, *Ann. N.Y. Acad. Sci.*, 220, 135, 1973

[152] E. Borello, A. Zecchina and M. Castelli, *Ann. Chim. (Rome)*, 53, 690, 1963

[153] A. Zecchina, G. Ghiotti, L. Cerruti and C. Morterra, *J. Chim. Phys.*, 68, 1479, 1971

[154] V.B. Kazansky, *Kinet. Katal.*, 11, 455, 1970

[155] A. Cotton and G. Wilkinson, *Advanced Inorganic Chemistry*, Wiley Interscience, New York, 4th edn., 1980

[156] M.F. Hazenkamp and G. Blasse, *J. Phys. Chem.*, 96, 3442, 1992

[157] G.A.M. Dalhoeven and G. Blasse, *Chem. Phys. Lett.*, 76, 27, 1980

[158] F. Gonzalez-Vilchez and W.P. Griffith, *J. Chem. Soc. Dalton Trans.*, 1416, 1972

[159] M.P. McDaniel and S.J. Martin, *J. Phys. Chem.*, 95, 3289, 1991

[160] M.P. McDaniel, *J. Catal.*, 76, 29, 1982

[161] M. Anpo and Y. Kubokawa, *Rev. Chem. Intermed.*, 5, 105, 1987

[162] M. de Boer, J. van Dillen, D.C. Koningsberger, M.A. Vuurman, I.E. Wachs and I.W. Geus, *Catal. Lett.*, 11, 227, 1991

[163] A. Ellison, T.L. Overton and L. Bencze, *J. Chem. Soc. Faraday Trans.*, 89, 843, 1993

[164] A. Ellison, *J. Chem. Soc. Faraday Trans.*, 80, 2567, 1984; 80 2581, 1984

[165] R.K. Iler, *The Chemistry of Silica*, Wiley, New York, 1979

[166] M. Richter, P. Reich and G. Ohlmann, *J. Mol. Catal.*, 46, 79, 1988

[167] N.E. Fouad, H. Knozinger, H.M. Ismail and M.I. Zaki, *Z. Phys. Chem.*, 173, 201, 1991

[168] T. Baird and M.I. Zaki, *Inst. Phys. Conf. Ser.*, 90, 43, 1987

[169] G.A. Parks, *Chem. Rev.*, 65, 177, 1965

[170] J.P. Brunelle, *Pure Appl. Chem.*, 50, 1211, 1978

[171] Y. Iwasawa, Y. Sasaki and S. Ogasawara, *J. Chem. Soc.*

Chem Commun., 140, 1981

[172] M. Nishimura and J. M. Thomas, *Catal. Lett.*, 19, 33, 1993

[173] S. Haukka, *Analyst*, 116, 1055, 1991

[174] B. Fubini, G. Ghiotti, L. Stradella, E. Garrone and C. Morterra, *J. Catal.*, 66, 200, 1980

CHAPTER 2

The Characterization of Promoted Phillips Catalysts using X-ray Photoelectron Spectroscopy

1 Introduction

X-ray photoelectron spectroscopy (XPS) has proved to be a useful tool in catalytic research since:
(i) it observes chemical changes in the first few monolayers;
(ii) the binding energy values identify the elements on the surface;
(iii) binding energy shifts are informative of the chemical environment of the atom;
(iv) it has a high surface sensitivity (upto 10^{-4} monolayer), and
(v) the technique can be quantitative [35].

XPS was used in this study of a series of Cr/SiO_2 (Phillips) catalysts in order to obtain information on the chemical and electronic nature of the surface species before and after activation in oxygen. By also studying catalysts which contain promoters, here titania and alumina, which are used industrially, some insight into the role of these promoters in the surface chemistry of the system could be obtained. The dispersion of both chromium and promoter species could be measured, and were compared before and after activation in oxygen. Changes in dispersion indicate whether the metal species are mobile on the surface and if there is agglomeration or movement away from the surface into the bulk.

2 XPS:Theory

XPS is concerned with the measurement of core electron binding energies. The sample is bombarded with high energy X-rays (under UHV conditions) which cause emission of core electrons from the sample atoms. This is illustrated in figure 2.1.

Figure 2.1 *Schematic representation of the principle of XPS*
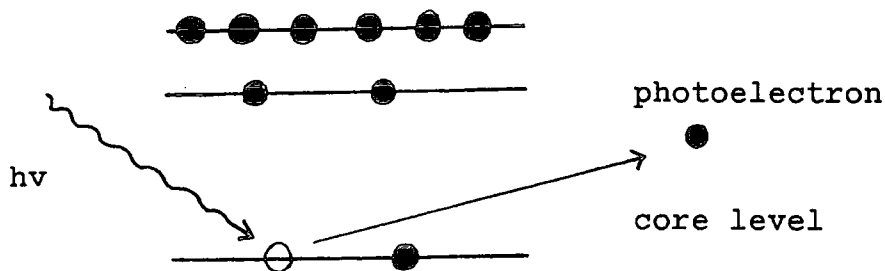
All photoelectrons whose binding energies are less than the energy of the exciting X-rays are ejected and their kinetic energies E_k are then measured with an energy

analyser. The binding energies are then obtained from the relationship:

$$E_b = h\nu - E_K - \theta$$

where θ = spectrometer work function, a constant for a given analyser

       $h\nu$ = energy of the exciting X-rays (for Mg K_α $h\nu$ = 1253.6eV)

Binding energies unambiguously define a specific atom: the energy of an ejected photoelectron is characteristic of the atom involved and its chemical environment [1]. The binding energy in the neutral free atom is taken as the standard from which shifts are measured. All core electrons that lie well within the valence orbital will exhibit the same shift because the potential due to a shell of charge is constant inside the shell. Such free atom core electron shifts typically have values of 1 Rydberg = 13.6eV [4].

2.1 Sampling Depth

After photoionization a photoelectron of energy E_K must travel through the solid and escape into the vacuum without energy loss before it can be energy analysed and detected. However, the stopping power of solids for electrons is several orders of magnitude greater than for X-rays, with the result that electrons in the energy range 50-1000eV will typically travel only 2-10 atomic layers before they lose energy through inelastic scattering events with other electrons and hence cannot contribute to the photoelectron peak at energy E_K. These inelastically scattered electrons give rise to a background spectrum [4]. Thus, the secondary electron must originate at, or very close to, the surface if it is to escape into the vacuum and be detected. The probability of an inelastic scattering event occurring is determined by both the electron energy and the material through which it is travelling [5]. It is described by:

$$I(x) = I_o \exp(-x/\lambda(E_K,Z).\cos\theta)$$

where: I_o = original photoelectron intensity

     $I(x)$ = intensity after travelling through material of thickness x

       θ = angle of emission with respect to the surface normal

  $\lambda(E_K,Z)$ = inelastic mean free path (it represents the depth at which photoelectrons have a probability of 1/e of escaping without energy loss)

Due to the exponential decay behaviour predicted by the above equation it is not possible to arrive at a unique value for the sampling depth d. Approximately 63% of the

photoelectrons contributing to a particular peak must
originate within a distance $\lambda\cos\theta$ of the surface and this
expression is used to give a practical measure of d. Since d
varies with $\cos\theta$ hence sampling depth may be controlled by
varying the angle of emission from $0°$ $(d=\lambda)$ to $80°$ $(d=0.17\lambda)$
[5], as shown in Figure 2.2.

Figure 2.2   *A diagram showing the relationship between the
electron take-off angle and the sampling depth.*
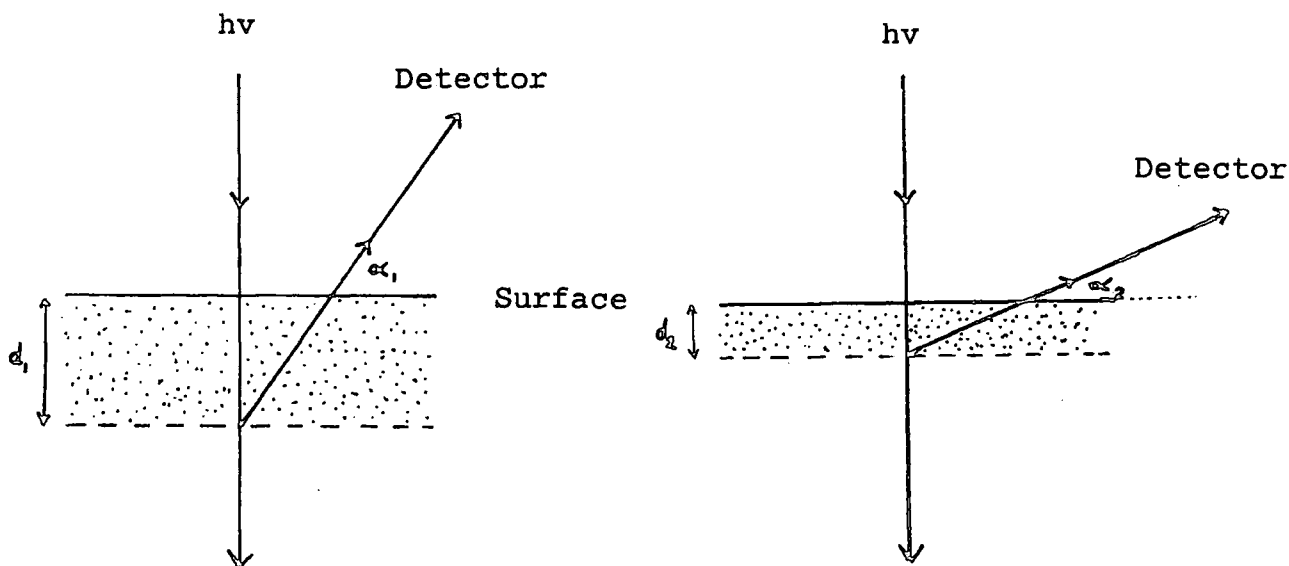
— Note that the take off angle α is measured relative to the
surface, the angle of emission θ relative to the surface
normal, $\alpha + \theta = 90°$.

    If the take-off angle α is made small the sampling depth
d is similarly reduced, which enhances the surface
sensitivity, and the XPS information is more characteristic
of the surface. It should be noted that angular effects are
observed with relatively flat surfaces rather than with
powders, where the surface is very rough [5,8].

    The number of photoelectrons produced from any given
core level of an element is determined by the
photoionization cross section (σ) of that level for the
photon energy (hv) concerned: is defined as the transition
probability per unit time for excitation of a single
photoelectron from the core level of interest under an
incident photon flux of $1cm^{-2}s^{-1}$. In particular is found to
depend on hv, binding energy, atomic number (Z) and the
relative directions of photon incidence and photoelectron
emission (θ) [5].

2.2 Chemical Shift

Often only a relative binding energy (chemical shift) is required. The binding energies of core electrons are affected by the valence electrons and thus by the chemical environment of the atom. When this is changed it alters the local charge environment and this, in turn, is reflected as a variation in the binding energies of all the electrons of that atom. This shift is inherent to the species involved and thus provides a means of chemical analysis. Chemical shifts can range from 0.1 to 10eV or more in magnitude [5]. From a purely Coulombic point of view the chemical shift arises in the initial state from the displacement of electronic charge from the atom towards the ligands reducing the electrostatic potential at the atom. In addition there is a final state shift due to the polarization of the ligands by the core hole on the central atom. Since the net effect depends on the combined effects of electronegativity and polarizability of the ligands a certain universality can be expected [4]. In solids chemical shifts are less predictable because the final state screening and the Madelung potential can vary from substance to substance. In general any parameter that affects the electron density about the atom (eg. oxidation state, ligand electronegativity or coordination) is expected to result in a chemical shift in electron binding energy: as the oxidation state becomes more positive an increase is seen in binding energy [1].

In longer experiments, sample damage is possible in cases where chemical changes caused by the electrons are irreversible or long lived. Chemical alteration of the sample due to the high x-ray flux can also occur and has been observed in photosensitive samples. In either of these cases it is often possible to detect radiation damage by the time dependence of the spectrum and/or by comparing the physical appearance of the sample before and after an experiment [11].

3 Instrumentation

All XPS spectrometers incorporate each of the following:
(i) a UHV environment
(ii) a controlled source of x-rays
(iii) a specimen manipulation system
(iv) an electron energy analyser
(v) a data recording, processing and output system [5].

A representation of a XPS spectrometer is shown in Figure 2.3.

Figure 2.3 *Schematic representation of a XPS spectrometer*
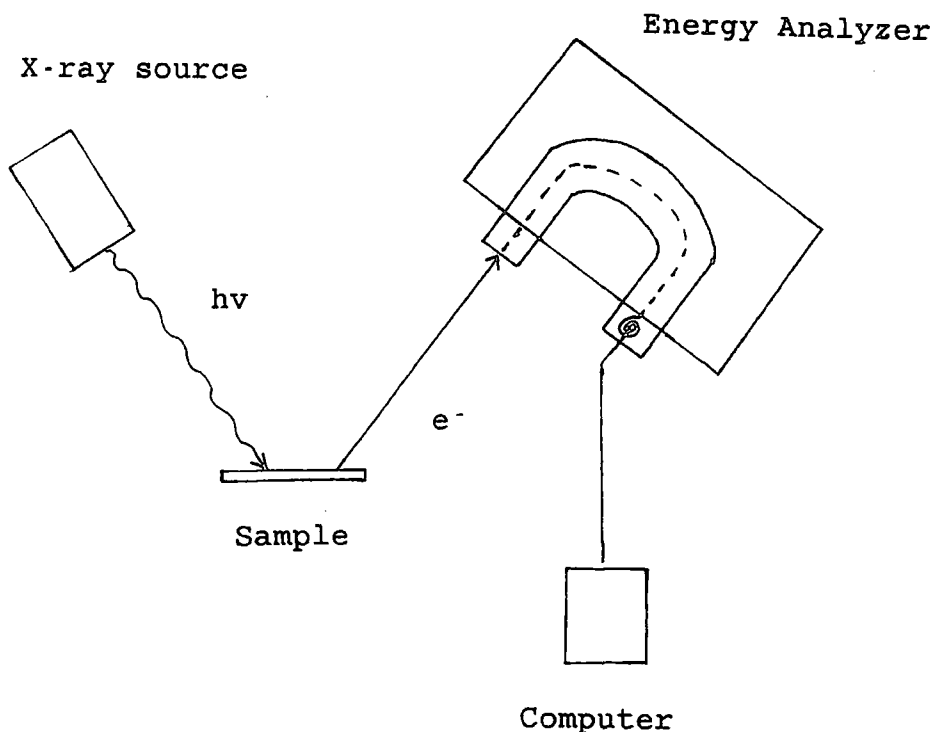
3.1 The X-ray Source

An ideal source must be sufficiently energetic to access core levels, intense enough to produce a detectable electron flux, have a narrow line width (since this is the major contribution to the full width at half maximum, FWHM, of an XPS peak) and be simple to use and maintain. Magnesium and aluminium sources are the most widely used since they have sufficiently energetic and narrow lines and are also stable. Dual Mg/Al anodes are standard. The operating conditions are typically 15kV accelerating voltage and 20mA target current. To eliminate the series of source x-ray lines and the Bremsstrahlung continuum the radiation can be monochromated using a diffraction grating but the intensity is greatly reduced due to dispersion.

3.2 Analysers

Once produced the photoelectrons must be separated according to their energy and subsequently converted into a spectrum. The most common analysers are the Cylindrical Mirror (CMA) and the Concentric Hemisphere (CHA), shown in Figure 2.4.

Figure 2.4 A Cross Sectional View of the Concentric
Hemisphere Analyser
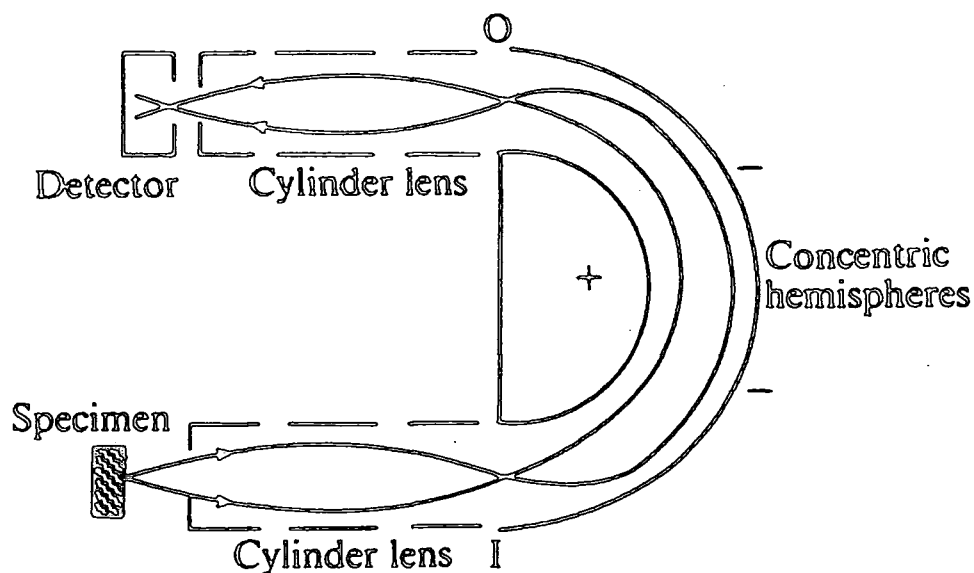
I = entrance aperture   O = output aperture

The CHA has two hemispherical surfaces of inner radius R_1
and outer radius R_2 positioned concentrically, with a
potential V applied such that the outer sphere is negative
and the inner positive (with respect to V).

Figure 2.5 A Schematic Diagram of the Concentric
Hemisphere Analyser
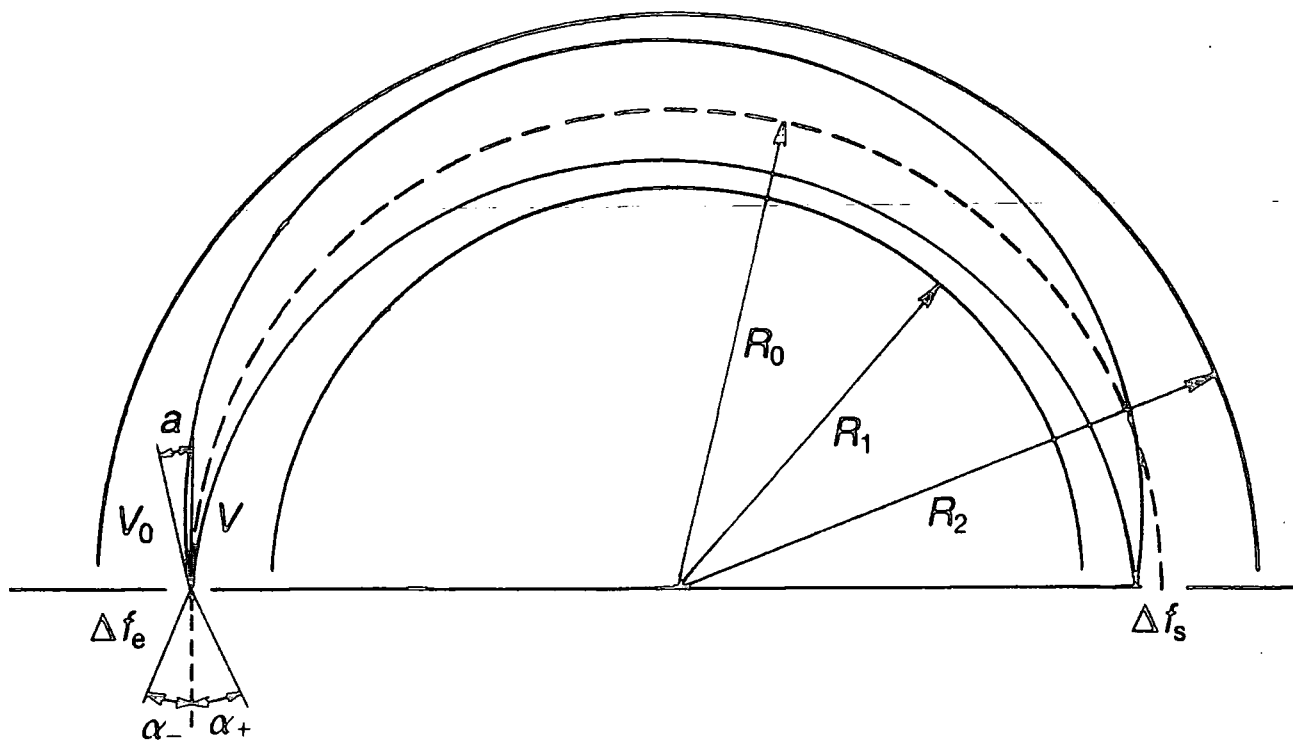
a is the angle at which the electron enters the analyser
Δf_e and Δf_s are the widths of the entrance and exit slits

There will be a median equipotential surface of radius R_o between the hemispheres and ideally $R_o = (R_1 + R_2)/2$. The entrance and exit slits are centred on R_o. For the ideal situation where an electron with kinetic energy E_k is travelling on the circular orbit of radius R_o, the relationship between the deflecting potential eV and E_k is:

$$eV = E_k(R_2/R_1 - R_1/R_2)$$

where the entrance and exit slits are separated by an angle of 180°. This results in focusing at a point [6,132]. It is desirable to work with as large an entrance angle α as possible whilst retaining adequate energy resolution, and the compromise reached is to choose α so that with a slit width w

$$\alpha^2 = w/2R_o.$$

For adequate resolution it is customary to pre-retard electrons as they enter the analyser, either to a chosen fixed analyser energy (the pass energy) or by a fixed ratio. Retardation is usually accomplished by placing planar grids across the entrance slit, but can also be achieved by a lens system [132].

When an XPS spectrum is run the spectrometer ramps down from the starting energy and photoelectrons of a certain energy E will pass through the exit slits of the analyser only when E-R = HV, where R = ramp voltage at any particular time, H = analyser constant and V = voltage between the hemispheres. The quantity HV is defined as the analyser "pass energy". Electrons which do not satisfy this condition will not reach the exit slit of the hemispheres (Figure 2.6).

Figure 2.6 Schematic representation of the requirements for photoelectron detection

E-R > HV

E-R >> HV

E-R = HV

E-R << HV

E-R < HV
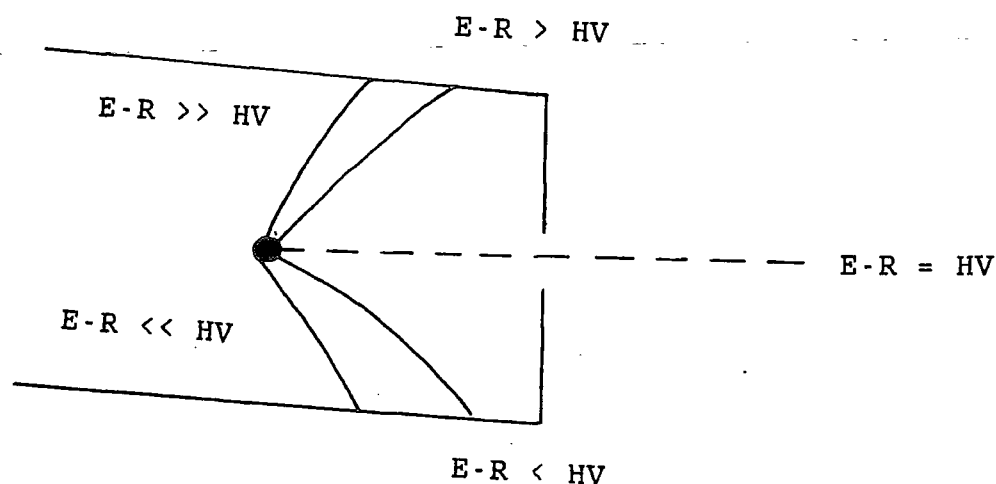
The CHA is normally operated in constant analyser energy mode for XPS thereby yielding a constant energy resolution throughout the spectrum. For survey (wide scan) spectra the analyser would normally be operated with a resolution of 1eV to give fairly high transmission. For (narrow scan) high resolution spectra the resolution would be changed to 0.2 or 0.4eV to resolve fine structure and lineshape detail [5].

The relative resolution of the analyser is given by

$$E/E_o = w/2R_o + \alpha^2/4$$

where w is the slit width. Since $\alpha^2 = w/2R_o$, the relative resolution reduces to

$$E/E_o = 0.63w/R_o.$$

If the dimensions of the analyser, i.e. R_o, are fixed, then there is an inverse relationship between the pass energy E_o (HV) and the slit width w in the CAE mode. Thus CAE gives good resolution at low kinetic energy, but with poorer signal-to-noise (or sensitivity) than in CRR (constant retarding ratio) mode.

The current actually reaching the analyser exit slit following photoionisation is typically in the region of 10^{-16}-10^{-14}A, which is well below conventional current measuring techniques. Thus an electron multiplier is used as the detector. The multiplier output is taken through a preamplifier, an amplifier, a discriminator and a rate-meter system, with a computer interface situated between the discriminator and rate meter. The spectra are subsequently digitized and stored for future reference [6].

4 Spectral Information

An x-ray photoelectron spectrum is generated by plotting the measured photoelectron intensity as a function of binding energy. These can be wide scan, covering the whole range of binding energies (Figure 2.7, [6]) or narrow scan, focusing on a narrow binding energy region which allows fine structure and lineshape to be resolved (Figure 2.8).

Figure 2.7 Mg K$_\alpha$ XP Spectrum of Hg$_{0.6}$Cd$_{0.4}$Te grown via Metal Organic Chemical Vapour Deposition
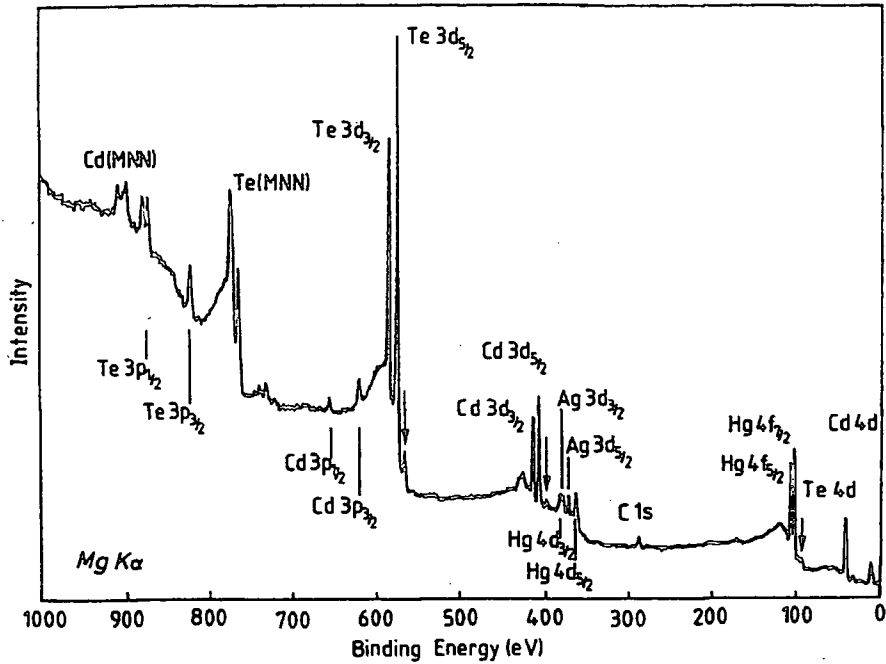
Figure 2.8 Mg K$_\alpha$ XP Spectrum of the Cu 2p region of a silica supported copper (II) acetate catalyst

68
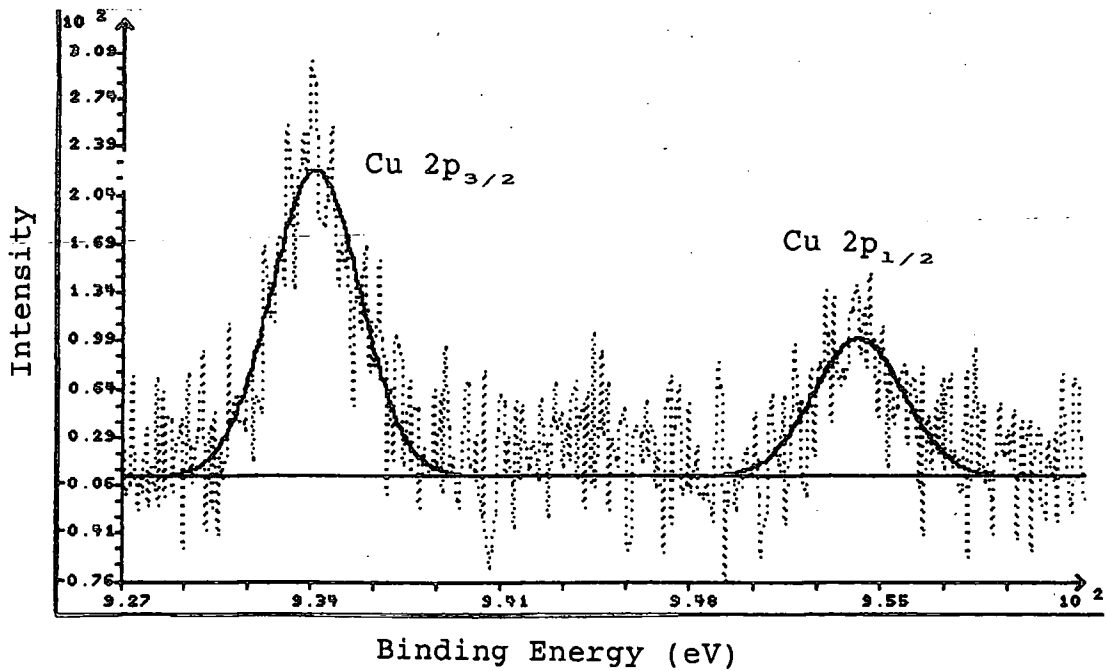
4.1 Spin-Orbit Coupling

Spectra may show detail due to spin-orbit coupling within the ionized core sub-shell, and in the case of open shell systems, detail associated with purely electrostatic coupling of the core hole with the partly filled outer sub-shell [49].

Initial state structure (electron energy distribution in the ground state) is dominated by the phenomenon of spin-orbit coupling. The spin orbit splitting of sub-shells with non-zero orbital angular momentum is resolved and can be used to confirm chemical identification [4]. If an electron is in a degenerate orbital (i.e. p, d, f, ...) the spin angular momentum, S, and the orbital angular momentum, L, can combine in different ways and produce new states that are characterized by the total electronic angular momentum J.
$J = |L\pm S|$ where: $L = 0,1,2,...,$ $S = 1/2$, $J = 1/2. 3/2, 5/2,...$
The energies of these new states are thus different because the magnetic moments due to the electron spin and orbital motion may oppose or reinforce each other. The degeneracies of these states is $2J+1$ and the relative intensities of these split peaks is given by the ratio of these degeneracies:
eg. Cr 2p   L = 1

$$J = |1\pm 1/2| = 3/2, 1/2 \implies Cr\ 2p_{3/2}\ and\ 2p_{1/2}$$

The relative intensities are $(2x3/2 + 1) : (2x1/2 + 1) = 2:1$ [6].

Within each core shell the lifetime width decreases, and the cross section increases, with increasing orbital angular momentum. As a result the core electron with the largest J value of a given shell generally gives the signal with the largest peak height and is most useful in chemical analysis [4].

If the system has electrons in a valence sub-shell then a core photoelectron signal may also show structure due to electrostatic coupling in the final state. The unpaired valence electrons will in general be delocalized over two or more atomic centres and so a significant, resolvable exchange splitting can be expected only in the case of a core photoelectron signal from an atom having appreciable share of the unpaired spin density [49].

4.2 Peak Structure

Some of the peak structure may arise through complex ionization processes in which ejection of a core electron is coupled simultaneously with excitation of one or more of the

other electrons (usually a valence shell electron). A coupled excitation involving an energy loss on the part of the outgoing photoelectron is termed a shake-up process and the additional signal at lower kinetic energy is termed a shake-up satellite of the main core photoelectron signal. If the additional excitation is a second stage of ionization (so that two photoelectrons emerge) the term shake-off is used. Normally shake-off processes do not lead to any discrete structure in photoelectron spectra.

Shake-up satellites are generally weak but interpretation can be difficult in the case of open-shell compounds where it may be confused with electrostatic coupling in the final state [49].

The measurables in a core electron spectrum are the positions, widths and shapes of the lines/peaks [4].

4.3 Line shape and peak fitting

Shape can often be ignored, but with unresolved overlapping lines numerical data analysis is necessary. The best approach is to fit a theoretical function to the data by least squares optimization.

Two processes are routinely carried out, namely deconvolution and curve fitting. Deconvolution is the process in which the broadening of a signal caused by instrumental effects is extracted from the true signal. Baseline resolution is not always obtained because the unbroadened signals may naturally overlap. Curve fitting is a reconstruction of the natural lines from the base line to fit the convolved envelope of signals.

In both cases no unique solution exists for an envelope. The main key to performing both processes is to have a thorough knowledge about the chemistry of the system and the photoelectron spectrum of the pure species of the convolved system. Therefore realistic parameters can be selected so that the number of solutions are significantly reduced [8,67,68].

A series of standard peaks, where the variables are the number, position, intensity, width, shape and type, are added together until the experimental spectrum is matched as closely as possible. The standard peaks are usually of Gaussian or Lorentzian form, or a form containing a mixture of the two forms, as these mathematical functions best maintain physical reality. The spectra in this thesis were fitted with pure Gaussian functions which have the form:

$$f(x) = h/(\{1/b^2\} \exp[(\ln 2)(x-x_o)^2/b^2])$$

where h = peak height

x_o = position of peak maximum
b = parameter proportional to the peak FWHM, the actual value being found iteratively

To begin curve fitting the baseline is set by drawing a straight line between two points on either side of the peak(s). Though this does not give absolute accuracy, good relative accuracy is obtained when used in a consistent manner throughout a series of spectra from the same material and it is easy and quick [8].

Fitting to the experimental spectrum is iterative and to start the iteration an initial approximation is input and visually compared to the spectrum in order to approximate the number of peaks and their respective parameters. A knowledge of the expected species and the nature of XPS spectra are used to set up an initial approximation. These data are also used to set up any links between parameters which are expected to vary together. The allowed range may be defined to keep it physically meaningful. Once a suitable starting point has been input, the iterative peak fitting routine is used. After the routine has converged to a solution the goodness-of-fit may be visually verified and the peak-fit parameters checked to see if they are in accord with physical constraints. Figure 2.9 shows the results of peak fitting for overlapping Mo 3d and S 2s peaks [134].

Figure 2.9   *Curve-fitting of Mo 3d and S 2s peaks: a) initial parameters; b) final parameters*

71

(b) Final parameters
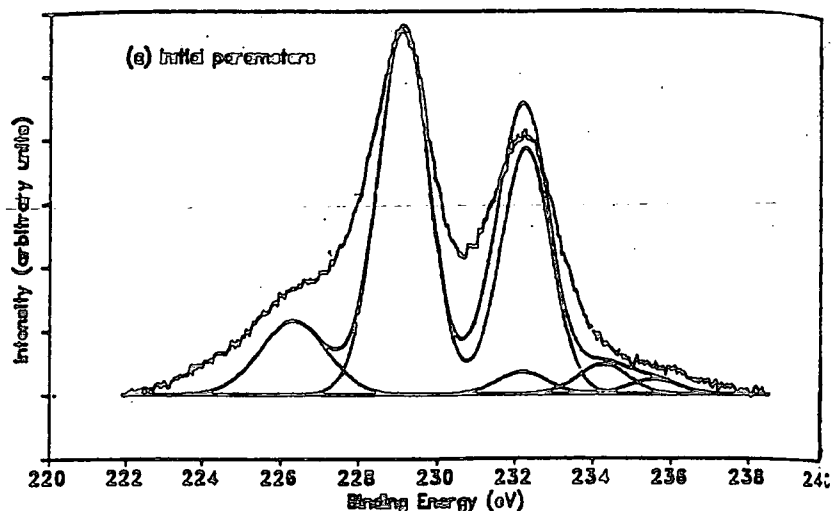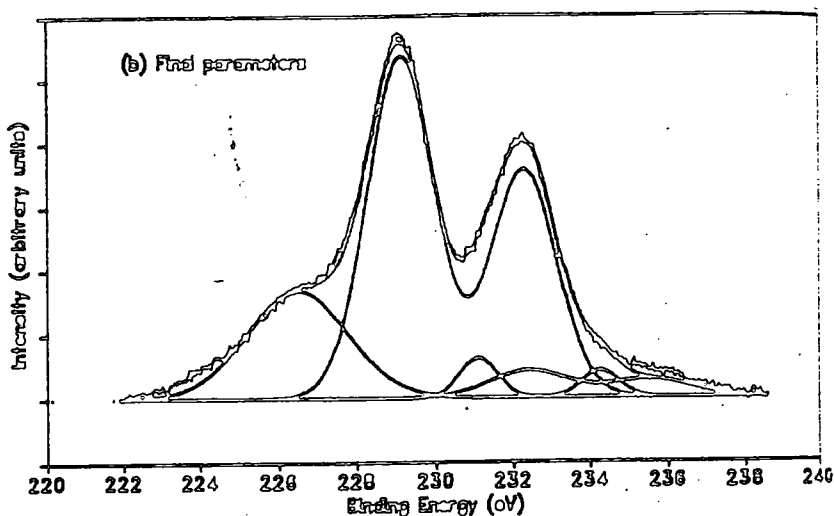
4.4 Line Width

The irreducible width of an XPS line is due to the lifetime of the core hole state created in the photoemission process. The resulting line shape is approximated by a Gaussian shape. A core hole has a number of decay channels whose contributions to the width are additive. De-excitation can occur by a two electron process in which one electron is emitted from an atom while the other makes a transition to the initial state core-hole. Singly ionized lifetimes are generally 10^{-14} to 10^{-15} seconds, giving rise to lifetime broadening contributions of between 0.1 and 5eV [5].

Measurement of the lifetime width of a core hole state is complicated by the existence of other contributions to the width of the experimental line from (i) instrument resolution, (ii) phonon broadening and (iii) inhomogeneous broadening.
(i) Where the x-rays are monochromatic the resolution function is significantly narrower and tends towards a Gaussian profile
(ii) Phonon broadening arises from vibrational modes of the crystal lattice, excited in ionisation. Most lattice modes are of very low energy so they cannot be resolved. In a solid, where the electronic energy levels form more-or-less broad bands, the widths of the peaks reflect this band width.
(iii) Inhomogeneous broadening arises from a superposition of lines with different chemical shifts and should be important mainly in disordered systems eg. amorphous materials [4].

4.5 Line Position (Binding Energy and Chemical Shift)

Binding energies are necessarily expressed relative to a reference level: the Fermi level is used for solids. For conducting samples the Fermi levels of the sample and the spectrometer coincide and can be determined by direct observation of the Fermi cut-off in a metallic sample. The work function does not enter into the calculation of the binding energy because the contact potential between the sample and the spectrometer changes the kinetic energy of the photoelectron appropriately as it enters the spectrometer [4]. Figure 2.10 shows the energy levels for photoemission.

Figure 2.10   Energy level diagram for photoemission
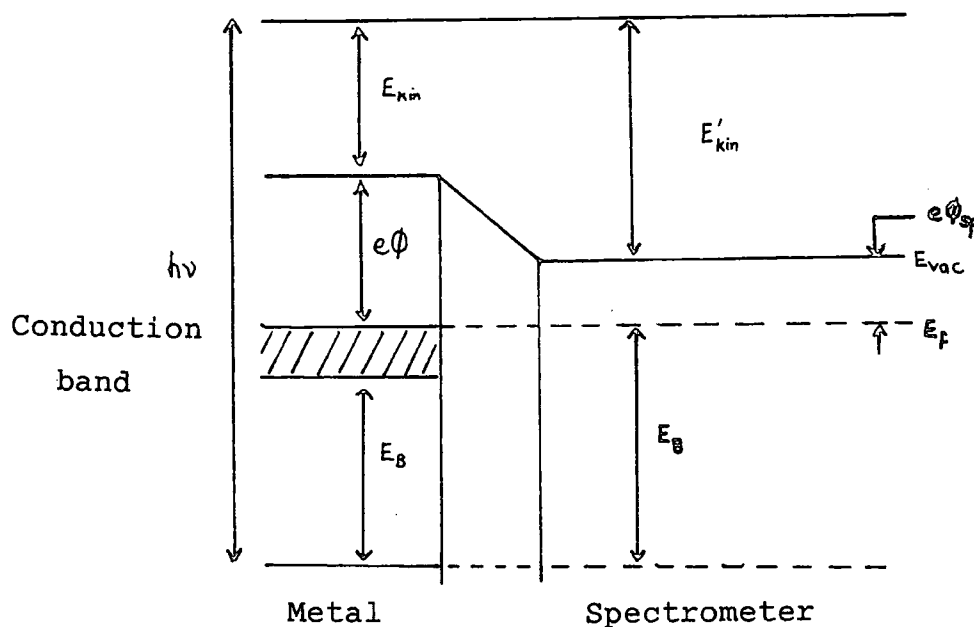
The sample is irradiated with X-rays of energy hν and electrons of binding energy E_b are ejected. The electrons have kinetic energy E_{kin} which can be measured in the spectrometer. ϕ is the work function of the sample and ϕ_{sp} that of the spectrometer. E_r is the energy of the Fermi level, E_{vac} that of the vacuum level.

Problems arise with insulating samples as the Fermi level could be anywhere within the band gap. Photoemission can also result in a build-up of positive charge near the surface resulting in a dipole layer. This arises because of the inability of insulating materials to replace the photoemitted electrons. Binding energies measured relative

to the Fermi level of the spectrometer are thus not valid. Lines from insulating samples are generally broad and appear at higher binding energies than expected due to charging: these shifts can be as large as, or even larger than, chemical shifts and can be confused with shifts due to changes in chemistry. Where spectrometers do not use monochromatic radiation the effects of charging are less severe and complications in spectral interpretation diminished [10].

In an attempt to compensate for this sample charging the surface can be flooded with low-energy electrons, but this is only a partial, and unreliable, solution. Alternatively an external reference can be used: a substance like gold can be deposited on the surface and one of its core levels used to define the energy scale [4], for supported catalysts a photoemission line of the support can be used or, most commonly, adventitious carbon, C 1s. This *in situ* carbon contamination can arise from the vacuum system of the spectrometer (the rotary and diffusion pumps) or can be found in the adhesive tape used for sample mounting [8,12]. When choosing a reference it must be in electrical contact with the sample and be chemically reliable and stable throughout the entire experiment, otherwise the determination of chemical states can become difficult and meaningless [8]. Since the C 1s lines are of substances of unknown, and perhaps varying, composition it has not been demonstrated that electrical equilibrium exsists. Also, with the gold decoration method there may not be a uniform layer but islands of gold on the sample surface. A better method is to calibrate the binding energies of insulators by reference to their vacuum levels, which doesnot rely on assumptions about the coincidence of Fermi levels, electrical equilibrium or changes in band levels [8,63].

In some cases the chemical shift occurs in a systematic fashion as the oxidation state changes, e.g. $Al^{\circ} \longrightarrow Al^{3+}$ show shifts from lower to higher binding energy as expected, since the ejected electrons from Al^{3+} are subject to less shielding from the valence electrons and a greater net positive charge from the atom than Al°. Unfortunately binding energy chemical shifts also depend on other factors such as electron relaxation and extra- and intraatomic forces. For example, the binding energies of Co 2p electrons increase from Co° to Co^{2+}, which is as predicted. However, Co_3O_4 has a lower Co 2p binding energy than CoO and a higher binding energy than the metal [72]. Therefore to evaluate the chemical nature of species on catalyst surfaces reference compounds must be examined using XPS in order to determine their chemical shifts. Then by comparing the chemical shifts of the catalyst and standard compounds a reasonable characterization of the chemical states of an element can be determined. This method can be complicated by the fact that many of the possible compounds on a catalyst

surface can have either the same, or very similar, binding energies [8].

5 XPS: Use in Catalysis and Quantitative Analysis

Qualitative identification of the metal species on the surface of supported metal catalysts is an important first step in catalyst characterisation. Quantitation of the various surface species provides a better assessment of the effect of catalyst preparation conditions, and the effects of additives and promoters on catalyst activity. Ultimately, the use of analytical techniques to determine quantitatively the distribution of supported metal species may aid in the prediction of catalyst activity and in the tailoring of catalysts for specific chemical reactions [13].

The kinds of information which can be obtained from XPS measurements and which are of direct importance to catalysis studies involve promoter distribution, dispersion studies, and surface conductivity as detected by charging effects.

One of the many factors contributing to catalyst performance is related to the distribution of promoter(s) on the support material. Surface chemical analysis by XPS can provide a measure of the distribution by monitoring the relative intensities (areas) of promoter and support electron lines.

It has been shown that the intensity ratio of supported phase and carrier XPS peaks is related to the dispersion of the supported phase [9,81-83]. Quantitative data is obtained by determining the peak areas and applying previously determined sensitivity factors.

For a homogeneous sample the number of photoelectrons per second in a given peak, assuming constant photon flux and fixed geometry is:

$$I = kN\sigma\lambda AT$$

where: K = constant
N = number of atoms of the element per cm^3
σ = photoionization cross section for the element
λ = inelastic mean free path for the photoelectrons
A = area of sample from which the photoelectrons eminate
T = analyser transmission function

If the sensitivity factor is defined as $S = K\sigma\lambda AT$, then

$$I = NS \text{ or } N = I/S$$

This gives semi-quantitative results for most situations except where heterogeneous samples are involved or where serious contamination layers obscure the underlying elements

[6]. Analysis of XPS intensity data is complicated by the porous nature of catalyst supports, since XPS cannot probe the internal surfaces [14,29,84].

5.1 Dispersion Models for Supported Catalysts

Kerkhof and Moulijn (KM) proposed a quantitative model that would allow XPS intensities to be used to quantitate the surface species on supported catalysts [9]. The model is applied to high surface area supports with monolayer coverage. The XPS intensity ratio of the promoter/support can be predicted by knowing the bulk ratio and their respective photoelectron cross sections. The model describes a catalyst as sheets of support of thickness t and a promoter of cubic crystallites with wall dimension c (Figure 2.11). Electrons are assumed to leave the support and the sample only in a direction perpendicular to the surface.

Figure 2.11 *The Kerkhof Moulijn Model of Supported Catalysts*

electrons leaving the support

electrons leaving the sample
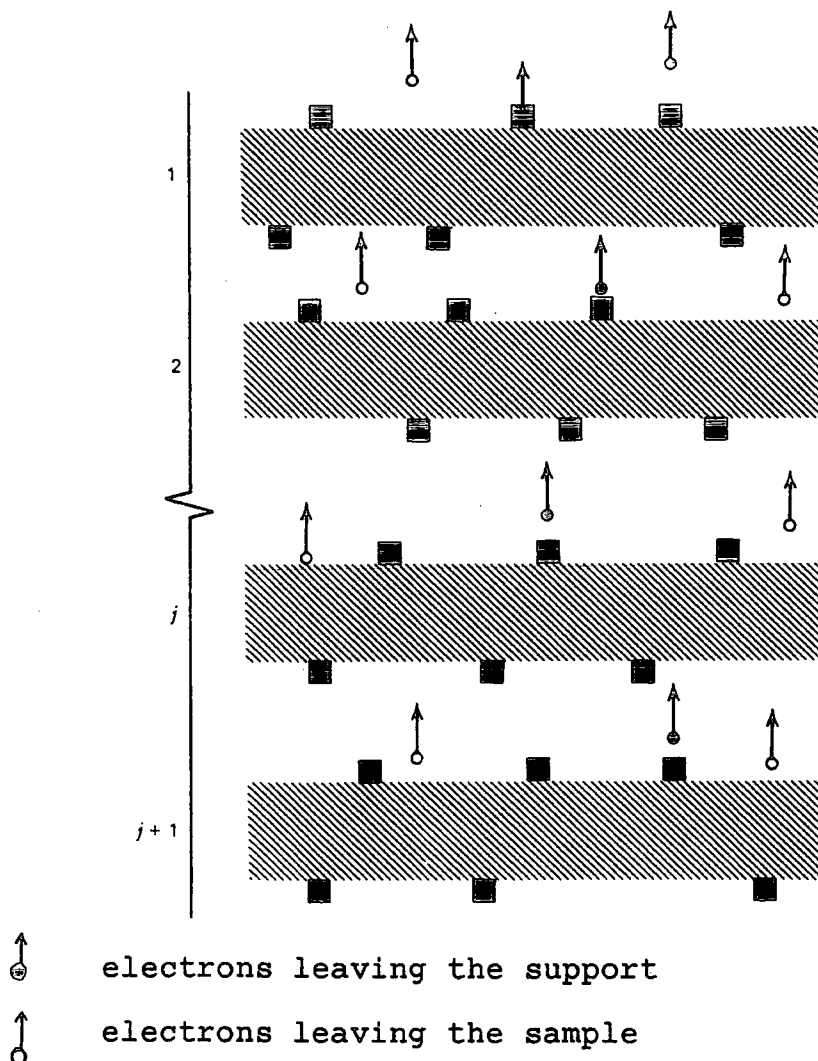
The intensity ratio of the promoter to the support is described by the following equation:

$$\left(\frac{I_P}{I_s}\right)_{expt} = \left(\frac{P}{S}\right)_{bulk} \frac{D_{\epsilon p}\,\sigma_P\,\beta_1\,(1-e^{-\alpha_1})(1+e^{-\beta_2})}{D_{\epsilon s}\,\sigma_s\,2\alpha_1\,(1-e^{-\beta_2})}$$

where: $\left(\frac{P}{S}\right)_{bulk}$ = bulk atomic % of the promoter and support

D_ϵ = detection efficiency (= kinetic energy of an electron)

σ_x = photoelectron cross section of x

β_1 = t/λ_{ss} (t= sheet thickness, λ_{ss} =escape depth of the support)

α_1 = c/λ_{PP} (c= crystalline size, λ_{PP} =escape depth of the promoter)

β_2 = t/λ_{sp} (= escape depth of a support electron through the promoter)

With monolayer coverage or less of the promoter the equation reduces to:

$$\left(\frac{I_P}{I_s}\right)_{expt} = \left(\frac{P}{S}\right)_{bulk} \frac{D_{\epsilon p}\,\sigma_P\,\beta_1\,(1+e^{-\beta_2})}{D_{\epsilon s}\,\sigma_s\,2(1-e^{-\beta_2})}$$

If the photoelectron lines have similar kinetic energies the equation reduces to:

$$\left(\frac{I_P}{I_s}\right)_{expt} = \left(\frac{P}{S}\right)_{bulk} \frac{\sigma_P\,\beta\,(1-e^{-\beta})}{\sigma_s\,2(1-e^{-\beta})} \qquad \beta = \beta_1 = \beta_2$$

The KM model has been shown to agree with XPS intensities in the literature. The model also allows the prediction of crystallite size of the supported material and the escape depths and cross sections to be evaluated [9].

There are some problems with the model: (i) an accurate escape depth for the component of a supported catalyst is difficult to obtain. However, it has been observed that the model is not sensitive to errors in the escape depth; (ii) nonuniform crystallite sizes will contribute to deviations from the model because one of the basic criteria of the model is uniform crystallite size, and (iii) inhomogeneous samples will deviate significantly from the model. Inhomogeneous coverage of supports will cause variations in the relative intensities of the support and the promoter [8].

On lower surface area supports the KM model should not be applicable in principle. For that case, a model considering formation of blocks of the supported phase as a function of its amount appears promising [80]. In the case of intermediate surface area supports (50 to 100m²g⁻¹) and of supports for which the layer modelling does not apply (i.e. microspheres of silica) testing new models with experimental data may be a direction of future research.

5.2 Effects of particle size on quantification

Variation in particle size of the supported species can affect the quantification of the surface by XPS [70]. Chin and Hercules [71] studied cobalt oxide catalysts on alumina: by plotting the Co/Al intensity ratios as a function of particle size it was observed that the larger the particle size the smaller the intensity ratio for the same catalyst loading. The results were in agreement with earlier experimental [70] and theoretical work [69]. The change in intensity ratios is caused by the limited escape depth of the ejected photoelectrons. As the cobalt particle size increases, electrons ejected from the central part of the particle do not have the ability to escape and be detected. Therefore variations in particle size must be considered when quantitative comparisons are made between catalysts of different loadings and calcination temperature [8].

6 The Phillips Catalyst

The Phillips catalyst (Cr(VI) on silica gel) for ethene polymerization is very important in the chemical industry since 40% of high-density polyethene is produced using this catalyst [36]. Its commercial importance has prompted a large body of reasearch, much of which has been devoted to characterization of the active site [37]. The catalyst has been prepared by impregnating wide pore silica with a chromium salt of almost any oxidation state and calcining in oxygen to activate: Cr^{VI} is the precursor of the active site, which is generated by reduction, either on contact with ethene (industrially) or with CO (most laboratory methods) prior to the onset of activity [21,40,45]. Evidence has been put forward that the active site is Cr^{V} [105-107], Cr^{IV} [108], Cr^{III} [111,114,117], Cr^{II} [109-113] and a combination of Cr^{III} and Cr^{II} [115,116]. Confusion has been compounded by the simultaneous presence of several oxidation states, that the active sites are only a small proportion of the surface chromium species [93,135,136] and by the fact that many researchers use preparations and conditions bearing little resemblance to the highly active commercial system [21]. Not only the oxidation state of the catalytically active metal, but its exact mode of attachment to the silica surface and the structure of the active site have yet to be unambiguously established [39].

McDaniel [26] has comprehensively reviewed work on the Phillips system and the unpromoted catalysts will not be discussed in detail here. This study has focussed on systems containing aluminium- and titanium promoters and used commercial catalysts in order to avoid the problems associated with laboratory preparations mentioned above.

6.1 Promoted Phillips Catalysts

There is a large body of patent literature containing studies of Phillips systems which are modified with many different promoters. There is considerably less published academic work examining these systems, perhaps not surprising in view of the lack of understanding of the parent system. Research has mainly been aimed at understanding the polymerization mechanism and kinetics, and promoter effect on this, with less detailed investigation of surface interactions between chromium and the promoter species. Studies of silica supported chromium catalysts promoted by titania and alumina prior to polymerization reaction are reviewed below.

6.2 Titania Promoters

Titania is not active itself but does act as a promoter for chromium, improving its activity and affecting some of the polymer characteristics [40], such as the molecular weight (MW - a lower MW polyethene is obtained and the MW distribution is broadened) [27,31,32], and the termination rate [28,32,43,98]. There is no, or a much shorter, induction period before polymerization occurs after titanium addition and the maximum rate of polymerization is 70% greater than for the unpromoted catalysts [26,43]. The effect of titania is thought to occur through a change in the electronic environment of chromium to which it is linked during calcination [26,30,31,40,43].

The incorporation of titania in the support as a cogel, where it is highly dispersed in the bulk, produces a polymer of a higher MW and narrower MW distribution in comparison to the polymer produced over a catalyst with a layer of titania on the surface of the support [31]. The shortened induction time suggests that titania addition makes Cr(VI) more easily reducible because the lower valent active sites come to life more quickly. This is also suggested by the increased polymerization rates, and the higher maximum rates may indicate an increase in the active site population, though this is not certain [26]. Lack of an induction period may also be due to facilitation of oxidation product removal [43].

McDaniel *et al* [32] found that the termination rate increases with increasing titania concentrations upto 1.5 Ti/nm² in cogel catalysts. Catalysts containing 0.3Cr/nm² with subsequent addition of a surface layer of titania by impregnation were found to have enhanced activity and RMIP (relative melt index of the polymer) at 760°C. The more titania added the higher the RMIP. McDaniel *et al* found that on cogel catalysts the RMIP and the activity dropped sharply at 870°C due to onset of sintering, which is also promoted

by titania [32].

The higher RMIP, higher shear response and broader MW distribution [121] imply that the increased electron density on chromium destabilizes the Cr-Cr bond, facilitating termination [43]. The chromium atom is positive relative to the growing polymer chain [122] and the increase in electron density at chromium might weaken the bond to the growing polymer allowing a higher rate of polymerization.

There are two methods of incorporating titania onto Cr/SiO$_2$ catalysts. The simplest involves allowing a titanium alkoxide to react with the silica surface hydroxyls:

$$\text{OH} \quad \text{OH} \quad \xrightarrow{\text{Ti(OR)}_4} \quad \begin{array}{c} \text{RO} \quad \text{OR} \\ \text{Ti} \\ \text{O} \quad \text{O} \\ \text{Si} \quad \text{Si} \end{array}$$
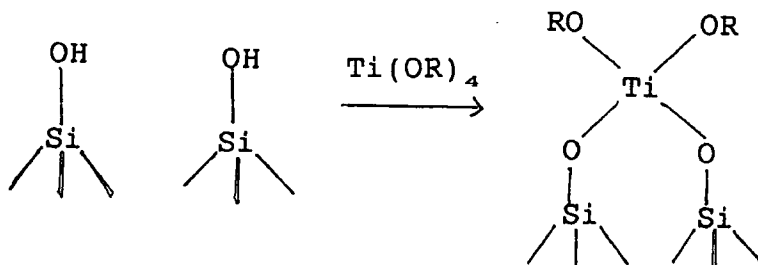
Unreacted OR groups are lost during calcination in dry air or nitrogen at 700°C [30-32,40,94,95]. Using this method silicas can be treated with upto 5-6% Ti, at which point saturation is usually reached [118].

The second method consists of coprecipitating hydrous titania with silica gel using a water soluble titanium salt [27]. This method gives a higher degree of dispersion throughout the bulk [26].

Table 2.1 *A comparison of Ti/Si XPS intensity ratios for three silica-titania catalysts prepared by impregnation and coprecipitation*

Ti/Si by XPS

Overall Ti/Si ratio	Coppt.	Impregnation
0.006	0.0056	0.0136
0.022	0.0167	0.0338
0.050	0.0340	0.0510

600°C activation [32]

80

From Table 2.1 it can be seen that coprecipitated samples yield a considerably lower contribution to the titanium intensity. Since XPS is a surface technique this indicates a lower surface concentration of titanium as expected [32].

Figure 2.12 shows the XPS derived Ti/Si atomic ratio for catalysts prepared by impregnation of silica gel with titania [27].

Figure 2.12 *The surface concentration of titanium measured as the atom ratio Ti/Si by XPS as a function of the titanium content*
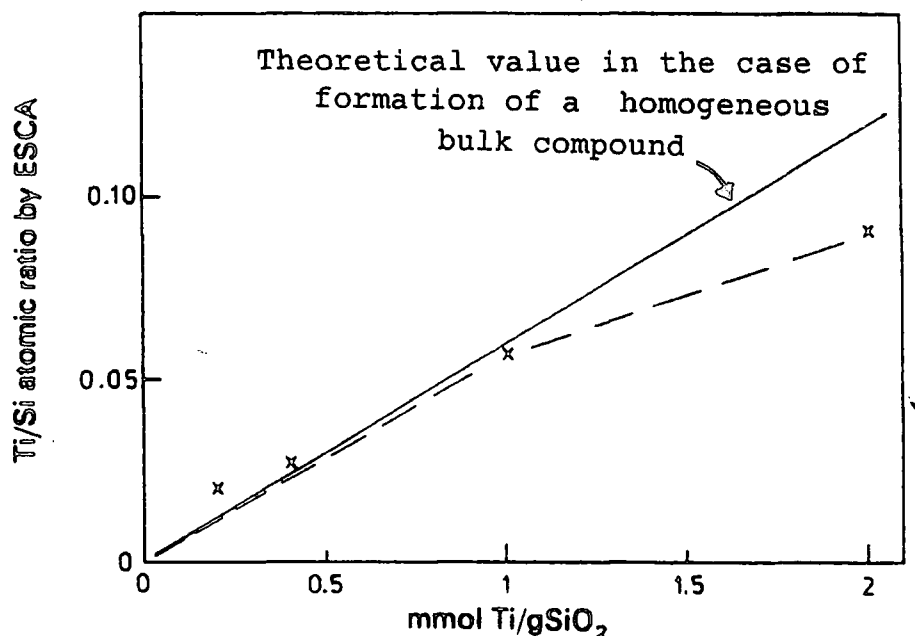
At low titania concentrations the Ti/Si intensity ratio indicates a high surface dispersion in the TiO_2/SiO_2 gel. At loadings of $2mmolTig^{-1}SiO_2$ substantial agglomeration is indicated [27]. This effect is stronger than with aluminium modified silica gel [27,34]. The integrated absorbance of the CO band obtained in a low temperature (-145°C, CO adsorption is relatively weak at room temperature) FTIR study (Figure 2.13) increases linearly with the titanium content for 0.2, 0.4 and $1mmolTi/gSiO_2$, with deviation for the highest loading, which was taken as further evidence for the agglomeration of titania. The deviation indicates that only some 70% of the titanium is present as coordinatively unsaturated surface ions, which agrees with XPS results. A band at $2188cm^{-1}$ increases in intensity with increasing titanium content and shifts to lower wavenumbers ($2183cm^{-1}$). A shoulder appears for 1 and $2mmolTi/gSiO_2$ samples, which may be from CO adsorbed on the small amount of crystalline anatase that was detected by XRD and XPS. The $2184/2180cm^{-1}$ band has been described previously [123] and was assigned to CO adsorbed on a coordinatively unsaturated Ti^{3+} surface

ion. It has also been assigned to octahedrally coordinated Ti^{4+} ions with one ligand removed [119,124,125].

Figure 2.13 *The FTIR spectra of CO adsorbed at low temperature (-145°C, 1 Torr CO) on TiO$_2$/SiO$_2$ gel samples obtained by impregnation*
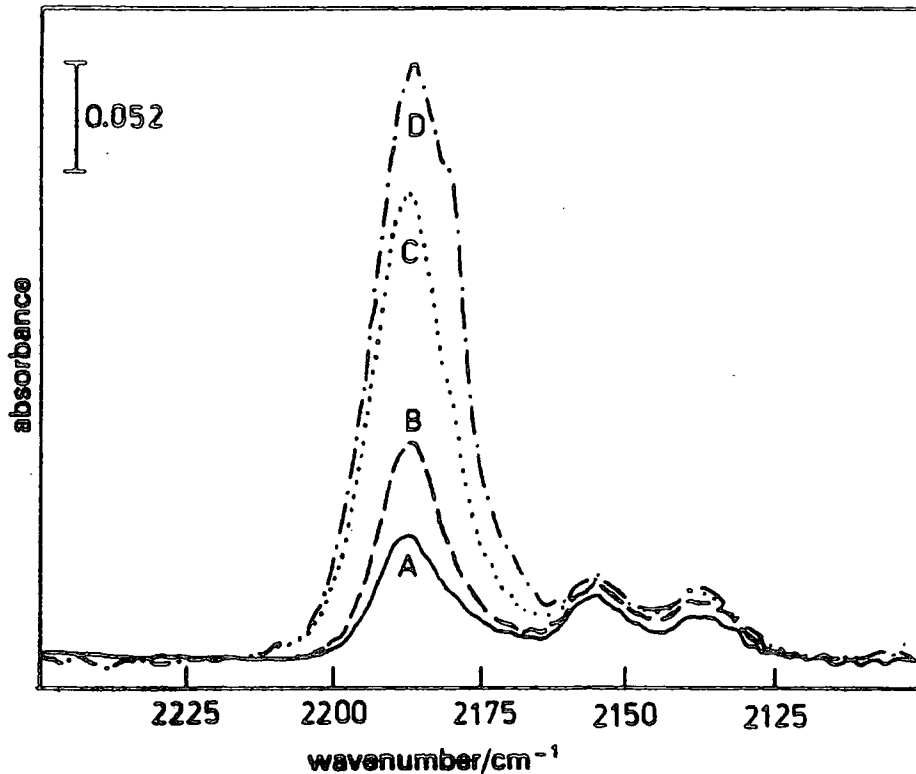
A 0.2, B 0.4, C 1, D 2mmolTi/g SiO$_2$

Table 2.2 contains the binding energies for these samples.

Table 2.2 *Binding energies of Ti 2p$_{3/2}$, Si 2p and O 1s for TiO$_2$/SiO$_2$ gel catalysts prepared by impregnation*

Binding energy (eV)

Sample	Ti 2p$_{3/2}$	Si 2p	O 1s
SiO$_2$		103.7(2.5)	533.2(2.4)
0.2mmolTi/g	459.7(3.1)	103.8(2.5)	533.2(2.5)
0.4mmolTi/g	459.7(3.0)	103.8(2.5)	533.2(2.4)
1.0mmolTi/g	459.1(3.0)	103.7(2.5)	533.1(2.4)
2.0mmolTi/g	459.0(2.8)	103.7(2.4)	533.1(2.4)
TiO$_2$	459.0(1.3)		530.2(1.5)

800°C activation, figures in parentheses are FWHM (eV) [27]

The Ti $2p_{3/2}$ binding energy decreases by 0.6-0.7eV from 0.2 to 2.0 mmolTi/gSiO$_2$ and the value of 459.0eV for the latter coincides with that of bulk titania. The higher binding energy obtained at lower titanium concentrations indicates some structural differences and could be explained by the formation of very small titania clusters [96] or by formation of surface titanium compounds [27].

Unlike mixed TiO$_2$/SiO$_2$ glasses [119], the silicon and oxygen core lines were constant, which was interpreted as showing that all titanium is external to the silica and that there is no mixed phase formed. The O 1s spectra confirm this: there is an increase in intensity on the low energy side of the O 1s peak, but the binding energy is not constant for different loadings. The low binding energy of 530.6eV at the highest titanium loadings suggests it is mainly due to Ti-O-Ti oxygen, whereas the higher binding energy (531.8eV) from the lower loadings suggests considerable interaction with silica, probably Si-O-Ti species.

Table 2.3 shows the effect of preparation and calcination temperature on the Ti/Si intensity ratios derived from XPS, where the catalysts contain the same titania concentration.

Table 2.3 *Ti/Si XPS intensity ratios for coprecipitated and impregnated TiO$_2$/SiO$_2$ catalysts containing the same concentration of titania*

<u>Ti/Si</u>

<u>Coprecipitated</u>	<u>Impregnation</u>
0.0338 (600°C)	0.0461 (450°C)
0.0389 (800°C)	0.0437 (750°C)
0.0411 (870°C)	0.0465 (900°C)

The Ti/Si intensity ratio increases as the calcination temperature increases for coprecipitated samples, indicating more titania near the surface and suggesting a migration from the interior. When titania is applied as a surface layer (using an ester, as above) it does not migrate, according to the XPS intensity ratios, which are approximately twice the value of coprecipitated samples containing the same overall titania content. This further confirms that cogellations leaves a good proportion of titania in the bulk, which in turn may change the geometry at the surface [26].

Sintering was observed to occur at 870°C [26], at a lower temperature than Cr/SiO$_2$, hence titania also promotes the sintering process, as impurities often lower the melting point of solids. The more titania added the lower the temperature needed to cause sintering. Sintering is

associated with a tendency towards phase separation between silica and titania in cogel samples: where titania is applied as a surface layer sintering behaviour is not affected [26]. No development of crystallinity was detected by XRD upto 950°C with either sample [32].

How chromium becomes attached to titanium is unclear: XPS, optical spectroscopy and polymerization kinetics have been used [28,43,98] to conclude that Cr^{VI} is attached directly as:

$$
\begin{array}{ccc}
O & & O \\
\diagdown\!\!& & \!\!\diagup \\
& Cr & \\
\diagup\!\! & & \!\!\diagdown \\
O & & O \\
| & & | \\
Ti & & Ti
\end{array}
$$

Pullukat and Shida [43] treated Cr/SiO_2 with a titanium ester prior to thermal activation. A trivalent chromium titanate species $Cr(OTi(OR)_3)_3$ was formed. After activation chromium is predominantly hexavalent but in a titanium chromate structure such as:

$$
\begin{array}{l}
\diagdown \\
\!\!-Si-O-Ti \\
\diagup \qquad\qquad\quad \diagdown \\
\qquad\qquad\qquad\quad O \\
\qquad\qquad\qquad\quad | \\
\qquad\qquad O\!=\!Cr\!=\!O \\
\qquad\qquad\qquad\quad | \\
\qquad\qquad\qquad\quad O \\
\diagdown \qquad\qquad\qquad \diagup \\
\!\!-Si-O-Ti \\
\diagup \qquad\qquad \diagup\diagdown
\end{array}
$$

A maximum promotional effect was noted at a Ti/Cr stoichiometry of 3.0, though McDaniel et al [32] found no optimum stoichiometry with their catalysts, which were prepared by impregnating chromium onto silica. In other procedures where Cr^{VI} salts were not used or titanium was not introduced as an ester, a different method of attachment must be assumed. Evidence of decreases in binding energies of Cr^{VI} were used to support the change in the chromium electronic environment. This is seen in Table 2.4.

Table 2.4 Comparison of the Cr $2p_{3/2}$, Ti $2p_{3/2}$, Si 2p and O 1s binding energies in CrO_3/SiO_3 and $CrO_3/TiO_2/SiO_2$ catalysts

	Cr $2p_{3/2}$	Ti $2p_{3/2}$	Si 2p	O 1s
SiO_2/CrO_3 (air,700°C)	579.6		104.7	534.3
$SiO_2/TiO_2/CrO_3$ (air,700°C) 2% Cr, 3.5% Ti	578.0	460.0	103.8	533.3

The decrease in chromium $2p_{3/2}$ binding energy can be explained by the increase in electron density at the chromium atoms due to the presence of less electronegative titanium [43], as is illustrated below.

$$-Ti-O-Cr-O-Ti- \quad \longleftrightarrow \quad -Ti-O-\overset{\delta+}{C}r-O-Ti-$$
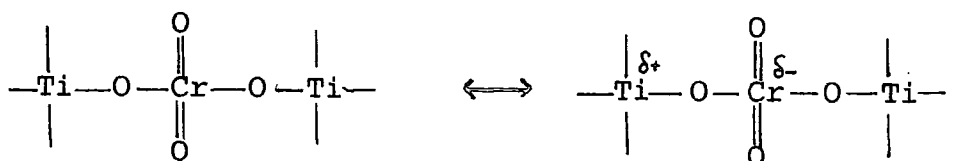
Many experiments suggest that the promotional effect of titania is due to formation of Ti-O-Cr bonds and that this is very dependent on subtle variations in the preparation of the catalyst - for example, impregnating most titanium salts onto Cr/SiO_2 as an aqueous solution does not result in promotion, whereas anhydrous titanium esters reacting with silanols are highly effective. In the former case the chromium remains attached to silica and doesnot link to the titania, whereas in the latter case much of the chromium is deposited onto the titania. Simultaneous impregnation of chromium and titanium leads to an intermediate promotional effect which thus seems to parallel the probability of forming Ti-O-Cr bonds [26]. A large promotional effect has been shown to occur only when titanium is added to silica first. This effect always decreased as the temperature increased, which could be interpreted as a migration of chromium away from titania [32].

The presence of titania during gellation tended to increase the initial surface area and to decrease the initial pore volume slightly [31]. The thermal stability of both is decreased by titania. The probability of chromium agglomeration increases as the surface area decreases, as chromium mobility also decreases with decreasing pore volume [47].

Confirmation that titania acts as a promoter through direct links to chromium was obtained by exposing silica to $TiCl_4$ vapour at 150-300°C, completely dehydroxylating the surface and saturating it with titanium. Residual chloride groups were hydrolysed at 200°C and CrO_2Cl_2 vapour added. This catalyst polymerized ethene without any high temperature activation. Extensive rearrangement is unlikely at 200°C so it is reasonable to assume that chromium actually attaches to titania:
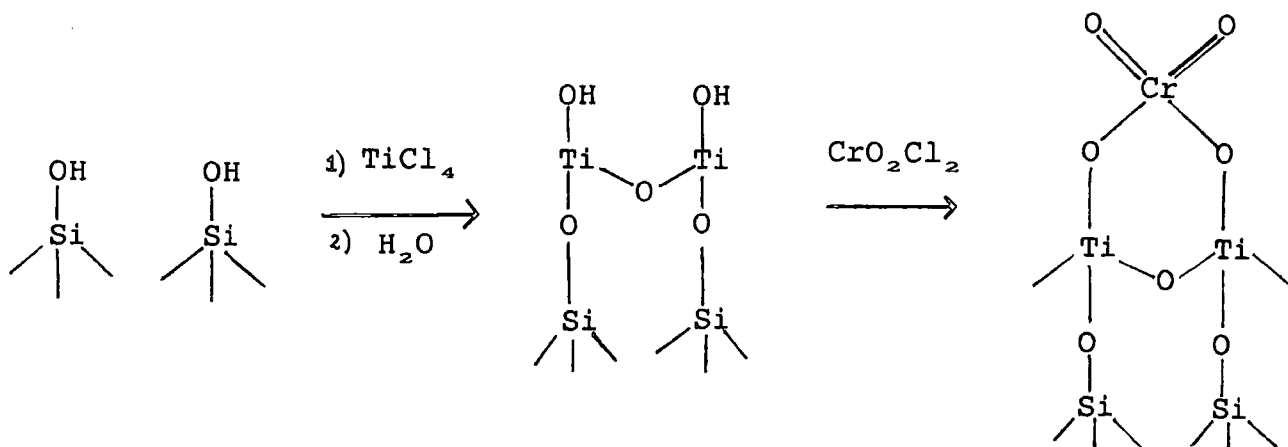
6.3 Aluminium Promoters

Even a minor amount of an aluminium alkyl has been found to have important effects on catalyst behaviour, greatly changing the kinetic profile: the induction period is eliminated and the polymerization reaches its maximum value very rapidly [46,100-102]. The alkyl is added to the reactor containing the catalyst and can act as either a strong reducing agent without forming inhibiting by-products or a scavenger of impurities such as aldehydes and ketones produced during reduction by ethene prior to the beginning of polymerization [33,46,55]. For a 1wt% Cr catalyst Woo and Woo [33] found a concentration of $Al(iBu)_3$ of > 0.765 mmol/l was required before polymerization occured.

Cr^{6+} can be reduced to a lower oxidation state and alkylated by the aluminium promoter, as occurs on Ziegler polymerization catalysts:

$+ \quad RAl(OR)_2 \quad (I)$

(II)
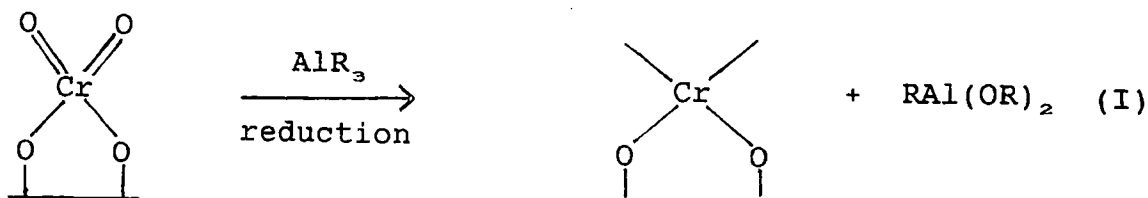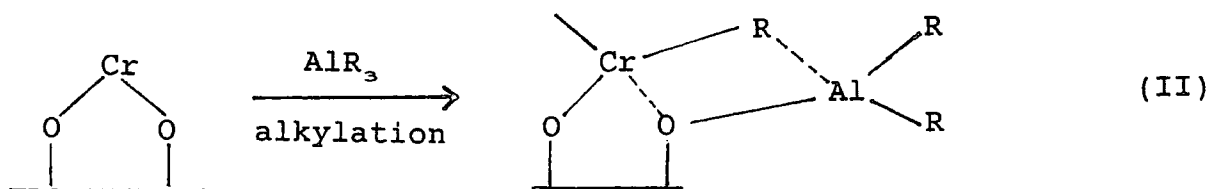
The lack of an induction period is due to instantaneous formation of active polymerization centres through reactions I and II. The more aluminium alkyl added the more rapidly the reaction reaches the maximum rate of polymerization.

Above 1.07 mmol/l of $Al(iBu)_3$ a decrease in the rate of polymerization occurs. Aluminium alkyl could play a role as a deactivator or/and terminator and deactivation could be due to over reduction of Cr^{2+} to Cr^{1+} or Cr^o.

Rebenstorf and Andersson [34] treated silica with aluminium (III) acetylacetonate in 99% ethanol to give 0.2, 0.4, 1 and 2 mmolAlg^{-1}. After calcination at 800°C the samples were impregnated with aqueous CrO_3 to give 0.074% Cr. Water was removed at 120°C in air.

After addition of a small amount of aluminium there is an initial increase and then a steady decrease in surface area.

Figure 2.14 The Surface area of Al_2O_3/SiO_2 gel samples as a function of the aluminium content
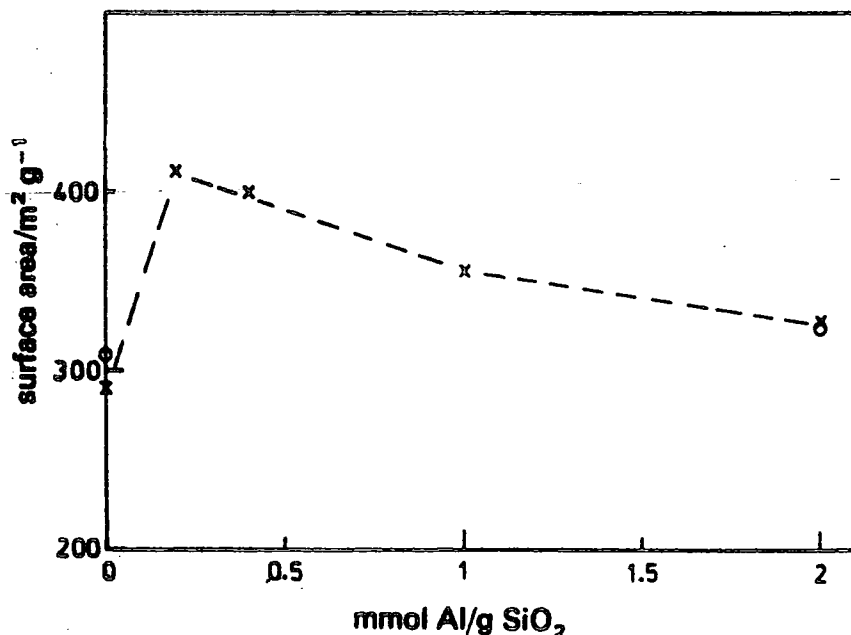
Measurements were made with micrometrics after degassing at 200°C for 1h (x) and gravimetric BET after degassing at 350°C for 16h (o)

87

At low aluminium concentrations the Al/Si intensity ratio is larger than the theoretical value, implying that aluminium is in the surface layer (Figure 2.15). The surface dispersion of the aluminium phase is very high for all samples. At the highest loading there is a substantial agglomeration of aluminium species. This agrees with the CO IR data: a band at $2229 cm^{-1}$ due to CO adsorbed on highly coordinatively unsaturated Al (III) surface cations with coordination number three [126] and two bands at 2191 (shifted to $2220 cm^{-1}$ for 1 and $2 mmol Al/g SiO_2$) and $2170 cm^{-1}$, due to CO adsorbed on Al (III) with coordination numbers four and five. The integrated absorbance of the CO IR bands have a linear relationship with the aluminium concentration for the two lower concentration samples, whilst at high aluminium concentrations less aluminium is present on the surface.

Figure 2.15 *Surface concentration of aluminium measured as the atom ratio Al/Si by XPS as a function of the aluminium content*
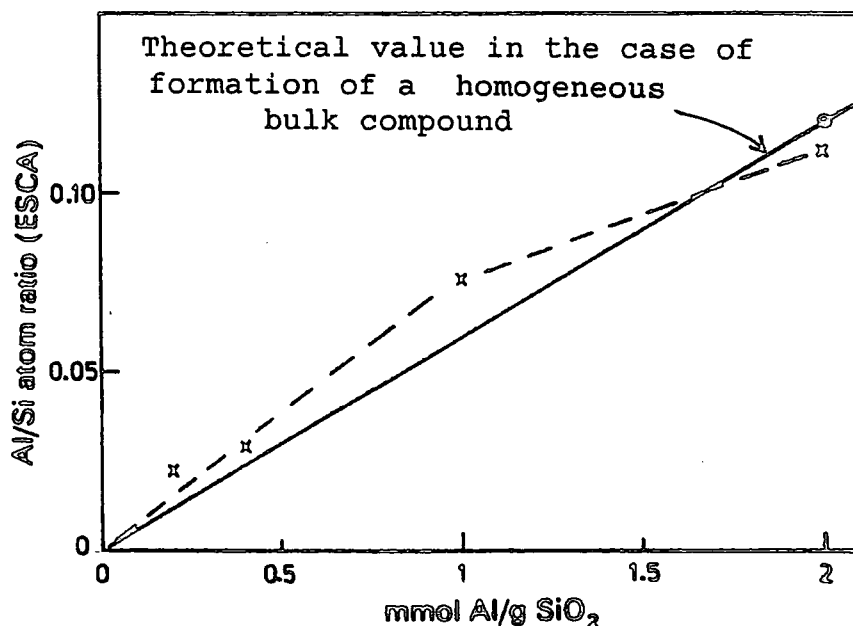
The binding energies of these catalyst samples are shown in more detail in Table 2.5.

Table 2.5 *Binding energies of O 1s, Si 2p and Al 2p for a series of Al_2O_3/SiO_2 catalysts*

Binding energy (eV)

Sample	Al 2p	O 1s	Si 2p
SiO_2		533.2 (2.4)	103.7 (2.5)
0.2mmolAl/g	75.0	533.1 (2.5)	103.6 (2.6)
0.4mmolAl/g	75.1	533.0 (2.3)	103.5 (2.5)
1.0mmolAl/g	75.0 (2.3)	532.6 (2.4)	103.2 (2.4)
2.0mmolAl/g	75.0 (2.5)	532.6 (2.4)	103.2 (2.4)
Al_2O_3	74.6 (2.6)	531.7 (3.2)	

Figures in parentheses are FWHM (eV)

The Al 2p binding energy is 75.0-75.1eV for all samples and the half width is 2.3-2.5eV. The binding energy is slightly higher than that measured for Al_2O_3 (74.6eV), indicating a slightly different interaction. This shift may be due to the formation of Al-O-Si bonds similar to those in aluminosilicates, in agreement with the shift observed between Al 2p in Al_2O_3 and various aluminosilicates [54,103,104].

The O 1s, Si 2s and Si 2p lines all shift with increasing aluminium loading. The peak shapes do not change and only a uniform decrease in binding energy is observed. Charging effects were ruled out since both C 1s and Al 2p lines were constant. The shifts do indicate the formation of aluminate since these binding energy values are usually lower for silicates than silica [54,103,104]. The shifts also agree with those observed for mixed TiO_2-SiO_2 gels [119] and do not increase further at the highest loading. This indicates that aluminium in excess of 1mmolg^{-1} does not give much more aluminium dissolved in the silica gel under present conditions, but possibly results in formation of an extra phase.

Comparison of the O 1s spectra of silica gel and 2mmol Alg$^{-1}SiO_2$ Al_2O_3/SiO_2 sample indicated the presence of some amount of Al_2O_3 at this loading.

Figure 2.16 The apparatus used to activate the catalyst samples prior to XPS
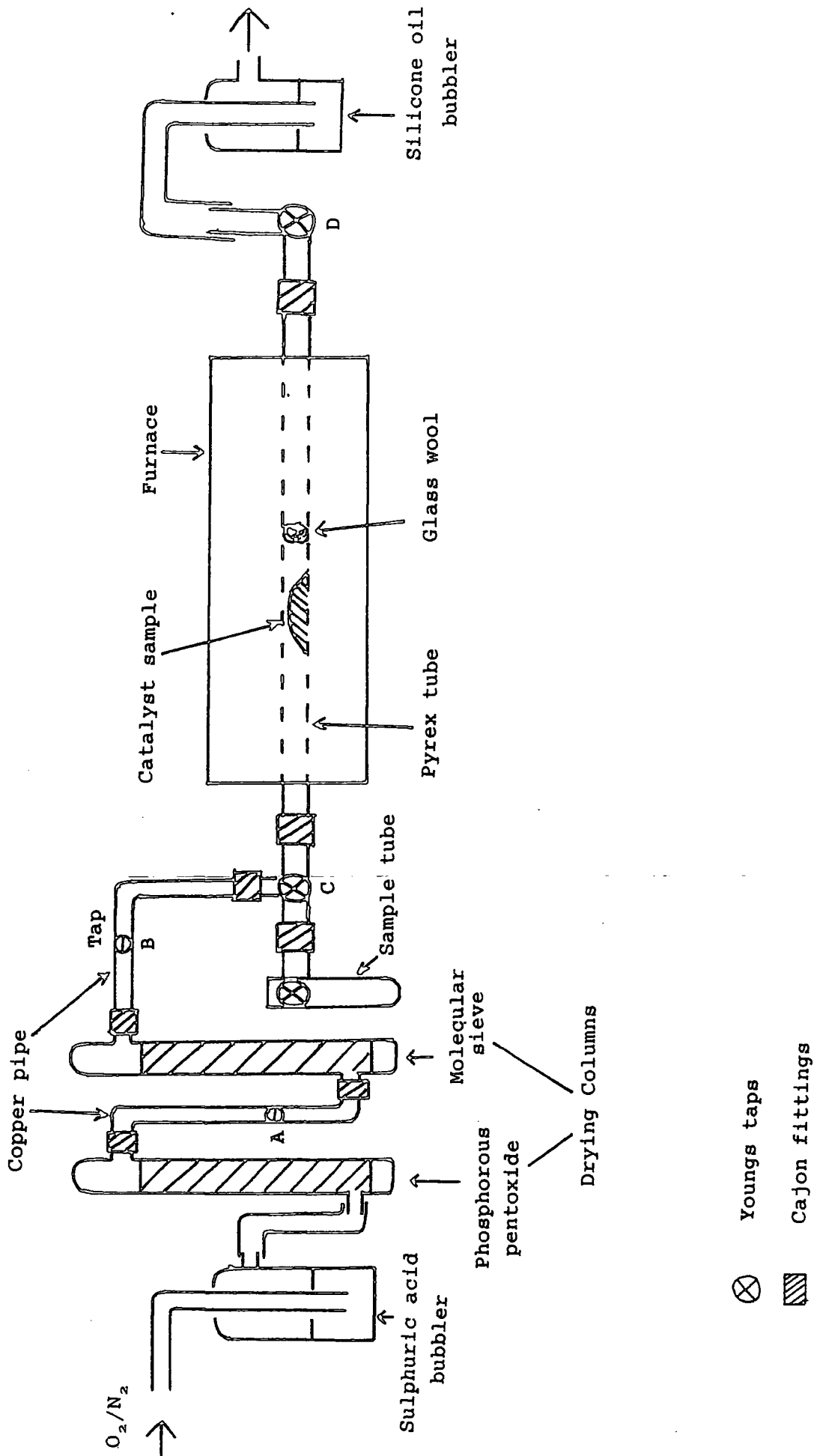
EXPERIMENTAL

1 Materials

The catalysts in this study were obtained from Crosfield Chemicals and used as supplied. Details of the materials are given in Table 2.6.

Table 2.6 Details of the Catalysts used in the XPS experiments

Ref	Description	wt%
EP10	amorphous silica, $300m^2g^{-1}$	
EP20	EP10 + chromium (VI) oxide	Cr 0.98
EP30X	EP10 + chromium (III) acetate	Cr 1.00
EP284	EP10 + TiO_2 + chromium (III) acetate	Cr 0.96 Ti 4.35
CS2066	EP10 + TiO_2 + chromium (III) acetate	Cr 1.00 Ti 2.50
EP200	EP10 + Al_2O_3 + chromium (III) acetate	Cr 0.52 Al 0.87
EP210	EP10 + aluminium alkyl + chromium (III) acetylacetonate	Cr 1.00 Al 1.00
EP55	EP10 + TiO_2 cogel	Ti 2.50
EP355	EP55 + chromium (III) acetate	Cr 1.05 Ti 2.53

Note: + indicates addition by impregnation, except for EP55 which is obtained by coprecipitation.

Nitrogen and argon (oxygen free, 99%) and oxygen (99%) were obtained from BOC and were all dried by passing through concentrated sulphuric acid, followed by columns of phosphorous pentoxide (May and Baker) and 4A molecular sieves (Lancaster). The latter was frequently regenerated by heating to 150°C *in vacuo* until no further water could be condensed into the cold trap. The gas handling system was designed to allow this operation to be carried out *in situ*.

2 Catalyst Activation

The activation was carried out in the microreactor shown in Figure 2.16.

The catalyst sample is placed in the quartz tube containing a glass wool plug and the apparatus assembled as shown. After flushing with dry oxygen for approximately ten minutes the gas flow is adjusted to 1.5l/h. The sample is then heated at a rate of 1°C/min until a temperature of 780°C is reached, which is maintained for five hours. Following cooling to room temperature at 1°C/min, the sample was flushed with dry nitrogen or argon (to prevent adsorption of oxygen) for a period of approximately ten minutes [33]. With the upper half of the furnace removed taps A, B, C and D were closed and the microreactor detached from the gas handling system. The activated catalyst can then be tipped into the collection vessel and sealed under nitrogen or argon, before transfering to the glove box attached to the X-ray photoelectron spectrometer.

3 XPS measurements

The XPS measurements were carried out on an AEI ES200 spectrometer having a base pressure of 1×10^{-9} Torr. Mg K_a x-ray radiation of kinetic energy 1253.6eV was used as the excitation source. The binding energy scale of the spectrometer was calibrated by setting the Au $4f_{7/2}$ peak of gold foil to 83.8eV, the Ag $3d_{5/2}$ peak of silver foil to 367.9eV and the Cu $2p_{3/2}$ peak of copper foil to 932.4eV. Data was aquired in the FAT mode (fixed analyser transmission energy, using a CHA pass energy of 65eV) and samples were analysed using an electron take-off angle of 30° from the surface normal. Data collection was controlled by an Opus PC. Samples were mounted on double sided adhesive tape on stainless steel probe tips: unactivated catalyst samples were introduced into the spectrometer from ambient conditions; the activated samples were introduced from a nitrogen atmosphere glovebox (approx. 10ppm water and approx. 1.5ppm oxygen). All XPS binding energies were referenced to the Si 2p binding energy in silica, which is taken to be 103.4eV in order to compensate for sample charging. All spectra were fitted using a Gaussian curve function which included a linear background subtraction routine [62]. Peaks were fitted to the Ti 2p and Cr 2p regions in the theoretical ratio of 2:1. Details of the peak fitting procedure are discussed in section 4.3 above.

RESULTS and DISCUSSION

The results are tabulated in Tables 2.8 - 2.17. For comparison Tables 2.18 and 2.19 contain binding energy and peak FWHM values for bulk and silica-supported chromium oxides, titania and alumina as reported in the literature. Spectra for all experiments are contained in a separate box file, but a selection are shown in Figures 2.19 - 2.40.

Experimental binding energies were obtained within an error of ±0.1eV. Tables 2.16 and 2.17 contain sets of average values obtained for each catalyst and a statistical analysis of the errors involved was carried out using standard deviation methods [133]. The analysis shows that there is little deviation from the average value and the binding energies and calculated metal dispersions are true representations of the catalysts behaviour, both unactivated and activated.

It was found that after activation all the catalysts were a bright orange colour, except for the cogel EP55 (2.5% Ti), which remained white. The orange colour was taken as indicative of Cr^{VI} formation [21]. Exposure to moisture, via incompletely dried nitrogen, argon or oxygen, or prolonged exposure to light led to colour changes: the former to green, indicating Cr^{III} formation, Cr_2O_3 being formed as a result of Cr-O-Si bond hydrolysis; the latter led to a dull orange or yellow colour, though light affects just the exposed surface of the sample rather than the bulk. Due to the catalysts photosensitivity sample tubes were kept covered in the glovebox prior to running XPS spectra.

Samples of CS2066 (2.5% Ti, 1% Cr) were used, following activation, to show the effects of light and exposure to ambient conditions (Table 2.7).

Table 2.7 *The effect of conditions on the Cr and Ti $2p_{3/2}$ binding energies and Cr/Si and Ti/Si XPS intensity ratios for catalyst CS2066*

Sample	Colour	Cr $2p_{3/2}$	Cr/Si	Ti $2p_{3/2}$	Ti/Si
051	yellow/orange	578.0	0.26	459.4	0.19
052	dark yellow	578.1	0.17	459.6	0.23
053	bright yellow	579.4	0.23	459.4	0.22
000	bright orange	579.6	0.26	459.6	0.24

051 sample left in glovebox 20hrs on adhesive tape
052 sample exposed to air 20hrs, mounted and run
053 sample exposed to air 24hrs but covered to exclude light
000 the average values for activated CS2066 from Tables 2.16 and 2.17

Light appears to have the greatest effect on Cr $2p_{3/2}$ binding energy, since exclusion of light little changes the value from that of a freshly activated catalyst. The yellow

colour could indicate a change in the chromium binding mode: that chromate predominates over dichromate, where the orange colour is associated with dichromate. Exposure to light is seen to dull/change the sample colour and reduce the chromium binding energies by over 1eV, indicating that light may catalyse the recombination of chromate/dichromate units to form the Cr-O-Cr linkages of bulk CrO_3 which is polymeric [56]:
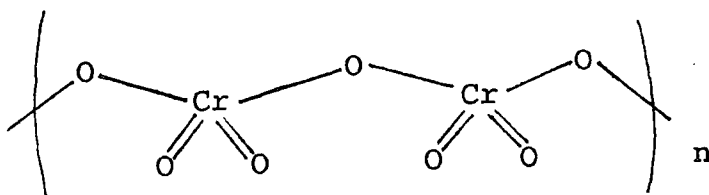
The Ti $2p_{3/2}$ binding energies are little changed in these experiments and hence the titanium species are unaffected by the exposure to light.

When collecting spectra the chromium region was always run first and obtained within 20 minutes in order to minimize photoreduction, as four scans were required to obtain a sufficiently intense spectrum and to increase the signal-to-noise ratio. McDaniel *et al* [21], Halada and Clayton [41] and Cimino *et al* [57] have all observed photoreduction of Cr^{VI} with prolonged exposure to x-rays, Halada and Clayton claiming significant reduction of CrO_3 powder after just five minutes, with evidence of CrOOH, Cr_2O_3 and CrO_2 formation. McDaniel *et al* [21] obtained their spectra in 30 minutes and found this allowed spectral collection without visible photoreduction.

1 XPS studies of silica and titania

The Si 2p binding energy was used as the internal reference and set at 103.4eV. This peak is attributed to the silicon atoms in silanol groups, Si-OH,; the much smaller peak at 101.5eV is attributed to silicon atoms in the siloxane bridges, Si-O-Si. The O 1s spectrum revealed two peaks at 530.7 and 532.8eV, the latter being the most intense. The peak at 532.8eV is attributed to the oxygen in Si-OH bonds, the less intense peak to the oxygen in siloxane bridges [48]. This is as expected, since for silica at ambient conditions the surface is hydrated (hydroxylated) and most of the siloxane bridges are buried too deeply to be detected using XPS, which is a surface technique.

	Si 2p	O 1s	
028	101.5, 103.4	530.7, 532.8	eV
		4.1 95.9	%

The values for titania were referenced to adventitious carbon, set at 284.6eV for C 1s.

	Ti 2p$_{3/2}$	O 1s	
014	457.9	528.6, 530.6	eV
		88.4 11.6	%

The O 1s peaks are attributed to Ti-O-Ti bonds (528.6eV) and Ti-OH bonds (530.6eV), the former being the more intense peak. This can be accounted for by considering the dispersion of OH groups on the titania surface at ambient conditions:
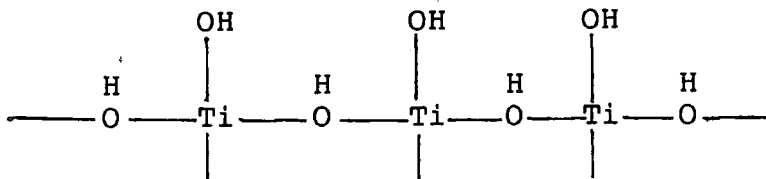
2 XPS studies of chromium/silica catalysts

Binding energy values for chromium VI oxide/SiO$_2$ (EP20) and chromium III acetate/SiO$_2$ (EP30X) are shown in Table 2.8 An average Cr 2p$_{3/2}$ binding energy of 579.2eV was obtained for unactivated EP20. The corresponding value for EP30X is 577.9eV, which increases to 579.4eV on activation. From Table 2.18 it can be seen that Cr 2p$_{3/2}$ values in the region 579-580eV have been reported in the literature for hexavalent chromium, both in bulk and supported oxides. The value of 577.9eV for Cr^{III} is in agreement with the results of Merryfield et al [21].

A measure of the dispersion of the chromium species on the silica surface is given by the Cr/Si intensity ratio (note: these values have not been corrected for sensitivity factors since only the relative composition of the samples is considered). For unactivated EP20 an average value of 0.25 was obtained, compared with 0.43 for unactivated EP30X. On activation and subsequent conversion to Cr^{VI} the value for EP30X falls to 0.29 (Tables 2.9, 2.17)

The higher dispersion of EP30X when unactivated is most likely linked to the fact that chromium III acetate has been shown to retain its trinuclear [Cr$_3$O(CH$_3$CO$_2$)$_6$(H$_2$O)$_3$]$^+$ structure on adsorption by silica [39]. On activation there is conversion to Cr^{VI} oxide, most probably attached as a

chromate-type structure (assigning a dichromate structure would account for the bright orange colour) and the dispersion falls to a value slightly higher than unactivated EP20. A decrease in dispersion can be associated with an increase in particle size, where crystallites are present, or formation of larger aggregates, since a lower fraction of atoms will contribute to the XPS signal and electrons are trapped in the particles due to the large escape depths of large crystallites. At higher temperatures the dispersion can decrease due to segregation at the surface or due to sintering: however, this can be ruled out for EP30X as sintering does not occur at temperatures below 900°C [26]. Encapsulation by silica has also been put forward as a reason for a decrease in the dispersion, as seen in Fe_3O_4/SiO_2 systems by Lund and Dumesic [127,128] and supported by the fact that a solid becomes mobile when at or above the Tamman temperature, $0.52T_m$ (T_m = melting point in K), which is 765°C for silica. However, Lund and Dumesic found the silica encapsulation process was promoted by the presence of water vapour and a reducing atmosphere.

There is evidence that agglomeration of chromium oxide occurs at higher temperatures. CrO_3 mobility increases during the activation process, as the average pore radius increases and it becomes less thermally stable above 823K. This results in its thermal decomposition and a decrease in the surface area of the support. As the surface area decreases the probability of agglomeration increases and di- or polychromates can easily be formed [47].

Also, Ellison [38] has reported that at concentrations as low as 0.5% Cr considerable clumping or clustering of the supported chromium occurs, so that 2- or 3-D aggregates of chromium oxide predominate [129]. SIMS results revealed that on heating the chromium oxide is further 'spread out' on the surface so that the texture, environment and therefore the properties of the chromium oxide clusters are similar (Figure 2.17).

Figure 2.17 *Schematic picture of chromium clusters on silica*
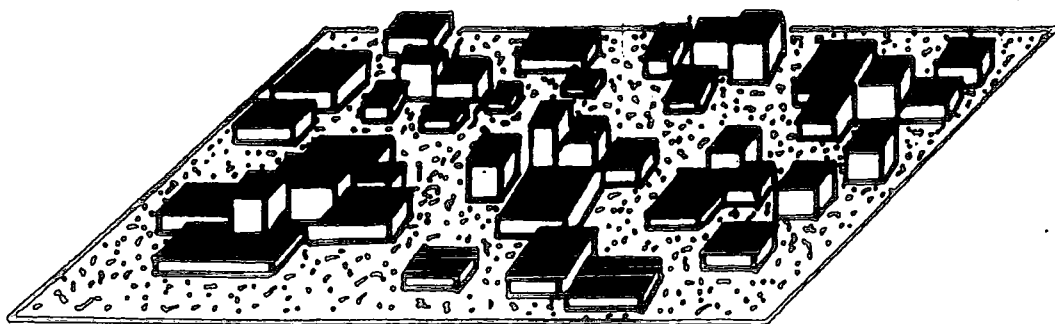
Ellison *et al* [25] found a small amount of CrO_3 aggregates or polychromates on activation at 700°C, and higher temperatures lead to greater aggregation. EP20 and EP30X were found to have a greater proportion of aggregated species than laboratory preparations.

It should be noted that the Cr $2p_{3/2}$ peaks have considerably larger FWHM values that those reported previously, by upto 4eV in some cases for the unactivated catalysts. It is also seen that the peaks are broadened further on activation for EP30X. There are a number of possible causes of this peak broadening:
(i)   spectrometer sensitivity
(ii)   photoreduction
(iii) sample charging
(iv)   the presence of chromium in more than one oxidation state/chromium species in different chemical environments

(i)   The spectrometer slit width was increased in order to increase the sensitivity as the chromium 2p signal was found to be quite weak. However, increasing the slit width also decreases the resolution and this can affect the measured peak half width [49]. This is supported by the fact that other peaks (Si 2p, O 1s, Ti 2p) are also broadened somewhat.

(ii) The effects of photoreduction are discussed above. This is not thought to be a problem since the Cr 2p region was always scanned first and obtained within 20 minutes, within the time limit reported by Merryfield *et al* [21] who found no visible evidence for photoreduction. The effects of photoreduction can be tested by observing the time dependence of the chromium 2p region: peaks will be shifted if photoreduction occurs.

(iii) The use of Si 2p as an internal reference compensates for the effect of charging on the chromium samples as long as this charging is uniform. However, the most prominent problem of charging is differential charging, which occurs when different areas or species of a sample charge by different amounts. This results in different kinetic energies of the electrons from atoms of the same element in different particles. Differential charging of a few tenths of an electronvolt causes peak broadening, at a few electronvolts multiple peaks result [10]. The peak broadening caused by differential charging leads to problems in evaluating overlapping signals when curve fitting. A number of studies have observed the effects of differential charging: rather broad silicon, oxygen and tungsten (W $4f_{7/2}$ FWHM 4.8eV, referenced to Si 2p) XPS peaks were found in a study of WO_3/SiO_2 catalysts [53] and the peak width attributed to differential charging of silica particles. Zingg *et al* [79] observed that sample charging led to

broadening of Mo 3d peaks and a shift to higher binding energy. The broadening was observed to increase with decreasing molybdenum loading. Note that charging results in shifting and broadening of all lines; differential charging affects only some of the lines.

Using monochromatic X-rays for excitation tends to exaggerate charging because the Bremstrahlung radiation is prevented from impinging on the sample surface. Without monochromatic X-rays charging is much less severe and spectral interpretation much easier [10].

Kerkhof *et al* [53] found a solution to the problem for their catalysts in making sure the samples were well powdered and slightly wetted with demineralsied water to form a paste. This was dried at 120°C and a coherent structure obtained.

That sample charging is occurring can be demonstrated by applying a slow-electron flood gun: if the XPS peaks move to lower apparent binding energy charging effects are present.

(iv) Cr^{III} species suffer more from peak broadening since they are affected by multiplet splitting due to unpaired electrons (Cr^{III} $3d^3$ *cf* Cr^{VI} $3d^0$). The shape and separation of the 2p doublet are modified by the unpaired orbital spin density. Experimentally each of the spin-orbit levels will be broadened by upto 2eV for complexes with unpaired d electrons.

The presence of more than one chromium oxidation state would lead to peak broadening, since Cr^{III} and Cr^{IV} signals would overlap to some extent with those of Cr^{VI} [41]. Even in freshly prepared Cr/SiO_2 catalysts not all chromium is present as Cr^{VI} ions: in particular, at low chromium contents partial reduction is evident. During the activation process some degradation of Cr^{VI} at the surface to lower valence states has been reported [47]. At an activation temperature of 1023K the average oxidation state of chromium was calculated to be 5.1 in 1% Cr^{VI}/SiO_2 catalysts, derived from chromium III acetate, using temperature programmed oxidation/reduction. This lowered valence was attributed to formation of Cr^{III} as Cr^{VI} decomposes. Ellison *et al* [25] found that activated samples of EP20 and EP30 always contain traces of Cr^{III}: Cr^{VI} and Cr^{III} were found to coexist on the surface.

Thus, samples are expected to contain a small amount of Cr^{III}, even after activation, and this can explain in part the broadening of the Cr 2p peaks. However, it is insufficient to explain in entirety the broadening observed here, since it is not only chromium peaks that are affected. It is thought that the spectrometer sensitivity is a major contributing factor to peak broadening, rather than any

charging effects. The fact that monochromatic X-ray radiation was not used results in charging being much less of a problem, although the absence of differential charging was not checked by use of a flood gun. Also, the Si 2p reference peaks were found to be very similar for all the catalyst samples in both FWHM and in being fitted by only one peak - additional peaks were not observed.

3 Titania promoted catalysts

(i) Silica/titania cogels

The binding energy values for the TiO_2/SiO_2 cogel (EP55) and the cogel impregnated with Cr^{III} (EP355) are given in Table 2.10. The unactivated cogel has an average Ti $2p_{3/2}$ binding energy of 459.0eV, which rises to 459.3eV on activation (Table 2.16). The activated value is comparable to those reported by Ingo et al [44] for titania in a cogel. The values obtained suggest that there is no insertion of titanium ions into the silica lattice to form a silicalite structure, and the Ti^{4+} ions are in their preferred octahedral coordination, similar to the bulk [58].

The Ti/Si intensity ratio is unchanged from 0.08 on activation (Tables 2.11, 2.17), indicating no migration of titanium to the surface with increasing temperature, as has been reported [27]. The very low ratio indicates much of the titania is in the bulk, as expected.

For EP355 the Ti $2p_{3/2}$ binding energy increases from 459.2 to 459.4eV on activation (Tables 2.10, 2.17), comparable with EP55, whilst the Cr $2p_{3/2}$ binding energy rises from 577.6 to 579.2eV, comparable with EP30X. 577.6eV is taken as indicative of Cr^{III}, 579.2eV of Cr^{VI}. The peak widths decreased slightly (3.9 -> 3.7eV on average) on activation. Narrower peaks are expected for Cr^{VI} compared to Cr^{III}, since the $3d^0$ systems do not lead to multiplet splitting due to electrostatic and exchange reactions from unpaired 3d electrons.

Many experiments suggest that the promotional effect of these catalysts is due to formation of Ti-O-Cr bonds and a decrease in Cr^{VI} binding energy has been used to support this hypothesis. It has already been shown that no decrease in the Cr^{VI} binding energy is observed and the Ti/Si intensity ratios of 0.12, for both unactivated and activated catalysts, indicate that most of the titania is in the bulk (Tables 2.11, 2.17). Therefore the probability of forming Ti-O-Cr bonds is low. Indeed the behaviour of the titania and chromium species parallel that of EP55 and EP30X respectively. However, the Cr^{III} dispersion is much lower in EP355 (0.27) compared to EP30X (0.43) for the unactivated catalysts. The activated value of 0.25 is comparable with

activated EP30X (0.29). Note that the chromium loading is the same in both catalysts. Addition of titania during gellation reduces the pore volume and the surface area of the support, which leads to the lower initial dispersion of chromium III acetate and limits the mobility of the chromium VI oxide formed on activation.

(ii) Silica impregnated with titania and Cr[III]

XPS data for the two catalysts are contained in Tables 2.12, 2.13, 2.16 and 2.17. Both CS2066 and EP284 are first impregnated with titania (2.50 and 4.35% Ti respectively), and then with chromium III acetate (1% Cr).

The titania is now applied as a surface layer and this can be seen in the higher Ti/Si intensity ratios as compared with the cogel catalysts (Tables 2.13, 2.17). For CS2066 there is little difference between unactivated and activated values (0.25 vs 0.24), suggesting sintering or agglomeration of titania is not occurring. The binding energy increases from 459.1 to 459.6eV, the highest titanium binding energy observed for any sample in this study. High Ti 2p binding energies have been associated with either very small titania clusters [96] or formation of surface titanium compounds [27]. Stakheev et al [60] associated the high binding energy with insertion of Ti^{4+} into tetrahedral sites of the silica framework as in $SiO_2 \cdot TiO_2$ glasses [130] and titanium silicalites [59,131].

A big difference is seen between the unactivated and activated Ti/Si ratios, 0.61 vs 0.49, in EP284. In the unactivated samples titania is very well dispersed and though this falls on activation, the dispersion is still twice that of CS2066, which also correlates directly with the titanium loadings. The binding energy rises from 459.0 to 459.4eV on activation. In titanium silicalites this level of titanium loading is associated with distorted square pyramidal titanium sites being dominant [59].

In CS2066 the Cr $2p_{3/2}$ average binding energy is 577.9eV when unactivated, the same as that for unactivated EP30X, clearly indicating the presence of Cr[III]. In EP284 the corresponding value is 578.0eV. On activation values associated with Cr[VI] are obtained, 579.6eV for CS2066 and 579.2eV for EP284. The dispersion on CS2066 is lower than found for EP30X when unactivated (0.28 vs 0.43) but it is little changed on activation (0.26). Compare this to EP284 where there is higher initial dispersion of the chromium III acetate precursor (0.37) which subsequently falls on activation (0.32).

It would be expected that incorporating titania as a surface layer would lead to greater Ti-O-Cr bond formation

Pullukat and Shida proposed a chromium III titanate structure for the unactivated catalyst, with a titanium chromate structure being formed on activation, containing Cr^{VI} [43]. However, this would lead to a decrease in Cr^{VI} binding energy, typically values of 578.0eV were obtained and clearly this study finds no such decrease. Since Pullukat and Shida were using titanium esters and Cr^{VI} salts as precursors, a different method of attachment must occur in the samples used in this study. It has been observed that the promotional effect of titania occurs only when added to silica prior to the chromium salt and that this effect decreases with temperature, which was interpreted as migration of chromium away from titania [32]. This is a plausible explanation for the behaviour of EP284 on activation. It appears that increased temperature causes the titania to agglomerate and form clusters and also causes migration of the chromium and similar agglomeration. Addition of titania is known to lower the surface area and pore volume, which in turn increases chromium agglomeration. It has been reported that at high polymerization temperatures titanium loadings above 4% reduce the activity of low temperature and plausible explanations, besides the formation of Ti-O-Cr bonds, have been offered, i.e. a change in surface geometry or the generation of Lewis acid sites by titania, which may affect the physical and/or chemical properties of the active chromium [30]. The increase in chromium agglomeration is demonstrated in EP284, but CS2066 behaves in a similar manner to EP355: the chromium and titanium dispersions are almost unchanged by activation. Thus the agglomeration and migration of chromium appears to be controlled by the titania loading and thus by changes in the surface geometry.

4 Alumina-containing catalysts

XPS data for EP200 and EP210 is shown in Tables 2.14, 2.15, 2.16 and 2.17. Values for bulk alumina and Al_2O_3/SiO_2 are shown in Table 2.19. EP200 contains only 0.52% Cr compared to 1% for all other catalysts, and 0.87% Al compared to 1% for EP210. For EP210 the aluminium is added as an alkyl which is converted to Al_2O_3 on activation, and chromium III acetylacetonate is the chromium precursor.

Average Al 2p binding energies of 75.1eV are obtained for both unactivated catalysts, which is in agreement with the literature values, Table 2.16, [34]. On activation the binding energy increases to 75.5eV for EP200 and 75.3eV for EP210. The binding energy is higher than for bulk alumina suggesting formation of Al-O-Si bonds similar to those in aluminosilicates [54,103,104]. Rebenstorf and Andersson [34] showed that bulk alumina was only observed when high loadings of alumina were used; at low loadings there is high dispersion and aluminium is in the surface layer. There is

surface area observed by Rebenstorf and Andersson [34] on addition of small amounts of alumina to silica. On activation it seems to lead to increased chromium mobility and ease of agglomeration, as with Ellison's model above.

In EP210 there is a higher chromium loading and the acetylacetonate has dispersed to a similar extent as the acetate in EP30X. The effect of aluminium on the chromium agglomeration is less marked due to the higher loading but clustering is again observed on activation. A model similar to that proposed for the impregnated titania-containing catalysts can be envisaged.

CONCLUSIONS

(i) For all catalysts it is clear from the Cr 2p binding energies that there is conversion of Cr^{III} to Cr^{VI} on activation.
(ii) Increased promoter metal binding energies indicate an interaction with the silica support: for cogels this obviously occurs during gellation, for alumina via formation of aluminosilicate at the surface and with impregnated titanium there is insertion of Ti^{4+} ions into the silica network.
(iii) Dispersion is dependent on chromium and promoter metal loadings. In general, chromium dispersion falls on activation, but most dramatically for EP200, which contains 0.5% Cr. Thus addition of a promoter species encourages the clustering of Cr^{VI} species. Promoter dispersions themselves are unaltered on activation except for EP284, which contains 4.35% Ti, a level at which the formation of small titania clusters occurs. The promoter appears to exert a structural effect in the activation stages.

Further work needs to be undertaken in order to understand more fully the promoter's role:
(i) the effects of varying the loadings of both chromium and promoter;
(ii) BET studies in order to study changes in surface area and pore volume, which affect the chromium mobility and hence its ability to agglomerate;
(iii) Raman studies to infer structural changes and the possibility of the formation of very small crystallites, together with SEM to determine the nature of the surface species;
(iv) it would be very informative to study the changes in polymerization activity of these catalysts and to link this with the surface characterization. Labelled probe molecules could hopefully allow the identification of the interaction sites;
(v) because of the charging effects in the XPS spectra it would be useful to look at the $\propto$ Auger parameter, as this is

insensitive to charging, and
(vi) the promotional effect has been suggested to be due to
the creation of more easily reducible chromium - TPR studies
would help to test this theory.

Figure 2.19   _The Si 2p XPS spectrum   of   catalyst   EP30X_
(unactivated)

Figure   2.20   _The Cr 2p XPS spectrum of   catalyst   EP30X_
(unactivated)

Figure 2.21 The Si 2p XPS spectrum of catalyst EP30X (activated)

Figure 2.22 The Cr 2p XPS spectrum of catalyst EP30X (activated)

Figure 2.23 The Si 2p XPS spectrum of catalyst CS2066 (unactivated)
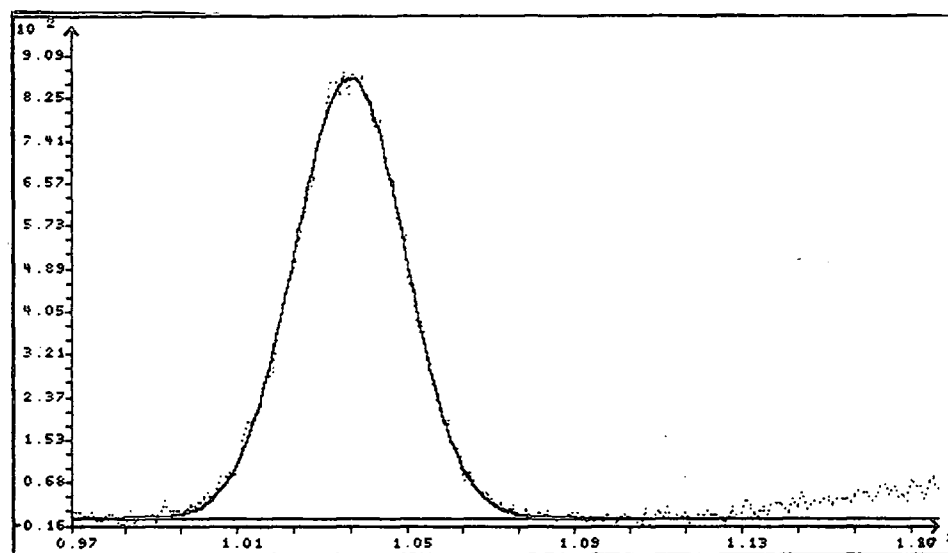
Figure 2.24 The Ti 2p XPS spectrum of catalyst CS2066 (unactivated)
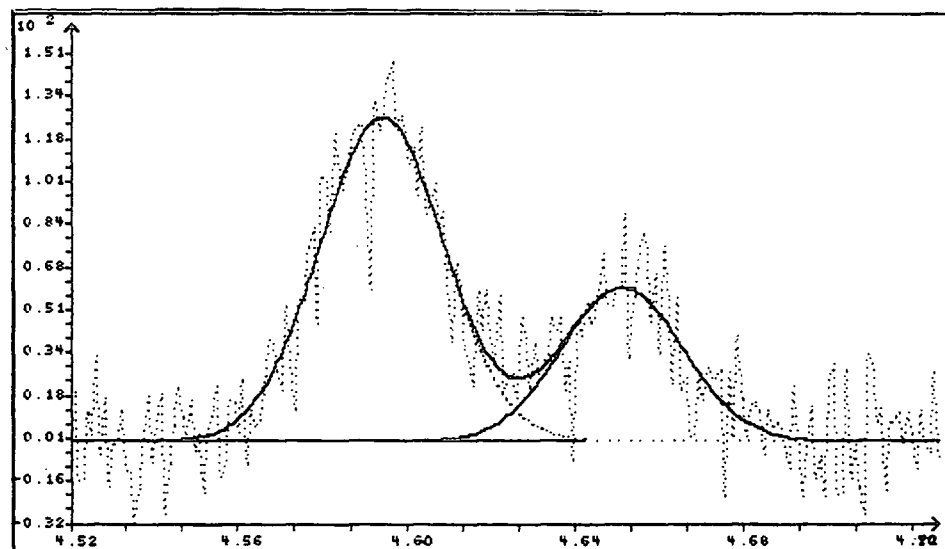
Figure 2.25 The Cr 2p XPS spectrum of catalyst CS2066 (unactivated)
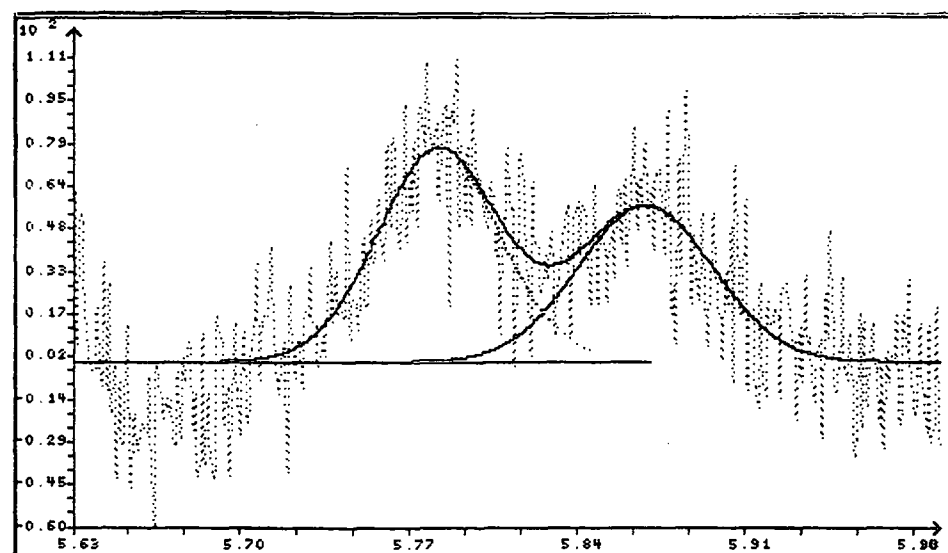
Figure 2.26 The Si 2p XPS spectrum of catalyst CS2066
(activated)
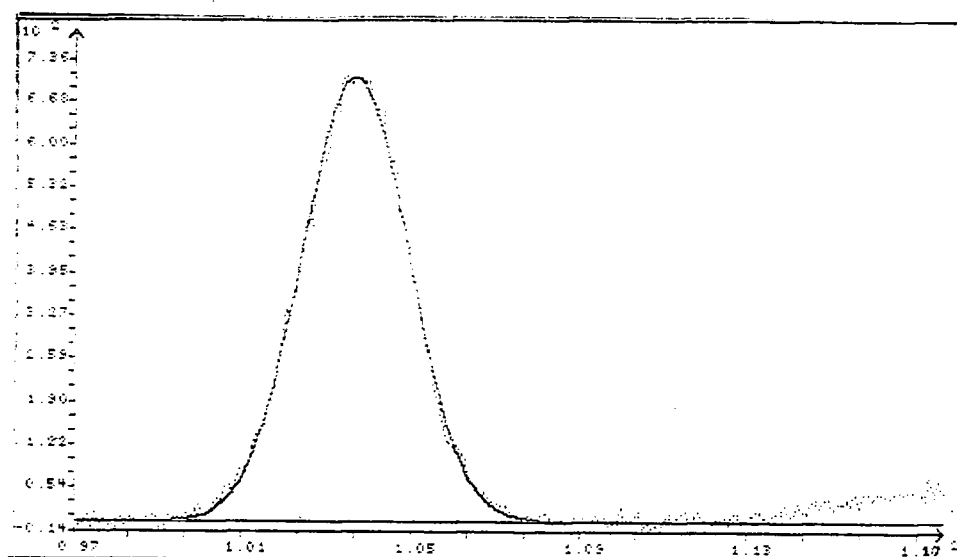
Figure 2.27 The Ti 2p XPS spectrum of catalyst CS2066
(activated)

Figure 2.28 The Cr 2p XPS spectrum of catalyst CS2066
(activated)
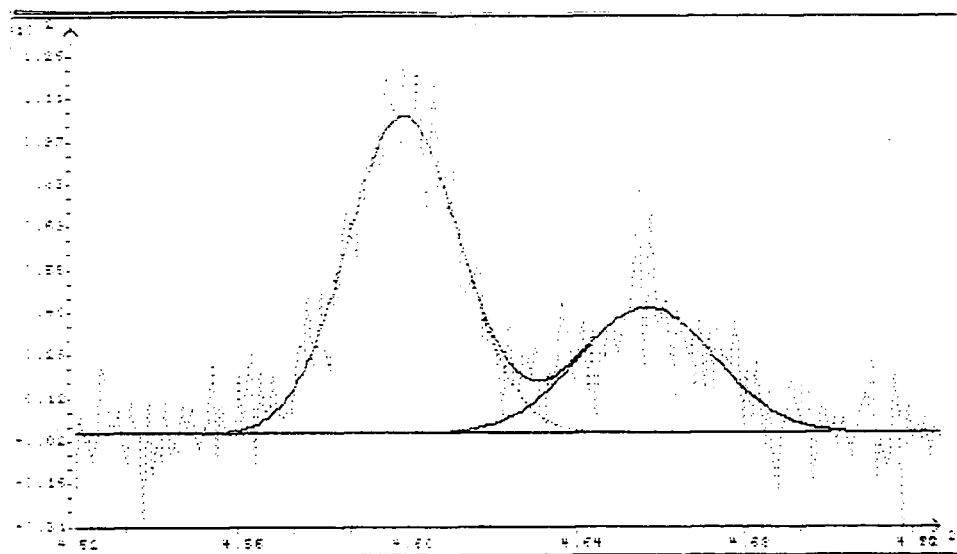
Figure 2.29 The Si 2p XPS spectrum of catalyst EP355 (unactivated)
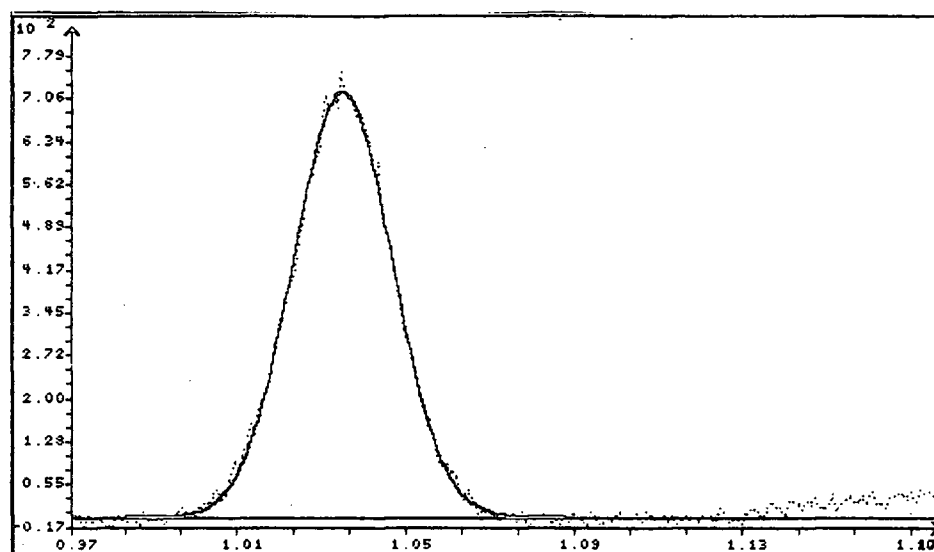
Figure 2.30 The Ti 2p XPS spectrum of catalyst EP355 (unactivated)
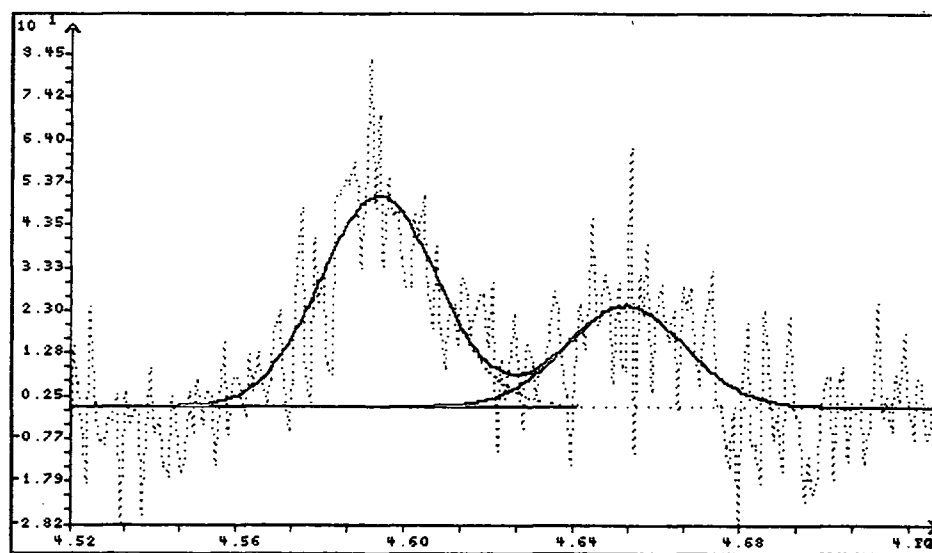
Figure 2.31 The Cr 2p XPS spectrum of catalyst EP355 (unactivated)
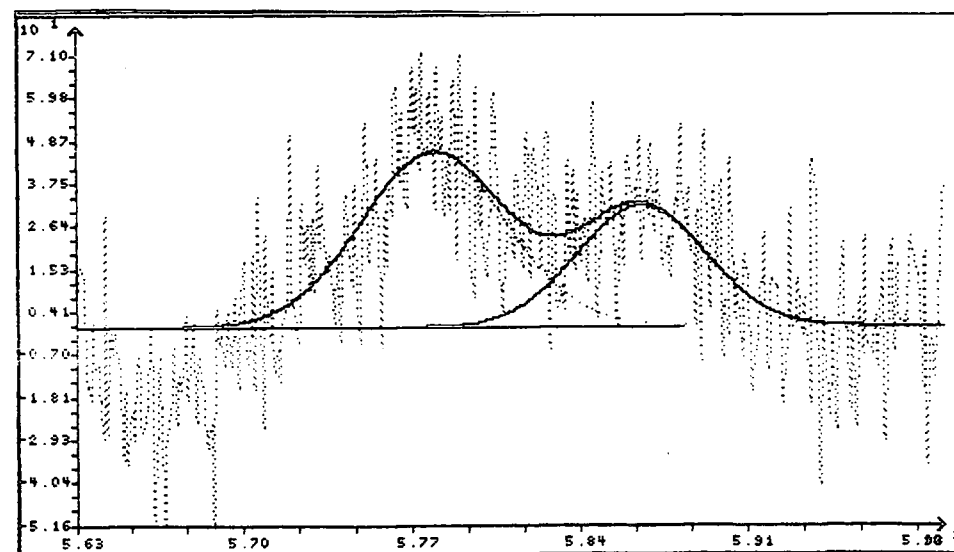
Figure 2.32   The   Si 2p XPS spectrum of   catalyst   EP355
(activated)
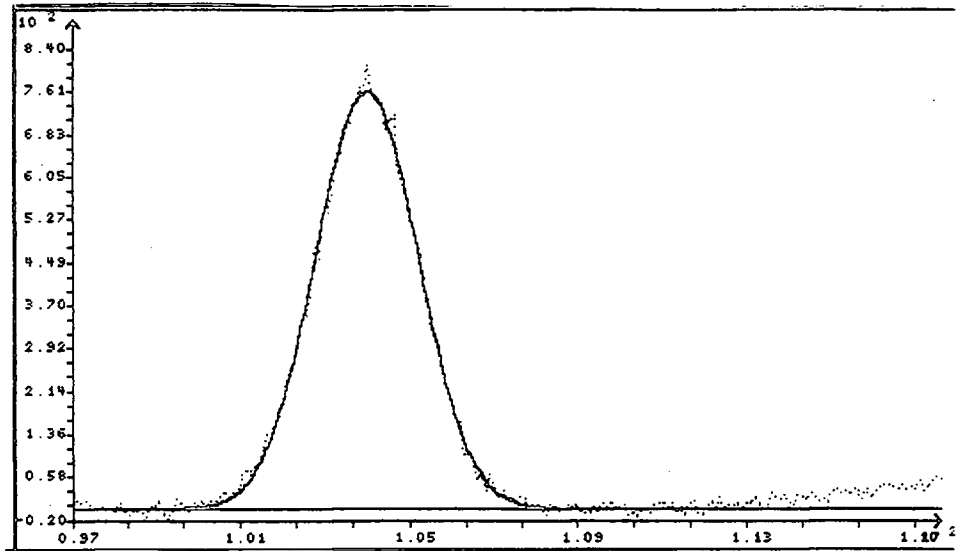
Figure   2.33   The   Ti 2p XPS spectrum of   catalyst   EP355
(activated)
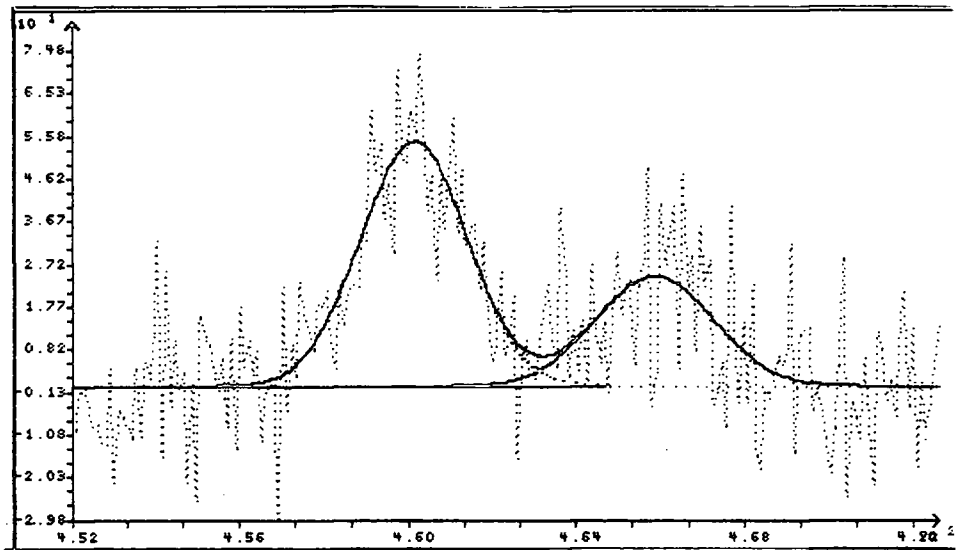
Figure   2.34   The   Cr 2p XPS spectrum of   catalyst   EP355
(activated)

Figure 2.35   The Si 2p XPS spectrum of catalyst EP200
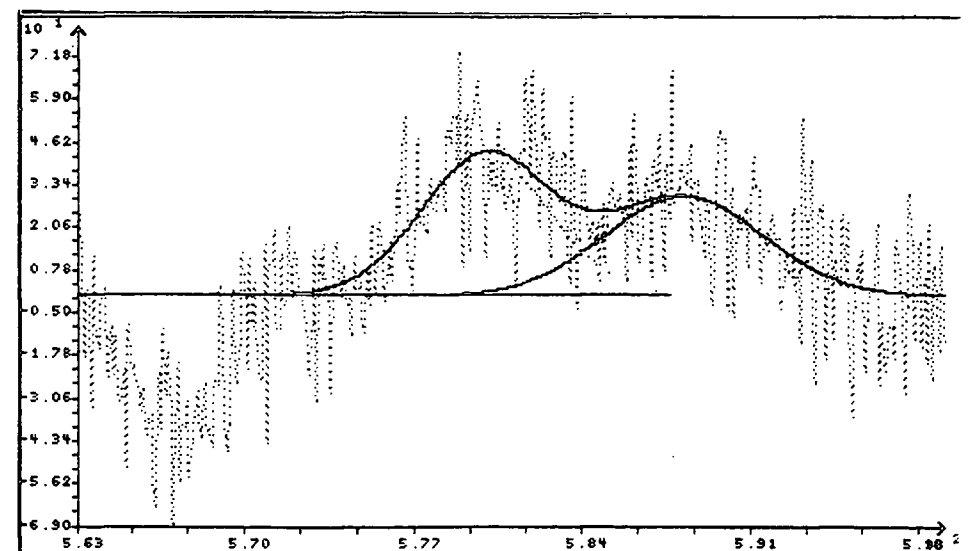
Figure 2.35   The Si 2p XPS spectrum of catalyst EP200
(unactivated)
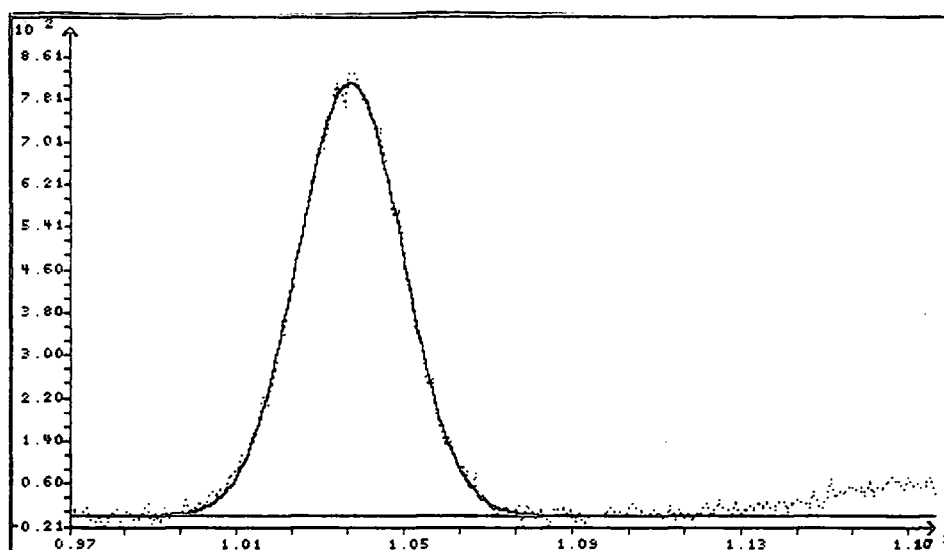
Figure 2.36   The Al 2p XPS spectrum of catalyst EP200
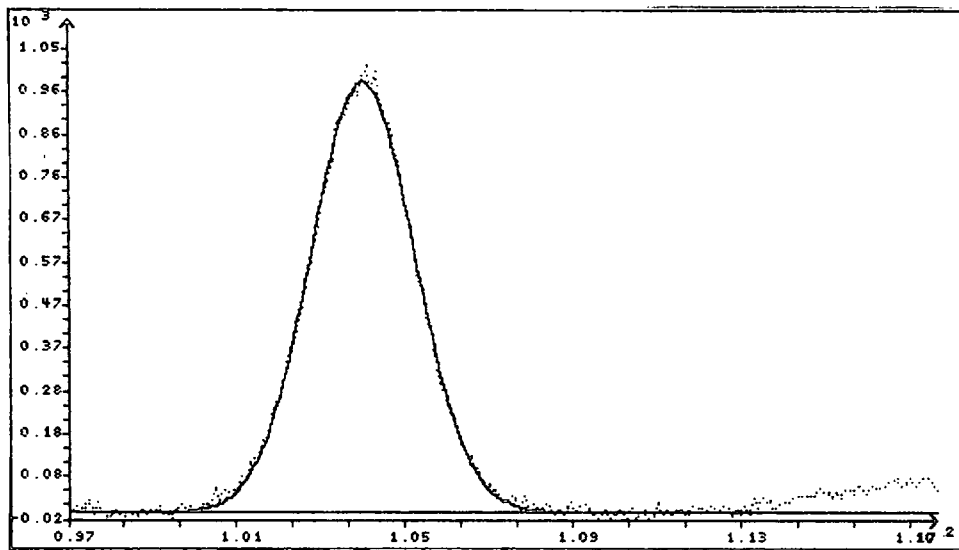(unactivated)
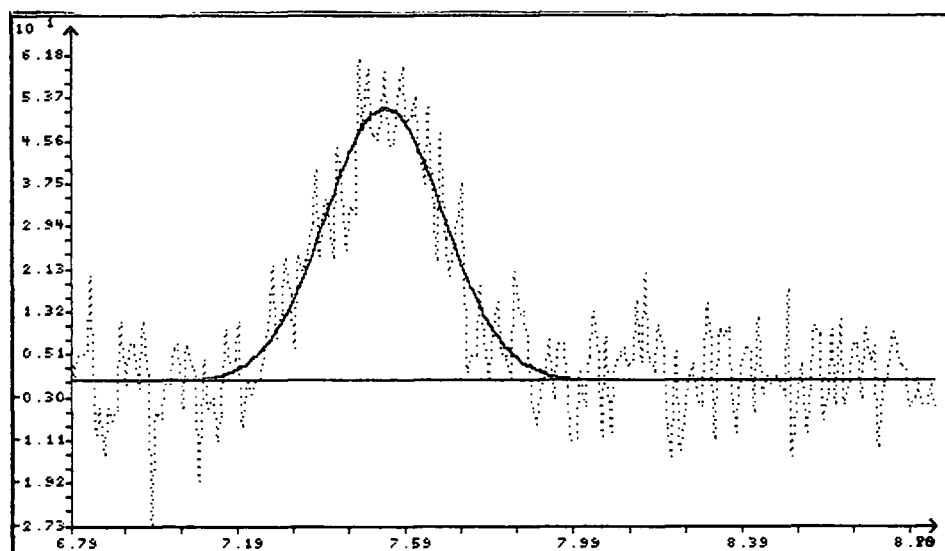
Figure 2.37   The Cr 2p XPS spectrum of catalyst EP200
(unactivated)
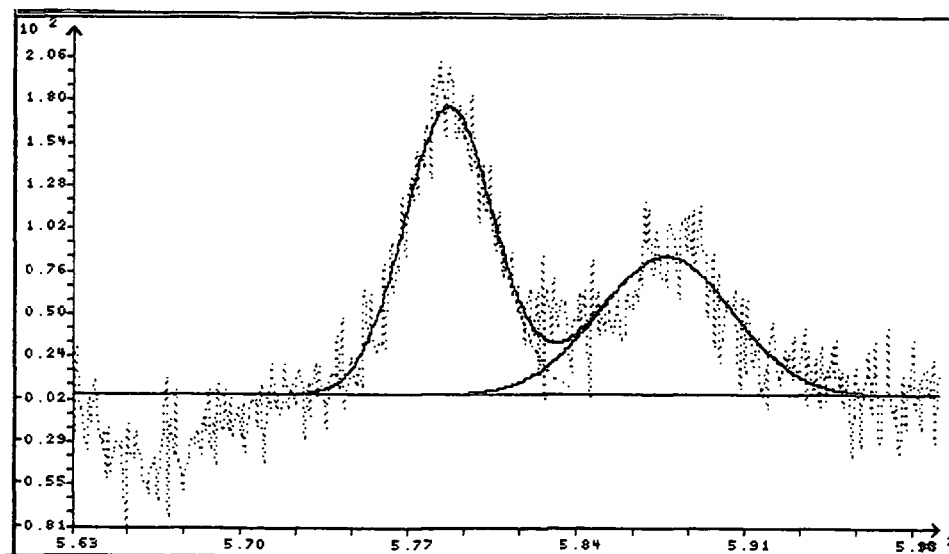
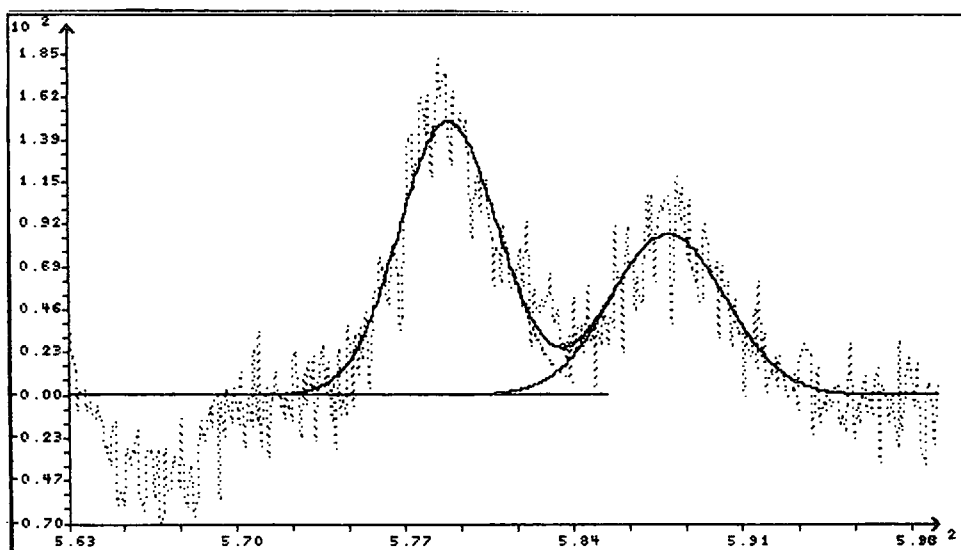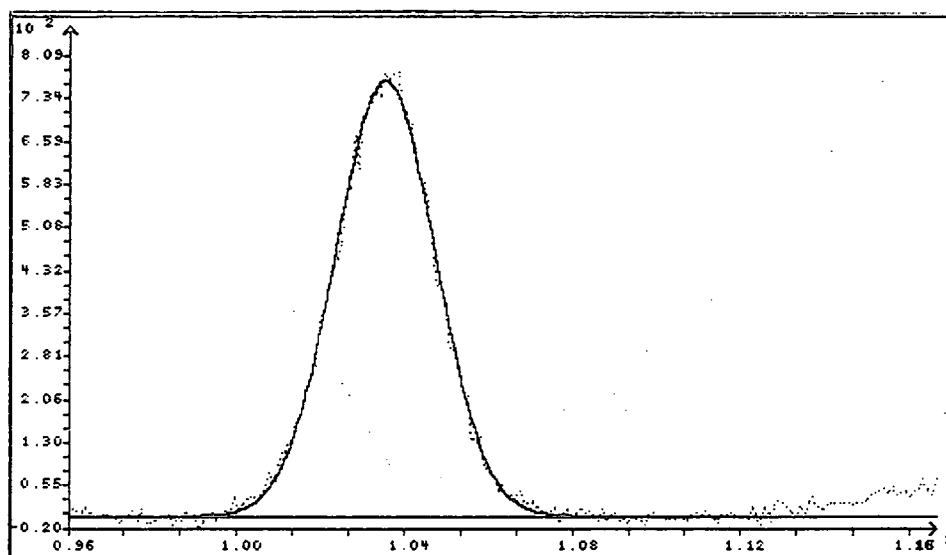_Figure 2.38_   The Si 2p XPS spectrum of catalyst EP200
(activated)
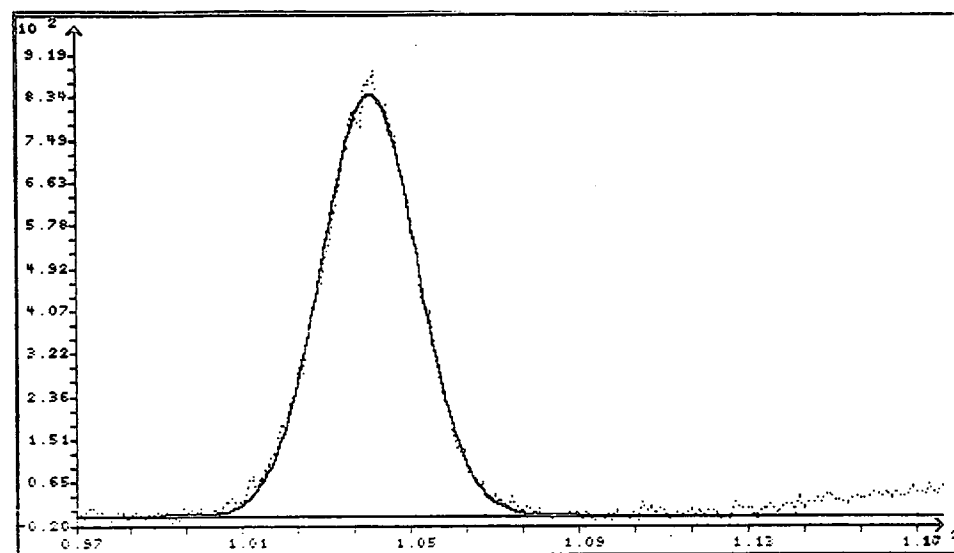
Figure 2.39   The Al 2p XPS spectrum of catalyst EP200
(activated)

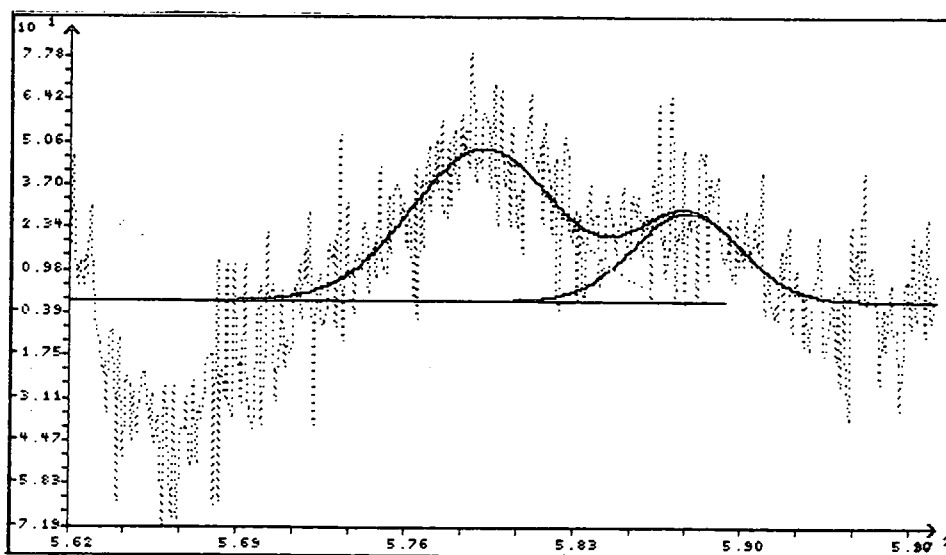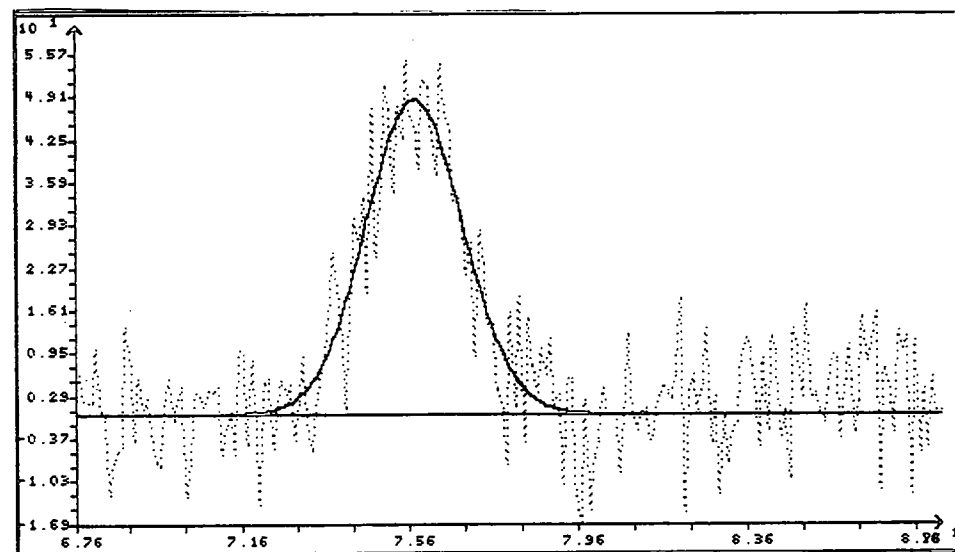_Figure 2.40_   The Cr 2p XPS spectrum of catalyst EP200
(activated)
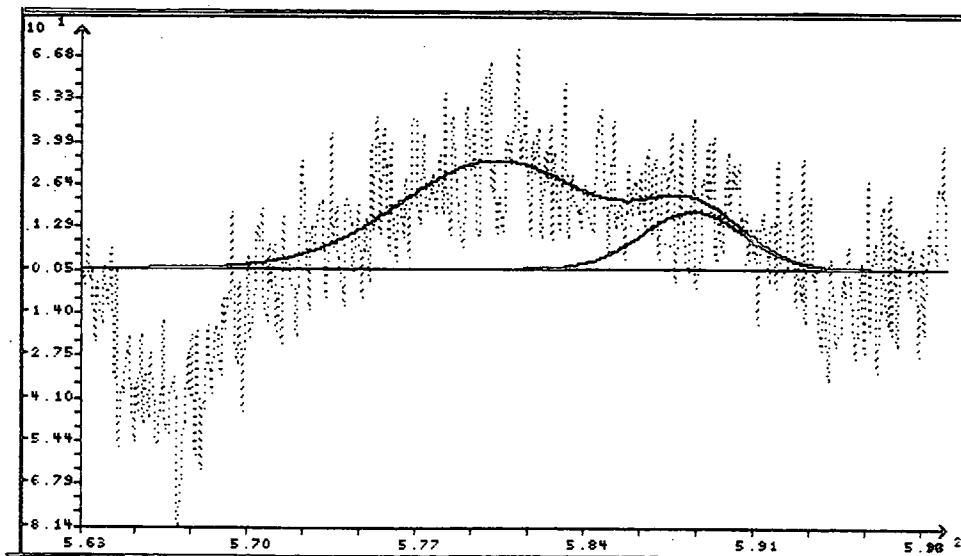
Table 2.8 Cr $2p_{3/2}$ binding energies and peak widths for silica-supported CrO_3 and Cr^{3+} (EP20 and EP30X)

Catalyst	Composition	Expt. No.	Cr $2p_{3/2}$ B.E. (eV)	Cr FWHM (eV)
EP20	CrO_3/SiO_2 Cr 0.98%	069	579.2	5.64
		103	579.3	7.01
		104	579.2	6.74
		122	579.2	6.19
EP30X	Cr^{3+}/SiO_2 Cr 1.00%	072	578.0	5.58
		073	578.0	5.12
		107	577.8	5.44
		108	577.8	5.00
Activated		062	579.5	7.29
		074	579.2	6.60
		132	579.5	10.04
		138	578.8	8.27

Table 2.9 Cr/Si XPS intensity ratios for silica-supported CrO_3 and Cr^{3+} (EP20 and EP30X)

Catalyst	Composition	Expt. No.	Cr/Si
EP20	CrO_3/SiO_2 Cr 0.98%	069	0.21
		103	0.22
		104	0.28
		122	0.27
EP30X	Cr^{3+}/SiO_2 Cr 1.00%	072	0.42
		073	0.38
		107	0.47
		108	0.44
Activated		062	0.30
		074	0.25
		132	0.32
		138	0.23

Table 2.10 Cr and Ti $2p_{3/2}$ binding energies for SiO_2/TiO_2 cogel and the cogel impregnated with Cr^{3+} (EP55 and EP355)

Catalyst	Composition	Expt. No.	Cr $2p_{3/2}$ B.E.(eV)	Cr FWHM (eV)	Ti $2p_{3/2}$ B.E.(eV)
EP55	SiO_2/TiO_2 cogel Ti 2.50%	092			459.1
		093			459.1
		121			459.0
		129			459.0
Activated		098			459.4
		099			459.2
		136			459.2
		137			459.5
EP355	SiO_2/TiO_2 cogel,Cr^{3+} Ti 2.53% Cr 1.05%	054	577.6	9.73	459.3
		090	577.6	8.23	459.0
		091	577.8	8.55	459.2
		117	577.4	9.40	459.2
Activated		094	579.0	7.32	459.5
		126	579.6	9.64	459.4
		140	579.1	9.01	459.4
		141	579.4	11.96	459.4

Table 2.11 Cr/Si and Ti/Si XPS intensity ratios for SiO_2/TiO_2 cogel and cogel impregnated with Cr^{3+} (EP55 and EP355)

Catalyst	Composition	Expt. No.	Cr/Si	Ti/Si
EP55	SiO_2/TiO_2 cogel Ti 2.50%	092		0.08
		093		0.09
		121		0.07
		129		0.07
Activated		098		0.07
		099		0.07
		136		0.09
		137		0.07
EP355	SiO_2/TiO_2 cogel, Cr^{3+} Ti 2.53% Cr 1.05%	054	0.24	0.12
		090	0.26	0.12
		091	0.27	0.13
		117	0.30	0.12
Activated		094	0.23	0.11
		126	0.22	0.11
		140	0.28	0.13
		141	0.27	0.11

Table 2.12   Cr and Ti $2p_{3/2}$ binding energies for $SiO_2/TiO_2/Cr^{3+}$ catalysts prepared by impregnation (EP284 and CS2066)

Catalyst	Composition	Expt. No.	Cr $2p_{3/2}$ B.E.(eV)	Cr FWHM (eV)	Ti $2p_{3/2}$ B.E.(eV)
CS2066	$SiO_2/TiO_2/$	080	577.8	6.12	459.1
	Cr^{3+}	109	578.0	7.45	459.0
	Ti 2.50%	110	577.9	7.39	459.1
	Cr 1.00%	128	577.7	6.96	459.2
Activated		064	578.7	5.68	459.6
		065	579.1	7.02	459.5
		066	579.9	6.87	459.6
		067	579.8	7.32	459.5
EP284	$SiO_2/TiO_2/$	032	578.0	5.09	459.0
	Cr^{3+}	077	578.1	5.94	459.0
	Ti 4.35%	113	578.0	5.88	459.0
	Cr 0.96%	114	577.9	5.88	459.1
Activated		070	579.2	6.58	459.4
		071	579.5	7.10	459.3
		082	579.0	6.16	459.4
		083	578.6	5.72	459.3

Table 2.13   Cr/Si and Ti/Si XPS intensity ratios for $SiO_2/TiO_2/Cr^{3+}$ catalysts prepared by impregnation (EP284 and CS2066)

Catalyst	Composition	Expt. No.	Cr/Si	Ti/Si
CS2066	$SiO_2/TiO_2/$	080	0.30	0.24
	Cr^{3+}	081	0.23	0.25
	Ti 2.50%	109	0.29	0.25
	Cr 1.00%	110	0.30	0.25
Activated		064	0.30	0.24
		065	0.29	0.22
		066	0.27	0.23
		067	0.23	0.26
EP284	$SiO_2/TiO_2/$	032	0.36	0.62
	Cr^{3+}	077	0.34	0.64
	Ti 4.35%	113	0.36	0.57
	Cr 0.96%	114	0.40	0.62
Activated		070	0.28	0.49
		071	0.30	0.48
		082	0.33	0.48
		083	0.36	0.49

Table 2.14   Cr and Ti $2p_{3/2}$ binding energies for $SiO_2/Al^{3+}/Cr^{3+}$ catalysts (EP200 and EP210)

Catalyst	Composition	Expt. No.	Cr $2p_{3/2}$ B.E.(eV)	Cr FWHM (eV)	Al 2p B.E.(eV)
EP200	$SiO_2/Al^{3+}/$	084	578.2	5.54	75.0
	Cr^{3+}	085	578.1	5.59	75.1
	Al 0.87%	125	578.1	5.86	75.1
	Cr 0.52%	135	578.1	5.10	75.2
Activated		078	579.8	8.64	75.5
		079	578.3	6.96	75.4
		088	579.5	11.06	75.5
		089	579.5	10.40	75.5
EP210	$SiO_2/Al^{3+}/$	086	577.9	5.82	75.3
	Cr^{3+}	087	578.0	5.45	75.0
	Al 1.00%	096	577.9	5.83	75.1
	Cr 1.00%	100	578.0	5.88	75.0
Activated		105	578.9	7.72	75.1
		106	579.5	7.93	75.4
		111	579.5	7.45	75.2
		112	579.4	9.44	75.3

Table 2.15   Cr/Si and Al/Si XPS intensity ratios for $SiO_2/Al^{3+}/Cr^{3+}$ catalysts (EP200 and EP210)

Catalyst	Composition	Expt. No.	Cr/Si	Al/Si
EP200	$SiO_2/Al^{3+}/$	084	0.58	0.07
	Cr^{3+}	085	0.59	0.07
	Al 0.87%	125	0.60	0.07
	Cr 0.52%	135	0.56	0.07
Activated		078	0.15	0.06
		079	0.13	0.08
		088	0.19	0.06
		089	0.16	0.06
EP210	$SiO_2/Al^{3+}/$	086	0.43	0.04
	Cr^{3+}	087	0.39	0.04
	Al 1.00%	096	0.44	0.03
	Cr 1.00%	100	0.39	0.04
Activated		105	0.31	0.03
		106	0.27	0.03
		111	0.27	0.03
		112	0.28	0.04

Table 2.16   Averaged binding energy values for Cr $2p_{3/2}$, Ti $2p_{3/2}$ and Al 2p

Catalyst	Composition		Cr (eV)	Ti or Al (eV)
EP20	SiO_2/CrO_3	U	579.20 ± 0.03	
EP30X	SiO_2/Cr^{3+}	U	577.89 ± 0.05	
		A	579.37 ± 0.11	
CS2066	$SiO_2/TiO_2/$ Cr^{3+}	U	577.87 ± 0.06	459.09 ± 0.03
		A	579.58 ± 0.25	459.55 ± 0.03
EP284	$SiO_2/TiO_2/$ Cr^{3+}	U	578.01 ± 0.04	459.02 ± 0.02
		A	579.21 ± 0.11	459.36 ± 0.02
EP200	$SiO_2/Al^{3+}/$ Cr^{3+}	U	578.14 ± 0.01	75.08 ± 0.04
		A	579.59 ± 0.12	75.50 ± 0.01
EP210	$SiO_2/Al^{3+}/$ Cr^{3+}	U	577.95 ± 0.02	75.07 ± 0.07
		A	579.46 ± 0.04	75.32 ± 0.05
EP55	SiO_2/TiO_2 cogel	U		459.04 ± 0.03
		A		459.31 ± 0.07
EP355	SiO_2/TiO_2 cogel/Cr^{3+}	U	577.61 ± 0.09	459.17 ± 0.06
		A	579.22 ± 0.22	459.43 ± 0.02

U = unactivated
A = activated

Table 2.17   The averaged Cr/Si,   Ti/Si and Al/Si XPS
                         intensity ratios

Catalyst	Composition		Cr/Si	Ti/Si or Al/Si
EP20	SiO_2/CrO_3	U	0.25 ± 0.02	
EP30X	SiO_2/Cr^{3+}	U	0.43 ± 0.02	
		A	0.29 ± 0.02	
CS2066	$SiO_2/TiO_2/$ Cr^{3+}	U	0.28 ± 0.02	0.25 ± 0.01
		A	0.26 ± 0.02	0.24 ± 0.01
EP284	$SiO_2/TiO_2/$ Cr^{3+}	U	0.37 ± 0.01	0.61 ± 0.02
		A	0.32 ± 0.02	0.49 ± 0.01
EP200	$SiO_2/Al^{3+}/$ Cr^{3+}	U	0.58 ± 0.01	0.07 ± 0.01
		A	0.17 ± 0.01	0.06 ± 0.01
EP210	$SiO_2/Al^{3+}/$ Cr^{3+}	U	0.41 ± 0.01	0.04 ± 0.01
		A	0.27 ± 0.01	0.03 ± 0.01
EP55	SiO_2/TiO_2 cogel	U		0.08 ± 0.01
		A		0.08 ± 0.01
EP355	SiO_2/TiO_2 cogel/ Cr^{3+}	U	0.27 ± 0.01	0.12 ± 0.01
		A	0.25 ± 0.01	0.12 ± 0.01

U = unactivated
A = activated

Table 2.18 Binding energy values for bulk and supported chromium oxides

Bulk chromium compounds

Compound	Cr $2p_{3/2}$ BE (eV)	FWHM (eV)	Spin-orbit coupling (eV)	Spectral ref.	Ref.
CrO_3	579.1	2.9	9.1	Si 2p	21
	580.3	2.8	9.1	C 1s	120
	577.1	2.3	8.7	Au $4f_{7/2}$	20
	578.3	1.4	9.2	C 1s	41
	579.9	1.6	9.0	C 1s	57
Na_2CrO_4	579.8	2.0	9.3	Au $4f_{7/2}$	19
K_2CrO_4	579.6	1.8	9.3	Au $4f_{7/2}$	19
$Na_2Cr_2O_7$	579.4	2.0	9.1	Au $4f_{7/2}$	19
$K_2Cr_2O_7$	579.4	2.3	9.4	Au $4f_{7/2}$	19
Cr_2O_3	579.2	3.5	9.8	Si 2p	21
	576.6	3.6	9.8	C 1s	120
	576.8	3.0	9.6	C 1s	57
	576.8	3.0	9.7	Au $4f_{7/2}$	20
	576.3	2.4	9.7	C 1s	41
$Cr(acac)_3$	577.7	3.3	9.7	Au $4f_{7/2}$	19

Supported chromium

Sample	Cr $2p_{3/2}$ BE(eV)	FWHM(eV)	Spectral Ref.	Ref
Cr^{VI}/SiO_2 (1.1;O_2;600°C)*	581.6	3.7	Si 2p	21
CrO_3/SiO_2 (2;air;700°C)	579.6		C 1s	43
CrO_3/SiO_2 (1;uncalcined)	580.4	3.7	Si 2p	42
(air;300°C)	579.9 577.5	3.7	Si 2p	42
(air;400°C)	579.9 577.4	4.3	Si 2p	42

(air;500°C)	577.1	3.1		Si 2p	42
(air;550°C)	577.1	3.1		Si 2p	42
(air;600°C)	577.1	2.9		Si 2p	42
Cr^{3+}/SiO_2 (1.1;wet N_2; 300°C)	577.6	4.9		Si 2p	21
$CrO_3/TiO_2/SiO_2$ (2,3.5;air;700°C)	578.0		(Ti $2p_{3/2}$ 460.0)	C 1s	43

* (wt% Cr, Ti; activation medium; temperature of activation)

Table 2.19   Binding energy values for bulk and supported
titania and alumina

Sample	Ti 2p$_{3/2}$ B.E. (eV)	FWHM (eV)	Ref.
TiO$_2$	458.7		60
	458.5		22
	459.0		24a
	459.3		44
Degussa P25	459.0	3.1	27
TiO$_2$	458.8	1.8	this work
SiO$_2$/TiO$_2$ (impregnated)			
0.2mmolTig^{-1}	459.7	1.3	27
0.4mmolTig^{-1}	459.7	3.0	27
1.0mmolTig^{-1}	459.1	3.0	27
2.0mmolTig^{-1}	459.0	2.8	27
SiO$_2$/TiO$_2$ (cogel)	459.2		44
Cogel;air;1000°C	459.3		44

Sample	Al 2p B.E. (eV)	FWHM (eV)	Ref.
Al$_2$O$_3$	76.6		34
	73.52		54
	74.1		8
a Al$_2$O$_3$ powder	73.65		54
Al$_2$O$_3$ sapphire	73.90		54
Sapphire (*in vacuo*;700°C)	74.12		54
SiO$_2$/Al$_2$O$_3$ (impregnated)			
0.2mmolAlg^{-1}	75.0		34
0.4mmolAlg^{-1}	75.1		34
1.0mmolAlg^{-1}	75.0	2.3	34
2.0mmolAlg^{-1}	75.0	2.5	34

Spectral reference is C 1s in all cases

REFERENCES

[1] H.H. Willard, L.L. Merritt, J.A. Dean and F.A. Settle, *Instrumental Methods of Analysis*, Wadsworth, California, 7th edn., 1988

[2] J.M. Hollas, *Modern Spectroscopy*, Wiley, Chichester, 2nd edn., 1992

[3] P.A. Cox, *The Electronic Structure and Chemistry of Solids*, Oxford University Press, Oxford, 1987

[4] A.K. Cheetham and P. Day, *Solid State Chemistry Techniques*, Oxford University Press, Oxford, 1988

[5] A.B. Christie, in *Methods of Surface Analysis*, ed. J.M. Walls, Cambridge University Press, Cambridge, 1989

[6] M.H. Kibel, in *Surface Analysis Methods in Materials Science*, eds. D.J. O'Connor, B.A. Sexton and R.St.C. Smart, Springer-Verlag, Berlin, 1992

[7] G.E. McGuire, in *Applied Electron Spectroscopy for Chemical Analysis*, eds. H. Windawi and F.F-L. Ho, Wiley, New York, 1982

[8] D.M. Hercules and J.C. Klein, in *Applied Electron Spectroscopy for Chemical Analysis*, eds. H. Windawi and F.F-L. Ho, Wiley, New York, 1982

[9] F.P.J.M. Kerkhof and J.A. Moulijn, *J. Phys. Chem.*, 83, 1612, 1979

[10] J.S. Brinen, *Acc. Chem. Res.*, 9, 86, 1976

[11] W.N. Delgass, T.R. Hughes and C.S. Fadley, *Catal. Rev.*, 4, 179, 1970

[12] J. Grimblot, L. Gengembre and A. D'Huysser, *J. Electron Spectrosc. Rel. Phenom.*, 52, 485, 1990

[13] M.A. Stranick, M. Houalla and D.M. Hercules, *J. Catal.*, 103, 151, 1987

[14] V. di Castro, C. Furlani, M. Gargano, N. Ravasio and M. Rossi, *J. Electron Spectrosc. Rel. Phenom.*, 52, 415, 1990

[15] L.H. Schapiro, *J. Electron Spectrosc. Rel. Phenom.*, 5, 369, 1974

[16] D. Briggs, *J. Electron Spectrosc. Rel. Phenom.*, 9, 487, 1976

[17] A.R. Gonzalez-Elipe, G. Munuera and J.P. Espinos, *Surf. Interface Anal.*, 16, 375, 1990

[18] W. Grunert, A. Yu. Stakheev, W. Morke, R. Feldhaus, K. Anders, E.S. Shpiro and K.M. Minachev, *J. Catal.*, 135, 269 (1992)

[19] G.C. Allen and P.M. Tucker, *Inorg. Chem. Acta*, 16, 41, 1976

[20] G.C. Allen, M.T. Curtis, A.J. Hooper and P.M. Tucker, *J. Chem. Soc. Dalton Trans.*, 1675, 1973

[21] R. Merryfield, M. McDaniel and G. Parks, *J. Catal.*, 77, 348, 1982

[22] K.S. Kim, W.E. Baitinger, J.W. Amy and N. Winograd, *J. Electron Spectrosc. Rel. Phenom.*, 5, 351, 1974

[23] S. Srinivasan, A.K. Datye, M. Hampden-Smith, I.E. Wachs, G. Deo, J.M. Jehng, A.M. Turek and C.H.F. Peden, *J. Catal.*, 131, 260, 1991

[24] a) M.A. Stranick, M. Houalla and D.M. Hercules, *J. Catal.*, 106, 362, 1987; b) G.B. Raupp and J.A. Dumesic, *J. Phys. Chem.*, 89, 5240, 1985

[25] A. Ellison, T.L. Overton and L. Bencze, *J. Chem. Soc. Faraday Trans.*, 89, 843, 1993

[26] M.P. McDaniel, *Adv. Catal.*, 33, 47, 1985

[27] B. Rebenstorf and S.L.T. Anderson, *J. Chem. Soc. Faraday Trans.*, 86, 2783, 1990

[28] R.E. Hoff, T.J. Pullukat and M. Shida, *J. Appl. Polym. Sci.*, 26, 2927, 1981

[29] M.P. McDaniel, C.H. Leigh and S.M. Wharry, *J. Catal.*, 120, 170, 1989

[30] S.J. Conway, J.W. Falconer and C.H. Rochester, *J. Chem. Soc. Faraday Trans. 1*, 85, 71, 1989

[31] S.J. Conway, J.W. Falconer, C.H. Rochester and G.W. Downs, *J. Chem. Soc. Faraday Trans. 1*, 85, 1841, 1989

[32] M.P. McDaniel, M.B. Welch and M.J. Dreiling, *J. Catal.*, 82, 118, 1983

[33] T.W. Woo and S.I. Woo, *J. Catal.*, 123, 215, 1990

[34] B. Rebenstorf and S.L.T. Andersson, *J. Chem. Soc. Faraday Trans.*, 86, 3153, 1990

[35] K.T. Ng and D.M. Hercules, *J. Phys. Chem.*, 80, 2094, 1976

[36] B. Rebenstorf, *Acta Chim. Scand.*, 45, 1012, 1991

[37] D.L. Myers and J.H. Lunsford, *J. Catal.*, 92, 260, 1985

[38] A. Ellison, *J. Chem. Soc. Faraday Trans. 1*, 80, 2567, 1984

[39] J.A. Chudek, G. Hunter, C.H. Rochester and T.F.S. Smith, *J. Catal.*, 136, 246, 1992

[40] M.P. McDaniel and M.B. Welch, *J. Catal.*, 82, 98, 1983

[41] G.P. Halada and C.R. Clayton, *J. Electrochem. Soc.*, 138, 2921, 1991

[42] S.A. Best, R.G. Squires and R.A. Walton, *J. Catal.*, 47, 292, 1977

[43] T.J. Pullukat, R.E. Hoff and M. Shida, *J. Polym. Sci. Polymer Chem Ed.*, 18, 2857, 1980

[44] G.M. Ingo, S. Dire and F. Babonneau, *Appl. Surf. Sci.*, 70/71, 230, 1993

[45] P.A. Zielinski, J.A. Szymura and I.G. Dalla Lana, *Catal. Lett.*, 13, 331, 1992

[46] R. Spitz, B. Florin and A. Guyot, *Eur. Polym. J.*, 15, 441, 1979

[47] C.S. Kim and S.I. Woo, *J. Mol. Catal.*, 73, 249, 1992

[48] A.P. Legrand, H. Hommel, A. Tuel, A. Vidal, H. Balard, E. Papirer, P. Levitz, M. Czernichowski, R. Erre, H. van Damme, J.P. Gallas, J.F. Hemidy, J.C. Lavalley, O. Barres, A. Burneau and Y. Grillet, *Adv. Colloid Interface Sci.*, 33, 91, 1990

[49] *Handbook of X-ray and Ultraviolet Photoelectron Spectroscopy*, ed. D. Briggs, Heyden, London, 1977

[50] W. Hill and G. Ohlmann, *J. Catal.*, 123, 147, 1990

[51] H. Collette, S. Maroie, J. Riga, J.J. Verbist, Z. Gabelica, J.B. Nagy and E.G. Derouane, *J. Catal.*, 98, 326, 1986

[52] C.V. Caceres, J.L.G. Fierro, J. Lazaro, A. Lopez Agudo and J. Soria, *J. Catal.*, 122, 113, 1990

[53] F.P.J.M. Kerkhof, J.A. Moulijn and A. Heeres, *J. Electron Spectrosc. Rel. Phenom.*, 14, 453, 1978

[54] C.D. Wagner, D.E. Passoja, H.F. Hillery, T.J. Kinisky, H.A. Six, W.T. Jansen and J.A. Taylor, *J. Vac. Sci. Tech.*, 21, 933, 1982

[55] M.P. McDaniel and M.M. Johnson, *J. Catal.*, 101, 446, 1986

[56] A.F. Wells, *Structural Inorganic Chemistry*, Clarenden Press, Oxford, 5th edn., 1984, p. 1197

[57] A. Cimino, B.A. DeAngelis, A. Luchetti and G. Minelli, *J. Catal.*, 45, 316, 1976

[58] D.R.C. Huybrechts, P.L. Buskens and P.A. Jacobs, *J. Mol. Catal.*, 71, 129, 1992

[59] D. Trong On, L. Bonneviot, A. Bittar, A. Sayari and S. Kaliaguine, *J. Mol. Catal.*, 74, 232, 1992

[60] A.Yu. Stakheev, E.S. Shpiro and J. Apijok, *J. Phys. Chem.*, 97, 5668, 1993

[61] B. Rebenstorf, *J. Polym. Sci. A*, 29, 1949, 1991

[62] A.R. Royston, University of Durham, 1991

[63] S. Evans, in *Handbook of X-ray and Ultraviolet Photoelectron Spectroscopy*, ed. D. Briggs, Heyden, London, 1977

[64] K. Siegbahn, C. Nordling, A. Fahlman, R. Nordberg, K. Hamrin, J. Hedman, C. Johansson, T. Bergmark, S-E. Karlson, L. Lindgren and B. Lindberg, *Nova Acta Regia Soc. Sci. Upsaliensis*, Ser. IV, vol. 20, 1967

[65] K. Siegbahn, C. Nordling, C. Johansson, J. Hedman, P.F. Heden, K. Hamrin, U. Gelius, T. Bergmark, L.O. Werme, R. Manne and Y. Baer, *ESCA applied to free molecules*, North Holland, Amsterdam, 1969

[66] G. Johansson, J. Hedman, A. Berndtsson, M. Klasson and R.F. Nilsson, *J. Electron Spectrosc.*, 2, 295, 1973

[67] D.M. Hercules, *ESCA and Auger Spectroscopy*, ACS, Washington DC, 1979

[68] A.F. Carley and R.W. Joyner, *J. Electron Spectrosc.*, 16, 1, 1979

[69] S.C. Fung, *Catalysis*, 58, 454, 1979

[70] J.S. Brinen, J.L. Schmitt, W.R. Doughman, P.J. Achom, L.A. Siegal and W.N. Deglass, *J. Catal.*, 40, 295, 1975

[71] R.L. Chin, Ph.D. Thesis, University of Pittsburgh, 1980

[72] R.B. Moyes and M.W. Roberts, *J. Catal.*, 49, 216, 1977

[73] T.A. Patterson, J.C. Carver, D.E. Leydon and D.M. Hercules, *J. Phys. Chem.*, 80, 1700, 1976

[74] A. Cimino and B.A. DeAngelis, *J. Catal.*, 36, 11, 1975

[75] A.W. Miller, W. Atkinson, M. Barber and P. Swift, *J. Catal.*, 22, 140, 1971

[76] A.W. Armour, P.C.H. Mitchell, B. Tolkesson and R. Larsson, *J. Less Common Metals*, 36, 361, 1974

[77] P. Gajardo, R.I. Declarak-Grimee, G. Delvaux, P. Olodo, J.M. Zabala, P. Canesson, P. Grange and B. Delmon, *J. Less Common Metals*, 54, 311, 1977

[78] P. Ratnasamy, *J. Catal.*, 40, 137, 1975

[79] D.S. Zingg, L.E. Makovsky, R.E. Tischer, F.R. Brown and D.M. Hercules, *J. Phys. Chem.*, 84, 2989, 1980
[80] J. Mendialdua, Y. Barbaux, L. Gengembre, J.P. Bonnelle, B. Grzybowska and M. Gasior, *Bull. Polish Acad. Sci. Chem.*, 35, 213, 1987
[81] P.J. Angevine, J. Vartuli and W.N. Delgass, in *Proc. 6th Int. Congr. Catal.*, London, 1976, vol. 2, p. 611
[82] C. Defosse, P. Canesson, P. Rouxhet and B. Delmon, *J. Catal.*, 51, 269, 1978
[83] S.C. Fung, *J. Catal.*, 58, 454, 1979
[84] M. Houalla, F. Delannay and B. Delmon, *J. Phys. Chem.*, 85, 1704, 1981
[85] F. Delannay, M. Houalla, D. Pirotte and B. Delmon, *Surf. Interface Anal.*, 1, 172, 1979
[86] C. Defosse, *J. Electron Spectrosc. Rel. Phen.*, 23, 157, 1981 and references therein
[87] H.P.C.E. Kuipers, H.C.E. van Leuven and W.M. Visser, *Surf. Interface Anal.*, 8, 235, 1986
[88] S.M. Davis, *J. Catal.*, 117, 432, 1989
[89] G.K. Wertheim, S.B. Di Cenzo and S.E. Youngquist, *Phys. Rev. Lett.*, 51, 2310, 1983
[90] G.K. Wertheim, S.B. Di Cenzo, D.N.E. Buchanan and P.A. Barnnett, *Solid State Commun.*, 53, 377, 1985
[91] A. Zecchina, S. Coluccia, E. Guglilminotti and G. Ghiotti, *J. Phys. Chem.*, 75, 2774, 1971
[92] A. Zecchina, S. Coluccia, L. Cerruti and E. Borello, *J. Phys. Chem.*, 75, 2783, 1971
[93] J.P. Hogan, *J. Polym. Sci. Ser. A 1.*, 8, 2637, 1970
[94] M.B. Welch and M.P. McDaniel, *J. Catal.*, 82, 110, 1983
[95] S.J. Conway, J.W. Falconer and C.H. Rochester, *J. Chem. Soc. Faraday Trans. 1*, 85, 79, 1989
[96] S.L.T. Andersson and R.F. Howe, *J. Phys. Chem.*, 93, 4913, 1989
[97] D.R. Witt, in *Reactivity, Mechanism and Structure in Polymer Chemistry*, eds. A.D. Jenkins and A. Ledwich, Wiley, Chichester, 1974, p. 431
[98] T.J. Pullukat, R.E. Hoff and M. Shida, in *Titanium Modified Chromium Catalysts for Ethylene Polymerization: Symposium on Transition Metal Catalyzed Polymerization*, Michigan Molecular Institute, August 1981
[99] C.G. Armistead, A.J. Tyler, F.H. Hambleton, S.A. Mitchell and J.A. Hockey, *J. Phys. Chem.*, 73, 3947, 1969
[100] M.P. McDaniel and M.M. Johnson, *J. Catal.*, 101, 446, 1986
[101] H.L. Krauss, *J. Mol. Catal.*, 46, 97, 1988
[102] W.E. Smith and R.L. Zelmer, *J. Polym. Sci. A*, 1, 2587, 1963
[103] J-F.R. Tempere, D. Delafosse and J.P. Contour, in *Molecular Sieves II*, ed. J.R. Katzer, ACS Symposium Series 40, ACS, Washington, 1977, p. 76
[104] S.L.T. Andersson and M.S. Scurrell, *J. Catal.*, 59, 340, 1979
[105] P.B. Ayscough, C. Eden and H. Steiner, *J. Catal.*, 4, 278, 1965

[106] V.B. Kazansky and J. Turkevich, *J. Catal.*, 8, 231, 1967

[107] D.D. Eley, C.H. Rochester and M.S. Scurrell, *Proc. R. Soc. London Ser. A*, 329, 361, 1972

[108] C. Eden, H. Feilchenfeld and Y. Haas, *J. Catal.*, 9, 367, 1967 and *J. Catal.* 11, 263, 1968

[109] H.L. Krauss and H. Stack, *Inorg. Nucl. Chem. Lett.*, 4, 396, 1968

[110] H.L. Krauss, in *Proc. 5th Int. Congr. Catal.*, North Holland, Amsterdam, 1973, vol. 1, p. 207

[111] L.K. Przhevalskaya, V.A. Shvets and V.B. Kazansky, *J. Catal.*, 39, 363, 1975

[112] H.L. Krauss, B. Rebenstorf and U. Westphal, *Z. Anorg. Chem.*, 414, 97, 1975

[113] H.L. Krauss and L. Mums, *Z. Naturforsch.*, Teil B, 34, 1628, 1979

[114] D.D. Beck and J.H. Lunsford, *J. Catal.*, 68, 121, 1981

[115] H.L. Krauss, in *184th ACS National Meeting Div. Colloid and Surface Chemistry*, Kansas City, USA, 1982

[116] G. Ghiotti and E. Garrone, in *184th ACS National Meeting Div. Colloid and Surface Chemistry*, Kansas City, USA, 1982

[117] B. Rebenstorf and R. Larsson, in *184th ACS National Meeting Div. Colloid and Surface Chemistry*, Kansas City, USA, 1982

[118] P.P.M.M. Wittgen, C. Groeneweld, J.H.G.J. Janssens, M.L.J.A. Wetzelsand and G.C.A. Schuit, *J. Catal.*, 59, 168, 1979

[119] C.U.I. Odenbrand, S.L.T. Andersson, L.A.H. Andersson, J.G.M. Brandin and G. Busca, *J. Catal.*, 125, 541, 1990

[120] Y. Okamoto, M. Fujii, T. Imanaka and S. Teranski, *Bull. Chem. Soc. Japan*, 49, 859, 1976

[121] T.J. Pullukat and M. Shida, *U.S. Patent* 3,780,011, 1973

[122] J.P. Hogan, in *Copolymerization*, ed. G.E. Ham, Interscience, New York, 1964

[123] A. Fernandez, J. Leyrer, A.R. Gonzalez-Elipe, G. Munuera and H. Knozinger, *J. Catal.*, 112, 489, 1988

[124] G. Busca, H. Saussey, O. Saur, J.C. Lavalley and V. Lorenzelli, *Appl. Catal.*, 14, 245, 1985

[125] G. Ramis, G. Busca and V. Lorenzelli, *J. Chem. Soc. Faraday Trans. 1*, 83, 1591, 1987

[126] B. Rebenstorf and R. Larsso, *Acta Chem. Scand. Ser. A*, 34, 239, 1980

[127] C.R.F. Lund and J.A. Dumesic, *J. Catal.*, 76, 93, 1982

[128] C.R.F. Lund and J.A. Dumesic, *J. Catal.*, 72, 21, 1981

[129] C. Groenveld, P.P.M.M. Wittgen, A.M. van Kersbergen, P.L.M. Mestrom, C.E. Nuijten and G.C.A. Schuit, *J. Catal.*, 59, 153, 1979

[1309] M.F. Brest and R.A. Condrate, *J. Mater. Sci. Lett.*, 4, 994, 1985

[131] M.R. Boccuti, K.M. Rao, A. Zecchina, G. Leofanti and G. Petrini, *Stud. Surf. Sci. Catal.*, 48, 133, 1984

[132] J.C. Riviere, *Surface Analytical Techniques*, Oxford

Science Publications, Oxford, 1990

[133] J.N. Taylor, *An Introduction to Error Analysis*, University Science Books, Mill Valley, California, 1985

[134] P.C. McCaslin, *J. Vac. Sci. Technol. A*, 9, 1421, 1991

[135] A. Clarke, *Catal. Rev.*, 3, 145, 1969

[136] V.A. Zakharov and Yu.I. Ermakov, *J. Polym. Sci. Pt. A 1*, 9, 3129, 1971

CHAPTER 3

<u>Characterization of the Phillips Catalyst using Thermal Decomposition and Mass Spectroscopy</u>

128

1 Introduction

The XPS experiments of Chapter 2 led to information being obtained regarding the chemical state and dispersion of the surface species of the catalysts after activation. In order to obtain information on the reactions and changes in surface chemistry during the entire activation process the evolved gases were analyzed using a quadrupole mass spectrometer. Finding the temperature at which the peak intensities are at their maximum value allows a picture to be obtained of the chemical changes occurring during the activation, and a mechanism to be proposed for these changes.

2 Mass Spectrometry

The mass spectrometer produces charged particles that consist of the parent ion and ionic fragments of the original molecule and it sorts them according to their mass/charge ratio [1]. The mass spectrum is a record of the relative numbers of different kinds of ions and is characteristic of every compound. MS has increased sensitivity over most other analytical techniques due to the action of the analyser as a m/z filter to reduce background interference and from the sensitive electron multipliers used for detection. The excellent specificity results from the characteristic fragmentation patterns which can give information about molecular weight and molecular structure.

All mass spectrometers perform three basic tasks:-
(i) creating gaseous ion fragments from the sample
(ii) sorting these ions according to m/z ratio and
(iii) measuring the relative abundance of ion fragments of each mass.

A mass spectrometer consists of the following basic units:
(i) an ion source where ions are formed from the sample;
(ii) an analyser which separates the ions according to their m/z values;
(iii) a detector which gives the intensity of the ion current for each species; the detector output can be displayed or stored, to yield the mass spectrum;
(iv) electronics of power supply and control to the three units above;
(v) various pumping systems [7].

A block diagram of these components is shown in Figure 3.1 [1].

Figure 3.1   *Schematic diagram of the components of a mass spectrometer*

Sample

```
┌──────────┐      ┌──────────┐      ┌──────────┐      ┌────────────┐
│ Inlet    │─────▷│ Ion      │────▷ │ Mass     │──▷  ─│ Ion        │
│ System   │      │ Source   │      │ Analyser │      │ Collection │
└──────────┘      └──────────┘      └──────────┘      │ System     │
                                                      └────────────┘

                  ┌──────────┐                        ┌──────────┐
                  │ Vacuum   │                        │ Data     │
                  │ System   │                        │ Handling │
                  └──────────┘                        │ System   │
                                                      └──────────┘
```
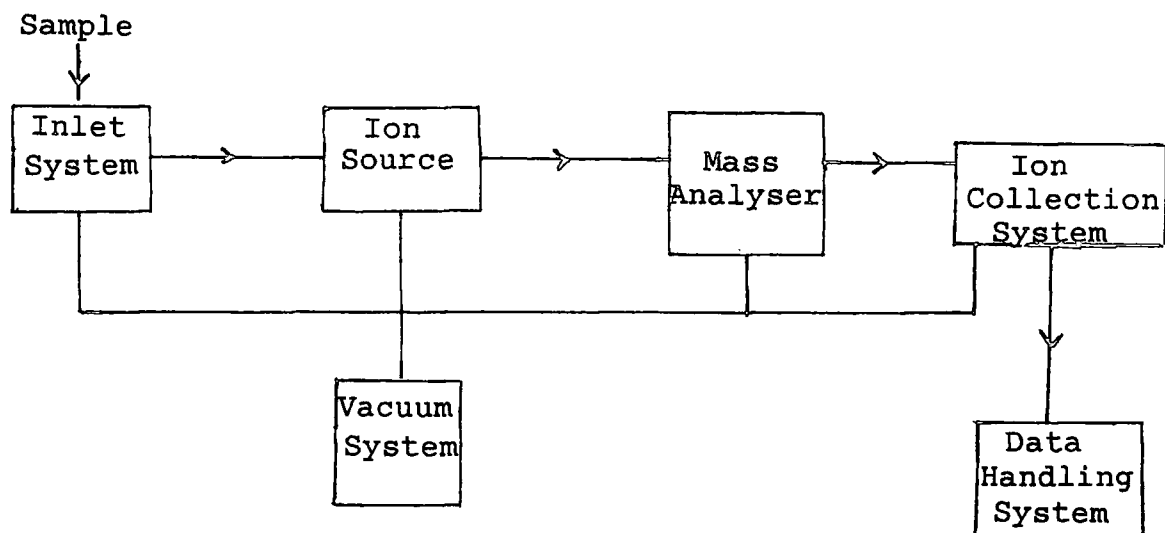
The operation of the mass spectrometer requires a collision-free path for the ions and to achieve this the pressure in the spectrometer needs to be less than 10^{-6} Torr. Gaseous samples are introduced through a leak valve into the ionisation chamber from the inlet system [1]. In this study gases evolved from the heated catalysts are passed, via the carrier gas (oxygen or argon), through a stainless steel capillary and leak valve into the vacuum system of the mass spectrometer.

2.1 Ionization Methods

Ion sources have the dual function of producing ions without mass discriminaton from the sample and accelerating them into the mass analyzer with a small spread of kinetic energies prior to acceleration. In all source designs there must be an ion withdrawl and focusing system, in which the ions are removed electrostatically from the chamber and accelerated towards the mass analyser. Several pairs of focusing elements and slits then control the direction, shape and width of the ion beam [1]. Figure 3.2 shows the design of an electron impact ion source.

Figure 3.2 *Electron impact ion source and ion-accelerating system*
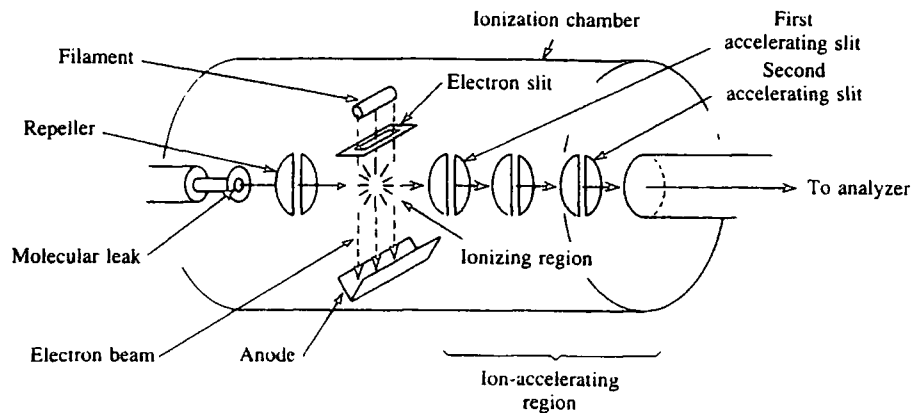
2.2 Mass Analyzers

The function of the mass analyzer is to separate the ions produced in the ion source according to their different mass/charge ratios [1].

2.3 Quadrupole Mass Analyzer

Special characteristics of the quadrupole instrument are the following:
(a) small size and weight
(b) relatively low cost
(c) rapid scanning of the mass spectrum
(d) linear operation to relatively high pressure (10^{-4} Torr)
(e) low source energy (<10eV) and
(f) electrical variation of the resolving power (by varying the dc/rf voltage ratio)
(g) a high mass range (>1000 amu)
(h) compatibility with other surface analytical techniques
(i) freedom from magnetic fields   [5,6,8].
However, it is not capable of the high mass resolution of a magnetic sector instrument [3,5].

A diagram of the quadrupole mass spectrometer is contained in Figure 3.3.

Figure 3.3   *Diagram of the quadrupole mass analyzer*
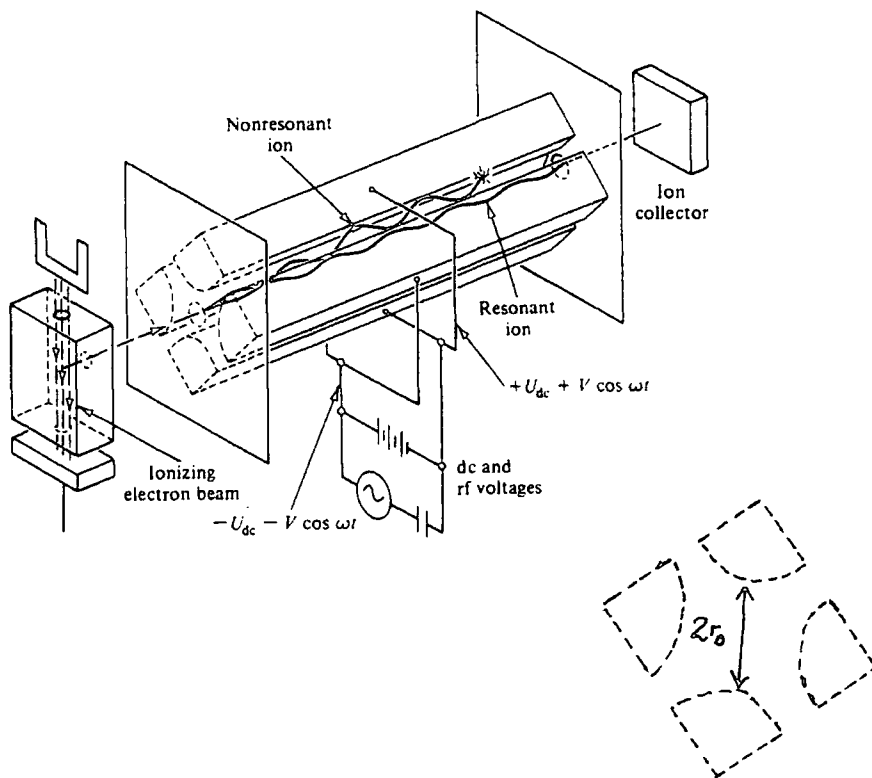
A quadrupole filter consists of four parallel electrodes with hyperbolic, elliptical, or circular cross-section. The diagonally opposite electrodes (arranged symmetrically with the minimum-radius curve innermost) are at the same potential and are separated by a distance equal to twice the minimum radius of curvature (i.e. $2r_o$) [7].

One diagonally opposite pair of rods is held at $+U_{ac}$ volts and the other pair at $-U_{ac}$ volts. A radio frequency oscillator supplies a signal to the first pair of rods that is $+V\cos\omega t$ and a rf signal retarded by 180° ($-V\cos\omega t$) to the second pair. The equipotential surfaces in the region between the four rods appear as oscillating hyperbolic potentials. Ions from the ion source are injected into the quadrupole array through a circular aperture, and as they proceed down the longitudinal z axis they undergo transverse motion in the x and y planes. The dc electric fields tend to focus positive ions in the positive plane and defocus them in the negative plane. As the superimposed rf field becomes negative during part of the negative half cycle of the alternating field, positive ions are accelerated toward the electrodes and achieve a substantial velocity. The following positive half cycle has an even greater influence on the motion of the ion, causing it to reverse its direction and accelerate even more. The ions exhibit oscillations with increasing amplitudes until they finally collide with the electrodes and become neutral

particles. The lighter the ion in mass, the smaller the number of cycles before it is collected by the electrode.

By controlling V_{ac}/V_{rf} the field can be established to pass ions of only one m/z ratio down the entire length of the quadrupole array. By simultaneously sweeping the dc and rf amplitudes ions of various m/z ratios are allowed to pass through the mass filter to the detector and an entire spectrum can be produced [1,3,4,8].

The quadrupole analyzer is not restricted to the detection of monoenergetic sources - ions are accepted within a 60° cone around the axis. Therefore, it does not require focusing slits, which results in higher sensitivity [1]. The sensitivity is roughly inversely proportional to the mass resolution: the better the resolution selected, the lower the sensitivity at that charge-to-mass ratio, and vice versa [2].The resolution is a function of the number of cycles the ion spends in the field. Increasing the rod length (usually 5-20cm) increases the resolution and the capability to handle ions of higher energies. If the rf frequency is increased, the length of the analyzer can be reduced. Rod diameters are also a factor: increasing the diameter increases the sensitivity by a large factor, whereas a decrease increases the mass range [1]. Typical mass resolutions achievable with QMS are in the range M/ ΔM 50 up to 1000, where M is the mass of the peak and ΔM is the width of the peak at 10% of the peak height [5]. The relative intensities of detected ions depend rather critically on the operational parameters of the quadrupole. This is because the transmission and mass resolution of the analyser are very sensitive to the axial and transverse velocities of the incoming ions (when comparing results from different analysers calibrants must be compared first) [3]. The energy of the transmitted ions needs to be as low as possible for good mass resolution. However, the transmission of the quadrupole decreases with decreasing energy.

Resolved ion beams, after passage through a mass analyser, sequentially strike a detector. The electron multiplier is most commonly used. For ion currents less than 10^{-15}A an electron multiplier is used. Either positive or negative ions are accelerated by the constant high voltage of a conversion dynode where they are converted into electrons and/or positive charged ions when they strike the plate. The currents created are then further multiplied by the electron multiplier with gains of 10^5- 10^7. The limiting factor is either the system noise level or the system background [1].

3 Types of ions, peaks and mass spectra

3.1 Ion species

The mass spectrum can contain signals from several species of ions, including the following:

singly charged monatomic ions X^+
singly charged polyatomic ions $XY...Z^+$
multiply charged ions X^{n+}, $XY...Z^{n+}$
molecular ions $XY^{+\cdot}$ (formed from the XY molecule - parent molecular ions)
fragment ions X^+, Y^+ (formed from the XY molecule)
rearrangement ions XRY^+ (formed from XYR or RXY)
metastable ions - generally formed by decomposition occurring between the ion source and the analyser
secondary ions formed by reactions between ions and molecules
negative ions ions (negatively charged) corresponding to those above [7].

Electron impact results in the formation of a molecular ion $M^{+\cdot}$ by removal of an electron, to leave the charged radical:

$$M + e^- \Longrightarrow M^{+\cdot} + 2e^-$$
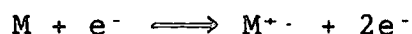
During the ionization, a certain amount of internal energy is transmitted to the molecule. This amount of energy is variable, and its magnitude determines whether one or more fragmentation reactions can occur. The reactions most likely to take place are those which have low activation energy and lead to relatively stable ionic or neutral species:

$M^{+\cdot} \longrightarrow$ ionic fragment + neutral fragment
          $(BC^{+\cdot})$ (radical, atom,
                                          molecule)

              ↓

       ionic fragment + neutral fragment

              ↓

          etc.
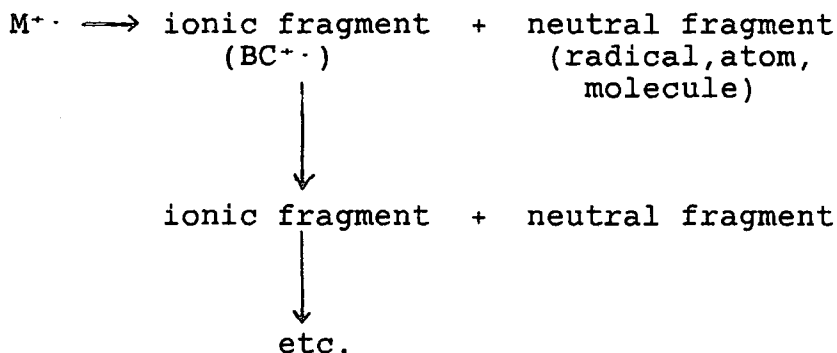
The successive fragmentation reactions lead, in general, to ions and radicals consisting of a single atom or group of atoms. It should be noted that in fragmentation the charge is located on the fragment with the lowest ionization potential. Thus in the fragmentation of $BC^{+\cdot}$ into B^+ and $C\cdot$ or into $B\cdot$ and C^+. if the ionization potential of B is lower than C, then the major fragmentation path will be into B^+ and $C\cdot$; similarly, for

134

fragmentation of an ion BC$^+$, under the same conditions the most probable fragmentation would be into B$^+$ and C, not into B and C$^+$.

Stable fragments can also be formed by a change in the relative positions of the atoms in a molecule, followed by decomposition of the ion. These changes are called rearrangement reactions [7].

Since many elements have several isotopes, for any given atomic composition the mass spectrum contains peaks corresponding to the different isotope combinations. Thus for methane the isotope peaks for $^{12}CH_4^+$ (m/z=16), $^{13}CH_4^+$ (m/z=17) and $^{12}CH_3D^+$ (m/z=17) will appear. As the abundance of ^{13}C is 1.08% and that of deuterium 0.016% the peak at m/z=17 will mainly be due to $^{13}CH_4^+$.

Electron impact ionisation of molecules containing polyisotopic elements such as C, H, N, O results in peaks at m/z values that are 1,2,3 etc. units higher than the peak for the ion containing the most abundant isotope of each element [7].

A species of mass number M can give rise to peaks at m/z = M and m/z = M/2, for its singly and doubly charged ions respectively [7].

3.2 Ion fragmentation mechanisms

The pattern of fragmentation of a molecular ion depends mainly on the chemical structure of the compound, and a number of empirical rules for predicting it have been established. Basically the cleavages are of three main types: simple sigma bond cleavage, cleavage induced by the presence of a radical site, and cleavage induced by charge displacement. The pattern will also depend on the particular groups and bonds which can be the sites of these events.

(i) Sigma bond cleavage

$$(A-B-C-D) \xrightarrow{-e^-} (A-B^+\cdot \; C-D) \longrightarrow AB^+ + \cdot CD$$
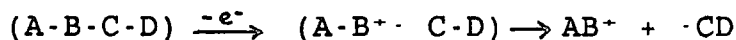
The site of ionisation is the molecular orbital bonding atoms B and C. The loss of one of the electrons leads to cleavage of the B-C bond.

(ii) Fragmentation induced by a radical site ('r' type)

A radical site is generated during ionisation by the loss of an electron from a double bond or a hetero-atom. The resultant unpaired electron in the bond forms a new bond with an adjacent (a) atom, and the fragmentation occurs between the a and b atoms.

$$X-X'-\overset{\cdot+}{Y}-Z-Z' \xrightarrow[\alpha \text{ cleavage}]{r} X\cdot + X' = Y^+ Z - Z'$$

(iii) <u>Fragmentation by charge displacement inductive cleavage ('i' type)</u>

$$X-X'-\overset{+}{Y}-Z-' \xrightarrow{\overset{\cdot}{i}} X-X'-Y + \overset{+}{Z}-Z'$$
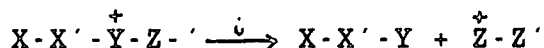
Here the ionisation potential of the $Z'-Z^+$ fragment is lower than that of the separated neutral $X-X'-Y$. The ionisation potential (IP) of the $Z'Z^+$ ion fragment is lower than that of the neutral fragment: $IP(Z'Z^+) < IP(XX'Y)$ [7].

4 Thermal Analysis

The principle thermal analysis techniques, thermogravimetry (TG) and differential scanning calorimetry/differential thermal analysis (DSC/DTA), provide physical measurements but give no direct chemical information on the processes being studied [13]. The solid material remaining at various stages in the thermal analysis experiment can be studied. However, although this approach can be very useful, there are certain disadvantages: frequently the samples are rather too small for accurate chemical analysis and so various instrumental methods are often used, such as XRD, which can have difficulties such as reversible high temperature phase changes not being detected on cooling to room temperature and decomposition reducing the crystallite size to a point where products appear amorphous to X-rays.

The solids produced by thermal decomposition often possess a large surface area and hence a high degree of reactivity, making them susceptible to attack by oxygen, carbon dioxide or water in the atmosphere. Unless rigorous precautions are taken to exclude even traces of these gases, the products observed on subsequent analysis may well be different from those produced in the original reaction [13,14].

In addition to these difficulties there are always problems arising from non-simultaneous techniques, i.e. those associated with the unambiguous association of two measurements made at different times and under possibly very different conditions. There will always be some uncertainty regarding any processes which may occur while the sample is being cooled to room temperature, prior to analysis [14]. Also, analysis at various stages of an experiment is very time consuming. Some of these objections can be overcome by using ancillary techniques simultaneously. However, this approach is rather specialized, expensive and not readily available. Fewer

problems are found in analyzing the gases which are evolved during thermal analysis.

5 Evolved Gas Analysis and Mass Spectrometry

Initially the concept of EGA was tested with a number of known chemical reactions releasing simple gaseous molecules [41]. Examples are shown in Figures 3.4 and 3.5 [12].

Figure 3.4 The release of volatiles from a germanium chelate

GeEDTA · 2 H_2O
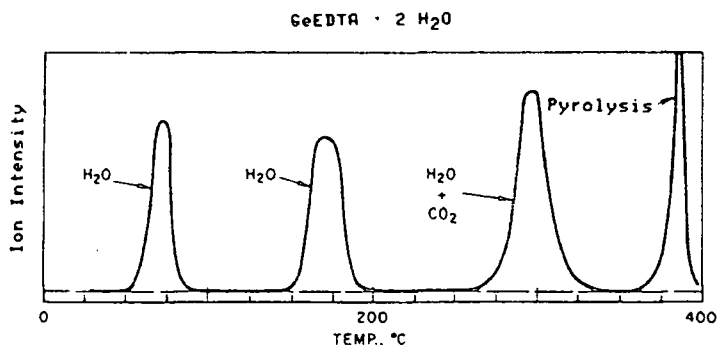
Figure 3.5 The release of volatiles from a chelating agent

H_4EDTA · 2 HCl · 2 H_2O
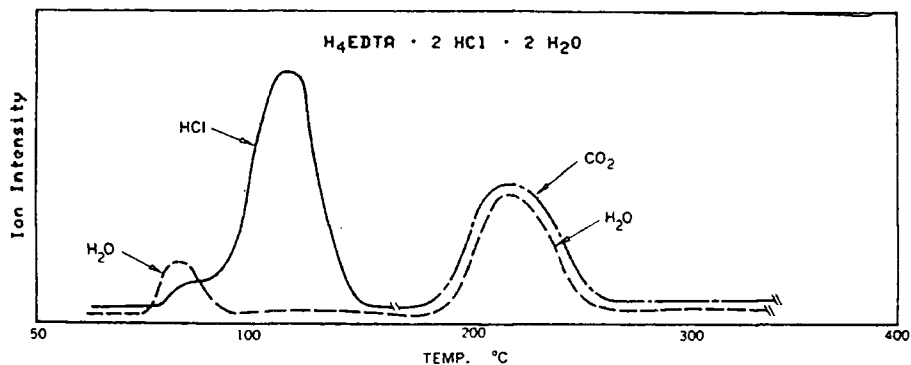
The need to identify evolved gases led to the first attempts to combine thermoanalytical methods with mass spectrometry in the 1960's [12]. Langer and Gohlke [38] and Friedman [39] have reviewed early work (prior to 1970) in the coupling of EGA to MS. The former authors established the two main techniques, the first of which, mass spectrometric thermal analysis, involves placing the sample in a specially designed mass spectrometer source [40,41]. This has a number of advantages over other methods, as very

137

small amounts of gas can be detected and, because the experiment is performed in the high vacuum of the spectrometer, there is no possibility of any gas phases reactions before the evolved materials are detected. A similar technique was developed by Price et al [42] who used a temperature-programmed solid insertion probe in a time-of-flight mass spectrometer to study the thermal decomposition of cadmium oxalate.

However, the very low pressure prevailing in the source of the mass spectrometer is also responsible for a number of serious limitations as it can greatly affect the processes which are pressure dependent, causing problems with the control and measurement of the sample temperature. Further, not only are the peak temperatures reduced markedly, but the resolution and general shape of the curve is changed. This makes correlation with TA experiments carried out at atmospheric pressure very difficult. Nevertheless, in some instances the results of MTA, when the MS is set to read the ion current at fixed m/e ratio, rather than scan a range of masses, appear similar to those of DTA, so that the processes giving rise to the DTA peaks can be identified.

To avoid these problems an alternative approach was developed, in which the sample is heated in an external furnace, or DTA etc., at normal pressures and the evolved gases led into the MS where they are analysed at the low pressure prevailing in the source [14]. Adaption of the MS to measure species evolved at ambient or intermediate pressures can be accomplished using a simple pressure-reducing device consisting of a 12 inch long uncoated capillary silica GC column of 70μm diameter. This device works particularly well for organic vapours [9,12,13]. Ertl et al [20] have qualitatively analyzed the evolved gases from an attached reactor using a differentially pumped heated capillary inlet.

Most workers have used this approach rather than MTA, as it is very much easier to correlate the results of DTA etc. and MS. A further advantage is that a standard mass spectrometer can be used with the minimum of reconfiguration [14].

5.1 Experimental Configuration

EGA is usually a coupled simultaneous method, in that the sample is heated in a separate apparatus and the vapour-phase products carried into the gas analyser, often using an inert purge gas, via a suitable connecting line. It is important that the high concentration of carrier gas does not swamp the smaller responses of the evolved gases and thus helium, with its low mass number is useful as a

carrier [9]. Argon can be used when it is necessary to detect D_2 at mass 4. Nitrogen is not useful when using MS detection because CO at mass 28 cannot be observed. The inert carrier gas must be purified as water can react with CO by the water gas shift reaction to form CO_2 [24]. Problems of identifying the evolved gas analysis results unambiguously with those of the thermoanalytic technique remain. However, the experimental design can be such that the time difference between the evolution of the gases and their detection is so small that it can be neglected. It is possible to reduce this time delay, for example, to less than one second, which is effectively instantaneous on the time scale of thermal analysis [13].

It is necessary to ensure that gases are evolved only from the sample and not from other surfaces. Also, the heating rate must be fast enough that the proportion of desorbed species accepted by the MS is characteristic of the desorption mechanism, i.e. there must not be time for significant adsorption and re-emission from the other surrounding surfaces to interfere with the signal. The heating rate must also not be so fast that readsorption occurs [2,15]. This is particularly important with products which are readily oxidised or changed catalytically. Frequently the materials used in thermal analysis equipment possess excellent catalytic properties. For example, platinum and its alloys are widely found in both thermocouples and in furnace windings. It is necessary, therefore, to design the system so that contact between the evolved gases and the equipment is minimised or eliminated [14].

Using EGA equipment under conditions of controlled transformation rate thermal analysis (CRTA) [45] solves these problems as the rate of production of the gaseous phase is permanently controlled, usually at a low value, so that the whole gas flow may be sent to the quadrupole analyser (with no risk of overpressure, no need of gas flow separator and no gas discrimination) and the temperature and pressure gradients through the solid sample may be lowered at will, which may avoid the overlap of successive steps of the reaction [15].

Once the evolved gases have been extracted safely, they must be transferred intact to the gas analysis equipment. Less volatile materials will tend to condense and steps must be taken to prevent this, not only to avoid the gas lines becoming blocked. This requires some form of heating for the lines carrying the gas-phase products from the point of their generation to the gas detector.

During the transit time the volatiles must be protected from degradation and this is often accomplished by using an inert covering on the interior of the gas line. A short

transit time further reduces the possibility of reaction with the walls of the line and also minimises the risk of any gas phase chemical processes [9,13,14].

Mass spectral data can be obtained in two ways:
(i) Linear histogram scanning (HIS) in which only the peak maximum is recorded, displayed and stored, and (ii) multiple ion monitoring (MIM) mode in which upto 16 specific ions can be selected, counted with a predetermined degree of precision, displayed as a time dependent plot and stored.

The method of analysis is to run in the LGH mode to obtain full spectral scans as a function of time (or temperature) owing to much greater mass fragmentation, and then to convert to time dependence all ions whose intensity changes significantly. Once a system's thermal behaviour is known, the evolution of specific species can then be followed more accurately using MIM mode [9,13].

These evolved gas profiles give specific information on the chemical reactions taking place and can be used for both qualitative and quantitative analysis. They are also particularly useful in studying the kinetics of thermal decomposition reactions as they enable the rates of evolution of individual components, in what may be a complex mixture, to be followed.

However, the complexity of the material being analysed, or of the gas phase components, often results in mass spectra which are difficult to interpret [14].

Wherever possible unambiguous peaks in the mass spectrum are selected on the basis of prior knowledge of the catalyst preparation. For example, peaks associated with nitrogen oxides (m/z = 30 and 46), carbon dioxide (m/z = 44) and water (m/z = 18 and 17) are scanned, if a calcined catalyst has been prepared by precipitation of carbonate from a nitrate solution. For commercial catalysts, or those of unknown origins, it is worthwhile examining the complete spectrum at several temperatures before selecting peaks and carrying out EGA on a fresh sample [19].

5.2 Applications

(i) Decomposition of calcium oxalate monohydrate

Figure 3.6 *Mechanism for the decomposition of calcium oxalate monohydrate*

$$CaC_2O_4 \cdot H_2O \implies CaC_2O_4 + H_2O$$

$$CaC_2O_4 \implies CaCO_3 + CO$$

$$CaCO_3 \implies CaO + CO_2$$
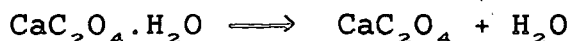
TG and DTG were recorded at a heating rate of 20°C/min under flowing argon. The MS was set up to scan the 0-50 amu range in the HIS mode. Figure 3.7 indicates the evolution of water, carbon monoxide with some carbon dioxide, and carbon dioxide respectively. No argon carrier gas is observed since a background subtraction facility was used before data storage. The presence of some carbon dioxide in the second decomposition stage may be attributed to two sources: disproportionation of the primary product, CO, into carbon dioxide and carbon, and/or partial oxidation of the CO by traces of oxygen in the purge gas. When higher levels of oxygen are present in the gas stream, its absorption may be monitored by the MS during the oxidation process.

Figure 3.7 *Mass spectra obtained at the time of maximum rate of weight loss for the three decomposition stages in calcium oxalate*

Water (m/e 18)
detected at 200°C

Carbon Monoxide
(m/e 28) and Carbon
Dioxide (m/e 44)
detected at 480°C

Carbon Dioxide
(m/e 44) detected
at 770°C
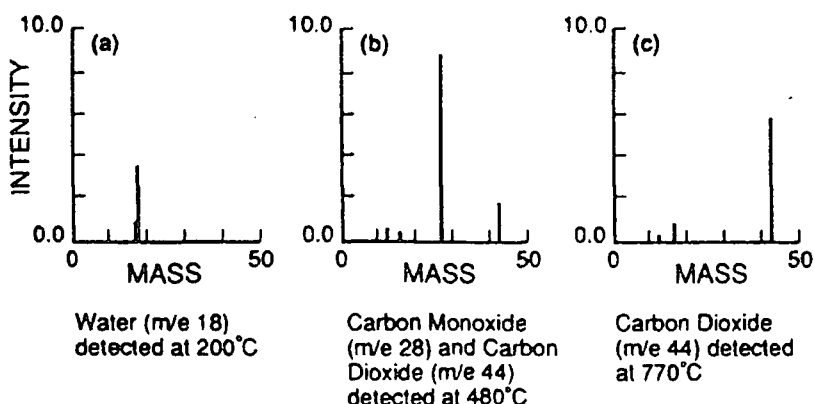
Simultaneous techniques such as TG-MS are particularly valuable in systems where reproducibility is difficult to achieve, since all the information is generated from the same sample under the same conditions [13].

(ii) Catalysis

Traditional forms of thermal analysis, such as thermogravimetry and differential thermal analysis, are particularly effective for detecting phase changes in catalyst precursors during drying and calcination [46].

When combined with methods of structural analysis, these techniques can be used to determine the stages in a complex series of transformations [47], but the information relates essentially to the bulk and so may only lead to some general predictions about the nature of the catalyst surface. Although there are other methods, e.g. microgravimetry, thermoelectrometry and microcalorimetry, which are sensitive enough to allow surface changes to be monitored, the results can be difficult to interpret. However, by detecting and identifying gaseous species desorbing from the surface of a solid sample, it is possible to achieve surface-specific thermal analysis [19]. TPD has been found to be useful for heterogeneous catalysis studies in a number of ways [24]:
- catalytic mechanism studies
- surface area measurements
- catalyst characterisation of fingerprint spectra
- studying differences in catalysts due to preparation procedure, composition, or dispersion of the metal
- determining binding energies and binding states of adsorbed molecules
- nature of the products of reaction between a catalysisng surface and one or more adsorbing molecules [2]
- an important area of application is the study of the kinetics of reactions which produce gaseous products. Of particular interest are thermal decomposition reactions where the evolved materials are complex and the reaction therefore cannot be studied successfully by conventional weight loss or pressure increase methods [14].

A big advantage of TPD techniques is that they are very sensitive probes of the surfaces of supported catalysts. Thus, they may be one of the best and quickest methods to fingerprint a supported metal catalyst. Studies can be carried out at atmospheric pressure on supported catalysts, oxides and commercial catalysts. Catalysts which have been used under reaction conditions and whose properties have been changed can also be studied by these techniques [24].

One traditional method of preparing catalysts is to thermally degrade a compound containing the elements of the catalyst, in such a way as to create the chemical structure, and particle shape, size and dispersion necessary for optimum performance. Short and his co-workers [43], in their studies of noble metal catalysts supported on pyrographite-coated carbon fibre paper, used MS to study the products of decomposition of platinum-ammonia

142

complexes, in conjunction with both DTA and TG, to investigate the structural and chemical properties and their dependence on preparative technique. Ciembroniewicz et al [44] used a quadrupole mass spectrometer to analyse the gases evolved in the decomposition in vacuo, in air and in an atmosphere of inert gas, of ammonium paramolybdate, in their study of the mechanisms of formation of molybdenum oxide catalysts [14].

In the studies of Baker et al [19] a sequence of related experiments have been carried out using a single apparatus in which the products of adsorption/desorption or heterogeneous reaction are analysed by QMS [48] during programmed heating of a sample of a copper-based catalyst. The results provide information about the contaminants on the surface of calcined Cu-metal oxides, the different stages during the subsequent reduction, the active sites on the resultant supported metal catalysts and the mechanism of the heterogeneous catalytic reaction.

Example: Cu-Zn-O

Figure 3.8   EGA of Cu-Zn-O
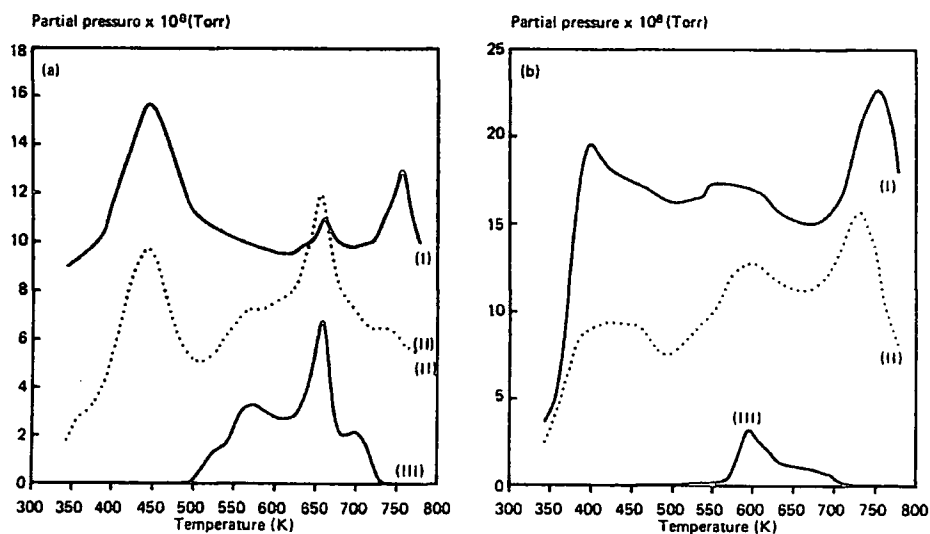
I m/e = 18 (H_2O^+)   II m/e = 44 (CO_2^+)   III m/e = 30 (NO^+)
a) Sample calcined in a muffle furnace at 625K
b) Sample calcined under flowing oxygen at 675K

Figure 3.8 shows the EGA traces for two Cu-Zn-O catalysts, which had been prepared by precipitating the mixed metal carbonate from an aqueous solution of the nitrates. In both cases, the precursor had been dried and calcined, but different conditions had been used during calcination. Sample A had been heated (625K;3h) in a muffle furnace [49]; the other (B) had been heated (675K; 10h)

under a flowing atmosphere of oxygen.

During EGA both samples yielded H_2O, CO_2 and NO (Figure 3.8), as well as trace amounts of NO_2. From the relative sizes of the peaks it is clear that the surface of sample B was much less contaminated with NO. It is also significant that, for sample A, a peak maximum for NO coincides with a maximum for CO_2. Coincident desorption generally indicates common surface species [50], but their nature is not immediately obvious in this case, and further investigation (e.g. by FTIR) will be necessary. The simultaneous desorption of CO_2 and H_2O (375-495K), from both samples, is easier to explain, because the proportions (after deducting the contribution from desorbing molecules of H_2O) suggest the dissociation of hydrogencarbonates

$$2HCO_3^- \text{ (surf)} \longrightarrow H_2O \text{ (g)} + 2CO_2 \text{ (g)} + O^{2-} \text{ (surf)} \quad (1)$$

Sample B yielded H_2O and CO_2 above its calcination temperature. The former is attributed to the desorption of surface hydroxyl species [51], whereas the CO_2 peak is very similar, in shape and position, to one observed after adsorbing $CO/CO_2/H_2$ on reduced Cu-Zn-O. This is believed to be due to the dissociation of carbonate species, which are readily formed on the surface of ZnO [52].

An important function of EGA is as means of determining when chemical stability of a catalyst surface is achieved. It is particularly effective for continuously monitoring the removal of the nitrogenous species, which can form inert nitrides during the reduction of a Cu-based catalysts and prevent the adsorption of CO [19].

EXPERIMENTAL

1 Materials

For the mass spectroscopic experiments Crosfield Chemicals catalysts EP30X, CS2066, EP55, EP355 and EP210 were used as supplied. Details are given in Table 3.1. However, due to industrial sensitivity not all the information on preparative conditions was available.

Table 3.1 *Metal loading and preparative details of the*
Crosfield catalysts

| Ref	Description	wt%	
EP10	Amorphous silica, $300m^2g^{-1}$		
EP30X	EP10 + chromium (III) acetate	Cr	1.00
CS2066	EP10 + TiO_2 + chromium (III) acetate	Cr	1.00
		Ti	2.50
EP55	EP10 + TiO_2 cogel	Ti	2.50
EP355	EP55 + chromium (III) acetate	Cr	1.05
		Ti	2.53
EP210	EP10 + aluminium alkyl + chromium (III) acetylacetonate	Cr	1.00
		Al	1.00

Note: + indicates addition by impregnation except for EP55,
which is obtained by coprecipitation.

Nitrogen and argon (oxygen free, 99%) and oxygen (99%)
were obtained from BOC and were all dried by passing
through concentrated sulphuric acid, followed by columns of
phosphorus pentoxide (May and Baker) and 4A molecular sieve
(Lancaster). The latter was frequently regenerated by
heating to 150°C *in vacuo* until no further water was
condensed into the cold trap. The gas handling system was
designed to allow this operation to be carried out *in situ*.

Figure 3.9 shows the apparatus used to carry out the
work reported in this chapter. All the equipment was
contained on a single moveable trolley and the uhv system
was kept continually running, with a base pressure of
$3x10^{-9}$ Torr. The gas drying system and the reactor were the
same as those described in Chapter 2 for the XPS
experiments.

The catalyst was heated in a flow of the appropriate gas,
which was then passed through the heated stainless steel
capillary, along with evolved gases from the catalyst
decomposition, and into the uhv system for analysis by the
quadrupole mass spectrometer. The capillary was kept as
short as possible in order to reduce the time lapse between
evolution and detection and to prevent reaction and
condensation prior to detection. To facilitate this the
capillary was heated using an electrically heated tape and
the temperature kept above 100°C at all times. The
capillary itself is 4/1000th inches in diameter and this
was further reduced by constriction with pliers to ensure
that the gas flow did not increase the pressure in the uhv
system beyond $5x10^{-6}$ Torr, which would damage the QMS.

Figure 3.9 A diagram of the apparatus used to study the Phillips catalysts by Evolved Gas Analysis and Quadrupole Mass Spectrometry
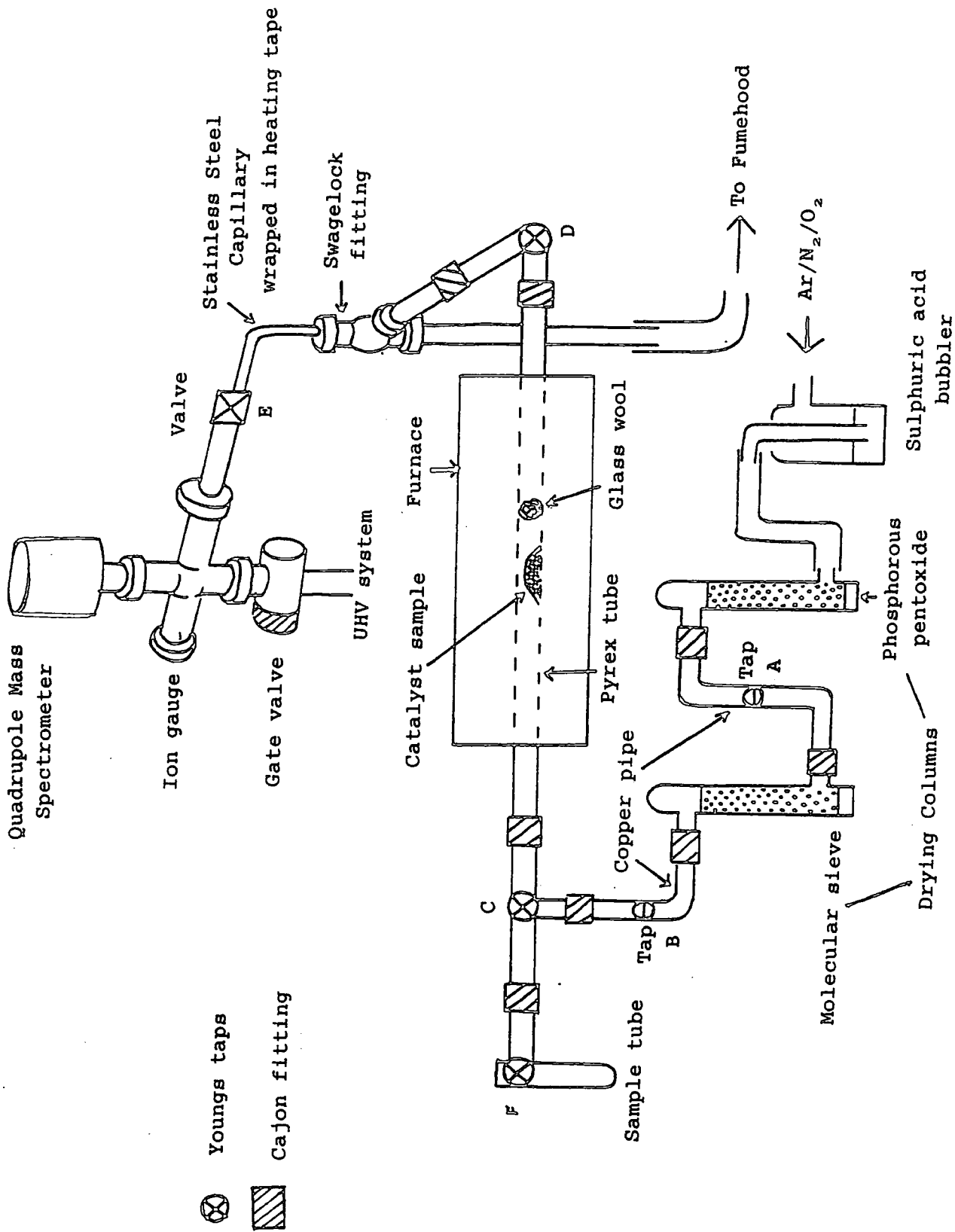
For each catalyst the experimental procedure was as follows. The reactor was assembled as described in Chapter 2 and dry gas allowed to flush the system by opening taps A, B, C and D in sequence (see Figure 3.9). A high flow rate was used initially to ensure the air is flushed from the system, and the outlet checked to ensure free flow of gas.

With the ion gauge turned off the valve E was slowly opened to allow gas to reach the mass spectrometer. When the ion gauge had settled a reading of the operating pressure of the system was obtained - usually in the region of $2x10^{-6}$ Torr.

The mass spectrometer and filament were then switched on; it was important to allow sufficient time for the filament to outgas and ensure the removal of the gases before use. The mass spectrometer was controlled by an IBM personal computer using the program QMSDEV [35]. This allowed spectra to be obtained over a range of masses and displayed in histogram form, and also allowed upto 50 selected masses to be studied in one experiment with the results displayed in graphical form.

Continual background spectra were run until peaks at m/e = 18, 28 and 44 ($[H_2O^+]$, $[N_2^+]$ and $[CO_2^+]$) were at their minimum intensity. When argon was the carrier gas the oxygen peak intensity was also monitored (m/z = 16, $[O^+]$ and m/z = 32 $[O_2^+]$). The calibration of the mass spectrometer was checked using a tune facility in the QMSDEV program prior to each experiment. The gas flow was then reduced to $1.5lh^{-1}$ and the background spectra monitored until the peaks at m/z = 18, 28 and 44 were stable and at a minimum (they do not disappear completely) and m/z = 32 has almost completely disappeared (with argon as carrier). The final intensities of these peaks were always noted prior to starting the catalyst studies.

Two types of experiment were carried out: (i) the decomposition studies using argon involved heating the catalyst at 1°C/min to 780°C, remaining at this temperature for 5 hours before cooling to room temperature at 1°C/min; (ii) the reactions occurring during activation in oxygen, using the same heating parameters, followed by heating under an argon flow. Note that the same catalyst is used, without exposure to air. With both types of experiment it was first necessary to collect the spectra over the mass range 0 - 80amu at time intervals of 5 minutes for the duration of the experiment. From the histogram display it is then possible to pick out the m/z values which have changes in intensity. The experiment is repeated using fresh catalyst, this time following the masses of interest during the whole experimental period. The computer program allows the individual masses to be run on different

147

amplifier gains in order to obtain the best sensitivity. Data analysis was then carried out on an Apple Macintosh computer.

On completion of the experiment valve E is closed (see Figure 3.9), followed by taps D and C. The gas supply was then disconnected. If required the catalyst can be tipped into a sample tube and sealed under argon by closing tap F. XPS can be carried out as described in Chapter 2, which provides information on the active catalyst surface.

RESULTS

1 Data handling

The mass spectral responses at the chosen mass numbers (m/z) were displayed graphically as a plot of intensity against time. 155 consecutive scans were taken, one every five minutes (corresponding to a 5°C rise in temperature) and plots of the consecutive responses within these scanning cycles allowed the desorption patterns for each mass number of interest to be followed during the course of the experiment.

The raw data was transferred to an Apple Macintosh computer for manipulation. For each mass of interest the background was subtracted, a correction made for the spectrometer gain, if different from that used for the carrier gas, and finally a ratio obtained of the intensity of this mass /the intensity of the mass of the carrier gas. This ratio was then plotted against temperature to obtain a desorption profile.

The background was taken as that at m/z = 21, chosen because no change in intensity was found experimentally for this particular value. The background was always obtained for each of the instrument gains used. It should be noted that actual intensity values as quoted in Tables 3.2 and 3.4 to 3.12 are obtained from the original mass spectral data, not after manipulation. These values are corrected for differences in the gains used. The values quoted are the intensities of the peak maxima, in arbitrary units. These values can be used semi-quantitatively, since the quadrupole mass spectrometer has an inverse relationship between sensitivity and mass resolution [2]. By choosing good mass resolution the sensitivity for each charge-to-mass ratio is lower.

An initial experiment was carried out using the apparatus without any catalyst, the quartz reactor tube containing just a glass wool plug, in order to establish that there is no desorption of gases from the apparatus on

heating and that subsequent results are due to "real" effects. The results of heating under argon are shown in Figure 3.10. These show that above 100°C there is no change in intensity for any m/z values. Below 100°C there are increases in intensity for m/z = 28 ([CO^+] or [N_2^+]) and m/z = 32 ([O_2^+]). There may be some desorption from the reactor and a rise and swift fall in the m/e = 32 trace is seen in other experiments. It can therefore be safely assumed that all changes in intensity observed above 100°C are due to decomposition and desorption from the catalysts.

2 <u>Studies of the heating of silica (EP10) under argon</u>

Figure 3.11 shows the changes in intensity of the m/z = 18 ([H_2O^+]) trace. This illustrates the typical pattern of dehydration and dehydroxylation of the silica surface as the temperature is raised:

< 400°C reversible
> 800°C irreversible
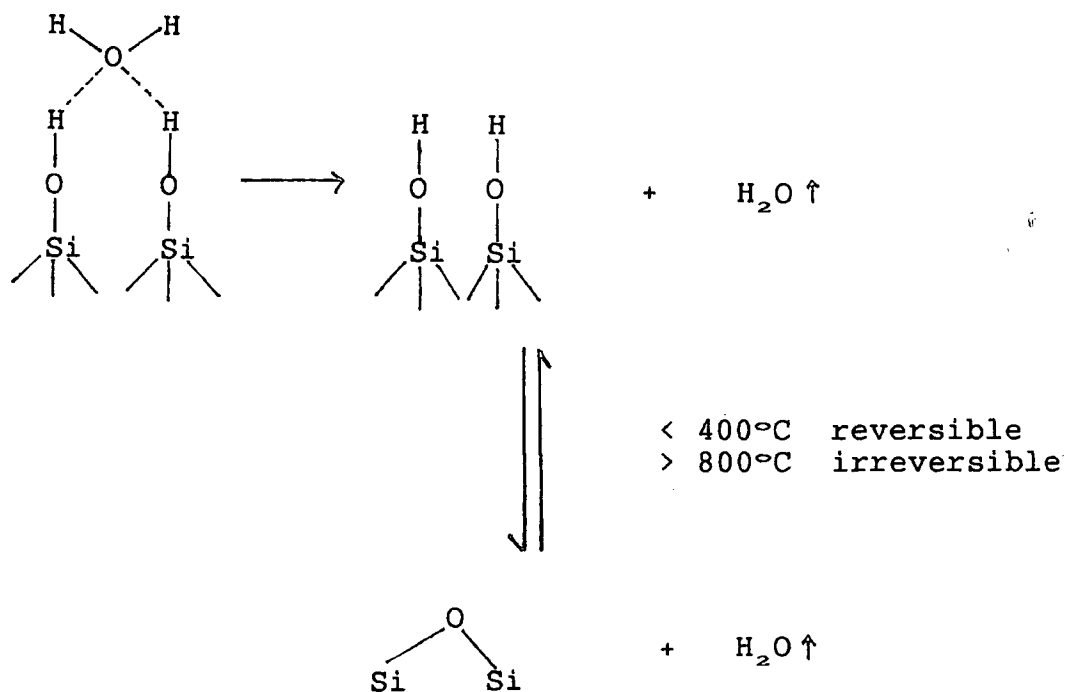
The m/z = 18 trace shows maxima at ca. 150 and ca. 475°C, the latter being a broad peak. The former peak corresponds mainly to the loss of physisorbed water, the latter to dehydroxylation, where neighbouring silanol groups are condensing to form additional oxo-bridges, which occurs over a much wider temperature range than the removal of adsorbed water.

Figure 3.10

A plot of intensity against temperature for ions having m/z = 18, 28, 32 and 44 when heating the empty reactor under argon
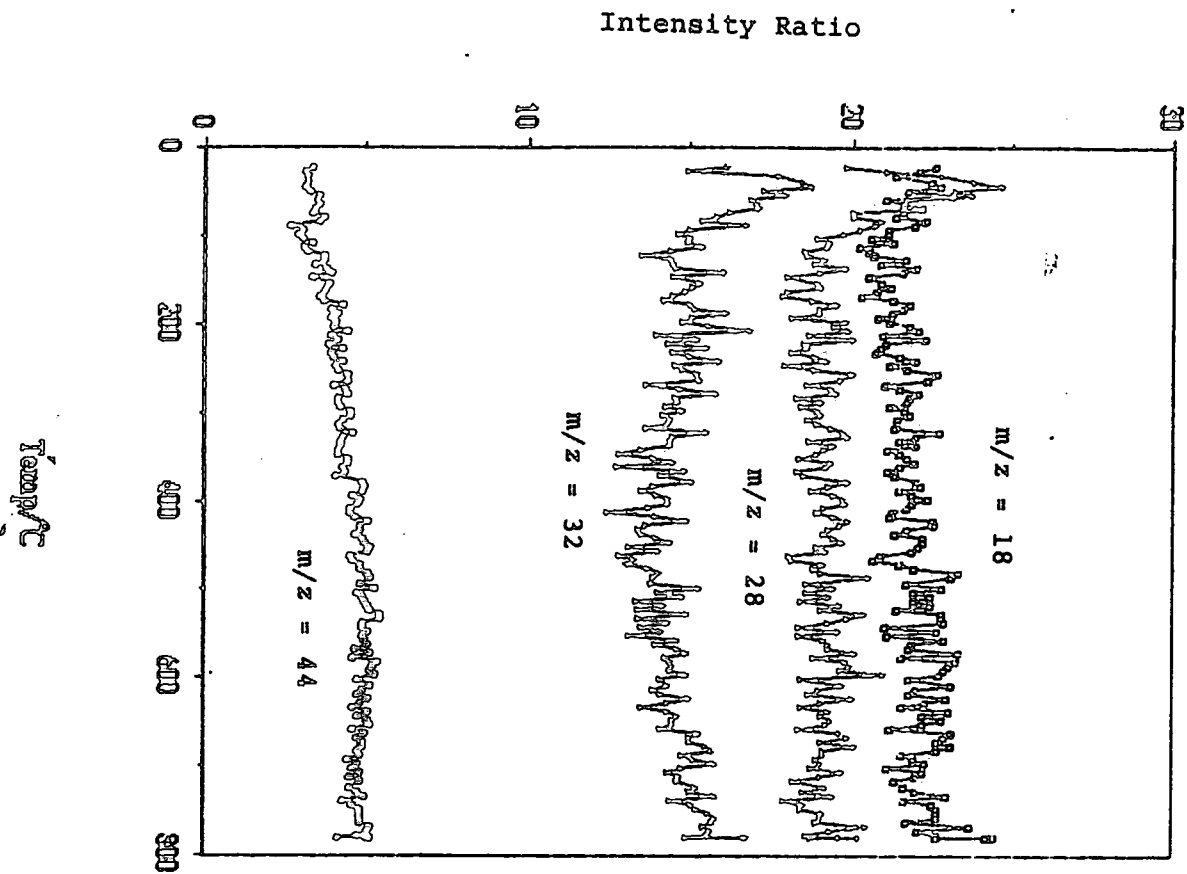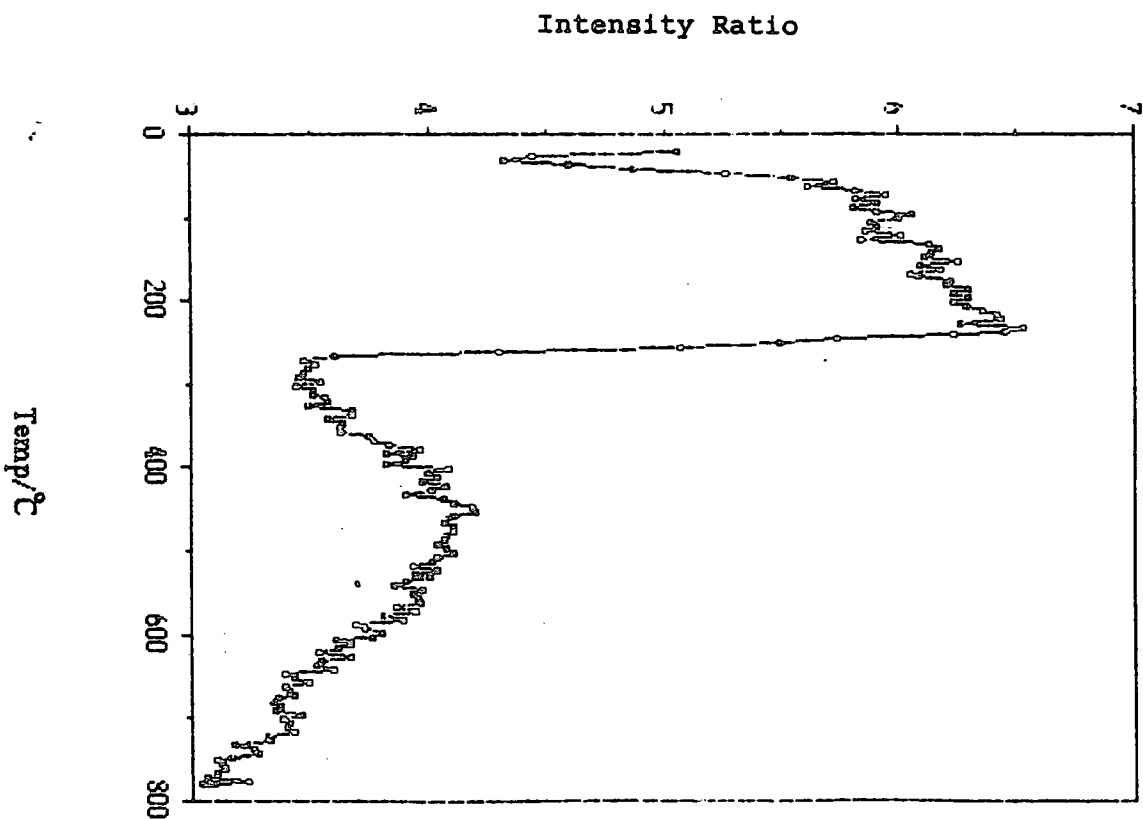

Figure 3.11

A plot of intensity against temperature for ions having m/z = 18 from silica heated under argon

3 <u>Studies of the heating of alumina (Degussa C) under argon</u>

   In general the alumina surface is dehydroxylated between 250 and 530°C [28] as indicated in Figure 3.12 which shows the changes in intensity of the water trace with increasing temperature. The loss of physisorbed water reaches a maximum at 150°C, with dehydroxylation occuring steadily upto 500°C.

4 <u>Studies of the heating of titania (Degussa P25) under argon</u>

   Surface dehydroxylation of titania is known to begin at 150°C and studies show that the greatest proportion of OH groups are removed from the surface at 300°C, with only a few isolated hydroxyls remaining at higher temperatures [28]:

```
   OH          OH          OH                          OH
    |           |           |            Δ              |
    |      H    |      H     |           ──→            |
 ──Ti──O──Ti──O──Ti──                  ──Ti──O──Ti──O──Ti──
```

This is reflected in Figure 3.13, which shows the change in intensity of the water trace with increasing temperature. Maxima for water loss occur at ca. 200°C, 300°C and 550°C, and even at 750°C loss of water continues, albeit at a lower rate.

Figure 3.12

A plot of intensity against temperature for ions having m/z = 18 from alumina heated under argon

Figure 3.13

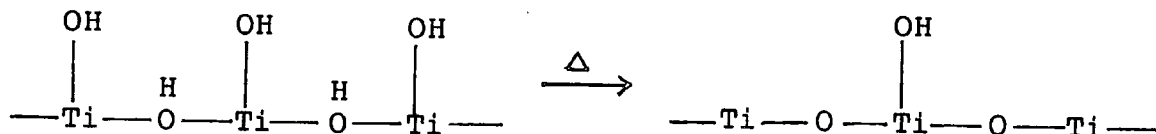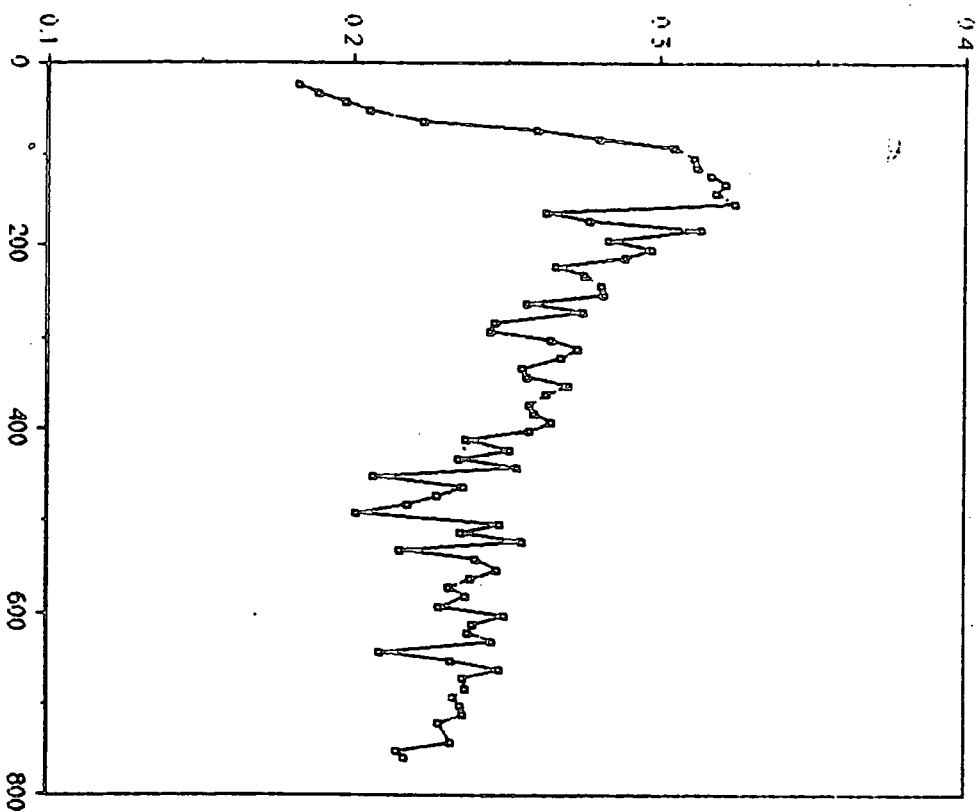A plot of intensity against temperature for ions having m/z = 18 from titania heated under argon

152
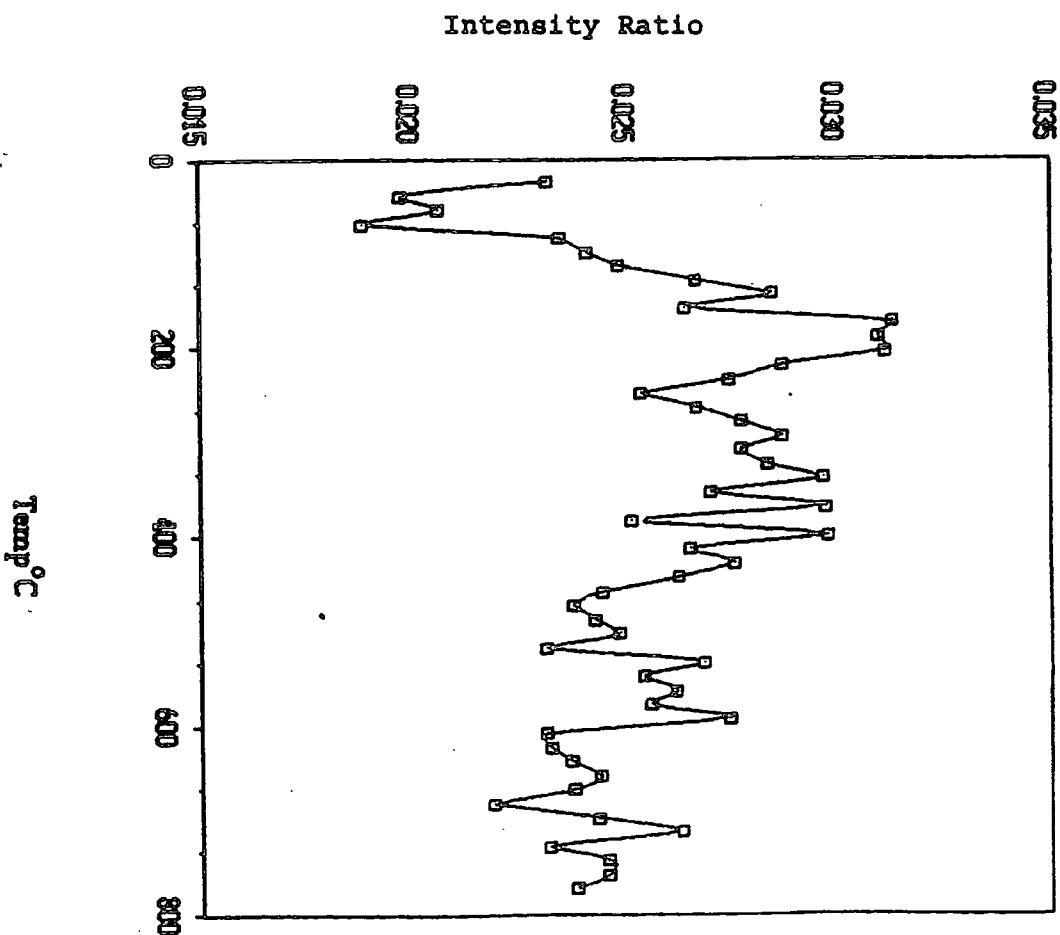
5 Studies of catalyst EP30X heated under argon

SiO$_2$/Cr (III) acetate   Cr 1.00%

The data for this experiment is contained in Table 3.2. The mass spectra are shown in Figures 3.15 to 3.28.

Table 3.2 *The temperatures at which ion m/z values reach a maximum intensity for catalyst EP30X heated under argon*

M/z (intensity)					Temperature/°C
18(139)					189
41(14)					335
29(13)					345
41(14)	42(7)				350
26(9)					360
42(8)					370
27(12)	29(13)				375
43(19)					380
13(27)	28(61)	29(13)			390
13(28)	14(37)	15(109)	16(93)	26(10)	400
28(60)	41(11)				
12(37)	27(12)	44(76)			406
13(11)					466
18(85)					582

Chromium (III) acetate is found as the neutral complex with three acetate groups bound to one central chromium atom, and also as a basic oxo-centred trinuclear complex. The structure of one such trinuclear complex is shown in Figure 4.12. It has been shown by IR that when basic chromium (III) acetate binds to silica it has the trimeric structure [30,32].

Figure 3.14 *Structure of [Cr$_3$O(O$_2$CH$_3$)$_6$(H$_2$O)$_3$]$^+$*
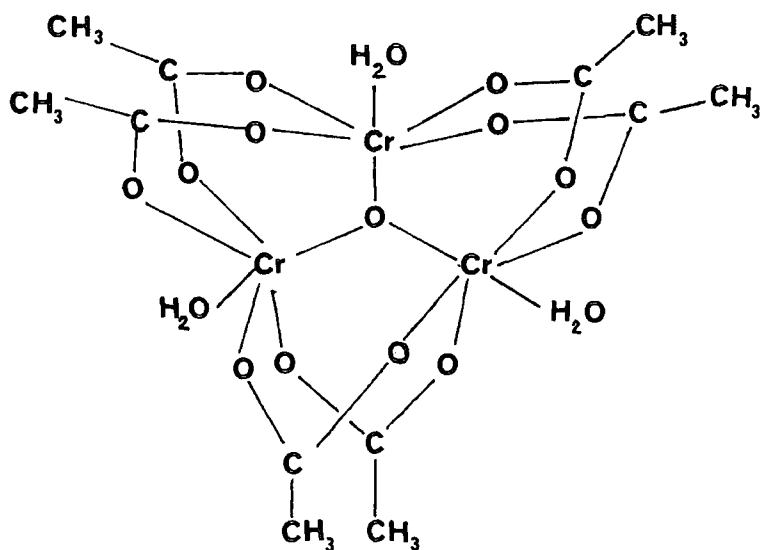
Grotowska *et al* [29] have studied the thermal decomposition of chromium (III) acetate salts under argon and air using simultaneous TG/DTG/DTA and a mechanism was proposed for the decomposition.

For $Cr(CH_3COO)_3.2H_2O$ under argon three steps were assigned:

1 353-480K $Cr(CH_3COO)_3.2H_2O \longrightarrow Cr(CH_3COO)_3 + 2H_2O$
2 598-781K $Cr(CH_3COO)_3 \longrightarrow Cr_2O_3.xCO_2 + C + CO + H_2O$
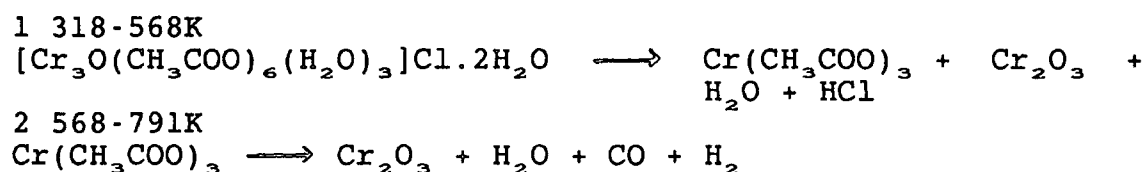3 781-883K $Cr_2O_3.xCO_2 \longrightarrow Cr_2O_3 + CO_2$
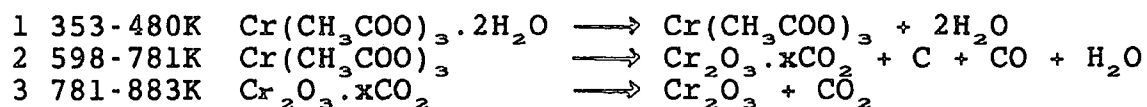
Evidence to substantiate the claim for $Cr_2O_3.xCO_2$ is presented by Meloche and Kalbus [53], although the known coordination of CO_2 requires the metal to be an electron rich centre. Alternatively carbonate groups may be formed on the decomposition, as found for other carboxylates [12, 37].

For $[Cr_3O(CH_3COO)_6(H_2O)_3]Cl.2H_2O$ two stages were as follows:

1 318-568K
$[Cr_3O(CH_3COO)_6(H_2O)_3]Cl.2H_2O \longrightarrow Cr(CH_3COO)_3 + Cr_2O_3 + H_2O + HCl$
2 568-791K
$Cr(CH_3COO)_3 \longrightarrow Cr_2O_3 + H_2O + CO + H_2$

The fragments obtained in the mass spectrum were assigned having due consideration of the chromium (III) acetate structure and are shown in Table 3.3.

Table 3.3   Assignments of fragments found in the mass spectra of EP30X during heating under argon

m/z	Proposed Assignment
44	$[CO_2^+]$; $[C_2H_4O^+]$ $([H_3C-C≡O^+])$ H
43	$[C_2H_3O^+]$ $([H_3C-C≡O^+])$
42	$[C_2H_2O^+]$ $([H_2C=C=O^+])$
41	$[C_2HO^+]$ $([HC≡C=O^+])$
29	$[CHO^+]$ $([HC=O^+])$ or $[C_2H_5^+]$
28	$[CO^+]$; $[C_2H_4^+]$
27	$[C_2H_3^+]$
26	$[C_2H_2^+]$
18	$[H_2O^+]$
16	$[O^+]$, $[CH_4^+]$
15	$[CH_3^+]$
14	$[CH_2^+]$
13	$[CH^+]$
12	$[C^+]$

The data of Table 3.2 show that the first step on

154

heating is loss of water (intense peak centred at 189°C), which is physisorbed on the catalyst surface.

Decomposition of the acetate ligands begins at around 330°C, though the major decomposition occurs between 390 and 410°C, where the most intense fragment peaks are found. Above 410°C conversion to the oxide appears to be complete, the colour change from grey to green suggesting Cr_2O_3 is the final product, the most stable of the chromium oxides [31].

There are low intensity peaks of m/z = 41, 29 and 42 between 330 and 390°C, which correspond to the loss of a $[CH_3C=O^+]$ grouping and its subsquent fragmentation, leaving possibly Cr_2O_3 and also $Cr(O_2CCH_3)_3$. At 390°C there is a relatively intense peak having m/z = 28 which is assigned to $[CO^+]$ or $[C_2H_4^+]$ arising from acetate decomposition. A very intense peak, m/z = 15, is observed at 400°C, together with other low m/z value peaks arising from $[CH_n^+]$ (n = 0-3) fragments. The intense peak, m/z = 44, at 406°C could be assigned to $[CO_2^+]$ or $[H_3CCH=O^+]$, but it would seem more likely to be $[CO_2^+]$ since the $[H_3CCH=O^+]$ group would fragment further and such fragments at lower m/z value are not observed. Grotowska et al [29] put forward $Cr_2O_3.xCO_2$ as an intermediate in the decomposition of $Cr(O_2CH_3)_3$, but not in that of $[Cr_3O(CH_3COO)_6]$ species. It is possible that this kind of complex could be formed having cleaved the Cr_3 structure and formed some Cr_2O_3. Subsequent decomposition would, of course, release CO_2. However, such a complex is unlikely due to the low thermal stability of carbon dioxide complexes (especially true at these temperatures) and the fact that they do not form with metals in this oxidation state. Thus it is more likely to be a carbonate that is obtained, which will also release carbon dioxide on decomposition. Thus by this temperature it appears that the acetate precursor has decomposed completely to yield the oxide.

Finally, a second peak maximum for water is observed, a quite broad peak centred at 582°C, which corresponds to the dehydroxylation of the silica surface (cf. silica alone, maximum intensity found at ca. 450°C).

A simple decomposition route is outlined below:

(1) $SiO_2/Cr_3O(CH_3COO)_6xH_2O \longrightarrow SiO_2/Cr_3O(CH_3COO)_6 + xH_2O\uparrow$

(2) $SiO_2/Cr_3O(CH_3COO)_6 \longrightarrow SiO_2/Cr(CH_3COO)_3 + SiO_2/Cr_2(CO_3)_3$
$+ [CH_3C=O^+]\uparrow$

(3) $SiO_2/Cr(CH_3COO)_3 \longrightarrow SiO_2/Cr_2O_3$
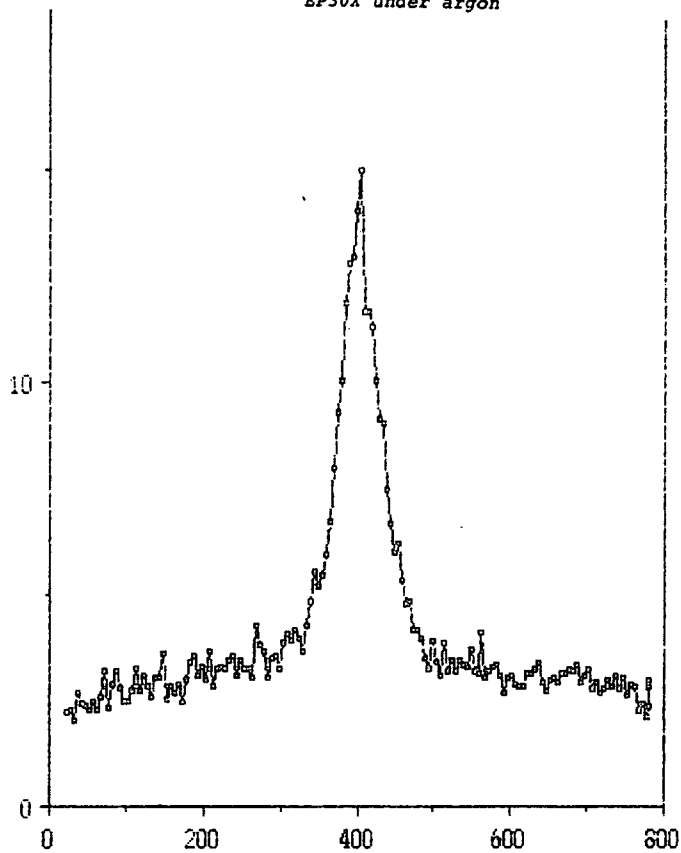$SiO_2/Cr_2(CO_3)_3 \longrightarrow SiO_2/Cr_2O_3 + CO_2\uparrow$

Figure 3.15 A plot of intensity against temperature for
ions having m/z = 12 from heating catalyst
EP30X under argon

Figure 3.16 A plot of intensity against temperature for
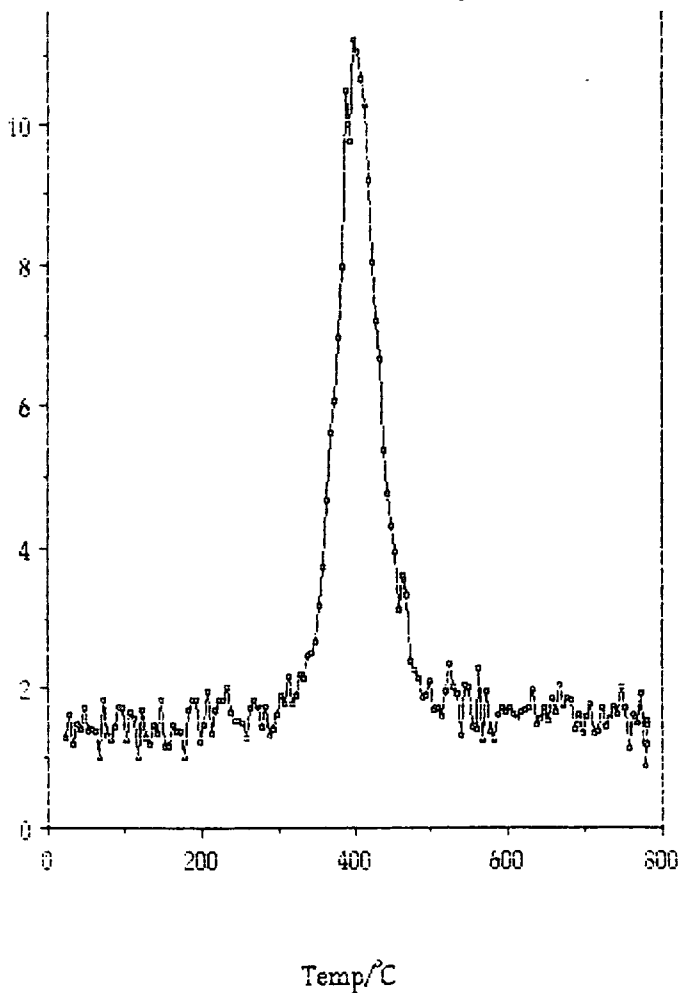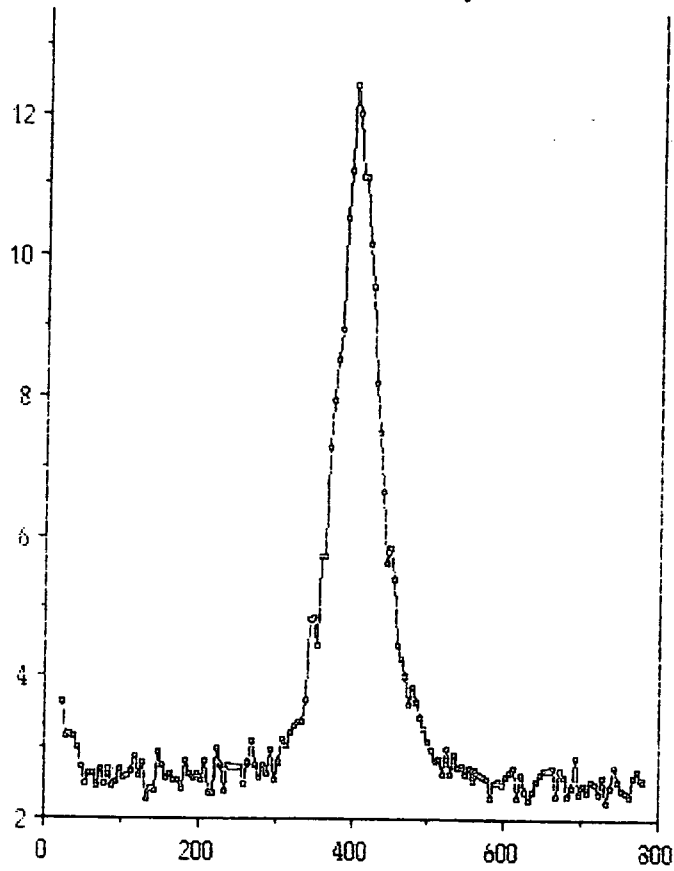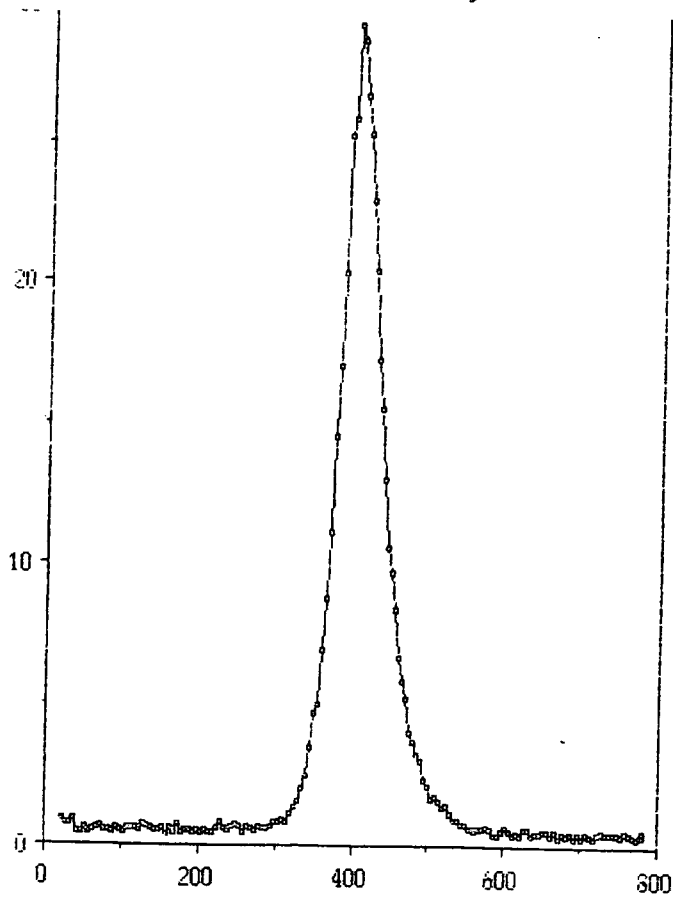ions having m/z = 13 from heating catalyst
EP30X under argon

Temp/°C

Figure 3.17 A plot of intensity against temperature for
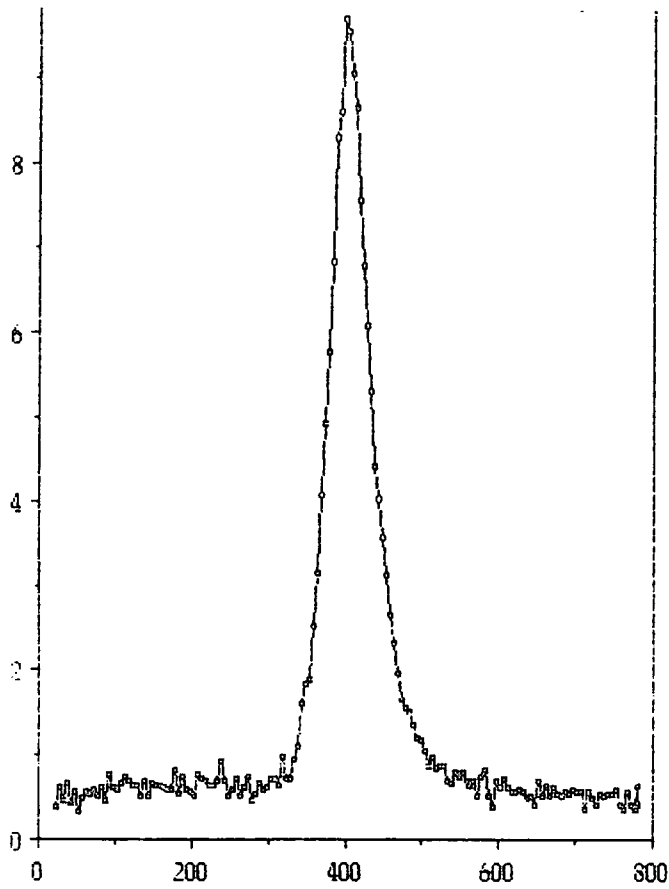ions having m/z = 14 from heating catalyst
EP30X under argon

Figure 3.17 A plot of intensity against temperature for ions having m/z = 14 from heating catalyst EP30X under argon

Figure 3.18 A plot of intensity against temperature for ions having m/z = 15 from heating catalyst EP30X under argon

Temp/°C

Figure 3.19 A plot of intensity against temperature for ions having m/z = 16 from heating catalyst EP30X under argon

Figure 3.20 A plot of intensity against temperature for ions having m/z = 18 from heating catalyst EP30X under argon
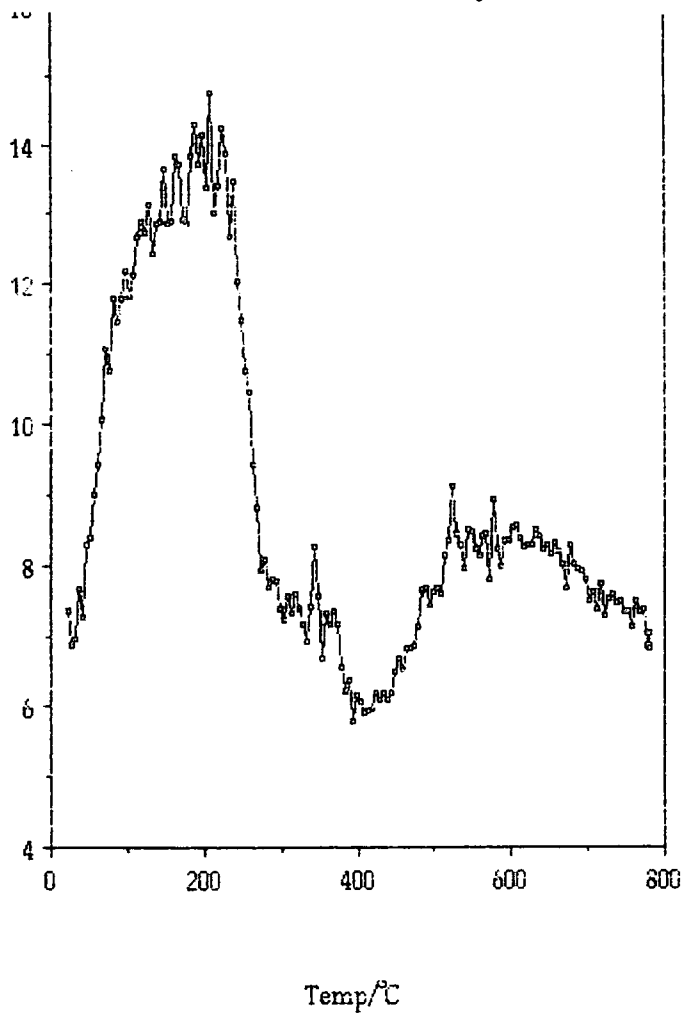
Temp/°C

Figure 3.21 A plot of intensity against temperature for
ions having m/z = 26 from heating catalyst
EP30X under argon

Figure 3.22 A plot of intensity against temperature for
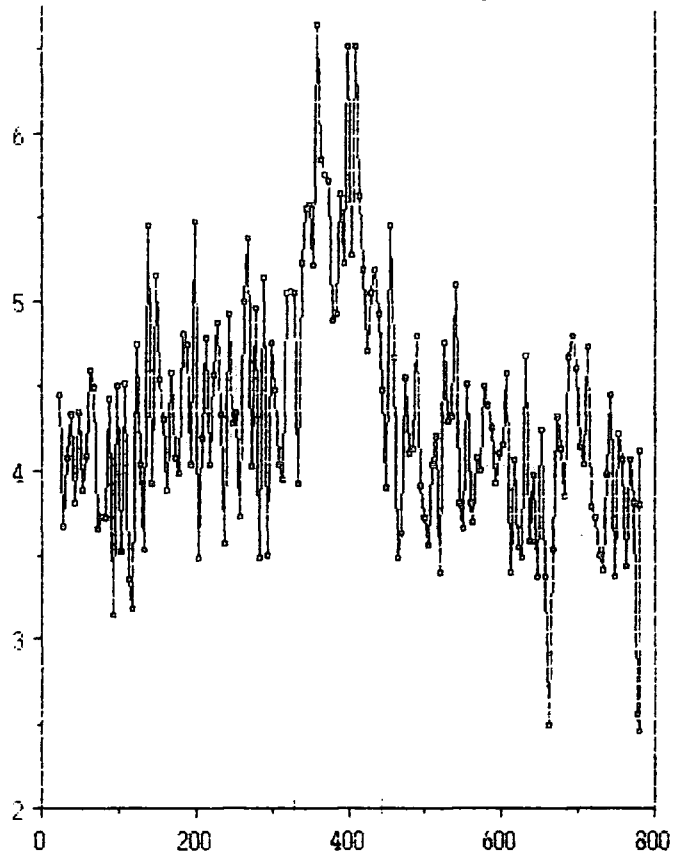ions having m/z = 27 from heating catalyst
EP30X under argon

Temp/°C

159

Figure 3.23 *A plot of intensity against temperature for ions having m/z = 28 from heating catalyst EP30X under argon*

Figure 3.24 *A plot of intensity against temperature for ions having m/z = 29 from heating catalyst EP30X under argon*
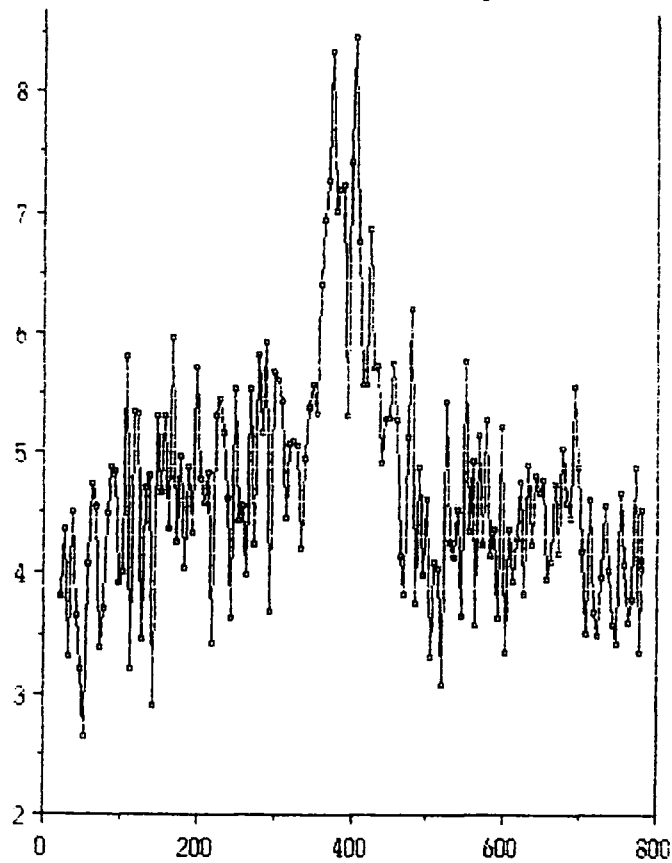
Temp/°C

Figure 3.25 A plot of intensity against temperature for ions having m/z = 41 from heating catalyst EP30X under argon

Figure 3.26 A plot of intensity against temperature for ions having m/z = 42 from heating catalyst EP30X under argon

Temp/°C

161

Figure 3.27 A plot of intensity against temperature for ions having m/z = 43 from heating catalyst EP30X under argon
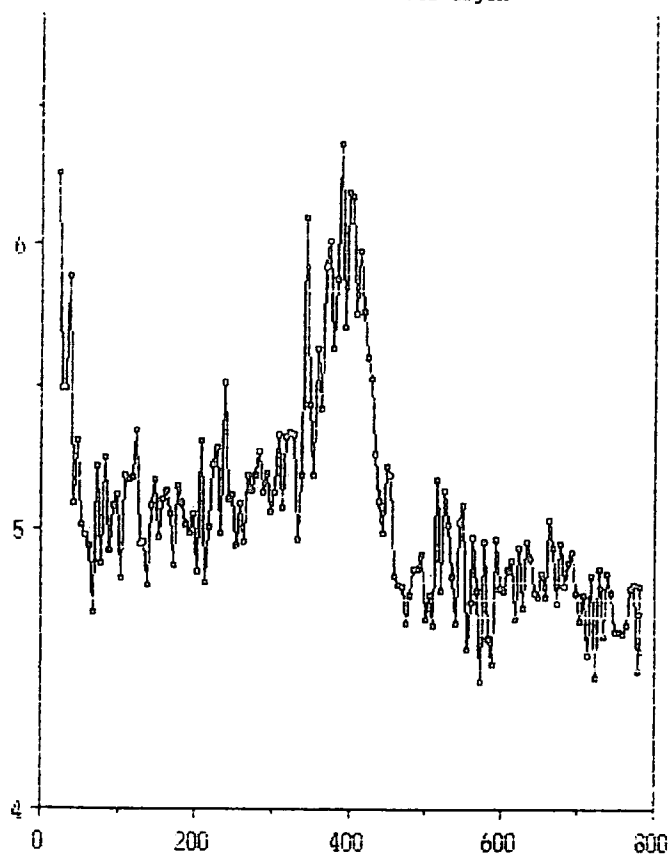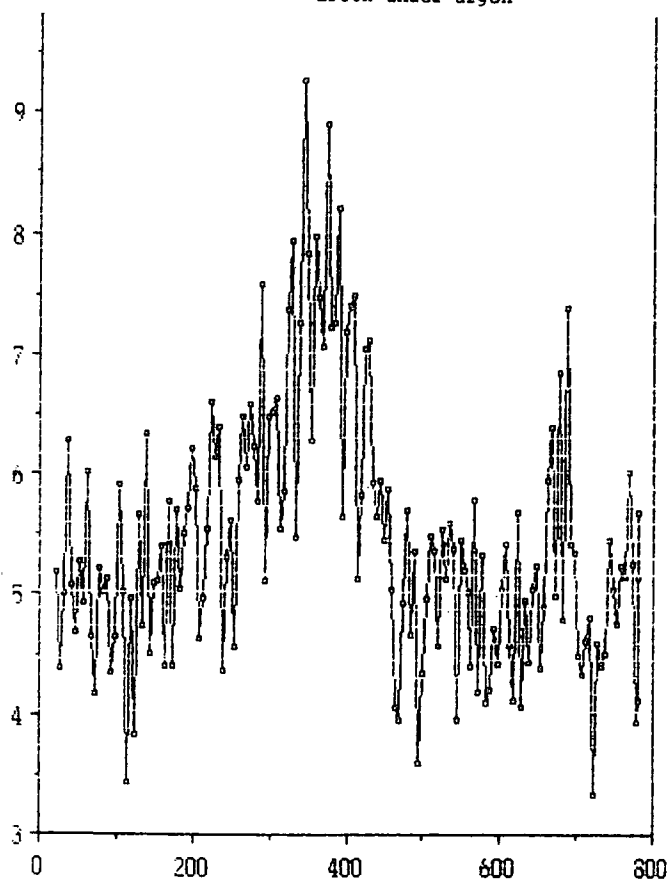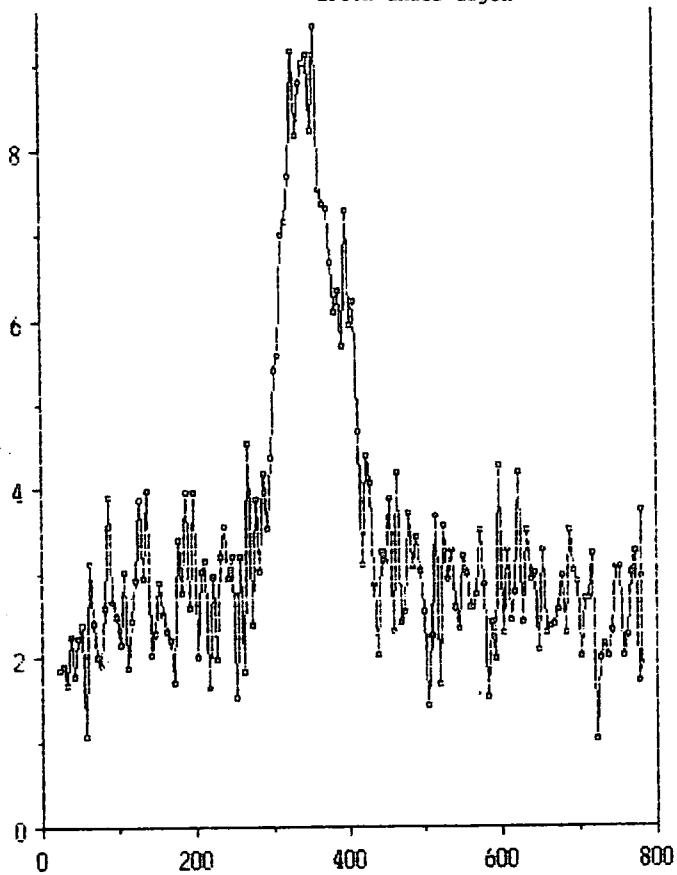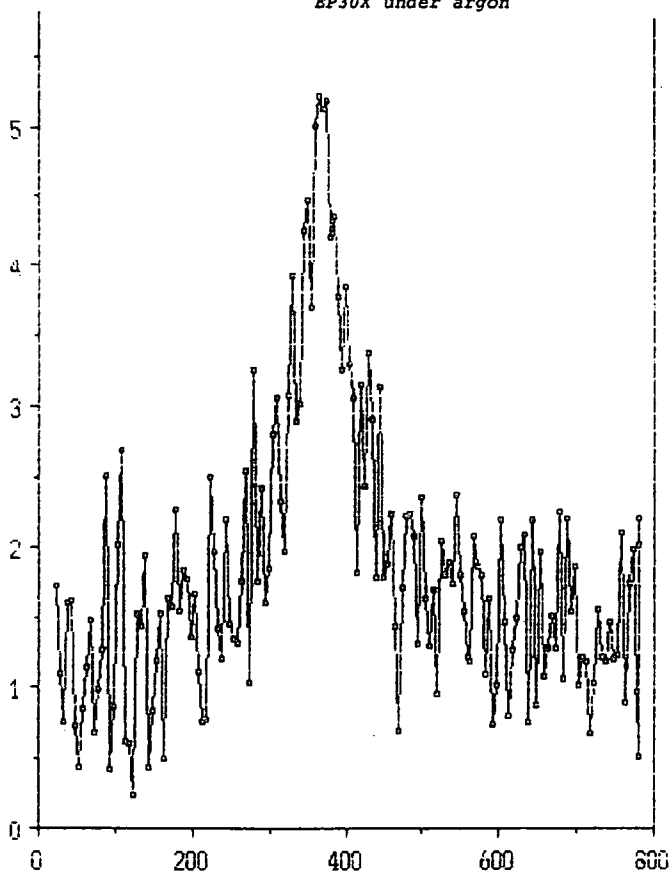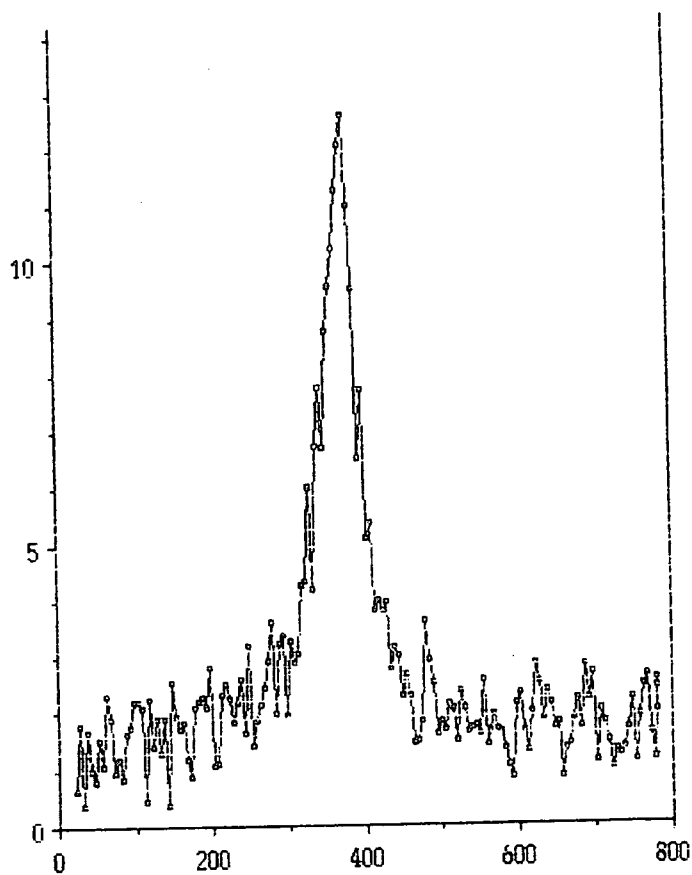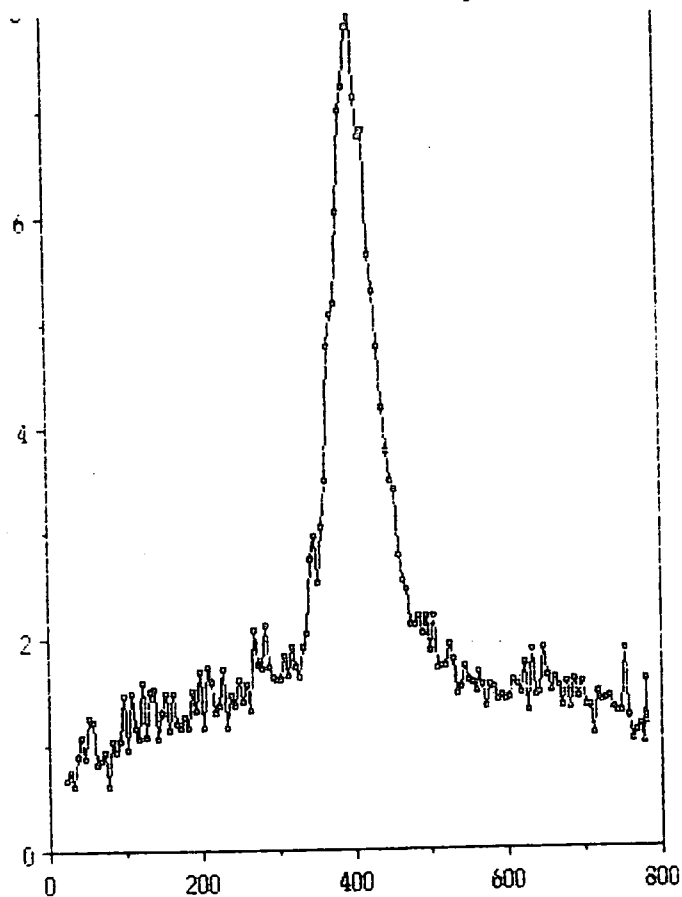

Figure 3.28 A plot of intensity against temperature for ions having m/z = 44 from heating catalyst EP30X under argon

Temp/°C

162

6 Studies of catalyst CS2066 heated under argon

$SiO_2/TiO_2/Cr$ (III) acetate   Ti 2.50%   Cr 1.00%

The data for this experiment is contained in Table 3.4.

Table 3.4   *The temperatures at which ion m/z values reach a maximum intensity for catalyst CS2066 heated under argon*

M/z (intensity)				Temperature/°C
26(7)	29(12)			110
27(9)	42(5)	43(12)		115
18(88)				125
42(31)				216
29(22)				220
15(44)	29(21)			286
13(21)	14(23)	43(109)	57(73)	291
26(20)				296
12(24)				301
27(34)				306
27(32)	41(51)			316
18(70)				371
44(60)				376
12(29)				386
27(40)				401
28(84)				406
14(16)				412
13(19)				427
15(34)	16(45)			432
42(17)				452
26(19)				472
26(17)				512
18(75)				623

It is immediately apparent that the decomposition is more complicated than for EP30X, and is spread over a wider temperature range. The peak assignments are made as for EP30X above.

There is a small amount of decomposition between 110-115°C giving peaks of low intensity. The values of m/z = 26,29,27,42 and 43 suggests a hydrocarbon/C=O fragment such as a ketone or aldehyde [7], and loss at such a low temperature suggest that the peaks arise from a solvent used in catalyst preparation, rather than any premature acetate group decomposition. Hill and Ohlmann [22] reported adsorption of organics on CrO_3/SiO_2 catalysts during storage, which is also a possible source of these fragments.

The loss of water occurs in three stages, at 125, 371

and 623°C. At 125°C the loss is physisorbed water from the catalyst surface, whereas at 623°C it is due to dehydroxylation of the support, the maximum intensity of the dehydroxylation occuring some 40°C higher than for EP30X. At 371°C the broad peak is attributed to loss of water from the acetate fragments as well as to dehydroxylation of titania.

The main decomposition of acetate occurs in the region 286-316°C, with a second region spread over a wider temperature range, 376-512°C. This may be compared with the compact region for EP30X, at 390-410°C. The addition of titania therefore promotes acetate decomposition and also provides a different route to the oxide. The colour change from dark green to black is suggestive of the formation of CrO_2, an oxide which is normally an intermediate in the decomposition of CrO_3 to Cr_2O_3. It is unlikely that CrO_3 is formed first here since this would require an oxidizing environment which does not occur under such conditions, and for similar reasons Cr (IV) also seems unlikely. The effect of the titania promoter could be structural, but an electronic effect seems more likely, especially in the light of XPS experiments which show increases in the binding energies of both promoter metal and chromium on activation.

In the 286-316°C region the very intense peak, m/z = 43, can be attributed to $[H_3C-C=O^+]$ derived from the acetate ligand. Similarly, $[HC=C=O^+]$ can be assigned to m/z = 41 and $[HC=O^+]$ to m/z = 29, but the remaining peaks (m/z = 27,26,15,14,13,12) indicate mainly hydrocarbon fragments. The peak having m/z = 57 is very intense, but this again is typical of a hydrocarbon fragment $[C_4H_9^+]$ [33], though its origin is unclear. If this temperature region involves mainly loss of hydrocarbon fragments then what remains is a

Cr-O
        \
         \C   grouping from which CO_2 (m/z = 44) can be lost.
        /
Cr-O

Alternatively the m/z = 44 peak could also represent the loss of the acetate-derived species $[H_3CCH=O^+]$, which may then give rise to fragments of m/z = 28, 27, 26, 16, 15, 14, 13 and 12. The mechanism of decomposition may then be similar to that of EP30X, with the loss of hydrocarbon fragments leading to a chromium oxide, which is stabilized by the titania promoter, and some acetate groups remaining in the complex $Cr(O_2CCH_3)_3$. These acetate groups then decompose at a higher temperature to give the chromium oxide alone.

7 Studies of catalyst EP55 heated under argon

SiO_2/TiO_2 cogel   Ti 2.50%

The data for this experiment is contained in Table 3.5

Table 3.5 *The temperatures at which ion m/z values reach a*
maximum intensity for catalyst EP55 heated
under argon

M/z (intensity)		Temperature/°C
44(27)		126
14(26)	18(234)	131
16(45)	28(198)	136
14(24)		144
44(22)		151
28(137)		327
18(84)		558

The most intense peak detected is that of water. With the cogel preparation leading to much of the titania being dispersed in the bulk of the silica and only a small dispersion at the surface, it is expected that loss of water is mainly from the bulk silica support. Observed changes are consistent with these expectations. There are two distinct peaks in the plot with maxima at 131°C (physisorbed water) and 558°C (dehydroxylation). It is noted that dehydroxylation is suppressed compared with silica alone, and the peak maximum is shifted to higher temperature.

The plot for carbon monoxide (m/z = 28) consists of a sharp peak with a maximum at 136°C and a broader peak centred at 327°C. This fragment was assigned to $[CO^+]$ rather than $[C_2H_4^+]$ since the latter normally also has fragments with m/z = 27 and 26, which were not observed. M/z = 44 was assigned to $[CO_2^+]$, m/z = 16 to $[O^+]$ (fragment of CO and H_2O) and m/z =14 to $[CH_2^+]$. These fragments may arise from surface contaminants (eg. residual solvents from industrial preparation).

There is no colour change after heating.

8 Studies of catalyst EP355 heated under argon

SiO_2/TiO_2 cogel/ chromium (III) acetate   Ti 2.53% Cr 1.05%

The data for this experiment is contained in Table 3.6.

Table 3.6   *The temperatures at which ion m/z values reach a maximum intensity for catalyst EP355 heated under argon*

M/z (intensity)	Temperature/°C
15(27) 18(132) 26(16) 27(28)	138
28(84) 29(43) 43(85) 57(8)	
14(29)	143
13(20) 42(26)	148
14(39) 28(92)	203
12(29)	208
42(32)	218
12(28) 13(28) 14(39) 28(95) 44(29)	223
15(42)	228
29(20)	238
43(87)	248
13(25) 27(21)	259
12(28) 57(60)	269
41(66)	274
12(29) 15(43) 27(23) 42(25) 43(83)	279
14(29)	284
26(19) 27(23) 43(82)	294
57(59)	299
29(14)	349
27(33)	364
26(10)	374
27(34) 42(16)	379
12(49) 28(92)	399
44(98)	404
13(33) 41(30)	410
12(46) 14(26) 15(73) 16(91)	420
26(9)	535
18(94)	601

The decomposition of the acetate precursor to the oxide is more complex than that seen for EP30X or CS2066, though similarities with CS2066 are discernible, notably the wide temperature range of decomposition and the three separate regions between 130 and 150°C, 200 and 300°C and 350 and 420°C. Peak assignments are as for EP30X.

Loss of physisorbed water occurs at a maximum at 138°C and water loss due to dehydroxylation of the silica surface is greatest at 601°C. The peak profile is very similar to that of silica alone and to that found for CS2066. It is notable also that no "intermediate" peak was observed, as is found for CS2066, where this peak (371°C) was, in part, attributed to dehydroxylation of titania. EP355 is prepared by impregnating the cogel EP55 with the chromium (III) salt and XPS has revealed that coprecipitation leads to a much lower surface dispersion of titania: the value for the titania dispersion was found to be 0.12 compared to 0.25

for CS2066. Thus it is unlikely that the dehydration of surface titania will be significant compared to that of silica.

There are intense peaks of m/z = 43 and 28 also having maximum intensity at 138°C. Because of their intensity they are thought to be due to decomposition of acetate groupings, m/z = 43 corresponding to the fragment [$H_3C-C=O^+$] and m/z = 28 to [CO^+] or [$C_2H_4^+$]. The less intense peaks of m/z = 42, 29, 27, 26, 15, 14 and 13 can also be linked to decomposition and fragmentation of the acetate ligand, representing both oxygenated (m/z = 42, 29) and hydrocarbon fragments. There is also a peak of small intensity (m/z = 57) which has been linked to a hydrocarbon fragment from solvent contamination and if this is correct, lower mass hydrocarbon peaks will also be detected from the solvent fragmentation. This temperature region (138-148°C) corresponds to the break up of the trimeric acetate structure (as put forward in the mechanism of decomposition for EP30X) which leads to formation of oxide. As with CS2066, the colour changes from grey to black after heating. Again, the addition of a titania promoter seems to stabilize this product. A lower dispersion leads to acetate decomposition at a lower temperature. The initial region of decomposition falls within the temperature range observed by Grotowska *et al* [29] for the same process using an unsupported chromium (III) acetate salt.

The same authors report a second temperature region, running from 295 to 518°C, where the remaining acetate groups are decomposed to leave the oxide. For EP355 further acetate decomposition begins below 200°C. There is an intense peak with m/z = 28 at 203°C and at 223°C which are assigned to [CO^+] or [$C_2H_4^+$]. The low m/z peaks (15-12) are attributed to [CH_n^+] (n = 0-3) fragments. The lack of fragments with m/z = 27 and 26 suggests that m/z = 28 is due to CO. A fragment having m/z = 42 ([$H_2C=C=O^+$]) is found at 218°C, together with further [CH_n^+] fragments. Acetate groups appear then to be lost in three stages with peaks having m/z = 43 ([$H_3C-C=O^+$]) at 248, 279 and 294°C and further fragmentation accounts for the presence of peaks having m/z = 42, 41, 29, 28 and 15-12. However, two relatively intense peak maxima are seen for m/z = 57. This has previously been assigned to a hydrocarbon fragment [7,33] though its origin is unclear. However, further fragmentation will lead to peaks with m/z = 28, 27, 26 and 16-12.

The final region of decomposition is similar to that of EP30X and CS2066 in terms of the ions detected and the temperatures at which they reach their maximum formation. By comparing the two catalysts m/z = 44 is assigned to [CO_2^+], possibly by loss from the
$$\begin{matrix} Cr-O \\ \quad \diagdown C \\ \quad \diagup \\ Cr-O \end{matrix}$$
unit
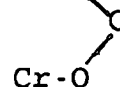
which remains after the loss of hydrocarbon fragments from acetate ligands (m/z = 27, 26) at slightly lower temperatures, or by loss from $Cr-O-\underset{O}{\overset{||}{C}}R \implies Cr-R$.

The presence of some residual acetate ligands is supported by the rather intense peaks at 410°C for m/z = 41, which corresponds to an [HC=C=O⁺] fragment.

9 Studies of catalyst EP210 heated under argon

SiO$_2$/aluminium alkyl/chromium (III) acetylacetonate
Al 1.00%   Cr 1.00%

The data for this experiment is contained in Table 3.7.

Table 3.7   *The temperatures at which ion m/z values reach a maximum intensity for the catalyst EP210 heated under argon*

M/z (intensity)	Temperature/°C
30(16)	128
32(68)	133
56(4)	188
18(181)	223
15(48)	313
56(5)	329
43(83)	334
14(62)	344
42(65)	364
56(6)	374
76(4)	379
50(7)	389
55(37)	405
44(114)	425
15(110) 16(142) 22(13)	425
12(52) 14(96)	430
28(88)	445
18(106)	661

The pattern of decomposition is much simpler than for the other catalysts, despite the fact that two decompositions are involved, that of the aluminium alkyl and that of the chromium salt. Note that it is chromium (III) acetylacetonate which is the precursor salt in this case.

Aluminium alkyls are very sensitive to moisture and therefore the preparative steps are presumed, in the

168

absence of information from Crosfields, to have been carried out in a dry organic solvent. The peak maximum intensities at 128°C (m/z = 30) and 133°C (m/z = 32) appear to be linked to fragmentation of residual solvent molecules since m/z = 30 corresponds to $[CH_2O^+]$, from an alcohol, aldehyde or ketone [7,33].

The maximum intensities for the water peak at 223 and 661°C correspond to loss of physisorbed water from the catalyst surface and dehydroxylation respectively. The latter is suppressed somewhat compared to silica alone and the maximum intensities for EP210 occur at higher temperatures than for the other catalysts studied.

The ions at m/z = 76, 56, 55 and 50 having low intensity peaks are assigned to hydrocarbon fragments of the aluminium alkyl. The m/z = 76 peak is thought to arise from a phenyl group but the other m/z values are linked with aliphatic fragments [33]. It is not thought that they arise from the acetylacetonate ligand because decomposition is likely to proceed via cleavage of the weaker single bonds, in this case C-O and C-C, rather than the multiple bonds of the acetylacetonate group. The peaks having m/z = 43, 42, 15 and 14 are associated with the fragments $[H_3C-C=O^+]$, $[H_2C=C=O^+]$, $[CH_3^+]$ and $[CH_2^+]$ respectively. There is a grouping of peaks between 420 and 445°C which result directly from acetylacetonate decomposition, for example, m/z = 44 $[CO_2^+]$, m/z = 12-15 $[CH_n^+]$ (n = 0-3), m/z = 16 ($[CH_4^+]$ or $[O^+]$) and m/z = 28 ($[CO^+]$). The colour change on heating from green to black indicates that the same form of chromium oxide is obtained as with catalysts EP30X and CS2066. Thus the promoters aluminium and titanium stabilize this oxide as opposed to EP30X, where Cr_2O_3 is the final product. It thus appears that addition of titanium and aluminium promoters have an electronic effect which modifies the chromium valence state in the final decomposition product.

10 Studies of catalyst EP30X heated under oxygen

SiO_2/Cr (III) acetate   Cr 1.00%

The data for this experiment is contained in Table 3.8.

Table 3.8 *The temperatures at which ion m/z values reach a*
maximum intensity for the catalyst EP30X heated
under oxygen

M/z (intensity)			Temperature/°C
18(381)	17(87)		178
27(16)			269
29(33)	30(19)		289
28(543)	45(12)	46(9)	294
12(51)	22(21)	44(592)	299
17(81)	18(358)		334

The oxidation of the acetate ligands leads to a much simpler pattern than the decomposition under argon, and the main oxidation reactions occur at lower temperatures, indeed below 300°C. The colour change is from grey to bright orange, due to formation of chromium (VI), probably as a di/chromate structure (by comparison with the XPS results). The trace obtained for water production is quite different from those seen previously (Figure 3.29). Two sharp peaks are obtained with maximum intensity at 178 and 334°C. The intensity of the latter peak then falls gradually over a further 200°C temperature span. This second peak arises due to oxidation of the acetate ligand producing water, together with dehydroxylation of the silica surface. These findings compare with the results of Kim and Woo [21] who found water peaks at 187, 377 and 447°C in a temperature-programmed oxidation study of chromium III acetate/silica catalysts.

The most intense peaks correspond to m/z = 28 ($[CO^+]$) and m/z = 44 ($[CO_2^+]$) at 294 and 299°C respectively, products of the oxidation of the acetate ligands. Kim and Woo [21] used the production of CO_2 as confirmation that the water peak at 377°C was indeed due to oxidation of the acetate group and the fact that CO_2 was observed first was explained by the interaction of the water produced with the catalyst. Ions at m/z = 12, 27 and 29 can be assigned to $[C^+]$, $[H_2C=CH^+]$ and $[HC=O^+]$, as noted above, and m/z = 30 to $[CH_2O^+]$, fragments of the acetate ligand. The origin of the ions having m/z = 45, 46 and 22 are not clear, though the ions at m/z = 45 and 46 have been assigned previously to an ether or alcohol [33]. An ether would appear to be the more likely, since fragments with m/z = 19 and 33 are also linked to alcohols [7].

Kim and Woo [21] also report the consumption of oxygen at 187°C without production of CO_2. The mechanism of this oxygen uptake is not fully understood, but it may be due to the partial oxidation of chromium (III) acetate. Cornet and Burwell have reported that a species of Cr (VI) is obtained by heating chromium (III) acetate in air at 140°C [56].

170

Figure 3.29
A plot of intensity against temperature for ions having m/z = 18 for catalyst EP30X heated under oxygen
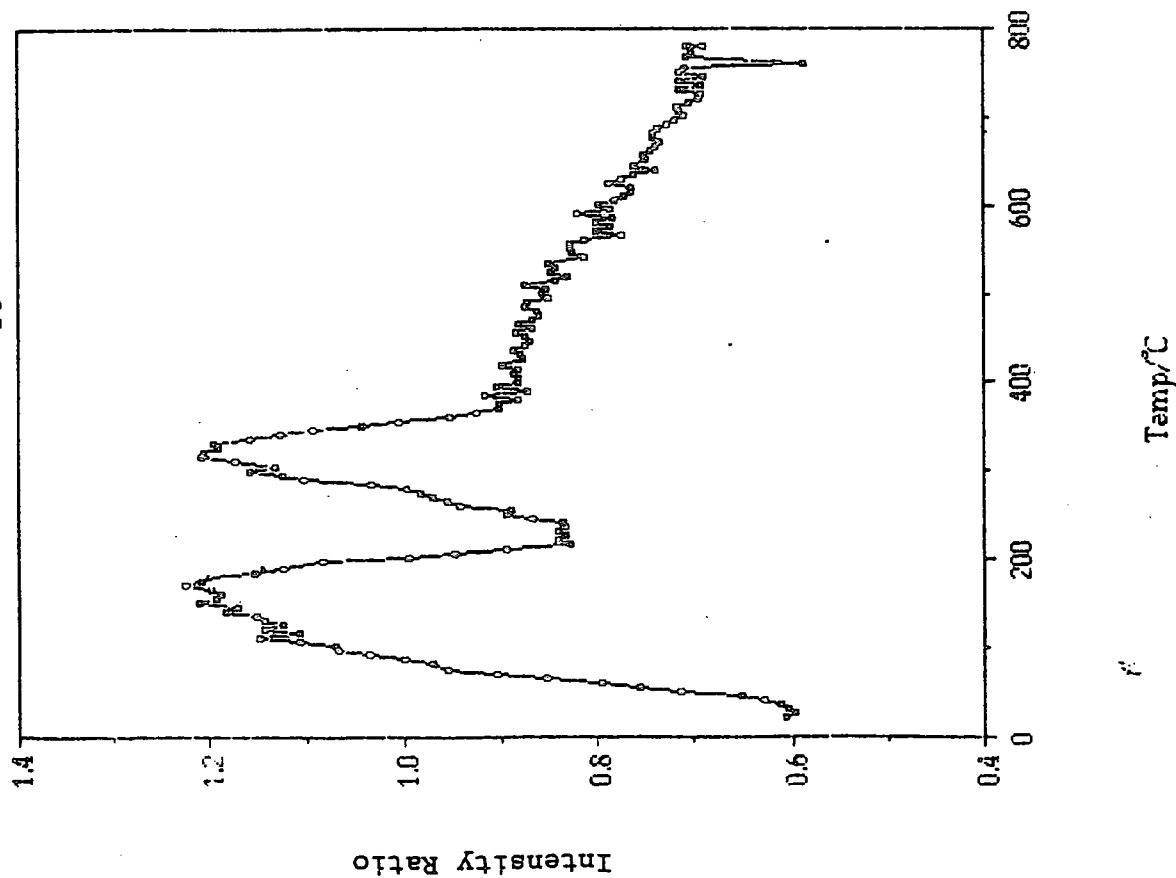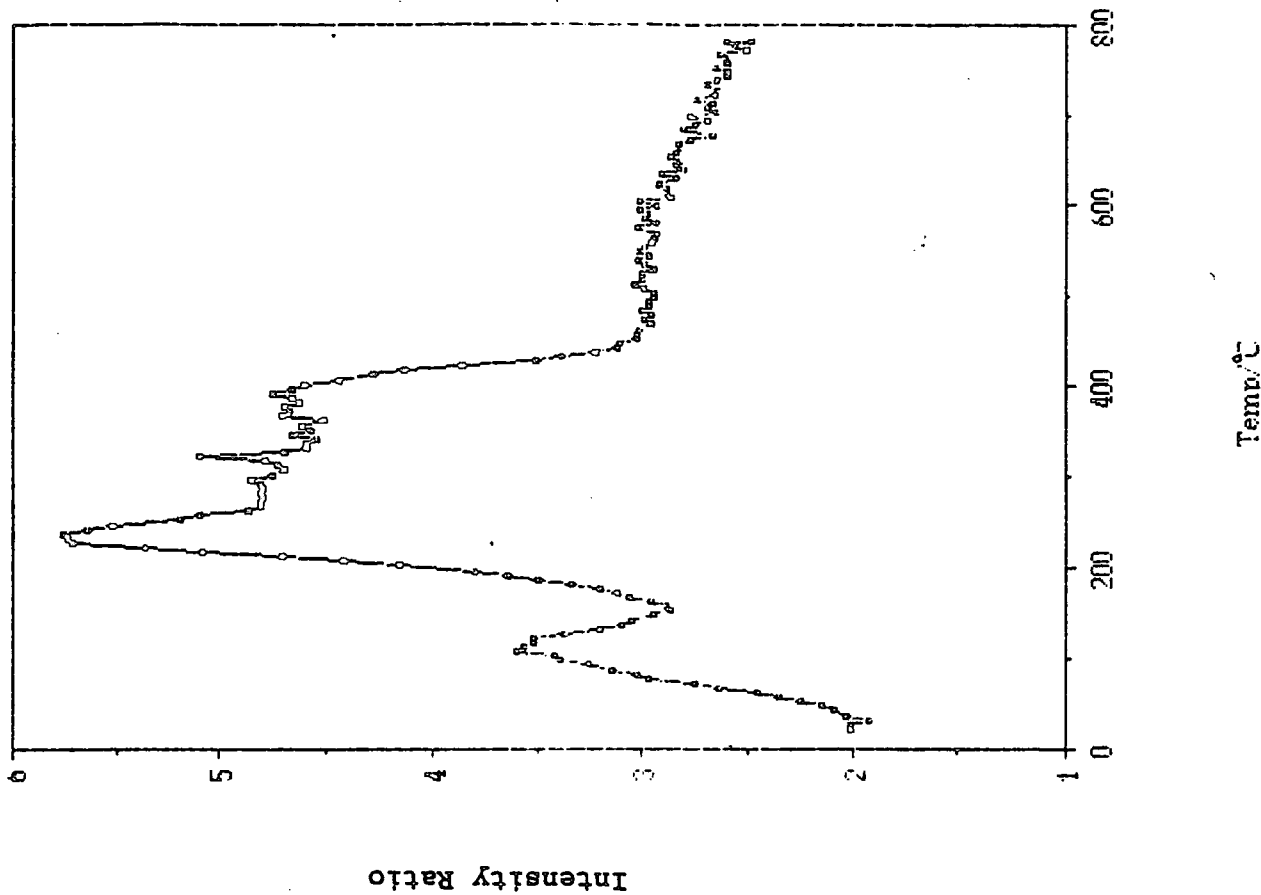

Figure 3.30
A plot of intensity against temperature for ions having m/z = 18 for catalyst CS2066 heated under oxygen

171

Therefore the authors suggest that one species of Cr (VI) was formed around 187°C and the other at 277-447°C. The colour changed from light green to yellow or orange after oxidation with air above 277°C. The amount of Cr (VI) reached a maximum at 550°C and decreased above this temperature. The decrease was mainly attributed to the thermal decomposition of chromium (VI) oxide and partly to the decrease in the support surface area.

Evidence from this study suggests the complete oxidation of chromium (III) acetate is occurring in a single stage over the temperature range 269-299°C.

After completion of this experiment the same catalyst sample was heated under argon using the same experimental conditions. There are no changes in the intensity of any of the m/z values, which indicates that there are no leaks in the system and no adsorption has occurred. There is a colour change, however, the bright orange colour of Cr^{VI} oxide becoming green, implying the formation of Cr_2O_3.

11 <u>Studies of catalyst CS2066 heated under oxygen</u>

SiO_2/TiO_2/chromium (III) acetate   Ti 2.50%   Cr 1.00%

The data for this experiment is contained in Table 3.9.

Table 3.9   *The temperatures at which ion m/z values reach a maximum intensity for the catalyst CS2066 heated under oxygen*

<u>M/z (intensity)</u>	<u>Temperature/°C</u>
43(14)	97
15(9) 29(25)	103
17(62) 27(8) 42(8)	108
18(265) 26(14) 45(25)	113
31(17)	118
46(13) 57(15)	223
14(34) 27(29) 30(60) 43(159) 45(66) 58(8)	228
12(72) 15(70) 18(418) 26(51) 28(637) 29(102) 31(30) 41(34) 42(58) 44(633)	233
30(60)	238
41(17)	304
12(105) 28(705) 44(1042) 45(52) 46(17)	324
17(80) 18(352)	399

The pattern of intensities is again simplyfied compared to heating under argon, but there are two main temperature

regions where reaction is occurring: 223-238°C and 304-324°C. The colour change is from dark green to bright orange, implying formation of chromium (VI) in the di/chromate structure.

The trace obtained for water is again quite different from that obtained for silica alone or for the same catalyst under argon (see Figure 3.30). The sharp peak having a maximum at 113°C corresponds to loss of physisorbed water, but there follows broad peaks with maxima at 233°C and 399°C, with a gradual decline in intensity from 400-780°C. This second peak corresponds, in part, to dehydroxylation of silica but also to formation of water in the oxidation of the acetate ligands.

The peaks of m/z = 43, 42, 29 and 15 have been associated with the acetate ligand in previous experiments, the ion at m/z = 43 corresponding to the fragment $[H_3C-C=O^+]$. Ions at m/z = 27 and 26 are associated with the hydrocarbon fragments $[H_2C=CH^+]$ and $[HC=CH^+]$. The origin of the ion having m/z = 45 is not clear, although it has been seen in the spectra from catalyst EP30X. It has been attributed to an ether and the presence of a peak with m/z = 31 assigned to $[HCHOH^+]$ has previously been used to confirm this [7,33]. However, the intensity of the peaks grouped in this temperature range (97-118°C) is low relative to those thought to arise from the main oxidation process.

There is a major concentration of peaks in the temperature range 223-238°C. The most intense are those due to $[CO^+]$ and $[CO_2^+]$ (m/z = 28, 44). The less intense peaks are associated with oxygenate groups: m/z = 43, 42, 41, 30, 29 are associated with acetate fragmentation, m/z = 58, 27, 26, 15, 14, 12 with hydrocarbon fragmentation, and m/z = 45 and 31 with alcohol or ether fragmentation.

At 324°C there is a second cluster of peaks, very intense $[CO^+]$ and $[CO_2^+]$ peaks, together with a small amount of carbon (m/z = 12) and ether or alcohol (m/z = 45, 46).

It thus appears that the two stage decomposition of acetate seen when the catalyst is heated under argon is also found under oxidation conditions, but the temperature ranges are much smaller. There may be partial oxidation of acetate initially, with some chromium (VI) being formed, with complete oxidation at the higher temperature. Kim and Woo [21] suggest two species of chromium (VI) are formed in the oxidation process.

After completion of this experiment the same catalyst sample was heated in argon. The results were as for EP30X: conversion to Cr_2O_3 was suspected as a light green colour

was observed following heating.

12 Studies of catalyst EP55 heated under oxygen

SiO_2/TiO_2 cogel   Ti 2.50%

The data for this experiment is contained in Table 3.10.

Table 3.10 *The temperatures at which ion m/z values reach a maximum intensity for the catalyst EP55 heated under oxygen*

M/z (intensity)	Temperature/°C
18(37) 28(44)	119
18(33)	134
28(44)	139
18(13)	621

Only two ions, m/z =18 and 28, showed changes in intensity with temperature. For water there are sharp peaks with maxima at 119 and 134°C, corresponding to loss of physisorbed water on the silica surface, and a much less intense peak centred at 621°C (dehydroxylation). The latter peak is much less intense than that seen for the studies of heating under argon, and the peak is shifted to higher temperature than under argon. M/z = 28 is again assigned to $[CO^+]$, arising from the oxidation of surface contamination, although it is not clear why m/z = 44 $[CO_2^+]$ is not also seen.

There is no colour change following heating.

After completion of this experiment the same catalyst sample was heated in argon. No changes were observed and there was no colour change following heating.

13 Studies of catalyst EP355 heated in oxygen

SiO_2/TiO_2 cogel/chromium (III) acetate   Ti 2.53% Cr 1.05%

The data for this experiment is contained in Table 3.11.

174

Table 3.11 *The temperatures at which ion m/z values reach a maximum intensity for the catalyst EP355 heated under oxygen*

M/z (intensity)	Temperature/°C
14(30) 28(385)	54
31(20)	135
14(55) 15(50) 44(284)	140
26(46) 27(54) 28(434) 29(204) 30(33) 42(14) 43(54) 45(49) 46(8)	145
17(85) 18(390)	150
12(38)	155
45(52)	230
12(85) 26(38) 27(46) 28(715) 44(769)	235
14(77) 15(93) 17(91) 18(418) 22(24) 29(264) 30(52) 31(23) 42(23) 43(71) 46(14)	240
26(16) 27(25)	306
12(133) 28(928) 29(101) 44(1312) 45(69) 46(23)	316
14(50) 22(41) 30(34)	321

Again the pattern of intensities is simplified compared to the experiment under argon. There are three very clearly defined regions of reaction, 135-155°C, 230-240°C and 306-321°C, similar to the results for catalyst CS2066. The colour change on heating is from grey to bright orange, implying that chromium (VI) is formed.

The peak maxima at 54°C are assigned to $[CO^+]$ (m/z = 28) and the carbon ion (m/z = 12), which probably arise from decomposition and oxidation of surface contaminants.

The oxidation of catalyst EP355 follows the same pattern as for catalyst CS2066. In the temperature region 135-155°C there is indication of a breakup of the acetate ligand with loss of fragments having m/z = 43, 42, 30, 29 and 15. The ions m/z = 27,26, 15, 14 are associated with hydrocarbon fragments, again originating from the acetate group, and m/z = 46, 45, 31 are linked to an ether or alcohol. Ions at m/z = 28 and 44 are assigned to $[CO^+]$ and $[CO_2^+]$ arising from oxidation of the acetate fragments. Between 230 and 240°C there is a similar decomposition and loss of acetate ligands.

The final temperature region occurs between 306 and 321°C where the $[CO^+]$ and $[CO_2^+]$ peaks are very intense. The less intense peaks are associated with oxygen-containing fragments $[CHO^+]$, $[CH_2O^+]$ (m/z = 29, 30), ether or alcohol (m/z = 46,45) and their associated hydrocarbon

Figure 3.31

A plot of intensity against temperature for ions having m/z = 18 for catalyst EP355 heated under oxygen
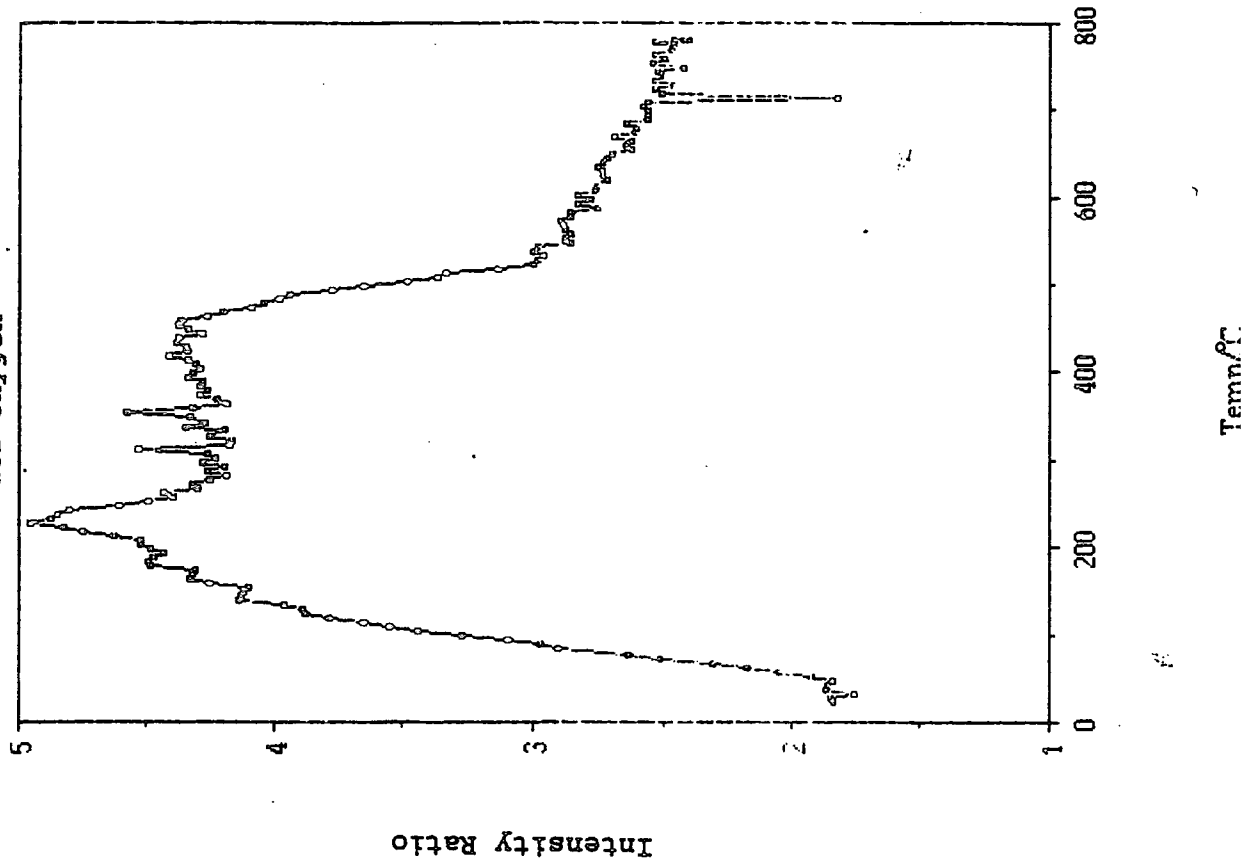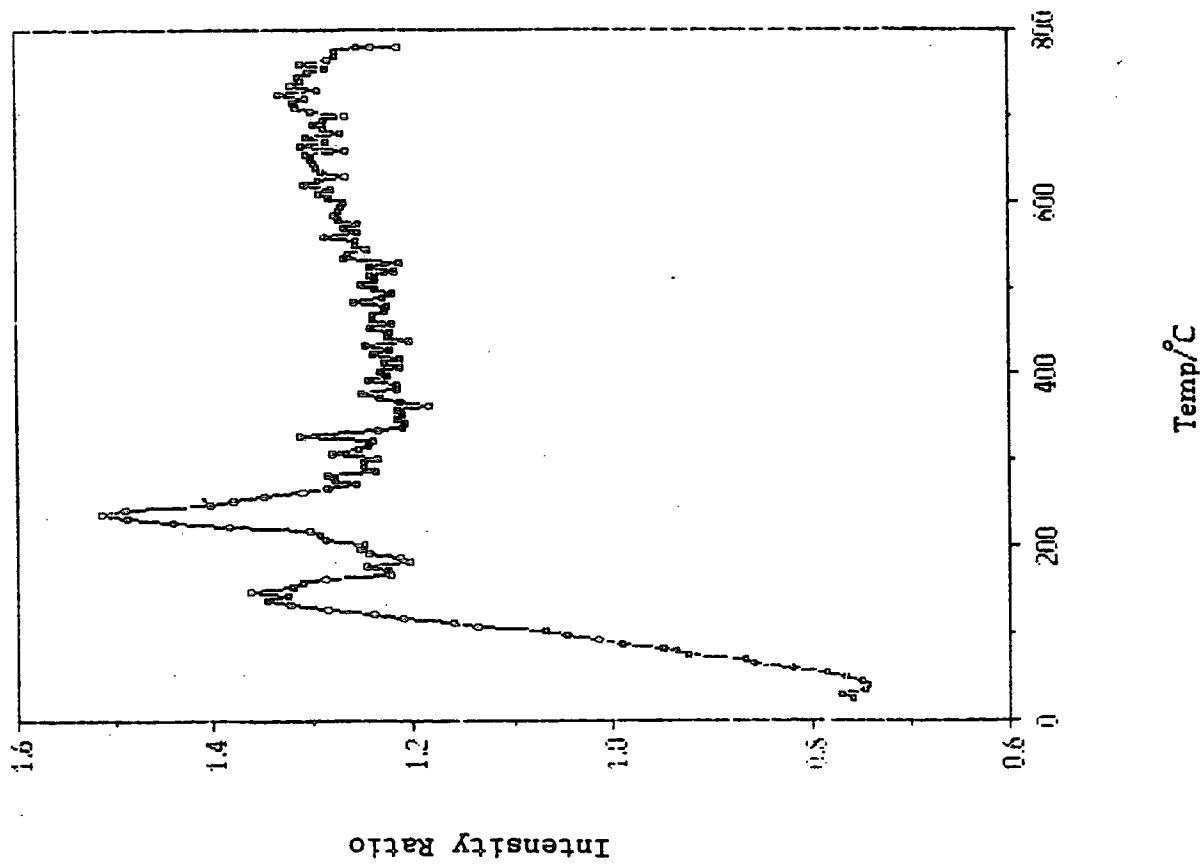

Figure 3.32

A plot of intensity against temperature for ions having m/z = 18 for catalyst EP210 heated under oxygen

fragments (m/z = 14,12).

The changes in the water trace are shown in Figure 3.31. Again, there is an initial sharp peak having a maximum at 150°C, with a second peak maximum found at 240°C linked to production of water by oxidation of the acetate groups. The dehydroxylation of the silica surface follows at higher temperatures.

Thus titania as a promoter leads to similar oxidation pathways at similar temperatures and to the same final product, whether added as a cogel or by impregnation. Hence dispersion doesnot seem to be the controlling factor in the decomposition of the chromium (III) acetate, and electronic rather than structural effects appear to be operating.

After completion of this experiment the same catalyst sample was heated in argon. No changes were observed in the intensities of the ions observed. However, the catalyst is a dark orange colour after heating, which suggests that the di/chromate structure of the activated catalyst is converted to the polymeric chains of CrO_3 [36].

14 Studies of catalyst EP210 heated under oxygen

The data for this experiment is contained in Table 3.12.

Table 3.12   *The temperatures at which ion m/z values reach a maximum intensity for the catalyst EP210 heated under oxygen*

M/z (intensity)	Temperature/°C
14(21)	44
14(21)	83
15(19)	114
30(24) 31(20)	119
17(114) 18(297) 22(16) 25(6) 26(15) 27(14) 30(42) 31(34) 43(81) 46(10)	229
14(36) 15(86) 28(417) 42(16) 44(567) 45(22)	234
12(90)	239
14(22) 15(38) 28(504) 46(12)	335
12(118) 22(22) 44(781) 45(30)	340
17(105) 18(275)	446

There are two distinct regions of oxidation falling between 229 and 239°C and 335 and 340°C. The formation of chromium (VI) is indicated by the colour change from green to bright orange.

Below 130°C there are several low intensity peaks which are attributed to hydrocarbon fragments (m/z = 30,15,14) and to an ether or alcohol fragment, m/z = 31. It is thought that these peaks arise from decomposition and oxidation of surface contaminants.

The two regions of oxidation are related closely in both temperature and fragmentation loss to those found for catalysts CS2066 and EP355, even though for catalyst EP210 the precursor is the acetylacetonate and the promoter is an aluminium alkyl.

In the lower temperature region, 229-239°C, the most intense peaks are those of $[CO^+]$ and $[CO_2^+]$. Peaks having m/z = 43, 42, 39, 27, 26, 25, 15 and 14 are linked to hydrocarbon fragments which can arise from the promoter alkyl groups or the acetylacetonate group. Ions having m/z = 45, 31 are indicative of oxygen-containing species arising from an alcohol or ether, and m/z =43, 42, 15, 14 may be linked, as for the argon case, to $[H_3C-C=O^+]$, $[H_2C=C=O^+]$, $[CH_3^+]$ and $[CH_2^+]$ respectively. The origin of the peak having m/z = 22 is thought to be $[CO_2^{2+}]$.

In the region 335-340°C the most intense peaks are again those for $[CO^+]$ and $[CO_2^+]$. The less intense peaks are limited to low mass hydrocarbon fragments (m/z = 15,14,12) and some ether fragments (m/z = 46,45).

The water trace is shown in Figure 3.32. The peak is very broad, with local maxima at 229 and 446°C. These are assigned to loss of physisorbed water on the catalyst surface and the product of oxidation of the acetylacetonate/alkyl ligands respectively. Towards higher temperature there is dehydroxylation of the silica surface.

178

DISCUSSION

1 Chromium containing catalysts heated under argon

In general, heating the catalysts under an argon atmosphere leads to a complex decomposition process, with many mass spectral peaks being observed over a wide temperature range.

Chudek et al [30] have reported that the trimeric structure is retained when basic chromium (III) acetate is supported on silica, and in the light of the complexity of the decomposition pattern observed experimentally, together with the lack of data on preparation method from the catalyst supplier, it is assumed that this is also the case with the catalysts under study. The range of fragments observed would be unlikely were the acetate simply bound as a monomer.

Three steps were proposed by Grotowska et al [29] for the decomposition of the simple acetate: the first involves dehydration (80-207°C), the second loss of the acetate ligand to yield a complex $Cr_2O_3 \cdot xCO_2$ (325-508°C), and finally loss of CO_2 from this complex to yield the chromium (III) oxide (508-610°C). For the trimeric salts this reduces to a two stage mechanism. The first step involves dehydration and loss of counter ions (45-295°C), the second loss of the acetate ligands to yield the chromium (III) oxide (295-518°C).

The results show that for catalyst EP30X (Cr 1.00%) dehydration, mainly of the silica support, is the first step, with some decomposition of the acetate occurring between 330 and 390°C, where large fragments are detected: $m/z = 43$ $[CH_3-C=O^+]$, $m/z = 42$ $[CH_2=C=O^+]$ and $m/z = 41$ $[CH=C=O^+]$. Between 390 and 410°C there is a definite region of decomposition linked to smaller fragments, in particular CO and CO_2. Grotowska et al [29] proposed $Cr_2O_3 \cdot xCO_2$ as an intermediate to oxide formation but this is not likely due to the nature of the bonding between transition metals and CO_2. Such complexes require electron-rich metal centres to bond to the Lewis acidic carbon atom of CO_2, and are not thermally stable to temperatures in this range [54]. What is more likely is that the initial decomposition of acetate groups leads to formation of a carbonate, which corresponds with the known chemistry of oxalate complexes under thermal decomposition [12,37]. Oxide may be present also at this stage, to be followed by decomposition of the carbonate which releases CO_2 and leaves the metal oxide alone.

The three stages are thus envisaged in the decomposition of chromium (III) acetate on silica:

(1) Dehydration (mostly of silica) and loss of surface contaminants (80-207°C)

(2) decomposition of acetate ligands leading to formation of a carbonate and possibly some oxide (Cr_2O_3) also (330-390°C)

(3) decomposition of carbonate to give the oxide alone, with loss of CO_2 (390-410°C)

The titanium promoted catalysts EP355 and CS2066 both have more complex decompostion patterns spread over a wider temperature range. There are two main regions where peak maximum intensities are associated with acetate decomposition for catalyst CS2066 (Ti 2.50%, Cr 1.00%): 286-316 and 376-512°C. The corresponding values for catalyst EP355 are 200-300 and 350-420°C. Note that step (2) occurs at a lower temperature for both titanium promoted catalysts than for catalyst EP30X. The fact that the same ion m/z values occur in the first region for catalysts EP30X, CS2066 and EP355 suggests a common intermediate (i.e. the carbonate).

The addition of titania appears to promote the initial acetate decomposition, but it leads to a black product for both catalysts EP355 and CS2066, rather than the green Cr_2O_3 of catalyst EP30X. Initially this product was thought to be CrO_2, an intermediate in the decomposition of CrO_3 to Cr_2O_3, but Cr (IV) would require an oxidation reaction to take place. Preliminary XPS results of catalyst CS2066 following heating showed a Cr $2p_{3/2}$ binding energy of 577.6eV (cf. 577.9eV for the untreated catalyst) and a Ti 2p binding energy of 459.4eV (cf. 459.1eV for the untreated catalyst), which suggests chromium is in a <u>lower</u> oxidation state than 3+ and titanium, which cannot be in a higher oxidation state than 4+, has been involved in some electron transfer.

The chromium dispersion was on average 0.19, lower than for the fresh catalyst (0.28); the titanium dispersion was 0.23 on average, cf. 0.25 when untreated. It is possible that there is structural and electronic interaction between titanium and chromium which results in incorporation of chromium into the TiO_2 lattice (hence the lower chromium dispersion) to yield a perovskite type structure (perovskite = $Ca^{II}Ti^{IV}O_3$). The chromium (II) ion is between 20 and 30% larger than Ti^{IV} (61pm) and hence the metatitanate $Cr^{II}Ti^{IV}O_3$ is the likely structure. Where M^{II} is approximately the same size orthotitanates M_2TiO_4 are obtained. The formation of Cr-Ti species, thought to be dichromate-like has been put forward by Ellison and Overton [55] from SIMS and TPR evidence. However, for catalyst EP355 the amount of titanium at the surface is small (titanium dispersion in the fresh catalyst is 0.12 cf. 0.25 for catalyst CS2066). This suggests that the promotional effect is not related to loading but to dispersion and

structural factors.

XPS studies would be useful to investigate the chromium and titanium binding energy changes and changes in dispersion, which would result from mixed oxide formation.

Thus, the decomposition of acetate to form carbonate remains a possible second step after dehydration, but as the temperature is increased the carbonate breaks down to yield CO_2 as before, and chromium is forced into interaction with the titania lattice.

The interpretation of the results for catalyst EP210 (Al 1.00%, Cr 1.00%) is made more difficult by lack of information on the industrial preparation. Hydrocarbon fragment peaks were generally assigned to decomposition of the aluminium alkyl groups. In this case the precursor is chromium (III) acetylacetonate and the pattern of decomposition appears to be much simpler, with $[CO_2^+]$ and $[CO^+]$ fragments found in the temperature region 420-445°C. This is higher than for the other chromium containing catalysts. It is not clear if the acetylacetonate decomposition follows similar steps to the other catalysts containing the acetate precursor: it also leads to the final catalyst colour being black. Preliminary XPS measurements found the average Cr $2p_{3/2}$ binding energy to be 577.9eV (cf. 578.0eV in the fresh catalyst) and the Al 2p binding energy to be 75.0eV (cf. 75.1eV in the fresh catalyst). The dispersion of aluminium is unchanged from that of the fresh catalyst (0.04) but the chromium dispersion is decreased, 0.32 vs. 0.41. Spinel structures where aluminium combines with Cr^{II} impurities to form a mixed oxide phase are known and have the general formula $A^{II}B_2^{III}O_4$ i.e. $Cr^{II}Al_2O_4$ [31] and it is thus possible that the black colour arises from the formation of such a complex. The inclusion of chromium would explain the lowered dispersion but there should be a more noticeable difference in the Cr $2p_{3/2}$ binding energy if the oxidation is 2+. Therefore further XPS studies would be useful on this system.

2 Chromium containing catalysts heated under oxygen

Activation under oxygen leads to much simpler decomposition patterns. The final colour of the chromium containing catalysts (bright orange) is suggestive of oxidation to Cr (VI) and the formation of the di/chromate structures which were proposed from examination of the XPS data in Chapter 2.

For catalyst EP30X there is one region of decomposition and oxidation, with the peak maximum intensities occurring between 269 and 299°C. The most intense peaks are those of m/z = 28 $[CO^+]$ and m/z = 44 $[CO_2^+]$, products of acetate oxidation. XPS results indicate that after heating to 700°C there is some probable aggregation of chromium species and

possibly some CrO_3, as well as di/chromate structures.

The decomposition/oxidation of acetate from the mass spectral data appears to be complete by ca. 350°C, with no further products detected other than water from the dehydroxylation of the silica support.

The promoted catalysts EP210, EP355 and CS2066 again have decomposition patterns which are much simpler than those obtained on heating under argon. For catalysts CS2066 and EP210 there are two main regions of reaction, at similar temperatures: 223-238 and 324°C for catalyst CS2066 and 229-239 and 335-340°C for catalyst EP210. The ion m/z values found in each region are similar and it appears that a similar decomposition/oxidation pathway occurs for both. This is different from catalyst EP30X whose single decomposition/oxidation region occurs midway between those for catalysts CS2066 and EP210. The lower temperature region certainly involves oxidation of acetate/acetylacetonate groups since a peak with m/z = 18 [H_2O^+] is also seen - similar to the findings of Kim and Woo [21].

The higher temperature region is dominated by [CO^+] and [CO_2^+] peaks for both catalysts, which must be oxidation products. There are clearly two steps in the oxidation of the chromium salts on both catalysts but it is not clear how these can be related to chromium oxide structures: there are possibly two species of Cr (VI) as Ellison and Overton [55] and Kim and Woo [21] have suggested. The latter quote the species forming at 187 and 227-447°C.

The former authors have also put forward evidence of dichromate-like Cr-Ti species and these cannot be wholly discounted. The XPS results suggested Cr (VI) species were present on both catalysts EP210 and CS2066 after activation. Both the Ti and Al 2p binding energies had increased on activation which may be due to electronic and structural interactions arising from movement of chromium ions into the titania or alumina lattice. The nature of the promoter does not seem important but loading may be. Note also that there is a different chromium precursor for EP210.

Catalyst EP355 has three clearly defined regions where ion m/z values are a maximum: 135-155, 230-240 and 306-321°C. The latter two fit with the pattern observed for catalysts EP210 and CS2066. The first region contains peaks of m/z = 44 and 28 which have been linked previously to decomposition of acetate ligands. Evidence is also available for the presence of hydrocarbon fragments linked with the acetate ligand as well as oxygen-containing fragments from the acetate ligand itself.

At the higher temperatures the hydrocarbon and oxygen-

containing fragments are more in evidence than with the other chromium containing catalysts. This may be an effect of preparation since catalyst EP355 is prepared by impregnation of the cogel: CS2066 and EP210 are prepared by impregnation only.

It appears that there are three stages of acetate decomposition, leading to Cr (VI) which is confirmed by XPS data. It may be that there is partial oxidation, several species of Cr (VI) formed (Kim and Woo [21] above) or some Cr-Ti species is also formed. It is not clear which of these is correct, but the lower titanium surface dispersion appears to lead to decomposition/oxidation at a lower temperature, as with the heating under argon, compared to the other chromium containing catalysts. Thus it may be that the "better" promotional effect is obtained by use of the cogel.

On completion of the activation experiments the same catalyst samples were heated under argon: this led to the thermal decomposition of the chromium (VI) oxides, giving the green Cr_2O_3. In the case of catalyst EP355 the colour merely darkened. This suggests that the di/chromate structures proposed for the activated catalyst are polymerized to give CrO_3 chains. Further XPS experiments would be useful, together with some structural work such as Raman/SEM in order to probe the question of Cr-Ti/Cr-Al complex formation.

REFERENCES

[1] H.H. Willard, L.L. Merritt, J.A. Dean and F.A. Settle, *Instrumental Methods of Analysis*, Wadsworth, California, 7th Edition, 1988

[2] J.C. Riviere, *Surface Analytical Techniques*, Oxford, 1990

[3] J.C. Vickerman, in *Spectroscopy of Surfaces*, eds. R.J.H. Clark and R.E. Hester, Wiley, Chichester, 1988

[4] M. Prutton, *Surface Physics*, Oxford University Press, Oxford, 2nd edition, 1983

[5] D.E. Sykes, in *Methods of Surface Analysis: Techniques and Applications*, ed. J.M. Walls, Cambridge University Press, Cambridge, 1990

[6] H.E. Duckworth, R.C. Barber and V.S. Venkatasubramanian, *Mass Spectroscopy*, Cambridge University Press, Cambridge, 2nd edition, 1990

[7] E. Constantin and A. Schnell, *Mass Spectrometry*, Ellis Horwood, Chichester, 1990

[8] J.H. Batey, *Vacuum*, 37, 659, 1987

[9] M.E. Brown, *Introduction to Thermal Analysis*, Chapman and Hall, London, 1988

[10] R.L. Schmid and J. Felsche, *Thermochim. Acta*, 59, 105, 1982

[11] M.R. Holdiness, *Thermochim. Acta*, 75, 361, 1984

[12] H.R. Langer, *Thermochim. Acta*, 100, 187, 1986

[13] E.L. Charsley, S.B. Warrington, G.K. Jones and A.R. McGhie, *American Laboratory*, 22, 21, 1990

[14] P.A. Barnes, *Thermochim. Acta*, 114, 1, 1987

[15] J. Rouquerol, S. Bordere and F. Rouquerol, *Thermochim. Acta*, 203, 193, 1992

[16] S. Bernal, R. Garcia and J.M. Rodriguez-Izquierdo, *Thermochim. Acta*, 70, 249, 1983

[17] P.A. Barnes, *Anal. Proc.*, 27, 150, 1990

[18] P.A. Barnes, E.A. Dawson and G. Midgley, *J. Chem. Soc. Faraday Trans.*, 88, 349, 1992

[19] J.E. Baker, R. Burch and S.E. Golunski, *Thermochim. Acta*, 142, 329, 1989

[20] M. Muhler, R. Schlogl, S. Eder and G. Ertl, *Surf. Sci.*, 189/190, 69, 1987

[21] C.S. Kim and S.I. Woo, *J. Mol. Catal.*, 73, 249, 1992

[22] W. Hill and G. Ohlmann, *J. Catal.*, 123, 147, 1990

[23] H.E. Curry-Hyde, H. Musch, A. Baiker, M. Schraml-Marth and A. Wokaun, *J. Catal.*, 133, 397, 1992

[24] J.L. Falconer and J.A. Schwarz, *Catal. Rev. Sci. Eng.*, 25, 141, 1983

[25] K. Christmann, *J. Vac. Soc. Jpn.*, 33, 549, 1990

[26] P. van der Voort, I. Gillis-D'Hamers, K.C. Vranken and E.F. Vansant, *J. Chem. Soc. Faraday Trans.*, 87, 3899, 1991

[27] M.L. Hair, *Vibrational Spectroscopies for Adsorbed Species*, American Chemical Society, Washington, 1980

[28] Y. Iwasawa, *Tailored Metal Catalysts*, Reidel,

Dordrecht, 1986

[29] M. Grotowska, R. Wojciechowska and W. Wojciechowski, *J. Thermal Anal.*, 36, 2365, 1990

[30] J.A. Chudek, G. Hunter, C.H. Rochester and T.F.S. Smith, *J. Catal.*, 136, 246, 1992

[31] N.N. Greenwood and A. Earnshaw, *Chemistry of the Elements*, Pergamon Press, Oxford, 1982

[32] F.A. Cotton and G. Wilkinson, *Advanced Inorganic Chemistry*, Wiley, New York, 4th edition, 1980

[33] F.W. McLafferty, *Interpretation of Mass Spectra*, University Science Books, Mill Valley, California, 3rd edition, 1980

[34] W. Hill and G. Ohlmann, *React. Kinet. Catal. Lett.*, 38, 289, 1989

[35] A. Royston, University of Durham, 1992

[36] A.F. Wells, *Structural Inorganic Chemistry*, Clarendon Press, Oxford, 5th edition, 1984

[37] J.R. Darley and J.I. Hoppe, *J. Chem. Ed.*, 49, 365, 1972

[38] H.G. Langer and R.S. Gohlke, in *Gas Effluent Analysis*, ed. W. Lodding, Marcel Dekker, New York, 1967

[39] H.L. Friedman, *Thermochim. Acta*, 1, 199, 1970

[40] H.G. Langer and R.S. Gohlke, *Anal. Chem.*, 37, 433, 1965

[41] H.G. Langer and R.S. Gohlke, *Anal. Chem.*, 35, 1301, 1963

[42] D. Pryce, *Dyn. Mass Spectrometry*, 5, 216, 1978

[43] R.T. Short, *J. Chem. Soc. Faraday Trans. 1*, 76, 2310, 1980

[44] G. Ciembroniewicz, *J. Thermal Anal.*, 27, 125, 1983

[45] J. Rouquerol, *Thermochim. Acta*, 144, 209, 1989

[46] J.H.R. Ross, *Anal. Proc. (London)*, 22, 239, 1985

[47] S.E. Golunski, T.G. Nevell and D.J. Hucknall, *J. Catal.*, 88, 448, 1984

[48] P.E. Miller and M.B. Denton, *J. Chem. Ed.*, 63, 617, 1986

[49] G.J.J. Bartley and R. Burch, *Appl. Catal.*, 28, 209, 1986

[50] M. Bowker, R.A. Hadden, H, Houghton, J.N.K. Hyland and K.C. Waugh, *J. Catal.*, 109, 263, 1988

[51] D. Chadwick and P.J.R. O'Malley, *J. Chem. Soc. Faraday Trans. 1*, 83, 2227, 1987

[52] K. Atherton, G. Newbold and J.A. Hockey, *Disc. Faraday Soc.*, 52, 33, 1972

[53] W. Meloche and G.E. Kalbus, *J. Inorg. Nucl. Chem.*, 6, 104, 1958

[54] A. Behr, *Angew. Chem. Int. Ed. Engl.*, 27, 661, 1988

[55] A. Ellison and T.L. Overton, *J. Chem. Soc. Faraday Trans.*, 89, 4393, 1993

[56] D. Cornet and R.L. Burwell, *J. Am. Chem. Soc.*, 90, 2489, 1968

CHAPTER 4

Preparation and Characterization of some Triosmium Carbonyl Compounds and their use as Surface-Adsorbate Models

1 Introduction

In order to assist in the assignment of vibrational spectra obtained from adsorbates it is useful to have spectra of complexes of known structure in which ligands or molecular fragments adopt bonding geometries which may be observed for these fragments on surfaces. In this way a number of reference spectra can be obtained which later can be used in the surface studies. Organometallic cluster compounds provide a particularly useful area for such studies since ligands may adopt coordination geometries in which bonding to several metal atoms may occur. The "multi-metal-atom-site" in such a compound may mimic the kinds of adsorption sites present on metal surfaces. This type of cluster surface analogy has been proposed by Muetterties based on his experimental work, which claims that discrete metal cluster complexes may be reasonable models for the processes occuring in chemisorption and catalysis on metal surfaces [119]. If this is correct to at least a first approximation, it provides a route to a deeper understanding of the molecular processes occurring during chemisorption on surfaces, since details of structure, kinetic and mechanistic features of ligand mobility and reaction mechanisms are more easily obtained for model metal cluster complexes. The use of x-ray diffraction and NMR techniques yields the essential structural and stereochemical details of cluster complexes, but the lack of analogous surface science techniques makes the use of such models necessary. The stoichiometry of a surface complex is best studied using XPS and TPRS, structural information being provided by LEED, UPS and vibrational spectroscopy. Ideally all of these techniques should be used *in situ* to fully characterise an adsorbed species, since they provide complimentary information. However, it is usual to use a combination of these techniques, since the results from just one technique cannot always be interpreted unambiguously. Data from metal cluster complexes and surface species are most easily compared for vibrational spectroscopy since spectra of a ligand of known structure can help in the interpretation of spectra obtained from surface experiments, allowing some deductions of adsorbate structure and bonding. This approach has been used by Sheppard and Powell to study surface hydrocarbon species, for example [120-122], surface carboxylate [123] and surface alkoxide [124]. Metal carbonyls have been widely used to assist in the interpretation of CO bonding on metal surfaces [125].

Muetterties has reviewed the metal cluster types and their structure [119]. Cluster sizes range from two to more than thirty metal atoms with the metal in a formally low oxidation state. Compared with mononuclear complexes many more possible coordination sites are offered to organic ligands, a similar situation to the metal surface itself. However, it is important to remember that a flat metal

187

surface cannot in many cases be modelled by a small polyhedral cluster, since the coordination numbers are uniformly higher for surface atoms in metals than in clusters. Similarities can be expected between cluster chemistry and a highly dispersed metal, e.g. a supported catalyst. But in the context of chemisorption the bonding of the adsorbate to the metal may be little different on the surface or in a cluster and similarities in thermochemistry, structure and surface mobility might be expected.

For the cluster model to be useful there needs to be a close correspondence in structure and bonding features of the ligands in both the metal cluster complex and on the surface. Comparisons should ideally only be made when there is correspondence in (i) the metal, (ii) the ligand, (iii) the coverage by the ligand on both cluster and surface, and (iv) the crystallography. Point (i) presents no problem, though the cluster-surface analogy has proved to be useful even when the metal atoms in the cluster and those of the surface are different. This is so when, for example, ligand vibrational modes are of primary interest since these depend mainly on the local environment e.g. the modes of a CH_3 group in a CH_3-C-M ligand will not be particularly sensitive to the nature of M. A difficulty arises with point (ii) as it is not possible at present to synthesize cluster complexes where the only ligand is, for example, ethylene, though complexes can be prepared with such ligands in combination with others such as carbonyl. The choice of co-ligands is important when using vibrational spectroscopy in order to avoid spectral overlaps. CO is a good co-ligand as it absorbs in the region ca. 2200-1700cm^{-1}, whilst hydrocarbons absorb outside this region. The cluster complexes impose a constraint on the equivalent coverage requirement (iii). Most are coordinatively saturated and the analogue in surface chemistry is assumed to be monolayer coverage, therefore the cluster-surface model will be optimal for monolayer or near-monolayer coverages. The most problems arise with point (iv), matching cluster and surface geometries. In clusters there is a wide variety of metal geometries, from simple triangles, as in the Os_3 complexes, to rafts of metal atoms which replicate a fragment of a bulk metal (as found in some nickel complexes). Square faces are also found on surfaces and the so-called "butterfly" geometry, especially for alkyne clusters. This latter geometry has potential significance in representing a step or kink on a metal surface, which is believed to be a highly reactive site. The coordination sites offered by clusters have direct analogy with the geometries of sites present on surfaces with suitably chosen crystallography. For example, on fcc metals the (111) face represents triangular sites whilst (1000) presents only square sites. (110) offers the possibility of both 3 fold and 4 fold sites. In the sense that a cluster is a model for an aggregate of metal atoms it would be of interest to compare the properties of clusters

with small metal particles supported on oxides or deposited as films. However, in the sense that the cluster may provide a model for the mode of coordination of a ligand to a site of particular geometry, it becomes more interesting to compare the cluster model with a single crystal for which only the same type of site as in the cluster is present. The problem with deposited films or metal particles is that many different types of site may be present. Thus upon adsorption there may be many different types of sites which it is necessary to try and identify from spectra. The single crystal may offer a much more limited number of coordination sites and so allow a systematic study of how coordination geometry changes with site geometries offered.

Many modes of ligand coordination to a metal cluster are feasible models for the coordination of adsorbates to metal surfaces. There are a few exceptions, arising mainly from unlikely spatial arrangements which would not be found on a close packed metal surface, for example η^2 bonding of a diene to a single metal atom in a cluster complex. In some cases different types of ligands have similar orientations with respect to the metal core of the cluster, e.g. alkynes, alkyne fragments, diene and allylic groups, and benzyne groups. Alkyl and aryl groups can only be structurally characterized in edge bridging positions and alkylidenes only in face bridging positions - as the substituents on a carbon atom are reduced the mode of bonding changes to higher coordination to the metal atoms. Similar changes can be envisioned on metal surfaces during catalytic processes, especially on surfaces which are highly stepped or very rough.

Many ligands which are typically monodentate in mononuclear complexes exhibit multicentre bonding in cluster complexes and it is thus reasonable to expect that if structure, stereochemistry and bonding are so dramatically affected on going from mononuclear to multicentre transition metal clusters, cluster complexes and multicentre interaction will occur on clean metal surfaces. It can also be expected that the crystallography of the surface will be very important in determining the bonding mode. Studies of adsorption on metal surfaces have indeed shown multicentre metal-adsorbate interactions, and hence gives validity to the cluster-surface analogy, but there is insufficient structural data for the chemisorbed state to begin a comparison of stereochemistry between the two systems.

A comparison of the thermochemistry of metal clusters and chemisorption on metal surfaces, in principle, provides insight into the nature of the chemical bonding, though few studies of this nature exist for well defined surfaces or for cluster complexes. Major considerations in both cases are the number of metal atoms per bonding site, orientation and electronic character. For chemisorption additional

considerations are the availability and mobility of metal valence band electrons and the occurrence of extensive and long range interactions. Evidence is increasing from chemisorption studies that the coadsorbed species are primarily bonded to a small number of nearest neighbour metal atoms and the theoretical modelling of chemisorption is based on metal-adatom localized bonded complexes. Comparisons of metal-metal bonding energies of surface metal atoms and cluster atoms suffers from the necessary substitution of bulk energy values for surface values, and from extensive assumptions made in deriving metal-metal bonding energies from the measured enthalpies of formation of metal clusters. With the exception of the manganese triad, bulk metal-metal bond energies are on average 30% higher than for the estimated bond energies in cluster complexes.

It has been clearly shown in some cases that chemisorbed molecules and cluster ligands are not stationary and this mobility can arise from two basic processes: one is a dissociative process in which all the metal-ligand or metal-adsorbate bonds are broken and the dissociated molecule appears as a discrete species. The second process is non-dissociative and the molecule migrates around the periphery of the cluster surface. Electronic correlation between metal orbitals and ligand orbitals is not lost - as a ligand-metal bond begins to stretch and break a new bond is being formed. Migration processes can have very low activation energies, lower than the dissociative process, and are important in both systems with respect to catalysis. Experimentally it can be difficult to find out which process is operating. Solution NMR is useful for studying this phenomenon in clusters and field ion microscopy has proved useful for surface studies, though only migration of metal atoms can be observed by this latter method. The general lack of data makes a comparison of ligand mobility for cluster and surface impossible. Also, ligand mobility for metal surfaces with less than monolayer coverage cannot be simulated in clusters since these are coordinatively saturated. The validity of the comparison in ligand mobility is likely to be highest for stepped, kinked or corrugated metal surfaces where the spatial freedom above the surface is less limited [119,126,127].

To illustrate the comparison, surface and cluster chemistries of hydrocarbons and their oxygen derivatives are considered, and also an important study of pyridine [128]. Early work in this field was carried out by Sheppard *et al* [120b]. Infrared and Raman spectra of $HCCo_3(CO)_9$ and $DCCo_3(CO)_9$ were reported, and assignments made for the bands associated with the vibrations of the $HCCo_3$ grouping. The characteristic wavenumbers for the $v(CH)$ and $\delta(CH)$ modes of the cluster compound, in which the hydrocarbon grouping is bonded to an equilateral triangle of metal atoms, are very

similar to those obtained by dissociative adsorption of acetylene on Ni(111) planes which have triangular adsorption sites. This provides support for the assignment of the bands observed on nickel to a surface CH group. The same authors [120a] also report a detailed vibrational analysis of $CH_3CCo_3(CO)_9$ and its deuterated analogue. Comparison of these spectra with those obtained by EELS for a species resulting from the chemisorption of acetylene and hydrogen or ethylene on Pt(111) above 300K supports the identification of the latter as containing a $C.CH_3$ group. Ethylidyne ($C-CH_3$), ethylidene ($CH-CH_3$) and vinyl ($CH-CH_2$) species had been proposed previously. Table 4.1 shows the strong analogies between frequencies and intensities found in the IR spectra of the cluster complex and the EELS spectrum of ethylene adsorbed on Pt(111) above room temperature.

Table 4.1 *Comparison of surface species vibrational frequencies (cm^{-1}) with those of ethylidyne cluster compounds*

$CH_3CCo(CO)_9$	Surface species		Assignment
2930 (m)	-		v_{as} (CH_3)
2888 (m)	ca. 2920 (m)		v_s (CH_3)
1420 (m)	ca. 1420 (w)		δ_{as} (CH_3)
1356 (m)	1355 (s)		δ_s (CH_3)
1163 (m)	1130 (s)		v (CC)
1004 (s)	-		π (CH_3)
401 (m)	435 (m)		v_s (MC)

The A_1 modes for the CH_3CCo_3 grouping are also those with dipole changes perpendicular to the surface in the adsorbed species. Band positions and relative intensities for cluster and surface species are in remarkably close agreement. In the spectrum of the tricobalt fragment the 1356 and $1163cm^{-1}$ bands are prominent and of comparable intensity, but in the deuterated tricobalt fragment the corresponding bands, at 1182 and $1002cm^{-1}$, are of unequal intensity with the former band much stronger, presumably due to strong coupling between the v(C-C) and δ_s(CD_3) group motions in the actual normal modes. Exactly the same intensity pattern is found in the spectra of the adsorbed species.

The reaction of monofunctional alcohols, carboxylic acids, aldehydes and ketones on metal surfaces have been quite extensively studied in recent years [129]. Alcohol adsorption and reaction on transition metal surfaces is well documented. Of the group IB metals only copper metallates the OH bond of methanol to yield methoxide and surface bound hydrogen atoms. On heating recombination occurs to give methanol. Higher alcohols form surface alkoxides in a similar manner, but on heating there is dehydrogenation to

the corresponding aldehyde which is then rapidly desorbed from the surface [130]. These intermediates are found in near monolayer quantities, and the stability of the alkoxides can be related to the α-H bond energy. On silver and gold surfaces there is only weak bonding of the alcohol molecules.

Adsorption on the more reactive group VIII metals is not fully reversible, and, as on Ni(100) and Fe(100) for example, methanol may be bound via the oxygen lone pair of electrons at low temperature, methoxy groups being formed on heating and subsequently decomposing to CO and H_2 [131]. Similarly for Fe(100). Although methanol is decomposed on platinum and palladium, no methoxy species have been observed, and is attributed to the greater ability of both metals to break C-H bonds and to their higher surface-CO bond energies [132].

Greater reactivity is seen for the early transition metals, molybdenum and tungsten both dissociate methanol to carbon, oxygen and hydrogen atomic fragments [133,134]. The build up of the surface carbon and oxygen stabilizes the methoxy species, though the structure of the complexes has not been deduced.
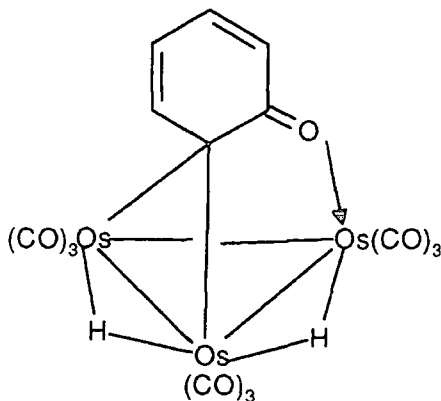
The formation of alkoxy species has an analogy in cluster complexes [135,136], e.g.

$$ROH + Os_3(CO)_{10}(C_6H_8) \longrightarrow HOs_3(CO)_{10}(OR)$$
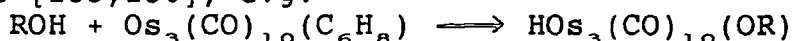
R = H,Et,Ph
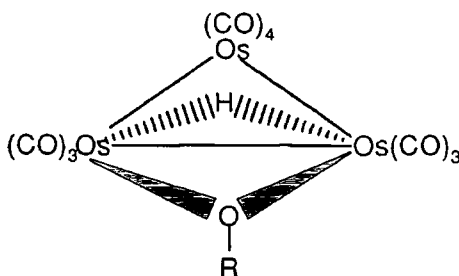
The phenoxy derivative can react further on heating to give a five membered metallacyclic ring as shown below.

192

Relatively little information is available on the reactivities of these alkoxy complexes, but the phenoxy derivatives have been vibrationally characterized in this work.

The adsorption and decomposition of formic and acetic acid has been studied extensively on Cu(110), Ag(110), Ni(100), Fe(100), W(100), Pt(111) and Ru(0101) [137]. Both acids decompose to CO_2, H_2 and in some cases CO and H_2O also. The intermediates in this decomposition process on all metals are surface carboxylates formed by metallation of the acidic OH bond. The most commonly adopted configuration of these surface carboxylate is with coordination of both oxygen atoms to the surface (either bidentate or bridging) with the OCO plane normal to the surface. Interestingly, Churchill et al [138] have synthesized $HOs_3(CO)_{10}(\mu-O_2CH)$, a model complex for formate adsorption, i.e.
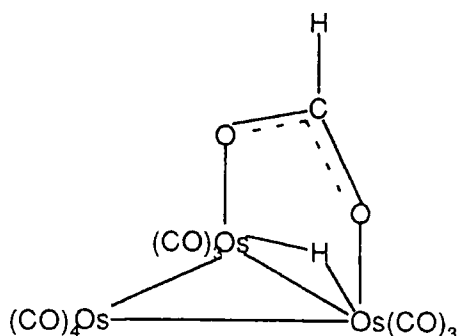
It's vibrational spectrum recorded both in solution and as a KBr disc, has been compared with the surface studies of formate on copper and silver by Sexton and Madix [123,139] using EELS, as detailed below.

Assignment	$HOs_3(CO)_{10}(O_2CH)$		Cu(100)	Ag(110)
v (CH)	2978	(w)	2910	2870
v_{as} (CCO)	1576	(vs)		1570
v (CH)	1370	(w)		
V_s (OCO)	1362	(w)	1330	1340
π (CH)	1031	(vw)		1060
δ (OCO)	794	(m)	760	760
v (M-O)			340	280

(all values cm^{-1})

In general there is good agreement except for v(CH) data, which is most sensitive to the charge on the formate species. The low frequency for the surface complex suggests that the formate group is largely ionic in character [127].

The reaction of pyridine at a metal surface is a classic

193

example of facile CH bond metallation brought about by steric constraints. Pyridine bonds to the surface via the nitrogen atom lone pair of electrons and the aromatic ring takes a position perpendicular to the surface. This brings the two α-CH bonds (α to nitrogen) close to the surface, and isotope scrambling experiments have shown reversible CH bond breaking. Metallation of an α-CH bond yields an α-pyridyl species. Interestingly, the corresponding cluster reaction also occurs.

$$Os_3(CO)_{11}(NC_5H_5) \longrightarrow HOs_3(CO)_{10}(NC_5H_4)$$
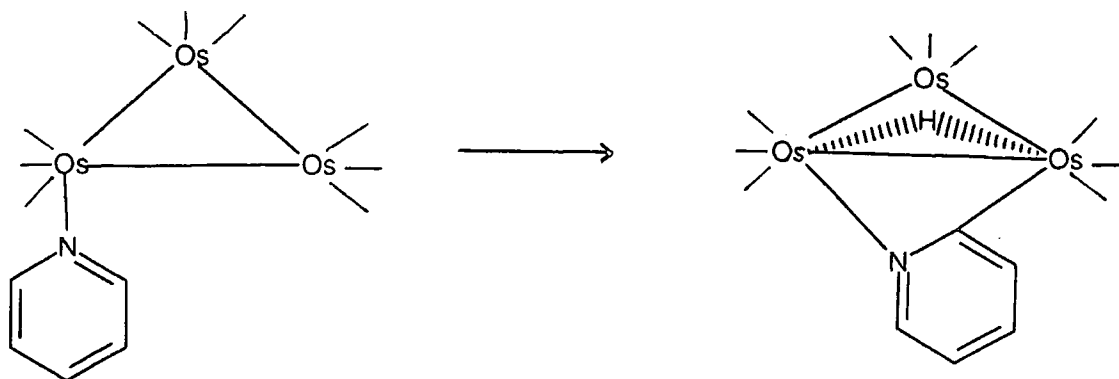
Both vibrational and electron energy loss spectroscopy of pyridine adsorbed on Ag(111) have shown the conversion of a π-bonded to a nitrogen-bonded pyridine as coverage increased [140]. Below 0.5 monolayer, pyridine adsorbs in a flat configuration, with the ring parallel to the surface plane. Above 0.5 monolayer there is a "phase transformation" to a nitrogen-bonded species. An EELS study of pyridine adsorbed on Ni(100) showed the existance of two nitrogen bonded species [141]. Of interest also are the infrared spectra undertaken on pyridine complexed in a variety of mononuclear transition metal complexes [142]. Interestingly, in these complexes pyridine is bonded to the metal atom through the nitrogen lone pair. Only minor shifts, 15-25cm^{-1}, in the vibrational frequencies of the pyridine ligand occur relative to those of the isolated molecule.

Muetterties [128] has used EELS and thermal desorption spectroscopy to study pyridine adsorption and a CH metallation on Pt(111). The spectra of the model osmium clusters, mentioned above, were used in the interpretation of the EELS spectra.

An attempt was made to assign the absorptions in the infrared spectrum of the $Os_3(CO)_{11}$py complex by comparison with those for $Os_3(CO)_{12}$. Of particular interest is the spectral region from 600 to 1650cm^{-1} since it contains the absorption bands of the pyridine and pyridyl fragments. Here

194

the assignment of bands is made by comparison with the vibrational spectrum of liquid pyridine (Table 4.2).

Table 4.2 Vibrational assignments of $Os_3(CO)_{11}(NC_5H_4)$ and $HOs_3(CO)_{10}(NC_5H_4)$ $(600-1650cm^{-1})$

symmetry	mode	description	NC₅H₅(NC₅D₅)	Os₃(CO)₁₁(NC₅H₅)		HOs₃(CO)₁₀(NC₅H₄)	
				b⁵	d⁵	b⁶	d⁶
A₁	4 (8a)	C–C, C–N stretch	1583 (1554)	1613	1571	1592	1554
	5 (19a)	C–C, C–N stretch	1483 (1340)	1490	1346	1459	1339
	6 (9a)	C–H in-plane bend	1218 (882)	1223	896	1222	869
	7 (18a)	C–H in-plane bend	1072 (823)	1075	838	1082	869
	8 (12)	asymmetric ring breathing	1032 (1014)	1050	1042	1057	1055
	9 (1)	ring breathing	991 (963)	1019	979	1029	1000
	10 (6a)	in-plane ring distortion	601 (579)	639		680	
B₂	23 (5)	o.o.p. ring distortion	1007 (828)	1019	838	1029	869
	24 (10b)	o.o.p. ring distortion	936 (765)		783		738
	25 (4)	C–H o.o.p. bend	744 (631)	762	650	758	680
	26 (11)	C–H in-phase o.o.p. bend	700 (526)	710	540	745, 740	680
	27 (16b)	ring o.o.p. distortion	403 (367)				
B₁	13 (8b)	C–C, C–N stretch	1581 (1546)	1578	1564	1549	1519
	14 (19b)	C–C, C–N stretch	1442 (1303)	1452	1328	1421	1298
	15 (14)	C–C ring stretch	1362 (1046)				
	16 (3)	C–C in-plane bend	1227 (1226)			1269	1216
	17 (15)	C–H in-plane bend	1143 (856)	1161	843	1162, 1117	825
	18 (18b)	C–H in-plane bend	1079 (835)	1075	838	1082	869
	19 (6b)	in-plane ring distortion	652 (625)	650		708	632

The correspondence of spectral frequencies between pyridine and the cluster allows use of the liquid phase assignments for guidance, although the pyridyl fragment, as would be expected, shows a frequency shift, here an average of $27cm^{-1}$ from liquid pyridine. Table 4.3 records the vibrational frequencies and their assignments for pyridine adsorbed on Pt(111).

symmetry	mode	description	$NC_5H_5(NC_5D_5)$	pyridine–Pt(111) $T = 300$ K		pyridine–Pt(111) $T = 120$ K	
				h^5	d^5	h^5	d^5
A_1	1 (2)	C–H stretch	3094 (2302)	3080	2275	3070	2270
	2 (13)	C–H stretch	3072 (2276)	3080	2275	3070	2270
	3 (20)	C–H stretch	3030 (2268)	3080	2275	3070	2270
	4 (8a)	C–C, C–N stretch	1583 (1554)	1570	1540	1610	1570
	5 (19a)	C–C, C–N stretch	1483 (1340)	1450	1330	1470	1330
	6 (9a)	C–H in-plane bend	1218 (882)	1150	860	1230	830
	7 (18a)	C–H in-plane bend	1072 (823)				
	8 (12)	asymmetric ring breathing	1032 (1014)	1010	1010	1050	1010
	9 (1)	ring breathing	991 (963)	1010	1010	1050	1010
	10 (6a)	in-plane ring distortion	601 (579)				
B_2	23 (5)	o.o.p. ring distortion	1007 (828)				
	24 (10b)	o.o.p. ring distortion	936 (765)				
	25 (4)	C–H o.o.p. bend	744 (631)				
	26 (11)	C–H in-phase o.o.p. bend	700 (526)			840	580
	27 (16b)	ring o.o.p. distortion	403 (367)				
B_1	11 (20b)	C–H stretch	3087 (2289)	3080	2275	3070	2270
	12 (7b)	C–H stretch	3042 (2256)	3080	2275	3070	2270
	13 (8b)	C–C, C–N stretch	1581 (1546)	1570	1540	1610	1570
	14 (19b)	C–C, C–N stretch	1442 (1303)	1450	1330	1470	1330
	15 (14)	C–C ring stretch	1362 (1046)				
	16 (3)	C–C in-plane bend	1227 (1226)	1230	1230	1230	1250
	17 (15)	C–H in-plane bend	1143 (856)	1150	860		
	18 (18b)	C–H in-plane bend	1079 (835)			1050	830
	19 (6b)	in-plane ring distortion	652 (625)	740	685	660	
						$\nu_{Pt–N}$	290

At room temperature the most significant aspect of the EELS spectrum is the prominence of the loss of the peak at 3080cm⁻¹. The frequency and the deuterium shift to 2275cm⁻¹ definitively identify the peak as a characteristic aromatic C-H stretching mode. Since these modes are intrinsically in-plane vibrations, their intensity in the specular direction indicates that pyridine is not adsorbed with its skeletal plane parallel to the metal surface. This conclusion is strengthened by the high intensities of bands observed in the spectral region 1000-1600cm⁻¹ where C-C stretching and C-H in-plane bending modes occur. TDS results suggest that a pyridyl species is formed by α-hydrogen abstraction. The infrared spectral data of the triosmium pyridyl complex correspond quite closely with the EELS data at this temperature.

For monolayer or submonolayer quantities of pyridine adsorbed on the Pt(111) surface at 120K, most of the modes observed in the specular direction can be characterized as primarily in-plane vibrations, as was seen in the room temperature spectrum. There are two new loss peaks at 660 and 840cm⁻¹ observed in the spectrum at 120K: the former was assigned to an in-plane ring distortion and the latter to a C-H out-of- plane bending motion. The relative intensities of the loss peaks differ greatly between spectra for room temperature and 120K adsorption. The relative intensities of

196

the in-plane modes suggests that the plane of the pyridine molecule is tilted away from the the surface, although there is still an appreciable interaction with the surface metal d orbitals and the π and π* orbitals of pyridine. This can be seen from the increase in frequency of the C-H out-of-plane bend from 700cm^{-1} for liquid pyridine to 840cm^{-1} for pyridine adsorbed on Pt(111) at 120K. At saturation coverage a value of 52° has been calculated for the angle between the pyridine ring and the Pt surface from NEXAFS data [143]. The bonding of pyridine at low temperatures appears to be through both the lone pair of electrons, which is localised on the nitrogen atom and delocalised molecular π orbitals of the ring. Of particular note, the infrared spectral data for the triosmium pyridine cluster corresponds more closely with the EELS data for adsorption at this temperature.

EXPERIMENTAL

1 General Aspects

All reactions were carried out in dry flasks under a continuous flow of dry nitrogen and manipulations were performed using standard Schlenk techniques. All solvents were dried using standard procedures [2] and transferred to the reaction vessel using syringes. Chromium hexacarbonyl (Aldrich), dimanganese decacarbonyl (Strem), triosmium dodecacarbonyl (Strem), 1,8 diazabicyclo-[5.4.0] undec-7-ene (DBU) (Lancaster), and triphenylcarbenium tetrafluoroborate (Lancaster) were all used as supplied. Trimethylamine-N-oxide (Me$_3$NO, Lancaster) was sublimed in vacuo from the dihydrate, 2-formylthiophene (Aldrich) and aniline (Lancaster) were distilled from potassium hydroxide under reduced pressure, pyrrole (Sigma) was distilled from sodium hydroxide under reduced pressure, furan (Lancaster) was distilled from potassium hydroxide under nitrogen, phenol (Aldrich) was sublimed in vacuo and cyclohexa-1,3-diene (Aldrich) was stored over molecular sieves. The manganese and chromium complexes were sensitive to both air and moisture and manipulations were carried out in a glove box under an atmosphere of dry nitrogen. The triosmium complexes are air-stable and this allowed the chromatographic separations to be carried out in air. Thin layer chromatography was carried out using 20 x 20cm x 0.25cm glass plates coated with silica gel (Keiselgel 60 PF$_{254}$) (BDH) which had been activated by drying at 120°C for one hour. Eluting solvents were dried before use.

Infrared spectra were recorded as KBr discs or as solutions using a solution cell with CaF$_2$ windows (path

length 0.1mm) on a Mattson Polaris FTIR spectrometer with database attached. Low temperature (-196°C) FTIR spectra were obtained using the cell shown in Figure 4.1.

Figure 4.1 *The apparatus for collecting low temperature infra red spectra*
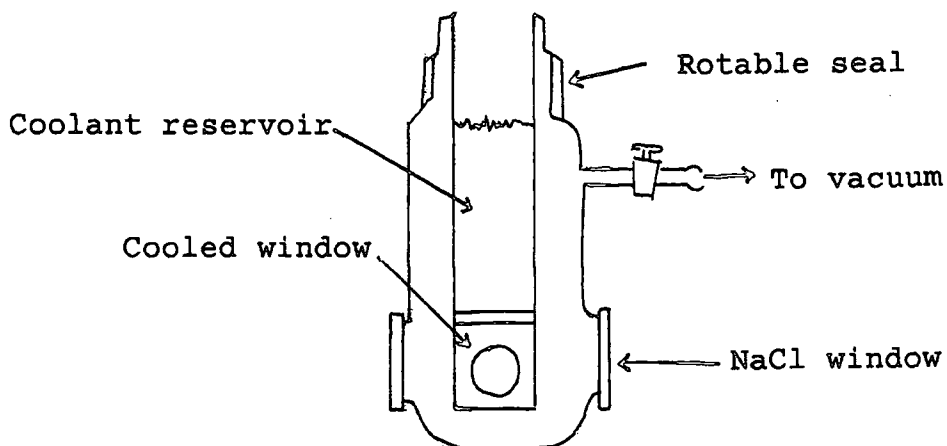
Having recorded spectra from a KBr disc at room temperature the disc was placed in the cell, the cell evacuated, fixed in place in the spectrometer sample cavity and the disc cooled to -196°C by addition of liquid nitrogen to the reservoir.

FT-Raman spectra were recorded at the University of East Anglia. Proton NMR spectra were recorded using a Brucker HX90E spectrometer at 250MHz and a Varian VXR400S spectrometer at 400MHz. ^{13}C NMR spectra were recorded at 100MHz using the Varian VXR400S spectrometer. Deuterochloroform solutions were used, unless stated otherwise, and TMS was the internal reference. C, H and N analyses were carried out by the departmental analyst using a Carlo Erba 1106 Elemental Analyser. NMR and elemental analysis data were found to be in close agreement with literature data for the complexes prepared.

2 Preparation of $(\eta^6 C_6 H_6)Cr(CO)_3$ [1a]

Chromium hexacarbonyl (1.79g, 8.4mmol), benzene (3ml) and monoglyme (7ml) were placed in a round bottomed flask, which was kept wrapped in aluminium foil, as $Cr(CO)_6$ is light sensitive. The mixture was heated under reflux, under a nitrogen atmosphere, for 9 hours. After cooling to room temperature a portion of diethyl ether (100ml) was used to dilute the mixture and the solution was filtered through a filter stick under gravity. The filtrate was collected and

the solvent removed *in vacuo* to leave a pale yellow solid. Recrystallization was carried out from petroleum ether (40-60°).

^{1}H NMR (CDCl$_3$, 250MHz, 25°C): 0.00 (s, TMS), 5.32 (s, C$_6$H$_6$), 7.27 (s, CHCl$_3$) ppm. Some broadening was detected and was due to paramagnetic impurities.
Literature values: (CDCl$_3$, 90MHz, 25°C) 5.3 (s, 6H) ppm [1b].

3 Preparation of Mn(CO)$_3$(C$_4$H$_4$NH) [8,9]

Dimanganese decacarbonyl (1.94g, 5mmol) and pyrrole (6ml) were added to octane (45ml) and the mixture heated under nitrogen under reflux for 14 hours. After cooling to room temperature the solvent was removed the yellow/orange solution *in vacuo* and a few mls of hexane added to the residue. This mixture was then placed on an alumina column and developed first with hexane. The addition of 1/4 (ratio by volume) dichloromethane/hexane eluted a yellow band which contained unreacted Mn$_2$(CO)$_{10}$. A more slowly moving yellow/orange band was obtained, containing the product. The solvent was removed *in vacuo* to yield a yellow/orange solid which was then purified by sublimation *in vacuo*.

^{1}H NMR (CDCl$_3$, 250MHz, 25°C): 0.00 (s, TMS), 5.54 (broad, H^y), 6.22 (broad, H^x), 7.27 (CHCl$_3$) ppm. Some broadening was detected and was due to paramagnetic impurities.
No literature values available.
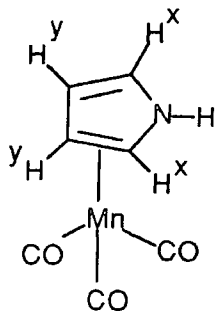
4 Preparation of H$_2$Os$_3$(CO)$_9$(μ$_3$C$_4$H$_3$N) [14]

Triosmium dodecacarbonyl (0.23g, 0.25mmol) and pyrrole (4ml) were added to degassed decalin (50ml) and the mixture heated under reflux under nitrogen for 4 hours. The yellow solution was allowed to cool to room temperature and the flask wrapped in aluminium foil to prevent any light sensitive decomposition. The solvent was removed *in vacuo* and the remaining yellow solid dissolved in hexane (5ml). The solution was separated into its components by thin layer chromatography on silica gel plates, eluting with petroleum ether (40-60°). Three bands were observed: the two minor bands of lower R$_f$ values were not characterized, but the

main broad yellow band having $R_f = 0.44$ was extracted with hexane in a soxhlet apparatus. The solvent was removed *in vacuo* and the remaining pale yellow solid was recrystallized by dissolving in the minimum volume of chloroform and precipitating with pentane.

^{1}H NMR: (CDCl$_3$, 250MHz, 25°C) -16.3 (s, OsH$_2$), 0.00 (s, TMS), 0.68 (s, CH$_x$), 1.56 (s, CH$_x$), 6.62 (dd, H^y), 7.27 (s, CHCl$_3$), 7.40(dd, H^x), 7.52 (dd, H^z) ppm.
Literature values: (CDCl$_3$, 100MHz, 27°C) -16.3 (s, OsH$_2$), 6.65 (dd, H^y), 7.43 (dd, H^x), 7.50 (dd, H^z) ppm [14,19].
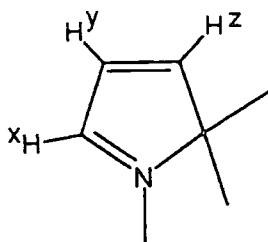
Found: C, 17.24; H, 0.70; N, 1.69%. Required: C, 17.50; H, 0.56; N, 1.57%

5 Preparation of HOs$_3$(CO)$_{10}$(μ,η^2-C$_4$H$_3$O)   [18]

Triosmium dodecacarbonyl (0.5g, 0.55mmol) was added to acetonitrile (350ml) in a two-necked round bottomed flask fitted with a pressure-equalising dropping funnel containing a solution of Me$_3$NO (0.2g) in acetonitrile (150ml). The Os$_3$(CO)$_{12}$ solution was heated to reflux under nitrogen and the Me$_3$NO solution added over 1 hour. Heating continued for ca. 6 hours until an IR spectrum of the solution showed that absorptions due to Os$_3$(CO)$_{12}$ and Os$_3$(CO)$_{11}$CNMe had disappeared. Ir spectrum Os$_3$(CO)$_{10}$(CNMe)$_2$ v(CO): 2077(w), 2025(sh), 2019(vs), 1982(s), 1953(m).

After cooling to room temperature the solvent was removed *in vacuo*. Furan (100ml) was added to the dark yellow residue by vacuum transfer. The flask was wrapped in aluminium foil and allowed to warm to room temperature. After stirring the mixture for 12 hours under nitrogen, the solvent was removed *in vacuo* to leave a dark red/orange solid. After addition of pentane (ca. 10ml) the components of the mixture were separated by t.l.c. on silica gel plates, eluting with pentane. Three bands were obtained: two minor bands of lower R_f value were not characterized but the major, broad orange band of $R_f = 0.4$ was extracted using pentane in a Soxhlet apparatus. The solvent was removed *in vacuo* and the red/orange coloured residue was recrystallized from pentane to yield orange needles.
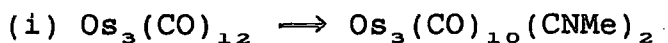
^{1}H NMR: (CDCl$_3$, 250MHz, 25°C) -15.34 (s, OsH), 0.00 (s, TMS), 1.25 (s, CH$_x$), 6.34 (dd, H^y), 7.26 (s, CHCl$_3$), 8.08 (d, H^z), 8.42 (d, H^x) ppm.
Literature values: (CDCl$_3$, 250MHz, 20°C) -15.36 (s, OsH), 6.31 (dd, H^y), 8.05 (d, H^z), 8.40 (d, H^x) ppm [18].
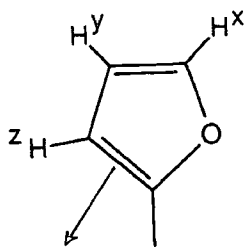
Found: C, 18.91; H, 0.61% Required: C, 18.30; H, 0.44%.

6 Preparation of H$_2$Os$_3$(CO)$_9$(C$_4$H$_2$S) [17,19]

(i) Os$_3$(CO)$_{12}$ ⟶ Os$_3$(CO)$_{10}$(CNMe)$_2$

Triosmium dodecacarbonyl (1.66g, 1.83mmol) was suspended in acetonitrile (ca. 100ml) and heated under reflux for 1 hour in order to bring about dissolution. Me$_3$NO (0.06g) in acetonitrile (ca. 50ml) was added, with continual stirring, to the cooled solution over 1 hour. The solution was allowed to cool to room temperature and an IR spectrum taken to ensure the production of the disubstituted complex. The solution was then filtered through silica gel on a filter stick to remove excess Me$_3$NO and decomposition products. The solvent was removed *in vacuo* to leave an orange/yellow residue of Os$_3$(CO)$_{10}$(CNMe)$_2$.

(ii) Os$_3$(CO)$_{10}$(CNMe)$_2$ ⟶ HOs$_3$(CO)$_{10}$(C$_4$H$_3$S.CHO)

Cyclohexane (30ml) and 2-formylthiophene (2ml) were added to the residue of stage (i) and the mixture heated under reflux for two hours. The solution was allowed to cool to room temperature and the solvent then removed *in vacuo*. The residue was dissolved in a small volume of petroleum ether (40-60°) and the components separated using t.l.c. on silica gel plates. The eluting solvent mixture was petroleum ether (40-60°)/dichloromethane (>90/<10 ratio by volume). Three bands were observed (in order of increasing R$_f$ value): a narrow orange band, a broad yellow band and a narrow yellow band. The broad yellow band was extracted with petroleum ether (40-60°) using a Soxhlet apparatus. After cooling and filtering the solution, the solvent was removed *in vacuo* to yield HOs$_3$(CO)$_{10}$(C$_4$H$_3$S.CHO).

(iii) $HOs_3(CO)_{10}(C_4H_3S.CHO) \longrightarrow H_2Os_3(CO)_9(C_4H_2S)$

Cyclohexane (50ml) was added to the residue of stage (ii) and the solution heated under reflux for 15 hours. After cooling to room temperature the solvent was removed from the clear yellow solution *in vacuo* and the residue dissolved in a small volume of petroleum ether (40-60°). The components were separated by t.l.c. on silica gel plates using petroleum ether(40-60°)/pentane/dichloromethane (40/40/20 ratio by volume) as eluant. Three bands were obtained: R_f = 0.22, yellow; R_f = 0.31 yellow, narrow, and R_f = 0.42 yellow, broad. The products were extracted with petroleum ether (40-60°) using a Soxhlet apparatus. Following recrystallization from pentane/dichloromethane (10/1 ratio by volume) the band of lowest R_f value gave insufficient material to characterize. The band having R_f = 0.31 yielded a pale yellow solid, and the band of highest R_f value gave a red/orange solid. This was characterized as a mixture of the *endo* and *exo* isomers of $H_2Os_3(CO)_9(C_4H_2S)$.

^{1}H NMR (red/orange solid): $(CDCl_3,$ 400MHz, 25°C) -13.66 (s, OsH), 0.00 (s,TMS), 1.25 (s, CH_x), 1.56 (s, CH_x), 7.19 (broad, H[y]), 7.26 (s, $CHCl_3$), 7.82 (dd, H[z]), 7.88 (dd, H[x]) ppm.
Literature values: $(CDCl_3,$ 300MHz, 56°C) -14.88 (s, OsH), 7.00 (broad dd, H[y]), 8.07 (broad s, H[z]), 8.69 (d, H[x]) ppm [20].
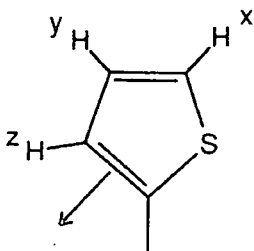
7 Preparation of $HOs_3(CO)_{10}(NHC_6H_5)$ [21]

A solution of $Os_3(CO)_{12}$ (0.3g, 0.33mmol) in aniline (20ml) was heated under reflux for 1.25 hours. The dark brown solution was allowed to cool to room temperature and the solvent removed under reduced pressure to leave a very dark brown oily residue. This was dissolved in a small volume of dichloromethane and the components separared by t.l.c. on silica gel plates using pentane/dichloromethane (90/10 ratio by volume) as eluant. A number of bands were observed: a narrow yellow band, two purple bands, an orange/red band and a broad yellow band of R_f = 0.5. The products were not isolated from the bands of lowest R_f value. The orange and yellow bands were extracted using CH_2Cl_2 in a Soxhlet apparatus. The solvent was removed under reduced pressure and the products recrystallized from

pentane/dichloromethane. The orange band yielded an orange solid. The yellow band was recrystallized from pentane from which an orange solid precipitated. The solvent was removed from the mother liquor under reduced pressure and a yellow solid was obtained from recrystallization with pentane/CH_2Cl_2. The yellow solid was characterized as $H_2Os_3(CO)_9(HNC_6H_4)$ and the orange solid as $HOs_3(CO)_{10}(NHPh)$.

^{1}H NMR (yellow solid): ($CDCl_3$, 250MHz, 25°C) -14.11 (s, OsH_2), -14.10 (s, OsH_2), 0.00 (s, TMS), 1.25 (s, CH_x), 1.56 (CH_x), 5.31 (broad, NH), 6.78 (m, C_6H_4), 7.23 (dd, C_6H_4), 7.26 (s, $CHCl_3$) ppm.

Literature values ($H_2Os_3(CO)_9(HNC_6H_4)$): ($CDCl_3$, 100MHz, 27°C) -14.47 (s, OsH), -14.03 (s, OsH), 5.25 (broad, NH), 6.51 (m, 3H C_6H_4), 7.49 (dd, 1H C_6H_4) ppm [21].

^{1}H NMR (orange solid): ($CDCl_3$, 250MHz, 25°C) -14.09 (s, OsH), 0.00 (s, TMS), 1.56 (s, CH_x), 6.78-7.23 (m, Ph), 7.26 (s, $CHCl_3$) ppm.

Literature values ($HOs_3(CO)_{10}(NHPh)$): ($CDCl_3$, 100MHz, 27°C) -14.13 (d, OsH), 5.8 (broad, NH), 6.7-7.3 (m, Ph) ppm [21].

8 Preparation of $HOs_3(CO)_{10}(OPh)$ and $H_2Os_3(CO)_9(OC_6H_4)$ [24]

(i) Preparation of $HOs_3(CO)_{10}(OPh)$

Triosmium dodecacarbonyl (0.4g, 0.44mmol) and phenol (1.5g) were added to xylene (130ml) and the mixture heated under reflux for 10 hours. After cooling to room temperature the solvent was removed under reduced pressure to leave a dark yellow/orange oil. This was dissolved in the minimum volume of petroleum ether (40-60°) and the components separated by t.l.c. on silica gel plates using petroleum ether (40-60°)/toluene (9/1 ratio by volume) as eluant. An orange and purple band were observed at low R_f values, together with two yellow bands, one broad (R_f = 0.5) and the other narrower (R_f = 0.33). Both were separately extracted using petroleum ether (40-60°) in a Soxhlet apparatus. The narrower band did not yield sufficient material for characterization, but the broad band yielded a yellow solid following recrystallization from pentane.

^{1}H NMR: ($CDCl_3$, 250MHz, 25°C) -12.18 (s, OsH), 0.00 (s, TMS), 1.25 (s, CH_x), 1.56 (s, CH_x), 6.45 (d, H^2, H^6), 6.89 (m, H^3-H^5), 7.26 (s, $CHCl_3$) ppm.
Literature values: ($CDCl_3$, 100MHz, 27°C) -12.20 (s, OsH), 6.43 (d, H^2, H^6), 7.0 (m, H^3-H^5) ppm [24].
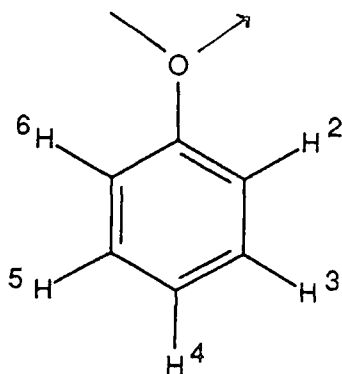
(ii) <u>Preparation of $H_2Os_3(CO)_9(OC_6H_4)$</u>

The product of stage (i) was dissolved in decalin (100ml) and heated for 9 hours at 130°C. After cooling to room temperature the solvent was removed under reduced pressure and the remaining yellow/brown oil dissolved in the minimum volume of petroleum ether (40-60°). The components were separated by t.l.c. on silica gel plates using petroleum ether (40-60°)/toluene (9/1 ratio by volume) as eluant. There was a narrow yellow band at low R_f value and one broad, bright yellow band at R_f = 0.4. Both were extracted separately using petroleum ether (40-60°)/toluene (9/1). The broad band proved to be unchanged starting material, but the low R_f band gave the required product in very low yield as a yellow solid on recrystallization from pentane/CH_2Cl_2.

<u>^{1}H NMR</u>: ($CDCl_3$, 250MHz, 25°C) -13.85 (s, OsH), -11.45 (s, OsH), 0.00 (s, TMS), 1.74 (s, CH_x), 6.23 (m, H^4), 6.64 (d, H^6), 7.26 (s, $CHCl_3$), 7.45 (m, H^3), 7.90 (m, H^5) ppm.
<u>Literature values</u>: ($CDCl_3$, 100MHz, 27°C) -14.06 (broad s, OsH), -11.66 (broad s, OsH), 6.04 (ddd, H^4), 6.42 (d, H^6), 7.24 (dd, H^3), 7.69 (ddd, H^5) ppm [24].
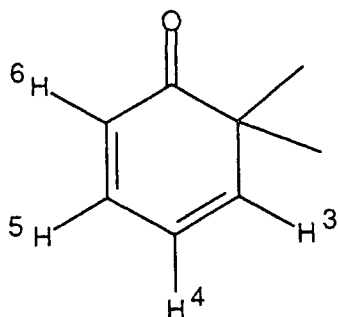
9 Preparation of Os$_3$(CO)$_9$(C$_6$H$_6$)   [26]

Triosmium dodecacarbonyl (0.39g, 0.43mmol) was added to n-octane (130ml) and the mixture heated under reflux at 125°C. Hydrogen gas (BOC, research grade) was bubbled through the refluxing mixture for ca. 2.5 hours and the dark purple solution then allowed to cool to room temperature. Cyclohexa-1,3-diene (1.5ml) was added to the solution and the mixture heated under reflux at 125°C for ca. 50 minutes. After cooling to room temperature the solvent was removed under reduced pressure and the residue extracted with dichloromethane (ca. 30ml). The solution was filtered and the volume reduced to ca. 15ml. [CPh$_3$][BF$_4$] (0.668g) was added to the solution in the glove box and the mixture heated under reflux for 30 minutes. After cooling to room temperature the dark solution was decanted to leave a bright yellow solid, which was washed with dichloromethane and dried *in vacuo*.

The solid was suspended in dichloromethane (ca. 60ml) and DBU (50µl) added in the glove box. The mixture was stirred for 20 minutes at room temperature to give a clear yellow solution which was then reduced in volume *in vacuo* to ca. 5-10ml. The mixture was purified by t.l.c. on silica gel using dichloromethane/hexane (60/40% ratio by volume) as eluant. A single pale yellow band was obtained which was extracted with the eluting mixture using a Soxhlet apparatus. A pale yellow solid was obtained after recrystallization from CH$_2$Cl$_2$/hexane and was characterized as Os$_3$(CO)$_9$(C$_6$H$_6$).

The changes in ligand bonding on exposure to light were investigated in the following manner. A sample of the benzene complex was dissolved in dry toluene in an nmr tube and allowed to stand in the light for several days. The solvent was removed under reduced pressure to leave a yellow solid which was then characterized by ^{1}H nmr and FTIR as H$_2$Os$_3$(CO)$_9$(C$_6$H$_4$) [27].

^{1}H NMR: (CDCl$_3$, 400MHz, 25°C) 0,00 (s, TMS), 1.55 (s, CH$_x$), 4.37 (s, C$_6$H$_6$), 7.26 (s, CHCl$_3$) ppm.
^{13}C{^{1}H} NMR: (CDCl$_3$, 100MHz, 25°C) 0.00 (s, TMS), 38.15 (s, C$_6$H$_6$), 77.01 (t, [13]CDCl$_3$), 175.24 (s, 6CO) ppm.
Literature values: ^{1}H NMR (CD$_2$Cl$_2$, 400MHz, 25°C) 4.42 (s, 6H) ppm.
^{13}C{^{1}H} NMR (CD$_2$Cl$_2$, 100MHz, 25°C) 175.86 (s, 6CO), 175.82 (s, 3CO), 38.15 (s, 6C) ppm [26].

After exposure to light:
^{1}H NMR (CDCl$_3$, 400MHz, 25°C) -18.99 (s, OsH), 1.25 (s, CH$_x$). 1.56 (s, CH$_x$), 4.37 (s, C$_6$H$_6$), 6.88 (m, H^2, H^3), 7.26 (s, CHCl$_3$), 7.88 (m, H^1, H^4) ppm.
Literature values: (CDCl$_3$, 80MHz, 25°C) -18.9 (s, OsH), 6.73 (dd, H^2,H^3), 7.84 (d, H^1, H^4) ppm [202].

RESULTS AND DISCUSSION

1 Introduction

Comparison of vibrational data represents one of the few means of examining a moiety as both a chemisorbate on a metal surface and as a ligand in a structurally well-characterized molecular metal complex. The use of model complexes containing only carbonyl groups beside the ligand of interest is particularly suitable for this task, and there has been success for vibrational studies of small molecular fragments on metal cluster compounds in the identification of species on catalytically important metal surfaces [46]. To facilitate such studies it is important to have a good understanding of the spectroscopic characteristics of the basic cluster framework.

1.1 Assigning Infrared Spectra of Solids

The task of assigning each vibration specifically is impossible without detailed normal coordinate analysis which is beyond the scope of these investigations. The method used here is one of comparison, using published vibrational spectral data for the free ligand molecules to assist in band assignment. Where possible spectra taken from the ligand in the solid state have been used. A problem is that almost all of the organometallic complexes prepared here lack any symmetry, which means that almost all of the Raman and IR vibrations should be allowed, though many may be weak. Analysis has been applied to the carbonyl vibrations in the manner of Anson and Jayasooria [34,45].

In solids, intermolecular forces are so great that treatments for isolated molecules are wholly inadequate [39]. The effects of randomness of environment and of quantised rotation are absent from IR spectra of crystalline solids and very sharp vibrational bands may be observed. The spectra of solid samples often contain more bands than expected on the basis of the molecular symmetry of single, isolated molecules. The molecule may be situated in a position where its environment has a lower symmetry than that of the isolated molecule itself. The point group of the site within the crystal lattice may therefore involve fewer symmetry operations than the point group of the free molecule and it is this site symmetry that governs the vibrational spectrum. Where this is the case bands previously IR or Raman forbidden may become allowed and bands arising from degenerate vibrations (E or T irreducible representations) may split in the solid.

Further complications of solid phase spectra can arise from factor group splitting (or correlation splitting). This is due to strong intermolecular forces where there are two or more molecules in the unit cell. The chief result is that

even modes that are non-degenerate when one molecule is considered can give rise to two or more components in the solid phase spectrum.

In the case of a crystalline solid there is also the possible appearance of lattice modes, which involve motions of whole molecules rather than of their constituent atoms. These are vibrations due to translatory and rotatory motions of a molecule in a crystal lattice [3]. A full factor group analysis of the motions of the entire cell is required to account for these [36,37]. The modes are usually of rather low frequency ($<300cm^{-1}$) and can often be ignored except in the far IR region and at low frequencies in Raman spectra. It is possible for such lattice modes to combine with higher frequency modes giving weak additional features near strong fundamental bands, or near the expected positions of weak or missing fundamentals. These can complicate the assignment of spectra of crystals, and care is needed in deciding on the numbers of active fundamentals in crystal spectra [38].

Where the compounds were prepared in sufficiently high yield FT-Raman spectra were obtained to provide information complementary to IR. The low temperature IR spectra have been obtained in order to assist further in the assignment of bands. The bands should be sharper, with smaller splittings. Changes are only seen in the low temperature spectra if phase changes occur, since rotational fine structure is removed at low temperatures [37].

1.2 Site and factor group analysis

According to Halford [40] the vibrations of a molecule in the crystalline state are governed by a new selection rule derived from site symmetry. This can be found using the following two conditions: (1) the site group must be a subgroup of both the space group of the crystal and the molecular point group of the isolated molecule, and (2) the number of equivalent sites must be equal to the number of molecules in the unit cell (Z). In general the site symmetry is lower than the molecular symmetry in an isolated state [3].

1.3 $Os_3(CO)_{12}$: An example of the factor group approach

$Os_3(CO)_{12}$ provides a useful example. The molecular point group is D_{3h}, but the compound crystallizes in the space group $P2_1/n$ (C_{2h}^5) with four molecules per primitive unit cell [41,42]. The isolated molecule is shown in Figure 4.2.

Figure 4.2   *The structure of $Os_3(CO)_{12}$*
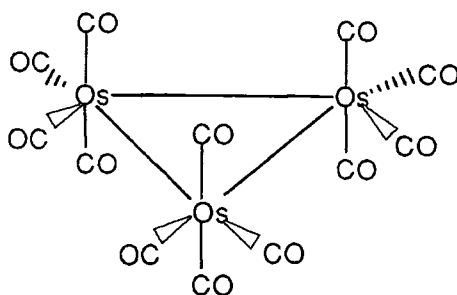
The use of group theory gives the irreducible representations for the equatorial (radial) and axial CO groups as follows:

$$\Gamma_{coaxial} = A_1' + E' + A_2'' + E''$$
$$\Gamma_{coradial} = A_1' + A_2' + 2E'$$

E' and A_2'' are ir active and hence four bands should be seen for the CO stretching modes of the isolated molecule.

The solution IR spectrum shows there are four bands at 2068 (E' axial), 2034 (A_2'' axial), 2018 (E' radial) and 1999 (E' radial) cm^{-1}. The axial vibrations are more intense than the radial as a result of the difference in π back bonding. The axial CO groups compete equally for a share of the π donation of electrons from the metal atoms, with the result that the CO bond order is higher, and hence the frequency of the vibrations is higher. The equatorial groups are opposite the metal-metal bonds and the π back donation will be greater, which in turn lowers the CO bond order and also the vibrational frequency. The effect on the Os-C bond lengths is to shorten those in the equatorial plane and to lengthen those in the axial plane: this is confirmed by x-ray crystallography, 1.912 vs 1.946A [48].

From Halford's table [40] the possible site symmetries for space group C_{2h}^5 are:
$$4C_1(2) \quad and \quad C_1(4)$$
where the number in front of the point group notation indicates the number of distinct sets of sites of that symmetry and the number in parenthesis denotes the number of equivalent sites for each distinct set. By applying the two conditions imposed above, the site group is C_1.

Correlation of the molecular symmetry species with the factor group symmetry species via the site group is shown below.

Molecular symmetry	Site group	Factor group
D_{3h}	C_1	$P2_1/n$ (C_{2h}^5)

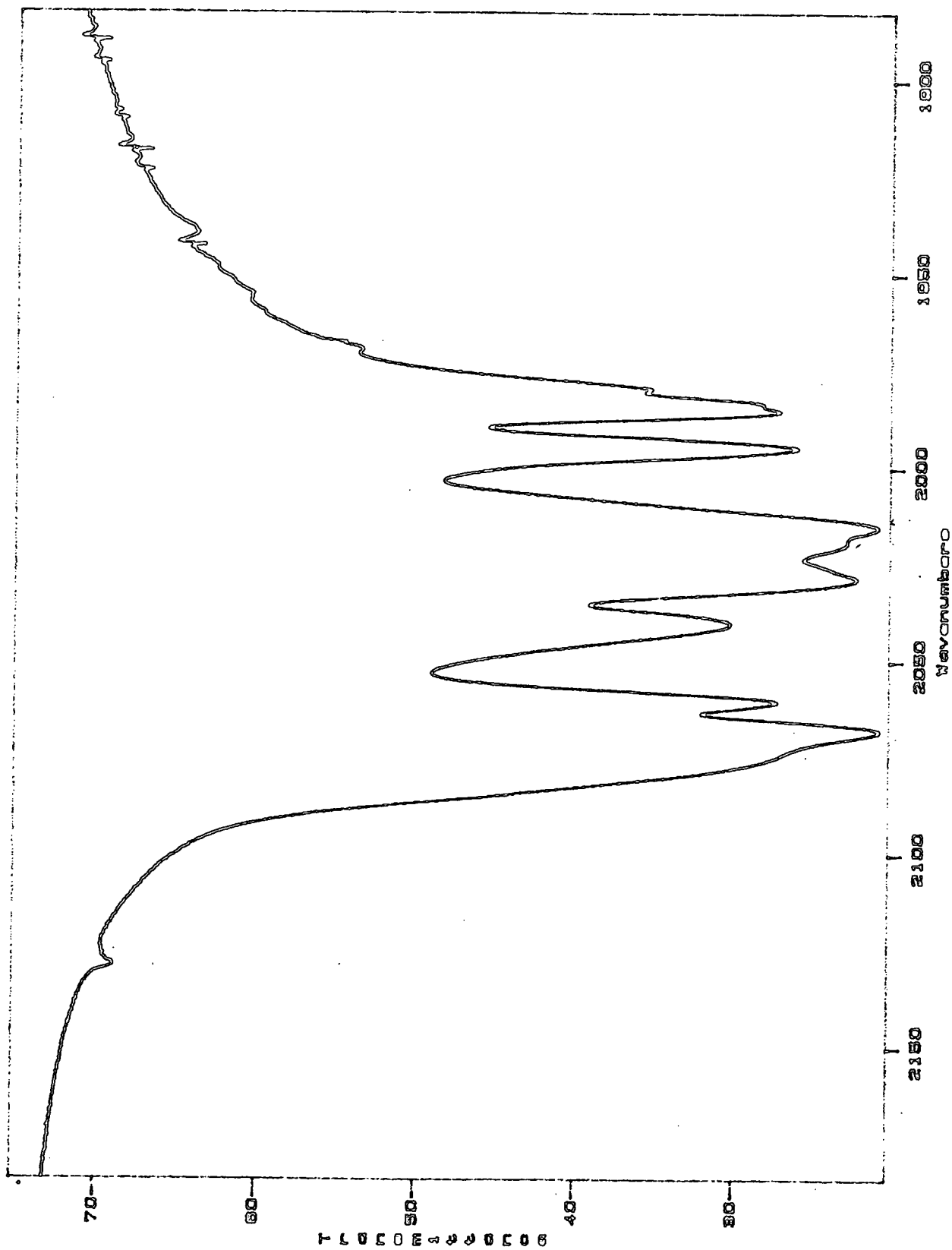| Molecular symmetry				Factor group
$2A_1'$				A_g (12)
$1A_2'$				B_g (12)
$3E'$		A		A_u (12)
$0A_1''$				B_u (12)
$1A_2''$				
$1E''$				

Under the C_1 site symmetry all the molecular modes have the A representation. Using correlation tables, the factor group symmetry gives rise to four modes of the representations shown. The doubly degenerate E modes will also be split so that they give rise to 2 x 3(A_g + B_g + A_u + B_u). There are 48 vibrations in total, 24 IR (A_u and B_u) and 24 Raman active (A_g and B_g).

However, on consideration of the solid state Raman and IR spectra [41,42] Anson and Jayasooria [34] found that many of the predicted features were weak or unobserved, and only half the predicted number of modes had significant intensity. Their examination of the crystal structure showed that it could be obtained by a relatively small distortion of the more symmetric structure of space group I2/m (C_{2h}^3) with Z = 4 [44]. The cluster molecules now occupy positions of C_s site symmetry. The correlation of the molecular symmetry with the new factor group symmetry species is shown below.

Molecular symmetry	Site group	Factor group
D_{3h}	C_s	I2/m (C_{2h}^3)
$2A_1'$ ————————	$2A'$ ————————	$2(A_g + B_u)$
$1A_2'$ ————————	A'' ————————	$(A_u + B_g)$
$3E'$ ————————	$3(A'' + A')$ ————————	$3(A_g + B_u + A_u + B_g)$
$1A_2''$ ————————	A' ————————	$(A_g + B_u)$
$1E''$ ————————	$(A' + A'')$ ————————	$(A_g + B_u + A_u + B_g)$

This site symmetry leads to 24 vibrational modes, 12 IR and 12 Raman active. Figure 4.3 shows the IR spectrum of $Os_3(CO)_{12}$ as a KBr disc at $0.5cm^{-1}$ resolution. Table 4.4 shows Anson and Jayasooria's assignment of the v(CO) region, together with the bands observed in this study.

Figure 4.3 *The infrared spectrum of the carbonyl stretching*
region of $Os_3(CO)_{12}$
(KBr disc, 0.5cm^{-1} resolution)

Table 4.4 *Assignment of the carbonyl stretching region of $Os_3(CO)_{12}$ and the spectral activities under the molecular symmetry and the latent factor-group and site group symmetries*

Molecular mode°	Latent site group C_s	Factor group $C_{2h}(P2_1/n)$	Activity under Molecular D_{3h}	Activity under Latent factor-group $C_{2h}(12/m)$	Frequency assignment [$Os_3(CO)_{12}$]
$\nu_1(a_1\cdot)$ 2120.0 (2130.0)		a_g	√	√	2130 s
		b_g	√	—	n.o.
		a_u	—	—	n.o.
		b_u	—	√	2131.5 vw
$\nu_5(e')$ 2061.2 (2069.0)	a'	a_g	√	√	2070 w
		b_g	√	—	n.o.
		a_u	√	—	n.o.
		b_u	√	√	2062.1 s
	a''	a_g	√	—	2063 w
		b_g	√	√	2034 w
		a_u	√	√	2073.3 vs
		b_u	√	—	2087.7 vw, sh
$\nu_2(a_1')$ 2036.0 (2038.0)		a_g	√	√	2023 vs
		b_g	√	—	n.o.
		a_u	—	—	n.o.
		b_u	—	√	2039.9 m
$\nu_4(a''_2)$ 2031.1 (2036.5)		a_g	—	√	2028 s
		b_g	—	—	n.o.
		a_u	√	—	2044.8 w, sh
		b_u	√	√	2030.8 s
$\nu_6(e')$ 2018.7 (2015.6)	a'	a_g	√	√	2004 m
		b_g	√	—	n.o.
		a_u	√	—	2015.8 mw
		b_u	√	√	2018.2 s
	a''	a_g	√	—	n.o.
		b_g	√	√	2017 m
		a_u	√	√	2021.5 s
		b_u	√	—	2027.4 m
$\nu_7(e')$ 2012.5 (2004.7)	a'	a_g	√	√	1985 m
		b_g	√	—	n.o.
		a_u	√	—	1988 w, sh
		b_u	√	√	1986.4 s
	a''	a_g	√	—	n.o.
		b_g	√	√	1997 m
		a_u	√	√	1995.1 s
		b_u	√	—	2002 w, sh
$\nu_3(a_2')$ 1999.5 (1987.0)		a_g	—	—	n.o.
		b_g	—	√	n.o.
		a_u	—	√	1968.1 w
		b_u	—	—	n.o.
$\nu_8(e'')$ 1994.5 (1995.5)	a'	a_g	√	√	1975 s
		b_g	√	—	n.o.
		a_u	—	—	1976.3 w
		b_u	—	√	1979.2 m
	a''	a_g	√	—	n.o.
		b_g	√	√	1980 m
		a_u	—	√	1982.6 m
		b_u	—	—	n.o.

The major transfer of IR intensity on going from solution to solid state seems to be from the higher frequency molecular modes to those at lower frequency. The former modes undergo very small shifts (0-$3cm^{-1}$, comparable to the shifts on cooling a polycrystalline sample from room to low temperature) but the modes at lower frequency show a solution to crystal reduction of up to $15cm^{-1}$.

The vibrational spectra in the range 650-$350cm^{-1}$ have been investigated to a much lesser extent, the main reason being the complexity of the spectra due to vibrations assignable to two types of internal coordinates $v(Os$-$C)$ and $\delta(Os$-$CO)$ [45].

Adams and Taylor [47] have identified the irreducible representations for the Os-CO stretching and deformation modes:

$$\Gamma_{v(CO)} = 2A_1' + 3E' + A_2'' + E'' + A_2'$$

$$\Gamma_{d(Os$-$C$-$O)} = 2A_1' + 4E' + 2A_1'' + 4E'' + 2A_2'' + 2A_2'$$

The correlation of the molecular symmetry with the new factor group symmetry species is shown below.

Molecular symmetry	Site group	Factor group
D_{3h}	C_s	$I2/m\ (C_{2h}^3)$

$v(Os$-$CO)$

$2A_1'$ ————————	$2A'$ ————	$2(A_g+B_u)$
$3E'$ ————————	$3(A'+A'')$ ——	$3(A_g+B_u+B_g+A_u)$
A_2'' ————————	A' ————	A_g+B_u
E'' ————————	$A'+A''$————	$A_g+B_u+B_g+A_u$
A_2' ————————	A'' ————	B_g+A_u

$\delta(Os$-$CO)$

$2A_1'$ ————————	$2A'$ ————	$2(A_g+B_u)$
$4E'$ ————————	$4(A'+A'')$ ——	$4(A_g+B_u+B_g+A_u)$
$2A_1''$ ————————	$2A''$ ————	$2(B_g+A_u)$
$4E''$ ————————	$4(A'+A'')$ ——	$4(A_g+B_u+B_g+A_u)$
$2A_2''$ ————————	$2A'$ ————	$2(A_g+B_u)$
$2A_2'$ ————————	$2A''$ ————	$2(B_g+A_u)$

For the Os-CO stretches 12 IR and 12 Raman modes are expected and for the deformations 24 IR and 24 Raman modes are predicted. The IR and Raman frequencies of Anson and Jayasooria are shown in Table 4.5, with the IR spectrum of $Os_3(CO)_{12}$ recorded in this study shown in Figure 4.4.

Figure 4.4 The IR spectrum of $Os_3(CO)_{12}$ in the region 700 - 400cm^{-1} (KBr disc, 4cm^{-1} resolution)
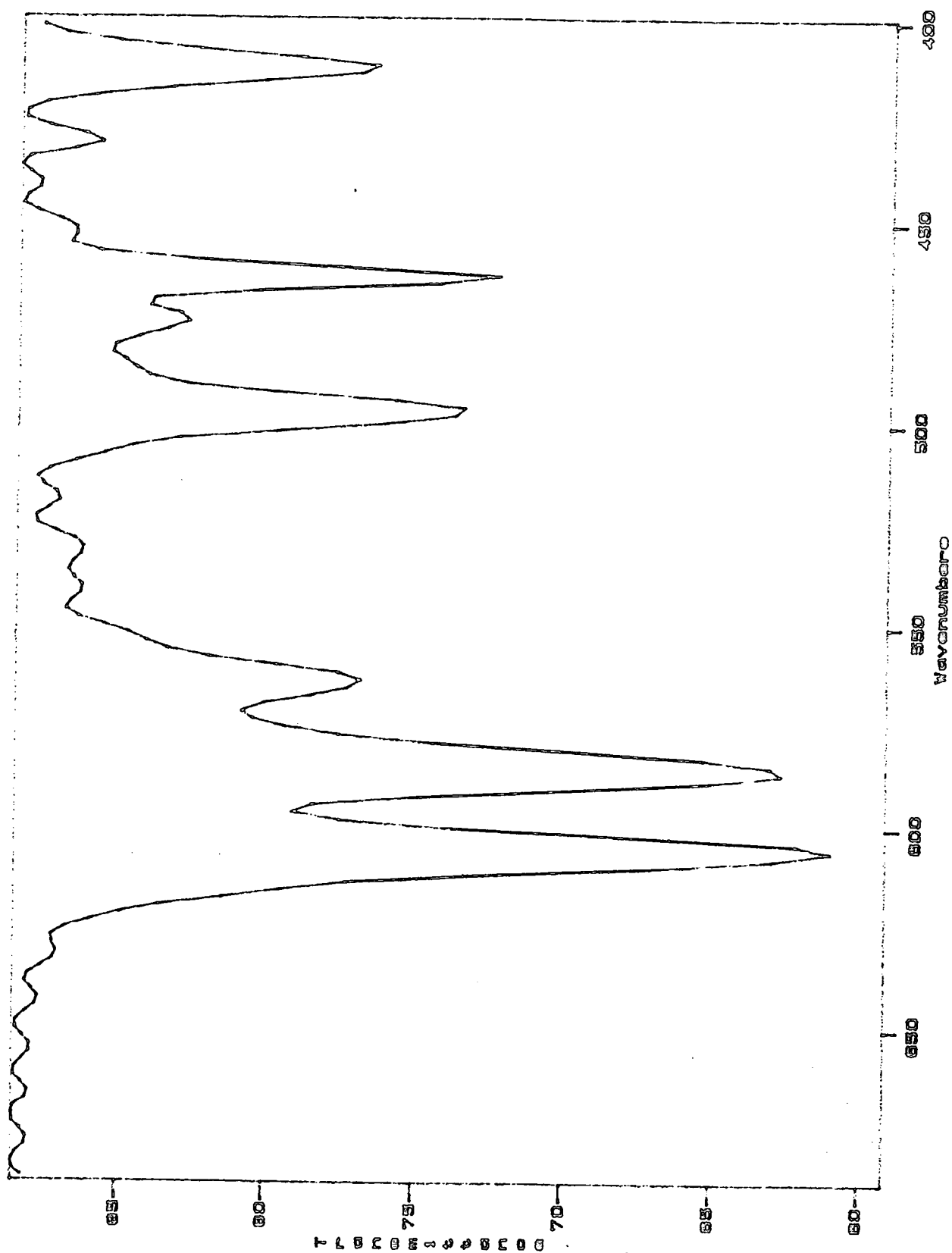
Table 4.5   *Vibrational assignments of OsCO deformation modes and Os-CO stretching modes in* $Os_3(CO)_{12}$

[Os₃(CO)₁₂] i.r.*	Raman†	Assignment‡		
620.5 vw,sh	621 w	$\nu_{10}\ a_1'$	⟩ δ_{MCO}	(eq, a_1)
618.6 w,sh / 618.1 w	615 vw	$\nu_{21}\ e''$	⟩ δ_{MCO}	(ax, a_2)
609.5 ms,sh / 606.5 s	610 vvw / 607 vvw	$\nu_{18}\ e'$		
593.5 m,sh / 589.2 s	590 vvw	$\nu_{20}\ e'$ —— δ_{MCO}		(eq, b_2)
585.3 ms	—	$\nu_{16}\ a_2''$	⟩ δ_{MCO}	(eq, b_1)
—	—	$\nu_{24}\ e''$		
571.8 w,sh / 567.5 w	565 w	$\nu_{23}\ e''$	⟩ δ_{MCO}	(ax, b_2)
563.6 m	—	$\nu_{15}\ a_2''$		
537.1 w / 534.7 vw	536 vw	$\nu_{22}\ e''$	⟩ δ_{MCO}	(eq, a_2)
531 vvw	—	$\nu_{12}\ a_1''$		
515.4 vw	516 m³ / 514 w,sh	$\nu_9\ a_1'$	⟩ δ_{MCO}	(*ax, a_1*)
502.4 s	504 w / 501 m	$\nu_{17}\ e'$		
498.1 ms	498 m	$\nu_{19}\ e'$ —— δ_{MCO}		(ax, b_1)
489.9 vw	491 vs§	$\nu_{26}\ a_1'$	⟩ δ_{MCO}	(eq, a_1)
479.2 m / 478.6 vw,sh / 474.9 m / 472.0 vw	478 w / 474 m / 470 vw	$\nu_{30}\ e'$		
465.3 s / 463 vw,sh	464 w	$\nu_{28}\ a_2''$	⟩ ν_{MC}	(ax, b_2)
458 vw / 450 vvw	455 w / 449 vw	$\nu_{32}\ e''$		
447 vvw	—	$\nu_{27}\ a_2'$	⟩ ν_{MC}	(eq, b_1)
434.9 m / 433.4 mw / 431.0 m	433 vvw / 430 vvw	$\nu_{31}\ e'$		
418.5 w,sh / 415.6 s / 414.2 ms	415 w	$\nu_{29}\ e'$	⟩ ν_{MC}	(ax, a_1)
405 w	404 m§	$\nu_{25}\ a_1'$		

* Infrared spectrum of cluster in CsI disc recorded at *ca* 95 K
† Raman spectrum recorded at *ca* 15 K

214

In general the deformation modes occur at higher frequencies than the stretches although there may be some overlap. 500cm^{-1} was proposed as the dividing frequency [49], with Adams and Taylor [47] suggesting some overlap does occur. Kettle and Stanghellini [50] found no evidence for intermolecular coupling but Butler et al [51] found site symmetry effects. The study of Anson and Jayasooria [45] using low temperature IR and Raman measurements showed for the first time the presence of significant intermolecular vibrational coupling in this frequency region. The equatorial Os-CO bonds are shorter than the axial bonds and are therefore expected to be slightly stronger and of higher frequency. There is overlap between the two, but the equatorial modes are generally to higher frequencies. However, no overlap was found between deformation and stretching modes, 491cm^{-1} being the upper frequency limit for the stretching modes. There is overlap between axial and equatorial deformation modes with the equatorial tending to higher frequency. It appears that a slight increase in the Os-C force constant leads to a similar increase in the Os-C-O force constant. A further observation is that in-plane equatorial bending modes are all at higher frequencies than the out-of-plane modes, presumably for steric reasons. An X-ray diffraction study [48] revealed the equatorial CO groups are alternatively above and below the Os$_3$ plane.

The IR data of Anson and Jayasooria's study [45] showed that both site splitting and factor group coupling are observed. The bands at 479.2, 478.6, 479.9 and 472.0cm^{-1}, assigned to v(Os-CO) of E' symmetry, reveal a site splitting of 4cm^{-1} and factor group splitting of upto 3cm^{-1}. The splitting of the A$_2$" mode (465.3 and 463.0cm^{-1}) can only result from factor group coupling. In general site splitting from modes in this region of the spectrum can be up to 5 cm^{-1}, whilst splitting resulting from intermolecular coupling is slightly smaller. This intermolecular coupling for both v(Os-CO) and δ(Os-CO) modes is of similar magnitude, even though the former might be thought to be "buried" within the molecule.

2 Triosmium carbonyl model complexes

Complexes containing ligands derived from pyrrole, furan, thiophene, aniline, phenol and benzene are discussed in turn below. Each section is split into three parts. The first deals with the organometallic chemistry of the complex, the second is concerned with the chemistry of the ligand as an adsorbate on metal surfaces and the third deals with the assignment of the vibrational spectrum. Finally, the usefulness of the complex as a model for the surface chemistry and in assisting the assignment of adsorbate vibrational spectra is discussed.

2.1 Complexes containing pyrrole ligands

2.1.1 Organometallic chemistry

Some confusion existed over the structure of the products of the reaction of pyrrole with $Os_3(CO)_{12}$. There was one isomer proposed for reaction in decalin at ca. 190°C, as illustrated below.
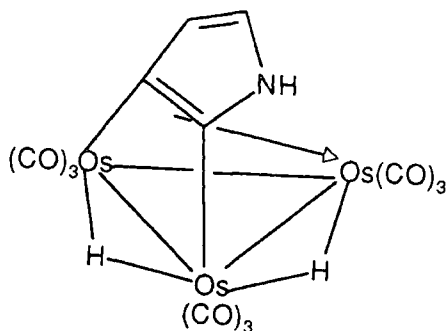
The pyrrole ligand is bridges three metal atoms, and is analogous to the benzene derivative $[Os_3H_2(CO)_9(\mu_3C_6H_4)]$ [14].

This reaction was re-examined by Deeming and co-workers [19] and three products were claimed for reaction at 174°C.
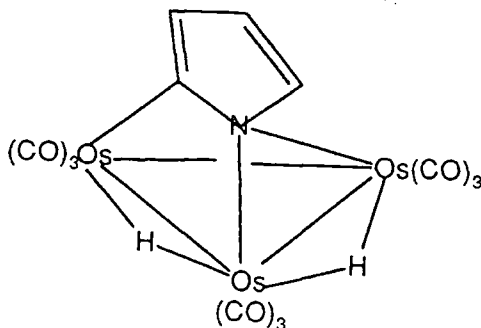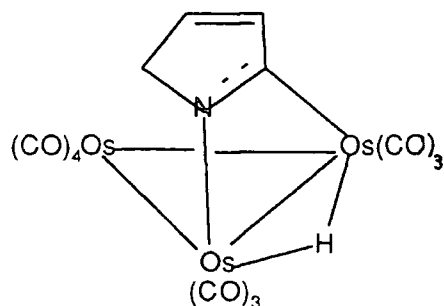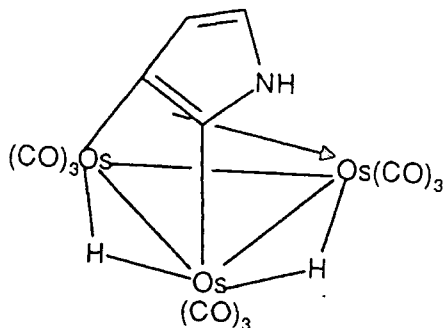
(1) 25%   (2) 40%   (3) 20%

Deeming and co-workers [15,19] subsequently used 2-

formylpyrrole for introducing pyrrole rings into triosmium clusters. The mildest entry into this chemistry is by displacement of acetonitrile ligands in $[Os_3(CO)_{10}(MeCN)_2]$ with oxidative addition of 2-formylpyrrole. There is cleavage of the aldehydic C-H bond to give the μ-acyl cluster $[Os_3H(\mu_2\text{-}NHCH=CHCH=CCO)(CO)_{10}]$ (4).
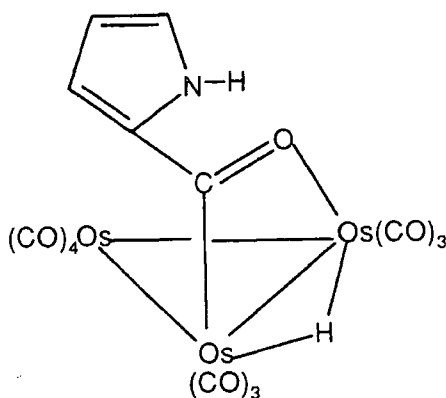
(4)

The X-ray structure has confirmed the cleavage at the aldehyde group rather than at the ring sites. The latter are known to be cleaved in the reaction of pyrrole with $[Os_3(CO)_{12}]$ [14,19]. Subsequent thermal decarbonylation of (4) (173°C, 15mins) gives two isomeric nonacarbonyl derivatives, (5) and (6), each of which contains a heterocyclic ring triply bridging an Os_3 cluster of atoms.
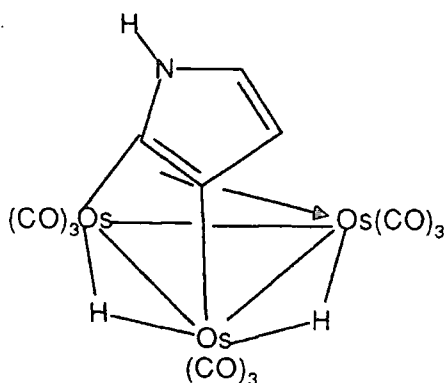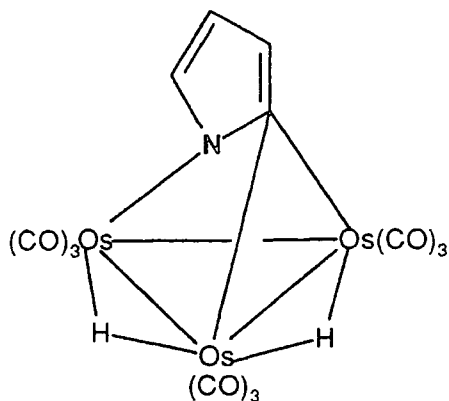
(5)   (6)

The structures of these compounds were initially based on spectroscopic evidence [14,19] but this did not uniquely define the structure of (6), previously assigned as (2). Cluster (6) has been characterised crystallographically (Figure 4.5) and the structure of (5) can be unambiguously assigned by comparison with the X-ray data of the N-methyl derivative also reported [16]. As expected the C_4N ring atoms of (6) are closely planar and this plane is perpendicular to that of the Os_3 (dihedral angle 93.0°). The small tilt is from the vertical towards Os(2), that is away

from the Os-Os edge that is not hydride-bridged. The interatomic distances in the ring are all fairly similar although the longer ones do correspond to those represented as single bonds in (6). The hydride ligands exchange (NMR coalescence) which could result from hydride migrations or the interconversion of form (6) with the less stable form (2) or from both processes. The fluxionality has not been studied in any detail.

Figure 4.5   *Molecular structure of the cluster* $[Os_3H_2(C_4H_3N)(CO)_9]$ (6)
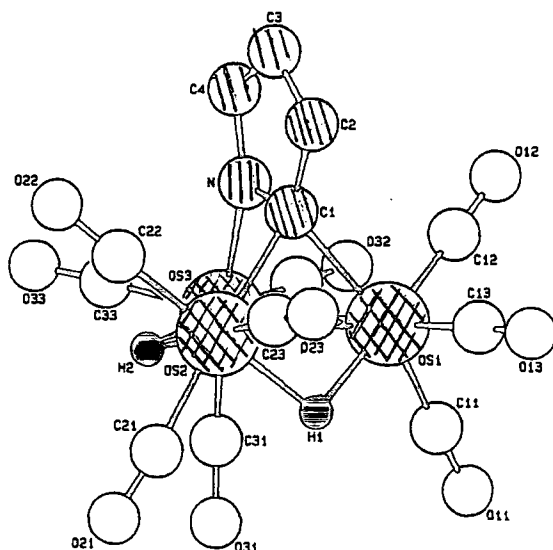

The conversion of (5) to (6) is related to that of the benzoyl cluster $[Os_3H(CO)_{10}(PhCO)]$ to the benzyne cluster $[Os_3H_2(CO)_9(C_6H_4)]$ [144,145]. There is a strong correspondence of IR and NMR data between the pyrrolyne cluster (2) and the benzyne cluster. Cluster (2) is isostructural with the N-methyl substituted analogue $[Os_3H_2(\mu_3-C_4H_2NMe)(CO)_9]$, which is extremely thermally stable and shows no tendency to isomerize at the temperatures at which (5) converts to (6). Therefore the conversion of (5) to (6) appears to depend on the presence of the NH group and likely involves the transfer of this hydrogen atom. This is not an intraligand process since $[Os_3H_2(C=CCH=CHND)(CO)_9]$ converts to $[Os_3HD(N=CHCH=CHC)(CO)_9]$. From this result it would seem that a metal hydride transfer to carbon gives the transient species $[Os_3H(C=CHCH=CHND)(CO)_9]$ followed by D atom transfer to osmium to give the product.

The structure of complex (3) is similar to those of other clusters of type $[Os_3H(\mu-X)(CO)_{10}]$ where X is a bridging ligand coordinated through adjacent atoms [145]. The formation of (3) requires hydrogen atoms to be shifted from the 1- and 2- positions of pyrrole to the metal atoms to form a hydride and an Os-C bond to the 3-position of the

ring, respectively. It is believed that this process cannot involve the u,η^2-pyrrolyl cluster [Os$_3$H(u,η^2-C=CHCH=CH=NH)(CO)$_{10}$] (7) since this is almost certainly the intermediate in the decarbonylation of (4) to give (5) initially and then (6) by isomerization. Cluster (7) closely relates to the known furanyl cluster [Os$_3$H(μ,η^2-C=CHCH=CHO)(CO)$_9$], which has been shown to convert to the furan analogue of (5) [18]. It is believed that (3) is formed as a result of oxidative addition of pyrrole with N-H cleavage in contrast to the C-H cleavage which leads to (5) and (6). Various hydrogen-transfer reactions could lead to either (8a) or (8b) shown below.
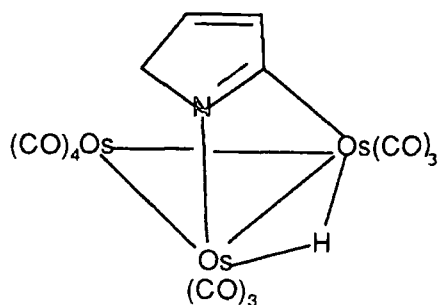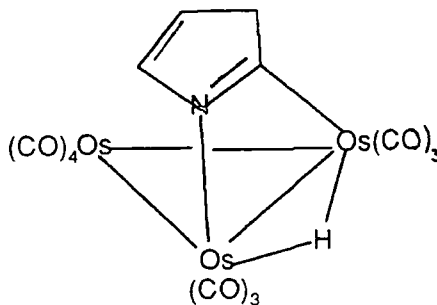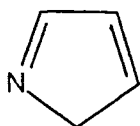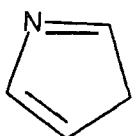

(8a)   (8b)

It is unlikely that the unstable tautomers A or B of pyrrole, shown below, are in sufficient concentration in equilibrium with pyrrole to react directly and competitively with pyrrole itself.
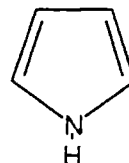
A   B   C

Almost all of this chemistry seems to be unique to triosmium clusters. For example there are no other reported examples of the pyrrole ligands found in (1) - (4). The only other organometallic compounds of pyrrole and substituted pyrroles seem to be limited to pyrrolyl complexes with M-N σ-bonds or with η^5 coordination as in azaferrocene and η^5 pyrrole complexes related to η^6 benzene complexes [146-148]. For example N-methylpyrrole forms complexes [Cr(C$_4$H$_4$NMe)(CO)$_3$] and [Fe(C$_4$H$_4$NMe)(C$_5$H$_5$)]$^+$, but the pyrrole ligands are only weakly coordinated in these species [149-152]. The sigma complexes reported by Deeming and co-workers [15] are remarkably stable, and the strength of the

σ bonds between Os and the C and N atoms are stong enough to stabilize each of the nonaromatic tautomers A and B of pyrrole.

2.1.2 Surface studies of adsorbed pyrrole

Five membered ring systems have received comparatively little attention in surface science related research although they are reaction intermediates in a number of catalytically important processes, or monomers for interesting polymers [53,60]. Pyrrole is of particular interest as a monomer in electrically conducting polymers [55,153]. Little is understood about the bonding between the conducting polymer and the electrode surface, or the orientation of the first monolayer on the substrate. The interaction of unsaturated molecules with surfaces is of great interest since such molecules have π and π^* molecular orbitals which should interact strongly with the surface [55].

Netzer *et al* [53] investigated the structure of pyrrole on Rh(111) using angle resolved UV photoelectron spectroscopy (ARUPS) in conjunction with LEED, TDS and work function measurements. The pyrrole molecules were found to interact with the surface via their aromatic π electron system. Analysis of the ARUPS data indicates that pyrrole is adsorbed at low temperature with its ring parallel to the surface, but that a fraction of pyrrole molecules splits off the N-hydrogen between 150 and 300K allowing additional interaction with the surface via the N lone pair electrons. At 300K, intact pyrrole molecules and molecules having lost their N-hydrogen coexist in the adlayer. A fraction of the molecules can be desorbed intact above 300K and in addition to hydrogen, HCN is observed as a decomposition product upon heat treatment.

The adsorption of pyrrole on Pt(111) has been studied using NEXAFS [55]. With annealing, the polarization dependence of the nitrogen K-edge spectra shows that the pyrrole becomes oriented with the molecular plane normal to the surface, whilst further annealing results in lower surface coverage and induces an orientational disordering of pyrrole and a further dissociation into N-containing species which remain on the surface. If the N-H bond remains intact it is not clear how the surface binds with the nitrogen atom. It is possible that pyrrole adopts a different structure on Pt(111) than on Rh(111) as is the case for pyridine [143,155].

Comparison has been made between the RAIRS spectrum of pyridine on Ni(100) at 300K, known to bond perpendicular to the surface, and that of pyrrole adsorbed on the Ni(100) surface at 200K [60]. Bands observed for pyridine include

δ(ring) 1620, very intense, δ(C-H) 1450, 1485, and v(C-H) 3080cm^{-1}. By contrast for pyrrole at 200K the ring modes at 1410 and 1450cm^{-1} are very weak and by applying the surface selection rule the ring must be parallel to the surface. Pi bonding occurs through the 1A$_2$ orbital. Pyrrole has been adsorbed on oxidized molybdenum and iron surfaces [60ref9,10] and was thought to adsorb via electron transfer from a π orbital to both surfaces.

Sexton [54] obtained EELS and TPS data for pyrrole adsorbed on Cu(100) at 85-300K. Adsorption is molecular and reversible.

Table 4.6 Vibrational frequencies of pyrrole adsorbed on Cu(100)

Vibrational mode and symmetry type [a]	Infrared vapour frequency [a]	Multilayer 85 K	Monolayer 200 K
γ(NH)(B$_2$)	565	600	560
γ(CH)(B$_2$)	768	760	760
δ(ring)(B$_1$)	869	880	
δ(CH)(A$_1$)	1047	1050	
δ(CH)(B$_1$)	1076		
δ(NH)(B$_1$)	1146	1160	
ν(ring)(A$_1$) ν(ring)(B$_1$)	1290 1380 1418 1466 1531	1310 1500	Screened
ν(CH)(A$_1$)	3133	3120	
ν(NH)(A$_1$)	3400	3380	

[a]Ref. [19].

γ = out-of-plane bending vibration. δ = bending vibration; ν = stretching vibration.

The molecular symmetry group for pyrrole is C$_{2v}$ with four different vibrational symmetries, A$_1$, A$_2$, B$_1$ and B$_2$. All A$_1$ and B$_1$ have dipoles in the ring plane whereas A$_2$ and B$_2$ modes involve displacements perpendicular to the ring. Thus the A$_1$, B$_1$ modes are diagnostic in-plane frequencies and B$_2$ as out-of-plane frequencies (A$_2$ modes are normally ir inactive). Screening of the intensity of either of these groups should occur for particular surface orientations if the surface-dipole selection rule is operating [156].

After warming to 200K only the B$_2$ symmetry modes of the molecule were found to be active. The screening of the other symmetry modes in the monolayer at 200K is clear evidence for orientation of the ring parallel to the Cu(100) plane. The activity of A$_1$, B$_1$ and B$_2$ modes at 170K, combined with two TDS peaks, is strong evidence for formation of a bilayer. The pyrrole rings in the second layer must be oriented with the ring planes non-parallel to the monolayer if the surface dipole selection rule is obeyed. At low exposures, the molecules are weakly π-bonded to the Cu(100) surface as the vibrational frequencies are essentialy

unperturbed   relative to the condensed phases.

Organometallic modelling of the adsorption of pyrrole on metal surfaces has not received the attention devoted to other heterocyclic systems, for example thiophene (Section 2.4), and therefore no detailed vibrational analysis has been undertaken.

2.1.3 Assignment of the FTIR spectrum of $H_2Os_3(CO)_9(\mu\text{-}C_4H_3N)$

Experimental data for this complex is contained in Table 4.7. The IR and Raman spectra are shown in Figures 4.6 and 4.7 respectively. ^1H nmr and IR data were consistent with the literature data for the structure shown below.
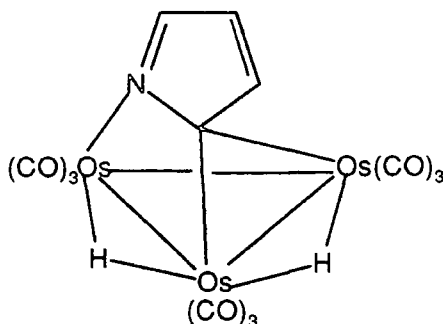
(i) Assignment of Os-C=O modes

The molecule belongs to point group C_1,   having no symmetry elements other than the identity element. The method used by,and results of, Anson and Jayasooria [34,45] have been applied here to the framework Os-CO vibrational modes, although assignments are made more difficult by the lack of symmetry. X-ray crystallography has shown that the Os-CO bonds vary between 1.85 and 1.91A [15], but the CO groups cannot be clearly defined as equatorial or axial (see Figure 4.5 in section 2.1.1).

However, replacement of three CO groups of the parent carbonyl complex $Os_3(CO)_{12}$ by bonds to N and C will affect the $v(C=O)$ frequencies since N is a good π donor and C a relatively poor one. Good π donation will lower the CO bond order and hence its frequency.

The crystal is in the space group $P2_1/c$ (C_{2h}^5) with z = 8, and this leads to a site symmetry of C_1 from Halford's tables [40].

Figure 4.6 The FTIR spectrum of $H_2Os_3(CO)_9(\mu_3\text{-}C_4H_3N)$
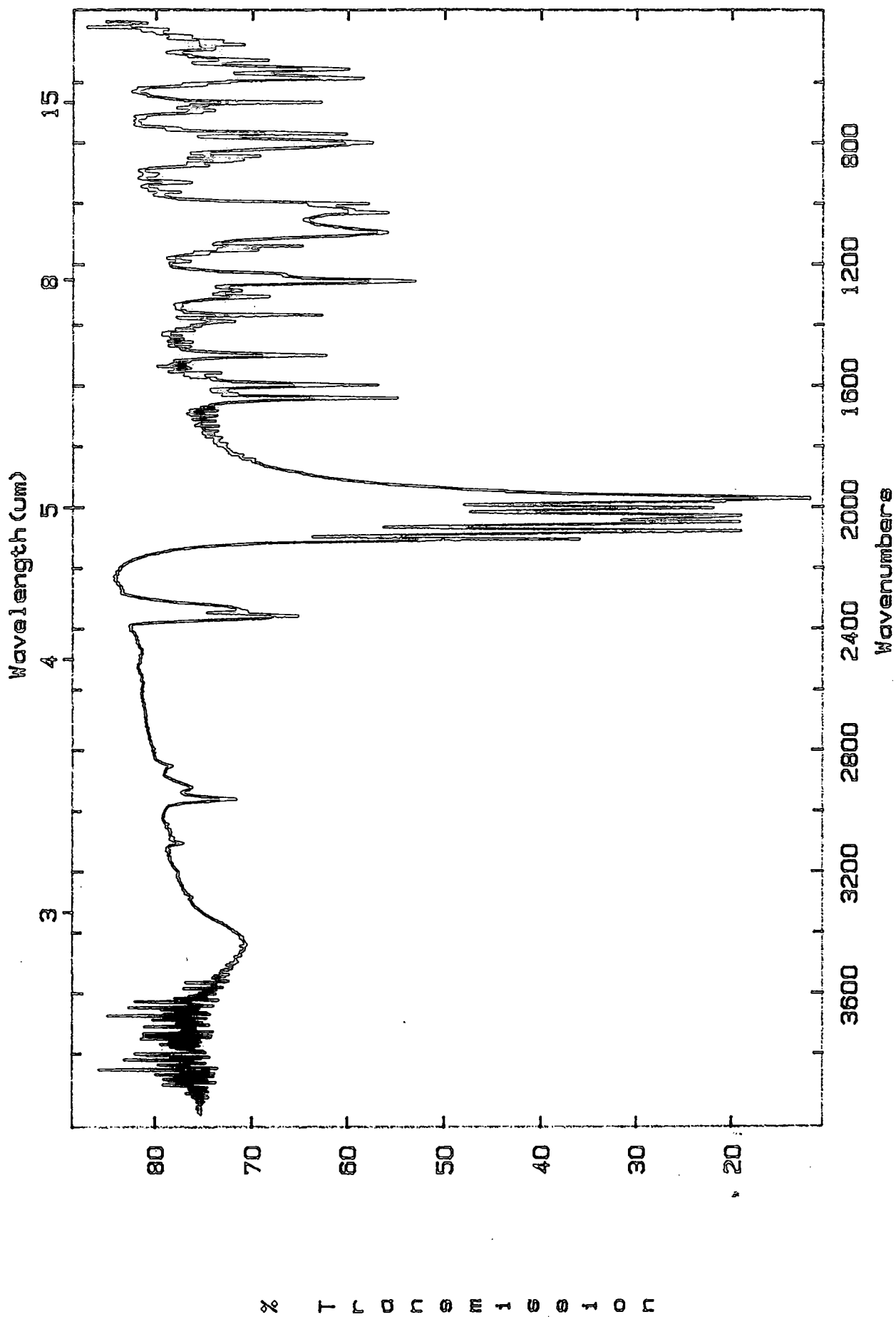
% Transmission

223

Figure 4.7 The Raman spectrum of $H_2Os_3(CO)_9(\mu_3-C_4H_3N)$
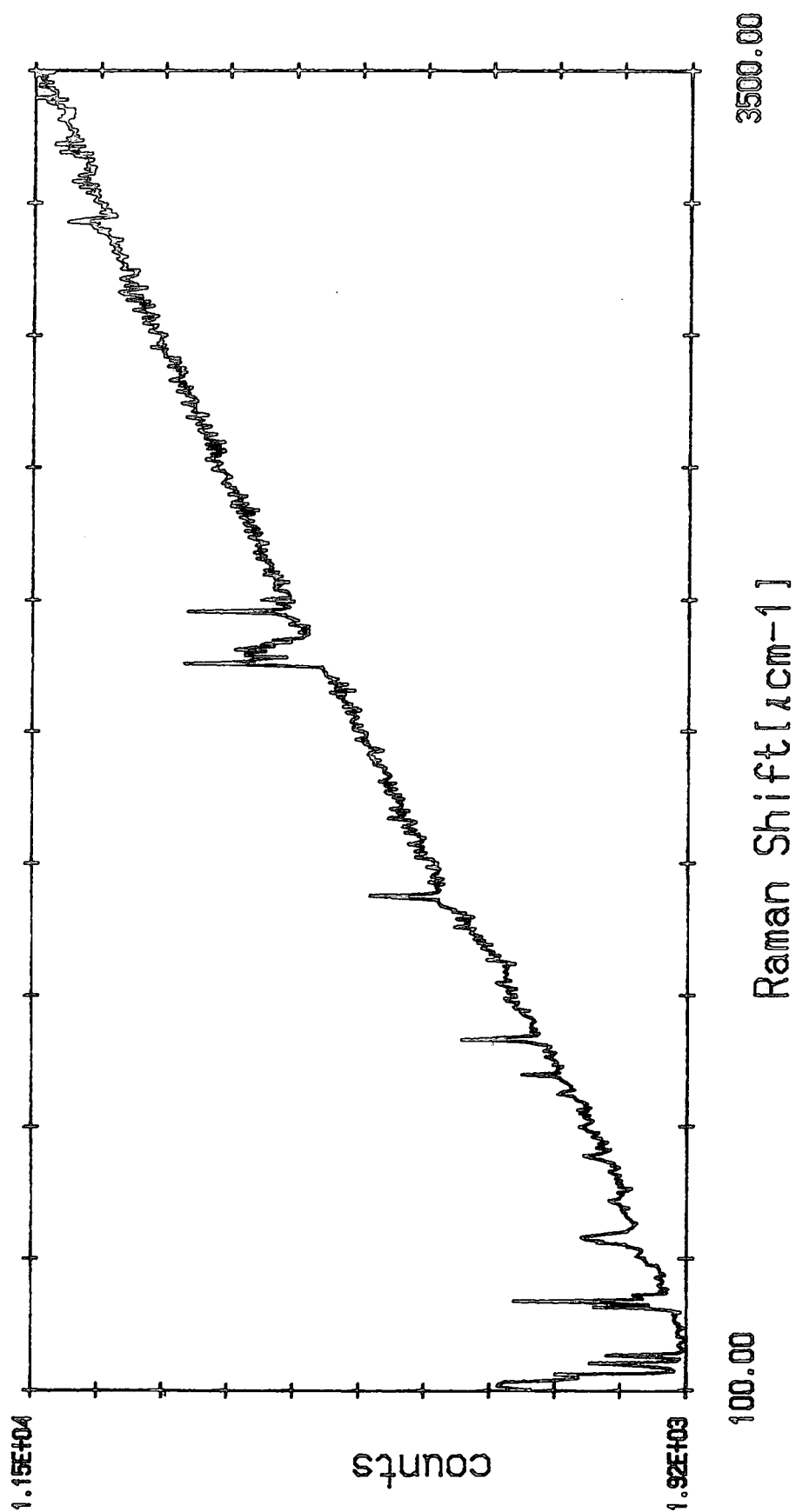
Table 4.7 Vibrational frequencies of $H_2Os_3(CO)_9(\mu_3-C_4H_3N)$

FTIR	Low temp. FTIR	Raman
3108 vw	3109 w	3109 w
3099 sh	3100 vw	
3089 vw	3058 vw	
2963 w	2963 w	
2924 w	2918 w	
2873 vw		
2853 vw	2851 w	
2108 m	2110 s	2110 s
2081 s	2083 s	2076 m
2052 s	2054 s	
2038 sh	2039 sh	2034 m
2030 s	2033 s	
2006 s	2008 s	2010 m
1985 s/sh	1985 sh	1998 m
1973 vs	1973 vs	1974 vs
1949 vw	1950 vw	
1937 vw	1939 vw	
1652 w		
1645 m		
1629 w		
1601 m		
1559 w		
1503 m		
1490 sh		
1405 vw		
1395 sh	1391 m	
1391 w		
1370 m	1373 m	1375 m
1308 m		
1297 vw	1296 w	
1290 w		
1259 m	1265 w	
1235 sh		
1193 w		
1168 w		
1156 w		
1148 sh	1146 m	
1144 m		
1106 m	1111 m	
1099 m		
1033 m	1036 m	
1023 sh		
1002 m	1007 m	1005 m
965 w		
954 w		
933 w		
911 vw	912 vw	915 m
905 vw	909 vw	

878 w	882 w	
864 w	864 w	
859 w		
847 w		
841 sh		
826 sh		
815 sh	818 sh	
803 m	806 w	
774 m	777 w	
768 m		
756 w	754 vw	
	745 vw	
702 w	725 vw	725 w
695 w	712 w	
680 w	673 w	
669 m	667 w	
611 w		
602 w	608 w	
590 m	590 w	
583 sh		
559 m	563 w	
545 sh		
529 m	532 w	
520 sh		
513 vw		
490 w	500 w	495 m
478 w	478 w	
469 w	465 w	
464 w		
450 w	451 w	
439 vw	440 vw	
427 vw		330 s
		315 m
		190 m
		170 m
		115 s

All values in cm^{-1}

FTIR: KBr disc, 2cm^{-1} resolution
Low Temp. FTIR: KBr disc, 4cm^{-1} resolution

Molecular symmetry	Site symmetry	Factor Group
C_1	C_1	$C_{2h}{}^2$

All 9 v(C=O) modes ———— A ══════════ A_g Raman active

have A representation ———————— B_g "

———————— A_u IR active

———————— B_u "

All nine v(C=O) modes should be observed in solution, where the site and factor group symmetries do not apply. In fact eight bands were observed experimentally in cyclohexane solution in this study and in the literature [14]. Each C=O stretching mode in the free molecule will lead to four modes in the solid state spectrum, two IR and two Raman active modes. Thus the nine modes of the free molecule should lead to 18 IR bands and 18 Raman bands in the solid state, although as with $Os_3(CO)_{12}$, a significant number of these will be weak or unobserved. In fact, ten IR carbonyl bands (2108-1937cm^{-1}) and six Raman bands (2110-1974cm^{-1}) are observed in this work (Table 4.7, Figures 4.6 and 4.7).

Anson and Jayasooria have placed the v(Os-C) and deformation modes δ(Os-C-O) in the region 650-350cm^{-1} for $Os_3(CO)_{12}$ [45]. The deformation modes occurred at higher frequencies, with 491cm^{-1} being the upper limit for v(Os-C) modes. The frequencies of these modes for the pyrrole derivative will be affected by the replacement of Os-CO bonds with Os-N and Os-C-C bonds and by the changes in the π back bonding to the metal from the remaining carbonyl groups. Where the back bonding is strong and the C≡O frequency is lowered, the Os-C bond is strengthened and the v(Os-CO) frequency will be increased. However, the frequency regions for both stretching and deformation modes are expected to be broadly similar to those of the parent carbonyl.

The IR spectrum obtained in this study (Figure 4.6) contains a number of weak bands in the region 400-702cm^{-1}, which can be assigned to v(Os-C) and δ(Os-C-O), the latter being assigned to bands occurring in the region 513-702cm^{-1}.

The Raman spectrum (Figure 4.7) was of little help in this region as the background fluorescence obscured the weaker bands. Anson and Jayasooria [45] found that CO deformation modes gave rise to much weaker features in the Raman spectrum than the Os-CO stretches. The only deformation modes giving rise to Raman peaks of any significant intensity were those just at a higher frequency than the totally symmetric v(Os-C) mode (500-520cm^{-1} for $Os_3(CO)_{12}$). It is likely that this pattern will be repeated in triosmium clusters derived from the parent carbonyl.

Intense bands were observed at 330, 315, 190, 170 and

115cm^{-1} in the Raman spectrum (Table 4.7) and were assigned to C-Os-C and C-Os-Os angle deformations, in agreement with the results of Adams and Taylor [47] who assigned Raman bands below 200cm^{-1} to these modes for Os$_3$(CO)$_{12}$.

(ii) Ligand vibrations

Deeming and co-workers [15] have pointed out that the pyrrolyl ligand is not aromatic in the cluster, and as a result the frequency associated with the symmetric stretching of the double bonds should be higher than in the aromatic free pyrrole molecule. Likewise, the other molecular modes associated with the ring will be at frequencies expected for aliphatic rather than aromatic molecules.

Bands in the region 3108-2853cm^{-1} can be assigned to C-H stretching modes following published work [10,11]. In free pyrrole the four v(C-H) modes were found at 3133 (A$_1$ and B$_1$), 3111 (B$_1$) and 3100 (A$_1$) cm^{-1} [13]. Thus the three bands observed at 3108, 3099 and 3089cm^{-1} in the IR spectrum (Figure 4.6, Table 4.7) were assigned to v(C-H) of the pyrrolyl ligand, with the remaining bands (2853-2963cm^{-1}) being assigned to aliphatic CH, thought to occur from oil contamination in the laboratory atmosphere, as bands at similar frequency were also seen in spectra of Os$_3$(CO)$_{12}$ recorded on the same instrument. The same KBr disc was used to obtain low temperature spectra and hence these bands remain. The Raman spectra shows only one band at 3109cm^{-1} in this region (A$_g$ or B$_g$ mode) as noted in Table 4.7.

The region 1700-1350cm^{-1} contains v(C=C) and v(C=N) modes. Figure 4.6 and Table 4.7 show that the higher frequencies of this region are partially obscured by rotational fine structure of atmospheric water vapour, which could not be completely flushed from the instrument, and bands at 1652 and 1645cm^{-1} are assigned to these molecules. The two bands of medium intensity, at 1601 and 1503cm^{-1}, were assigned to v(C=C) of the pyrrolyl ring. It is not clear if the v(C=N) band is visible since it is usually difficult to identify due to large variations in intensity and its proximity to the C=C stretching region [57].

The bands in the region 1400-700cm^{-1} are mostly weak and difficult to assign with certainty. This region contains CH deformation and wagging modes, the literature quoting regions of 1500-1250 and 1000-600cm^{-1} respectively [11]. Table 4.7 shows that in this work more intense bands are seen at 1370, 1380 (IR), 1375 (Raman), 1259, 1144, 1106, 1099, 1033, 1002, 803, 774 and 768cm^{-1} (IR). The bands at 1370 and 1308cm^{-1} are probably v(C=C) modes as these values are similar to those found for the pyrrole molecule. The presence of the Raman band at 1375cm^{-1} suggests a symmetric

ν(C=C) stretch, since A_g and B_g modes are Raman active, the former being the totally symmetric mode.

The remaining bands of this group are assigned to C-H deformations or wagging modes. The more intense modes between 1144 and 1036cm^{-1} could also be linked to ν(Os-H). The literature states that these bands are normally difficult to locate for bridging M-H bonds in polynuclear carbonyls [3]. They are usually rather broad at room temperature, though sharpened at low temperature, and found in the 1600-800cm^{-1} region. 1100cm^{-1} is the often quoted frequency, with a broad Raman band usually being in evidence. The sharper bands at 1146, 1111 and 1036cm^{-1} in the low temperature IR (Table 4.7) suggest the possibility of Os-H stretching modes, but no Raman band was observed in confirmation. It is thus more likely that these are in fact C-H deformation modes.

2.2 Assignment of the FTIR spectrum of $Mn(CO)_3(C_4H_4NH)$

This complex was prepared as a mononuclear example of a π bound pyrrole ligand. Although several authors have prepared this complex [8a-c], no crystal structure has been obtained or full IR or Raman spectrum published. IR data for the complex recorded in the present study are given in Table 4.8, and assignments are made by comparison with the spectrum of pyrrole [12], since the ring retains its aromaticity and is π bound to the metal. Unfortunately the C=C stretching region 1600-1300cm^{-1} was partially obscured by rotational fine structure of atmospheric water vapour which could not be completely eliminated from the spectrometer. Bands observed at 2926 and 2855cm^{-1} were assigned to aliphatic CH groups, which were thought to arise from oil contamination in the laboratory atmosphere.

The carbonyl stretching frequencies (2035 and 1944cm^{-1}) are close to those quoted in the literature for $Mn(Cp)(CO)_3$ (2025 and 1938cm^{-1}) [3]. This is in accordance with the number of bands predicted by assuming a local C_{3v} structure for the carbonyl groups. The Mn-C stretching and deformation modes fall below the 800cm^{-1} cut off for the recorded spectrum (Figure 4.8).

Figure 4.8 *The FTIR spectrum of* $(CO)_3Mn(C_4H_3NH)$

230
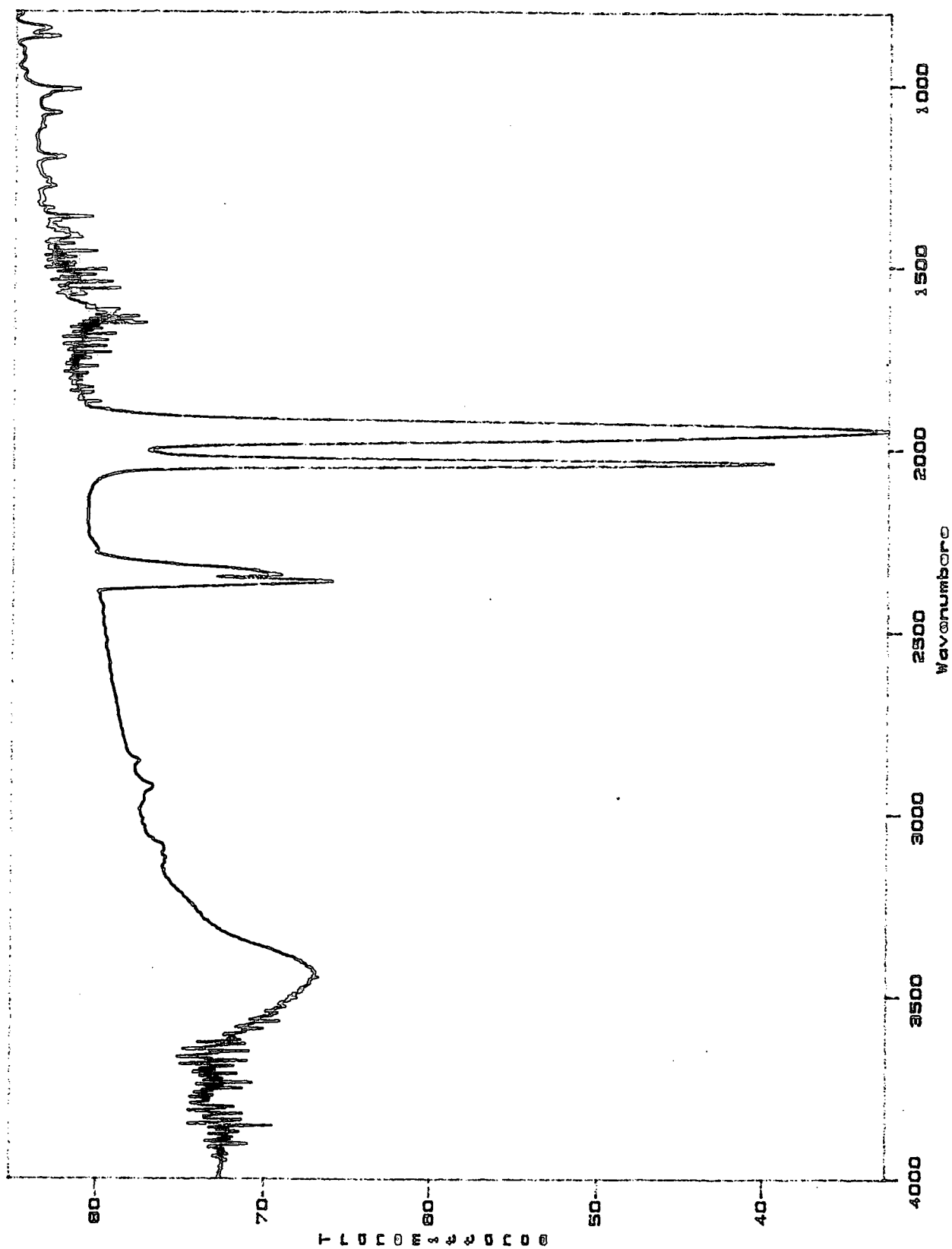
Table 4.8   _FTIR spectral data for Mn(CO)$_3$(C$_4$H$_4$NH)_

Frequency/cm^{-1}   **Assignment**

3119 w ν(C-H) pyrrole ligand
3096 w   "
2926 w ν(C-H) aliphatic
2855 w   "
2035 s ν(C=O)
1944 vs   "
1281 w
1262 vw
1198 w
1117 vw
1080 w δ(C-H) pyrrole ligand
1028 sh   "
1015 w   "
 970 vw
 928 vw
 907 vw
 870 w δ(ring) pyrrole ligand
 847 w δ(C-H)   "

2.3 Complexes containing furan ligands

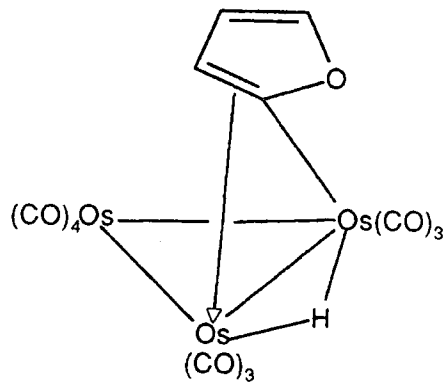### 2.3.1 Organometallic chemistry

Furan can in principle add to the triosmium cluster in various ways: by coordination of the oxygen atom and ortho-metallation to give the μ-2-furyl cluster (9), by dehydrogenation in $\propto$ and β positions to give the dihydride (10) and by ortho-metallation and η^2 coordination of the furyl group (11).
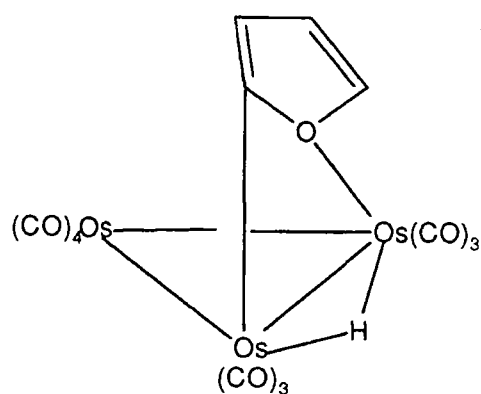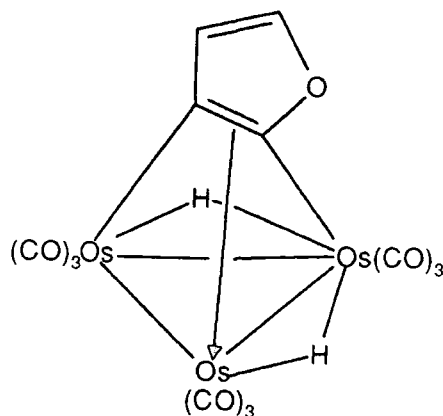
(9)   (10)

(11)

The structural types (9) and (10) are observed for the 2-methylimidazolyl ligand bound to a triosmium cluster [157] and the μ_3-pyrrole-2,3-diyltriosmium complex [14] respectively. On the basis of spectroscopic data structure (11) was assigned to the product which results from oxidative addition of furan, with metallation at the 2-position of the ring. The IR spectrum is very similar to those reported for the μ-vinyl complexes $[Os_3H(CR^1=CR^2H)(CO)_{10}]$ [158,159].

Vinyl ligands in the μ,η^2 mode are commonly found in a wide range of polynuclear organotransition metal complexes [17], and they represent intermediates in the formation of dihydrides [159-161]. However, heteroatom substituents can have a major effect on the nature of the metal-ligand bonding. Ligands with strong π donor ability lead to redistribution of the π electrons and the formation of systems with lower hapticity. Isomers of the furyl complex were not described in the original report of their preparation [18] but isomers (12a) and (12b), shown below, have been found to exist in solution (94% 12a, 6% 12b).
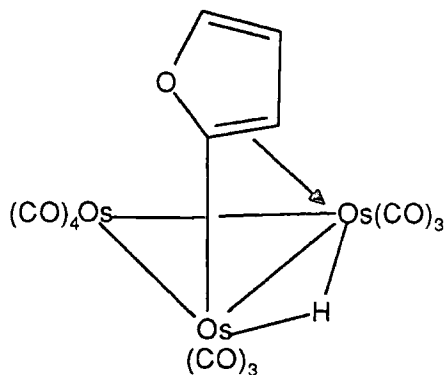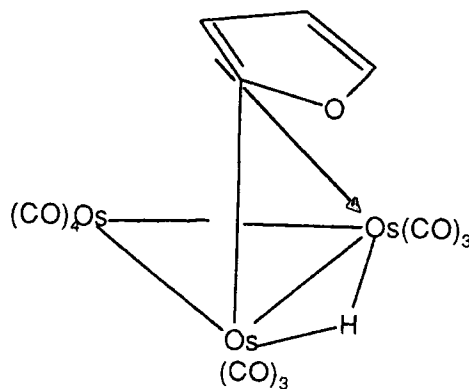
(12a)   (12b)

The isomers give separate signals in the ^{1}H NMR even at 75°C. At this temperature the signals for the minor isomer

232

have just started to broaden whereas those for the the major isomer still exhibit fine structure. It was proposed that the minor isomer is the *endo* isomer (12b) rather than a heteroatom coordinated form and the major isomer is the *exo* form (12a) as in the crystals. It is well known that μ,η^2-vinyl ligands, such as in $[Os_3(\mu H)(\mu CH=CH_2)(CO)_{10}]$ can rapidly oscillate between the metal atoms by interchanging the σ and η^2 bonding to the bridged metal atoms. Opposite faces of the ligand become succesively employed in the η^2 coordination as the ligand passes through a transition state with the ligand plane perpendicular to the metal plane. It is presumed that this occurs for compounds (12a) and (12b) but this is not the process that leads to *exo-endo* conversion. Isomers of this kind have not been observed with acyclic vinyl ligands, although different geometries have been observed in different compounds eg. when vinyl is CH=CHR and CPh=CHPh [162]. A clash of the Ph substituent at the α position with an axial CO ligand would destabilise the CPh=CHPh complex. In the cyclic systems described here there is little to favour one isomer over the other on steric grounds and both are observed in equilibrium. It is not known whether the heteroatoms are essential for rapid interconversion. If it is necessary it is very likely that the mechanism involves an intermediate with a coordinated heteroatom.

The bridging-ligand geometry of the furyl group is characterized by a carbon atom adjacent to the furyl oxygen atom which is strongly σ bonded to one osmium atom Os(1), as shown in Figure 4.9. The double bond is bonded asymmetrically by a weak π interaction to Os(2), to give an overall μ,η^2 bridging geometry. This is supported by other structural details, in particular the Os-furyl σ bond length 2.11A is virtually identical to that in the vinyl complexes $[HOs_3(CO)_{10}(CH=CHR)]$, R=H,Et,^tBu [159,160,163], in which the ligands are also σ,π bound. In contrast to the situation with these complexes, the π complexation of one furyl double bond to the second osmium atom is noticeably more asymmetric, as implied by markedly different Os(2)-C bond distances: 2.34 vs 2.63A for the π bond. The weaker η^2 π bonding of the furyl ligand to Os(2) is also reflected in the length of the Os(2)-Os(3) bond, 2.866A, which involves Os(3) of the $Os(CO)_4$ fragment and Os(2) coordinated with the olefinic double bond.

Figure 4.9   _The bridging ligand geometry in_
$[HOs_3(CO)_{10}(u, n^2-C_4H_3O)]$
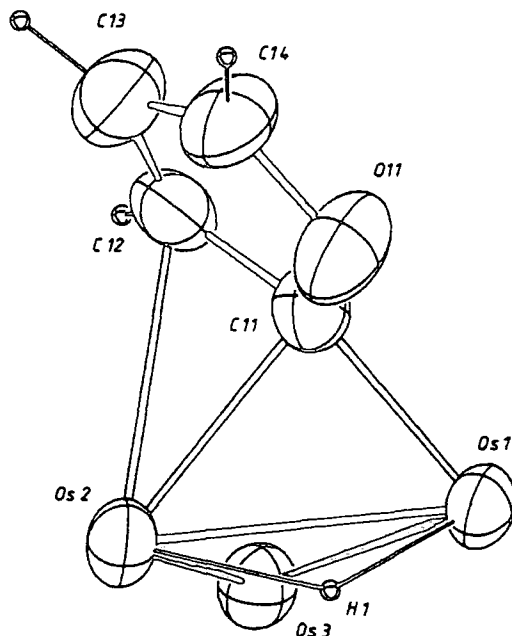
The weaker π coordination of the furyl group is probably a result of the presence of the more electronegative oxygen atom adjacent to the complexed double bond: its distances from Os(1) and Os(2) (2.97, 3,20A) are too long for bonding. The μ, η^2-bridging geometry results in an interplane angle of 48.3° between the furyl ring and the Os_3 triangle. The doubly bridged Os(1)-Os(2) bond (2.83A) is the shortest Os- Os bond in the cluster; apparently the lengthening effect of the bridging hydride upon metal-metal bonds is more than counterbalanced by the effect of the μ, η^2 furyl group.

2.3.2 Surface studies of adsorbed furan

Sexton [54] measured the EELS spectra for furan adsorbed on Cu(100) at 85-300K, and concluded that adsorption is molecular and reversible.

Table 4.9 Vibrational frequencies of furan adsorbed on Cu(100)

Vibrational mode and symmetry type	Infrared vapour frequency	Multilayer 85 K	Monolayer 170 K
γ(ring)(B₂)	603	600	600
δ(CH)(B₂)	745	760	760
δ(ring)(B₁)	871	880	⎤
ν(ring)(A₁)	995	1010	
δ(CH)(A₁)	1066	1070	
δ(ring)(B₁)	1180	1190	Screened
ν(ring)(A₁)	1384	1400	
ν(ring)(A₁)	1491	1510	
ν(CH)(A₁)	3140		
	3154		
		3150	
	3129		⎦
ν(CH)(B₁)	3161		

γ = out-of-plane bending vibration; δ = bending vibration; ν = stretching vibration.

Furan has 21 vibrational modes [164] of which nine were clearly resolved in the multilayer spectrum at 85K. The two out of plane bending modes occur at 600 and 760cm^{-1}, with A$_1$ and B$_1$ modes observed from 880 to 3150cm^{-1}. A single ν(CH) was observed at 3150cm^{-1}, with in-plane ring and CH bends from 880 - 1190cm^{-1}.

At 170K the 600 and 760cm^{-1} B$_2$ modes are still intense but other bands from 1000-3200cm^{-1} were almost completely attenuated, as with pyrrole. Thus the monolayer is adsorbed with the ring parallel to the surface, if the surface dipole selection rule is obeyed, and furan is weakly π bound.

A second layer is formed with the ring plane tilted toward the surface normal, since in plane vibrations become allowed. This is strongly supported by the known low temperature crystal structure of furan in which alternate layers of rings are inclined to one another.

The B$_2$ frequencies 600 and 760cm^{-1} in the monolayer or bilayer were identical to the multilayer indicating negligible chemical interaction with the surface.

Furan was also found to be only weakly bound to the Ag(110) surface, since the EELS frequencies were unshifted from those of the gas phase species [58].

Table 4.10 Vibrational assignments for furan and furan-d_4 on Ag(110)

| assignment	FTIR multilayer	FTIR monolayer	EELS monolayer
ν CH	3153 (2338)ᵃ vy		
ν CH	3144 (2350) m		
ν CH	3125 (2371) m		3120 (2350)ᵇ m
ν CH	3117 (2327) sh		
2 × 1553 = 3106	3087 vw		
1490 + 1553 = 3043	3017 vw		
869 + 755 = 1624	1617 w		
ν ring	1553 (1490) w		1530 (1480) sh
ν ring	1490 (1424) m		1470 (1400) w
ν ring	1382 (1315) m		(1280)
δ CH	1268 (1140) w		(1120)
δ CH	1162 (1054) s	1162 vw	1160 (1040) w
δ CH	1055 (920) m		1020 (910) w
δ CH	992 (791) s	987 w	(800)
δ ring	869 (727) s		860 (720) sh
γ CH	763 (597) vs	764 vs	770 (600) vs
γ ring	605 (500) s	602 w	600 (520) m
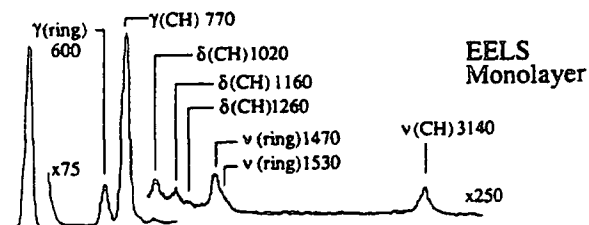
a) numbers in parentheses are gas-phase vibrational assignments for furan-d_4

b) numbers in parentheses are vibrational assignments for monolayer furan-d_4 on Ag(110)

In the RAIRS and EELS spectra only the out-of-plane modes are visible and the in-plane modes were screened. Thus the ring lies parallel to the surface at 130K, since only dipole modes perpendicular to the surface are detected.

A NEXAFS and XPS study by Madix and co-workers [59] of furan on the same surface found the furan rings tilted 22±7° from the plane of the surface for both sub- and monolayer coverages. It was suggested that this tilt arises from steric considerations and allows closer packing on the surface.

On the oxygen precovered Ag(110) surface the monolayer of furan appeared randomly orientated [58]. The EELS spectrum showed weaker out-of-plane modes and stronger in-plane modes suggesting that on average the furan molecule is tilted more towards the surface normal. When the multilayer is annealed at 204K two new vibrational modes appear in the EELS spectrum: 320, M-O stretch, and 3600cm⁻¹, O-H stretching of surface OH groups (Figure 4.10). This implies that hydrogen abstraction has occurred. After heating to 250K all molecularly bound furan leaves the surface and the hydrogen deficient furan rings bound to the surface remain. Vibrational spectra reveal the stronger in-plane modes of a tilted species. The tilt is thought to arise through bonding between the hydrogen deficient carbon atom of furan and the surface.

Figure 4.10 EELS spectra of furan on Ag(110) precovered with 0.25ML O$_{(a)}$
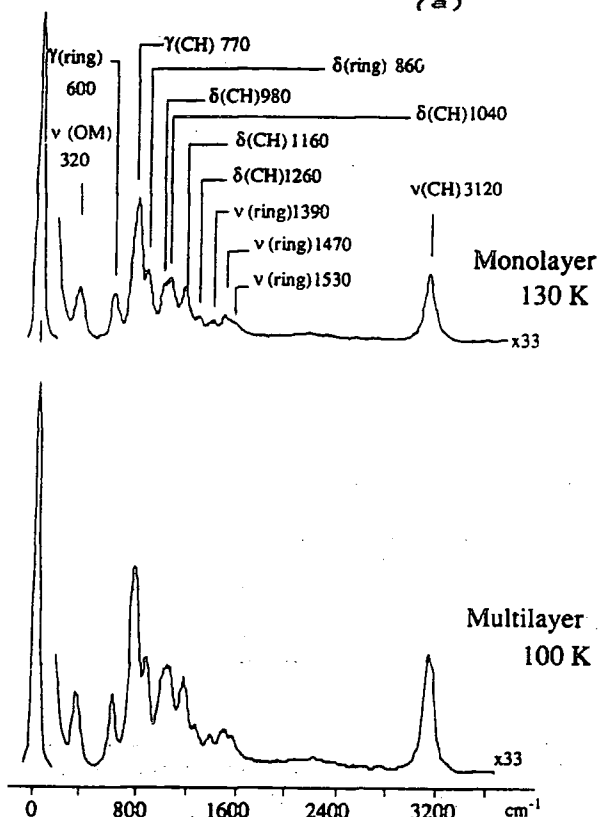
2.3.3   Assignment   of   the   FTIR   spectra   of [HOs$_3$(CO)$_{10}$(μ,η^2-C$_4$H$_3$O)]

Experimental data for this complex is contained in Table 4.11 and shown in Figure 4.11. ^{1}H NMR and IR data were consistent with the literature for the *exo* isomer, shown below.
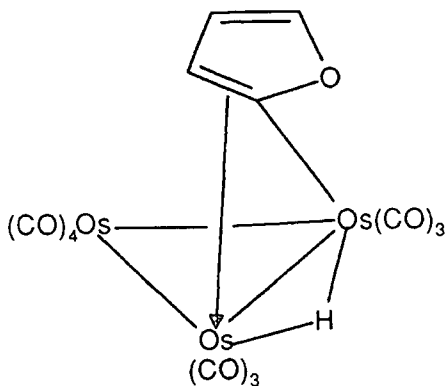
(i) Assignment of Os-C=O modes

The complex [HOs$_3$(CO)$_{10}$(μ,η^2C$_4$H$_3$O)] belongs to point group C$_1$, lacking all symmetry. The carbonyl stretching modes will therefore all be active in the isolated molecule,

237

Figure 4.11 The FTIR spectrum of $HOs_3(CO)_{10}(\mu,\eta^2-C_4H_3O)$

238
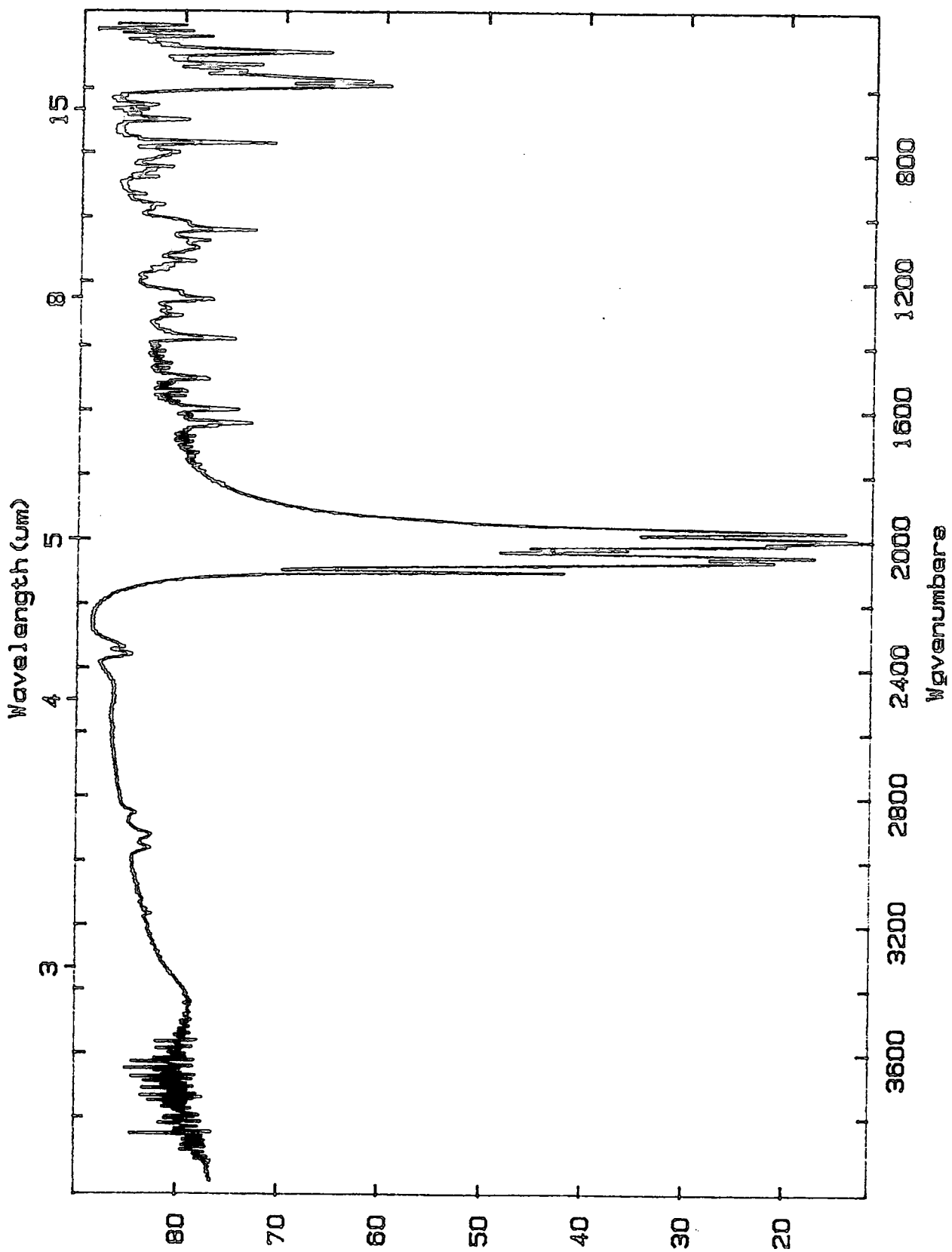
Table 4.11 Vibrational frequencies of $HOs_3(CO)_{10}(\mu,\eta^2-C_4H_3O)$

FTIR	Low temp. FTIR
3173 vw	3172 vw
3167 w	
3153 w	3153 vw
2963 w	2961 w
2953 w	
2944 vw	
2929 w	
2920 w	
2917 w	2918 w
2872 w	
2832 w	2851 w
2104 m	2106 m
2068 vs	2070 vs
2053 vs	2054 vs
2033 s	2035 s
2016 s	2018 vs
2001 vs	2002 vs
1994 sh	1994 sh
1977 vs	1977 vs
1971 sh	1971 sh
1653 vw	
1643 w	
1636 vw	1637 w
1601 w	1601 w
1545 w	
1539 w	
1507 w	
1503 w	
1382 w	1383 w
1364 sh	1364 sh
1356 vw	
1309 w	1312 vw
1298 vw	
1288 vw	
1283 vw	
1259 w	1262 w
1236 vw	1240 vw
1192 vw	
1168 vw	1168 w
1156 vw	
1142 w	1140 w
1110 vw	
1099 w	1101 w
1077 w	1078 w
1044 w	1047 w
1021 vw	1024 vw
978 vw	978 vw
964 vw	968 vw
933 vw	934 vw

879	vw	882	vw
848	vw	862	vw
		851	vw
801	vw	802	vw
774	w	774	w
746	vw	756	vw
701	w	700	w
680	vw	679	vw
669	vw	670	vw
654	vw	656	vw
603	sh		
594	m	596	m
579	m	583	m
567	sh		
548	w	550	w
529	w	530	w
520	vw		
511	vw	513	vw
495	sh		
490	m	490	m
477	sh		
466	vw		
455	vw		
442	w	444	w
435	vw		
425	w	428	w
		411	w

All values in cm^{-1}

FTIR: KBr disc, 2cm^{-1} resolution
Low Temp. FTIR: KBr disc, 4cm^{-1} resolution

and nine such modes are observed in the solution IR spectrum recorded in this work, in keeping with the literature [18]. The crystal has $P2_1/n$ symmetry (C_{2h}^2) with $z = 4$. This leads to a site group symmetry of C_1 from Halford's tables [40].

Molecular symmetry	Site symmetry	Factor Group
C_1	C_1	C_{2h}^2

All 10 $v(C=O)$ modes ——— A ——————————— A_g Raman active
have A representation B_g "
                                          A_u IR active
                                          B_u "

Therefore the solid state IR and Raman spectra should both contain 20 bands for the CO stretching region, although as for the pyrrolyl complex discussed above, a significant number of these will be weak or unobserved. The IR spectrum contains nine bands, both at room temperature (2104-1971 cm^{-1}) and at -196°C (2106-1971cm^{-1}) (Table 4.11). The Raman spectrum could not be obtained due to fluorescence.

The carbonyl group bond order will be affected by the changes in π back donation to the carbonyl as a result of the presence of the furyl ligand. There is one $Os(CO)_4$ unit remaining from the parent $Os_3(CO)_{12}$ where the axial CO groups compete equally for π electron density and have a higher bond order (and hence a higher frequency) than the equatorial CO groups, which are opposite Os-Os bonds. At the other two Os atoms the amount of competition for metal π donated electrons will depend on the acceptor abilities of the ligands. This is expected to be weak for the furyl ligand, and hence the CO groups will be the recipiants of π donation. Since these groups are not strictly axial or equatorial there is likely to be a more even competition resulting in higher bond orders.

The $v(Os-C)$ and $\delta(Os-C)$ vibrations will occur in the region ca. 700-350cm^{-1}. The IR spectrum contains a large number of weak bands between 425 and 701cm^{-1} (Table 4.11, Figure 4.11), and following the results of Anson and Jayasooria [45] the deformation modes are expected at higher frequency (511-701cm^{-1}) and the stretching frequencies below ca. 500cm^{-1} (495-425cm^{-1}). These values compare with those for the pyrrolyl complex above. Equatorial modes are, in general, expected to be at higher frequencies than the axial within both regions, due to increased π back bonding to equatorial CO giving a shorter Os-C bond. It is expected, however, that mixing of axial and equatorial modes will occur as with the parent carbonyl.

(ii) Ligand vibrations

The furyl ring is expected to have vibrational

frequencies in a similar region to the pyrrolyl complex, but at lower frequencies than the free furan molecule, since there is coordination to an electron acceptor (osmium). Bands in the region 3173-2832cm^{-1} are assigned to v(C-H) modes. In the furan molecule four such modes were observed at 3159 (A$_1$), 3148 (B$_1$), 3128 (A$_1$) and 3120 (B$_1$) cm^{-1} [13]. In the complex, the three bands at 3173, 3167 and 3153 are assigned to these v(C-H) modes. The bands at lower frequency arise from aliphatic CH and are thought to occur due to oil contamination (see pyrrolyl complex).

The C=C stretching modes of the ring occur in the region 1550-1350cm^{-1} for the free molecule [13]. For the complex there are a number of weak bands in the region 1636 - 1300cm^{-1}, bands at 1637 and 1601cm^{-1} being the only ones observed with any significant intensity at low temperature. The bands having frequencies of 1601, 1545, 1539, 1507, 1503 and 1382 are the more intense for this region, and have counterparts in the pyrrolyl IR spectrum (Figures 4.6, 4,11, Table 4.11). They are assigned to ring stretching vibrations. The bands at 1653 and 1643cm^{-1} are assigned as previously to rotational fine structure of atmospheric water vapour which could not be completely flushed from the spectrometer.

The bands in the region 1350 - 700cm^{-1} are mostly very weak, and are difficult to assign with any certainty. The region contains CH deformations and wagging modes, 1500-1250 and 1000-600cm^{-1} [11], and also ring deformation modes (873, 613 and 601cm^{-1} in free furan). More intense bands are found for the complex in this region at 1309, 1259, 1142, 1077, 1044 and 774cm^{-1}, and these also find comparison in the pyrrolyl complex. The v(Os-H) frequency is uncertain, as these bands are usually difficult to locate for polynuclear carbonyls having bridging hydrogens [3]. Thus the higher frequency bands in this group are assigned to CH and ring bending modes, the lower frequency bands to CH wagging modes.

The first mononuclear complex containing furan π bound was prepared by Chaudret and Jalon [61] and is shown in Figure 4.12. However, this complex is unstable and has only been observed in solution. Thus there is no full characterization.

242

Figure 4.12 *Structure of* $(C_5Me_5)Ru^+(C_4H_4O)$
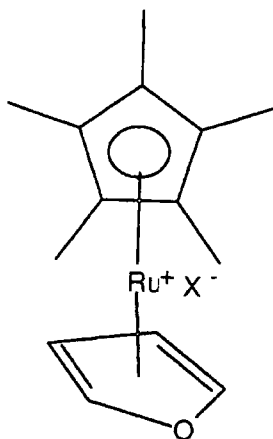
2.4 Complexes containing thiophene ligands

2.4.1 Organometallic chemistry

There is considerable interest in the organometallic chemistry of thiophene because of the commercial importance of hydrodesulphurization (HDS), where C-S bond breaking is an important reaction step in removing sulphur from thiophenic type rings in crude oil [17]. Thiophene is known to bind to single metal atoms in the η^1, η^4 or η^5 manner [6,7,165], but fewer studies have been made with transition metal clusters [166,167].

Deeming and co-workers [19] first reported the preparation of thienyl triosmium clusters via the oxidative addition of 2-formylthiophene, with cleavage of the aldehydic C-H bonds competing with C-H cleavage at the ring site, which leads to metallation at a ring site, as shown in structure (13).

(13)
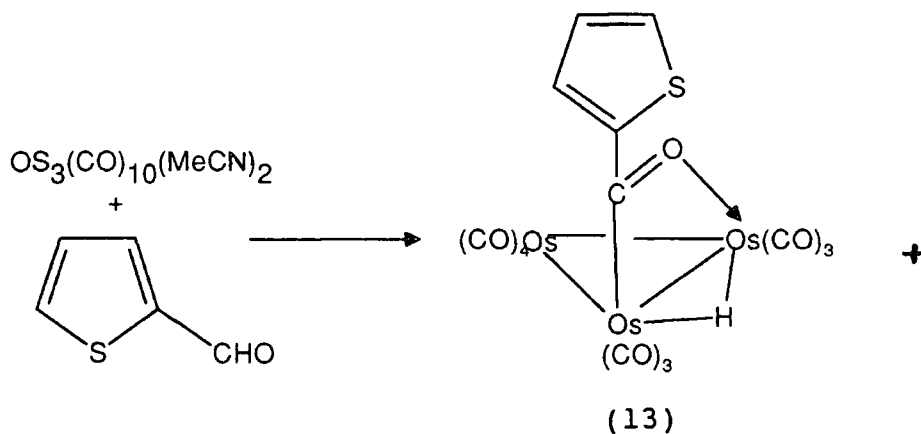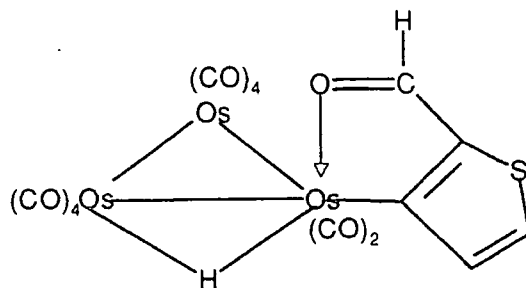
(14)

Structure (13) is related to the known bridging acyl compounds of the type $Os_3(\mu H)(CO)_{10}(\mu RCO)$ [148,168,169], and the two types of complexes showed similar v(CO) absorptions for the terminal CO ligands and the bridging acyl (1425-1435cm^{-1}).

In the minor product (14), the formyl group is preserved and is directly comparable with the aldehydic derivatives $Os_3H(CO)_{10}(RC=CHCHO)$ (R = Ph or Me) [170] which contain chelating α,β unsaturated aldeydes or ketones. Complex (13) readily undergoes thermal decarbonylation and was reported first to yield compound (15), shown below.
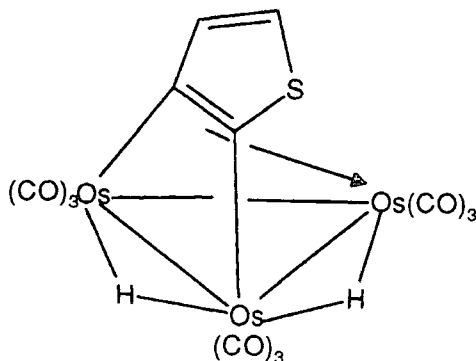
(15)

It was also found that thiophene itself will react with the bisacetonitrile complex in refluxing cyclohexane to give the oxidative addition hydrido product $Os_3(\mu H)(\mu C_4H_3S)(CO)_{10}$ (16), shown below, isolated as orange-red crystals (57%) [20]. Small amounts of the decarbonylation product $Os_3(\mu H)_2(\mu_3 C_4H_2S)(CO)_9$ (15) are also formed since decarbonylation occurs easily.

244

Formation of (16) can be compared with the furyl complex prepared in Section 2.3 above. Based on ^{1}H NMR, IR data and X-ray crystallography of the analogous complex derived from 2-methylthiophene, the structure has been established as having the S atom in an *exo* position, the ligand being coordinated in a μ,η^2 manner. The dihedral angle between the C_4S and the Os_3 planes is 55.4° for the 2-methylthiophene complex and the distance between the β carbon atom and the nearest Os atom is long (2.82A) and would be considered non-bonding under most circumstances. Os-C bonds are commonly 2.1-2.2A for σ bonds and 2.2-2.4A for η^n complexes.

The ^{1}H NMR spectrum showed the presence of isomers: at room temperature the spectrum of (16) showed four very broad resonances for the four hydrogen atoms and these were resolved into eight resonances at -55°C arising from *exo* and *endo* isomers. The structure of the isomers, (16) and (17), are shown below.

exo	*endo*
(16)	(17)
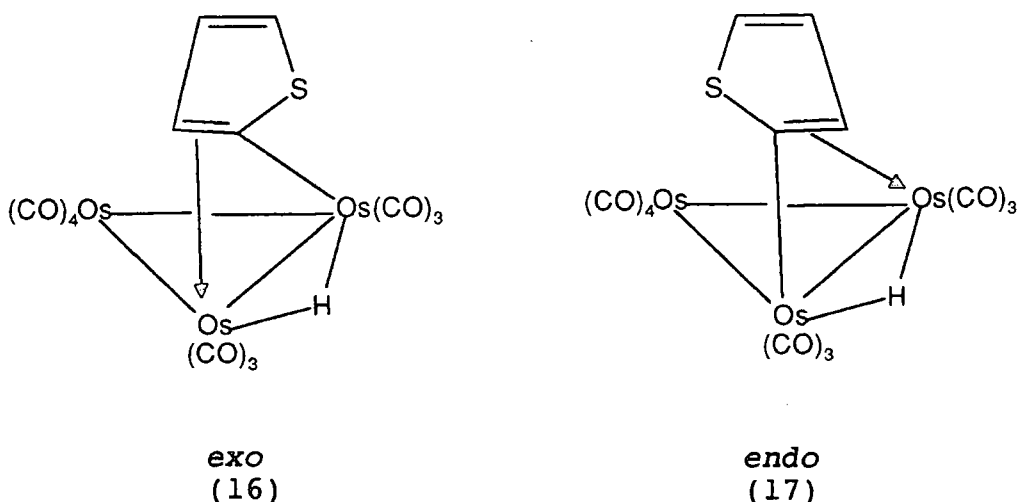
Rapid exchange of the isomers at room temperature leads to coalescence and both exist in solution. The relative concentration of the minor isomer is somewhat lower for the furyl complex (6%) for thienyl (20%) [17]. It was not believed that the change in population on replacing S by O atoms was consistent with the minor isomers having heteroatom coordination to osmium, since a much stronger preference for sulphur coordination over oxygen would be expected. Deeming and co-workers [17] estimated that the thienyl isomers have an exchange rate ca. 10^3 times that of the furyl isomers. The *exo* isomers were proposed to be the major isomer on the basis of this data, as they were in the crystal.

The ^{1}H NMR data obtained for the orange-red solid obtained in this study compares with that obtained for the

exo/endo isomers in Deeming's study [17]. The three resonances assigned to thienyl ring hydrogen atoms show resolution at 25°C and the signals to higher ppm values are associated with the *endo* isomer, as in reference [17]. Though the yellow band which occurred in chromatographic separation of the crude mixture was not characterized fully, it is thought to be due to the complex $Os_3(\mu H_2)(CO)_9(\mu C_4H_2S)$.

2.4.2 Surface studies of adsorbed thiophene

The study of thiophene adsorption is a very useful model for the understanding of hydrodesulphurization (HDS) reactions, which are important in the refining of crude oil in the petrochemical industry. Sulphur compounds act as poisons in several catalytic processes [62] and it is necessary to gain an understanding of the mechanism by which this occurs and that of their removal (HDS). Table 4.12 summarises the results of studies of thiophene adsorption on metal single crystals. Adsorption studies on molybdenum are particularly appropriate as molybdenum catalysts are most commonly used industrially in HDS reactions. On Mo, Ni and Pt surfaces cleavage of the C-S bond has been observed at, or below, room temperature, but on Cu no molecular decomposition has been detected [67].

For molybdenum, Roberts and Friend [64] report that the bonding of adsorbed thiophene changes with coverage. At low coverage the molecules are bound with the ring parallel to the metal surfce plane, whereas at high coverages a change in surface geometry occurs, with the thiophene ring becoming tilted. This allows less surface area to be occupied by each molecule. In this geometry the molecule is bound via Lewis base interaction of one of the sulphur lone pairs of electrons with the surface. Interestingly, organometallic complexes are known which contain thiophene molecules bound in both modes [171,172]. Such coverage-dependent geometry is also seen for pyridine [173-176]. The tilted geometry allows for regioselective a C-H bond scission to generate the $\propto$-thiophenyl intermediate as the temperature is raised.

Tysoe and co-workers [63] proposed that thiophene is chemisorbed into a four fold site on Mo(100) so that the sulphur atom is bonded to the Mo atom at the bottom of the site whilst simultaneously being π bonded to one or more surface Mo atoms.

The EELS spectrum of thiophene adsorbed on Ru(0001) [62] shows that the in-plane vibrations of the aromatic ring were visible at submonolayer coverage (v(C-C) 1410, v(C-H) 3025 cm^{-1}) together with a strong metal-sulphur stretching mode at 380cm^{-1}. If the surface dipole selection rule is obeyed

only modes perpendicular to the surface should be active, and in-plane vibrations should be screened. Since in-plane modes are observed, the molecule must be tilted toward the surface normal, and bonding occurs predominantly through the heteroatom. The frequency shift of the (CH) out-of-plane mode (712cm^{-1} in liquid thiophene) has been used to correlate the strength of adsorption. Large frequency shifts indicate stronger binding, as seen for multilayers of thiophene adsorbed on Mo(110) at 90K, where the (CH) out-of-plane mode had a frequency of 735cm^{-1} [66].

On Cu(100) Sexton observed that thiophene adsorbs molecularly [54].

Table 4.13 *Vibrational assignments for thiophene adsorbed on Cu(100)*

Vibrational mode and symmetric type	Infrared vapour frequency a)	Multilayer 85 K	Monolayer 210 K
δ(ring) (B₂)	452	460	430
δ(CH) (B₂)	712	730	730
γ(ring) (A₁)	839	830	860 (w)
δ(CH) (A₁)	1083	1090	1080 (w)
δ(CH) (A₁)	1036		
δ(CH) (B₁)	1256	1270	
ν(ring) (A₁)	1360	1370	
			1400 (w)
ν(ring) (A₁)	1409	1430	
ν(CH) (A₁)	3126		
	3098		
		3130	3130 (w)
	3125		
ν(CH) (B₁)	3086		

Screening of all the in-plane vibrations was detected for the monolayer at 210K, and hence the ring lies parallel with the surface plane. In the multilayer the vibrational frequencies of the ligand are essentially the same as in the vapour, whereas the out of plane vibrations become active, the rings being inclined to the surface plane.

The EELS and TDS data revealed two distinct adsorption sites for thiophene and a "compression" phase was identified as a likely model, where all or some of the rings are inclined as the coverage increases. A related model was also proposed by Stohr et al [54] for Pt(111), where Lang and Masel [65] also observed an increase in tilted ring species with increased temperature and coverage.

Considerable work has been done on organometallic modelling of the HDS reaction, in particular by Angelici [68] with mononuclear compounds, with some more limited work on polynuclear systems [69]. These have been used to model the reaction steps of either C-H or C-S cleavage, but no vibrational analysis has been undertaken.

Crystal	Technique	Ring binding	Reference
Mo(100)	ARUPS	Tilted, 25°	[63]
Mo(110)	TPRS/AES	Flat - low coverage Tilted 90° (S bound) - high coverage	[64]
Mo(110)	HREELS/AES/ TDS	"	[66]
Ru(0001)	TDS/TRPS/ XPS/EELS	Tilted	[62]
Rh(111)	ARUPS/TDS/ LEED/AES	Flat at all coverages	[67]
Ni(100)	EELS	Flat	[66,177]
Ni(111)	"	"	
Pt(111)	EELS	Flat	[62,177]
Pt(100)	XPS/TPD/ HREELS	Flat 170K Tilted, S bound, inc. temp.	[65]
Pt(111)	"		
Pt(210)	"		
Cu(100)	TDS/EELS	Flat - monolayer Flat and tilted - multilayer	[54]

2.4.3 Assignment of the FTIR spectra of $HOs_3(CO)_{10}(C_4H_3S)$

Experimental data for this complex is contained in Table 4.14 and Figure 4.13. ^1H NMR and IR data were consistent with literature data for the *exo/endo* isomers of $HOs_3(CO)_{10}(C_4H_3S)$ shown below.

exo

endo
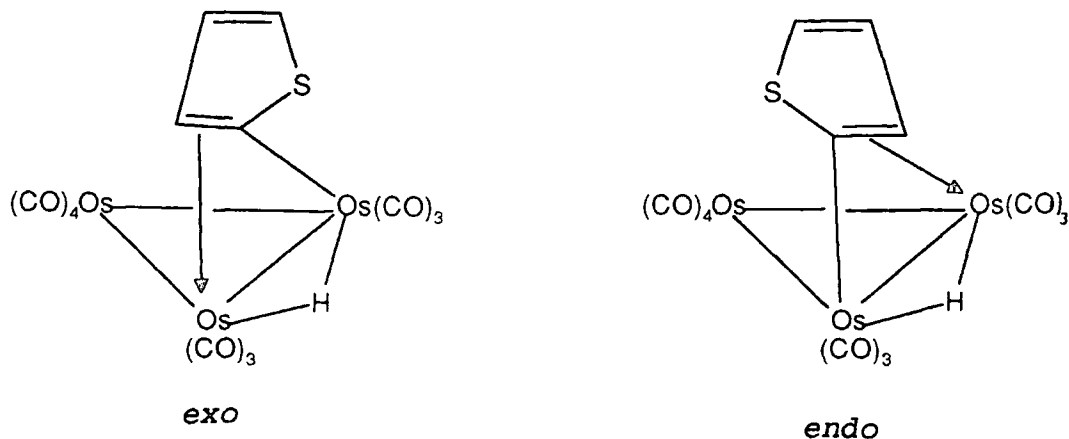
Figure 4.13 *The FTIR spectrum of* $HOs_3(CO)_{10}(\mu,\eta^2-C_4H_3S)$
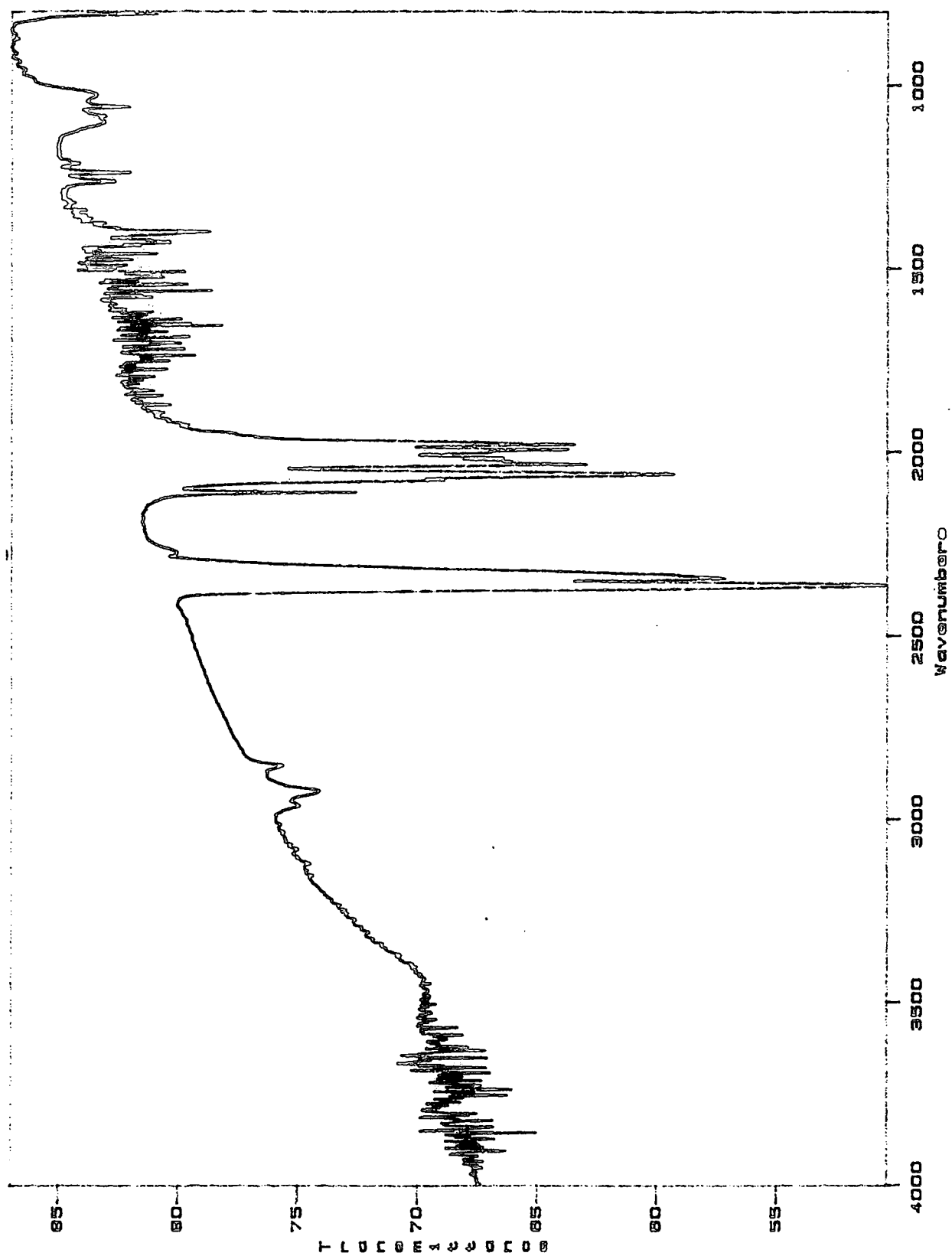
Table 4.14 *Vibrational frequencies of* $HOs_3(CO)_{10}(\mu,\eta^2\text{-}C_4H_3S)$

FTIR	Low temp. FTIR
3114 vw	3124 vw
3091 vw	3091 vw
3084 vw	3084 vw
2955 w	2955 w
2924 m	2924 m
2835 vw	2835 w
2104 m	2106 m
2066 vs	2066 vs
2052 s	2054 vs
2025 s	2027 s
2012 s	2014 s
1995 vs	1995 vs
	1985 s
1979 s	1979 s
1969 s	1969 vs
1647 w	
1630 w	
1618 w	
1516 m	
1466 w	
1458 w	
1452 w	
1410 w	
1391 m	
1358 m	
1302 vw	
1261 w	
1248 w	
1123 m	
1101 w	
1047 sh	
1024 w	
804 m	806 m
710 m	712 m
667 vw	668 vw
652 w	654 w
617 w	617 w
586 m	590 m
556 w	557 w
550 w	552 w
530 w	532 w
513 vw	513 vw
500 w	500 w
486 w	490 w
478 w	480 w
467 w	467 w
444 w	444 w
424 w	430 w

All values in cm^{-1}

FTIR: KBr disc, 2cm^{-1} resolution
Low Temp. FTIR: KBr disc, 4cm^{-1} resolution

The complex $Os_3(\mu\text{-}H)(C_4H_3S)(CO)_{10}$ is isostructural with the furyl complex considered above, and therefore the IR spectra and assignments are expected to be very similar.

(i) Assignment of Os-C=O modes

The crystal has $P2_1/n$ (C_{2h}^2) symmetry with z = 4 and this leads to site group C_1 and the expectation of 20 IR and 20 Raman bands for the v(CO) region, as with the furyl analogue. Nine IR bands are observed at room temperature and at -196°C (2108-1977cm^{-1}) in the present work (Table 4.14). Again, the competition for π back donation from the metal atoms will determine the C=O bond order, and sulphur is a better electron donor to osmium than oxygen. This π donation will reduce the bond order and hence lower the v(CO) frequency. Competition is more even for the π electrons at the osmium atoms bound to the thienyl ligand as the CO ligands are not strictly axial or equatorial. This is more the case for the $Os(CO)_4$ unit where the same arguments apply as for the parent carbonyl $Os_3(CO)_{12}$.

A large number of weak intensity bands are observed between 411 and 702cm^{-1} (Table 4.14) and these are assigned to the Os-C-O stretching and deformation modes. The deformation modes are assigned to bands at the higher frequencies (513-702cm^{-1}) and the stretching modes to those between 488 and 411cm^{-1}, by comparison with the results of Anson and Jayasooria [45]. The frequency will depend, as for the CO stretching region, on the extent of π back donation of electrons: where this is high the Os-C bond order is increased and consequently the stretching and deformation frequencies occur at higher energies.

(ii) Ligand vibrations

The thienyl and furyl rings were expected to have very similar frequencies, though thienyl was expected to have lower frequencies for the ring modes due to its greater aromaticity. Liquid thiophene has three v(C-H) bands at 3110 (A_1 and B_1), 3096 (A_1) and 3073 (B_1) cm^{-1}. The bands observed in the region 3078-3164cm^{-1} are thus assigned to v(CH) modes, with the bands between 2961 and 2851cm^{-1} assigned to oil contamination as previously mentioned for the pyrrolyl and furyl complexes above.

The rotational fine structure of atmospheric water vapour obscures bands in the 1700-1500cm^{-1} region, but a number of bands are found in the v(C-C) region from 1429-1330cm^{-1}. The bands at 1429, 1402 and 1385cm^{-1} are more intense and lie close to the frequencies found for the isolated thiophene molecule, and assignment is based on that for the free ligand.

The region 1300-729cm^{-1} contains a number of more intense

bands at 1098, 1084, 1061, 1024 and 808cm^{-1}. These
correspond to values found in the pyrrolyl and furyl
clusters assigned above.. The higher frequency bands are
assigned to C-H deformation, and the CH wagging or ring
deformation modes are assigned to those at lower frequency.

2.5 Complexes containing aniline ligands

2.5.1 Organometallic chemistry

Alcohols and thiols react with dodecacarbonyltriosmium to
give the complexes $HOs_3(OR)(CO)_{10}$ [21]. Alternatively if
there are two hydrogens on the heteroatom both may be
transferred to the metal eg. H_2S and $Os_3(CO)_{12}$ gives
$H_2Os_3S(CO)_9$. The treatment of primary amines with $Os_3(CO)_{12}$
was thus expected to give $H_2Os_3(CO)_9(NR)$. In reactions of
aniline two hydrogens are transferred to the metal, but also
one hydrogen can be derived from the ortho-position of the
ring. The aniline interaction may be described as a double
oxidative-addition and bears a superficial resemblance to
interaction of similar molecules with metal surfaces [21].

The main product obtained from reaction of aniline with
$Os_3(CO)_{12}$ is a yellow complex of general formula
$Os_3(CO)_8(aniline)_2$, which succesively reacts with CO to
give derivatives of general formulae $Os_3(CO)_9(aniline)$ and
$Os_3(CO)_{10}(aniline)$ [21,24].

From ^{1}H NMR data the nonacarbonyl was formulated as
$H_2Os_3(HNC_6H_4)(CO)_9$ ((18), shown below), rather than as the
expected product $H_2Os_3(NPh)(CO)_9$.
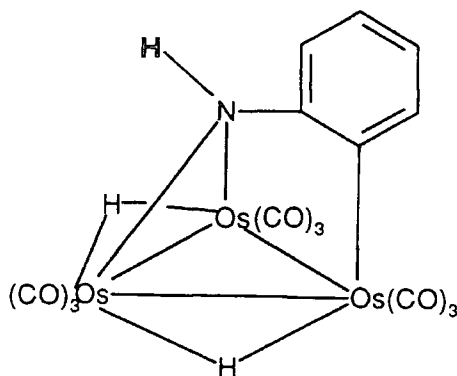
(18)

The NHC_6H_4 ligand triply bridges the three metal atoms
and is acting as a four electron donor. It is more likely
that the nitrogen lone pair rather than the π electrons of
the substituent ring are used in bonding to the metal. The

structure is very similar to that of the vinylidene complex $H_2Os_3(CCH_2)(CO)_9$ [179,180]. The octacarbonyl $Os_3(CO)_8(PhNH_2)_2$ is an aniline substituted derivative of complex (18), i.e. $H_2Os_3(HNC_6H_4)(CO)_8(PhNH_2)$. The substitution position of the $PhNH_2$ ligand was not determined. In the ^1H NMR spectrum the two NH signals were not completely resolved but had a total integrated intensity equivalent to three hydrogens, in agreement with the proposed formulations.

Complex (18) can react further with CO at 125°C to give $HOs_3(HNPh)(CO)_{10}$. In this reverse metallation reaction a C-H bond has been reformed, with a CO ligand providing the extra two electrons required by the metals. The complex was proposed to have the structure (19) [21].
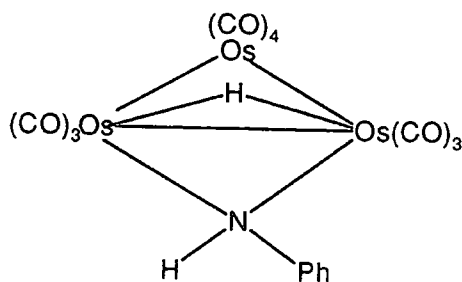
(19)

The action of heat on this complex gives complex (18) by *ortho*-metallation of the arene ring. Further reaction yields $H_2Os_3(NPh)(CO)_9$, the proposed structure of which is shown below as complex (20).
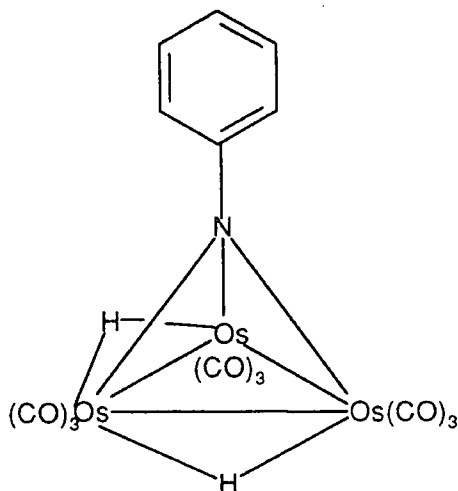
(20)

Only one sharp hydride singlet is obtained in the ^1H nmr spectrum of complex (20), even at -50°C, and the hydrido

ligands are most likely equivalent. Thus the complex of structure (18) is formed as the kinetically controlled product and the thermodynamically most stable complex of structure (20) is only formed by subsequent isomerisation. The thermodynamically most stable isomer is favoured in a closed system due to the reversibility of decarbonylation [21].

X-ray crystallography of the fluoro analogue of complex (18), $H_2Os_3(CO)_9(NHC_6H_3F)$, showed the nitrogen atom to be almost equidistant from the two osmium atoms to which it is bound, whilst the C_6 ring is sigma bonded to the third osmium atom. The ring C-C distances, 1.35-1.42A, showed it to be aromatic. The hydride ligands lead to asymmetry in the osmium-osmium bond lengths, Os(2)-Os(3) 2.996A, Os(1)-Os(3) 2.810A [21].

2.5.2 Surface studies of adsorbed aniline

Aniline is the monomer for the conducting polymer polyaniline and is also a model compound for the hydrodenitrogenation (HDN) of crude oil [70,72]. Despite the interest in the conducting properties of (polyaniline), little work has been carried out on the surface adsorption of molecular aniline. Early work function changes for aniline adsorbed on Pt(100) and (111) found the molecule to be bound parallel or almost parallel with the metal surface plane [181]. XPS studies of aniline on polycrystalline iron and nickel films found molecular adsorption via the ring π electrons and dissociative adsorption via an anion formed from release of a proton from the NH_2 group [182].

Netzer and co-workers [70] carried out a study of aniline adsorbed on Pd(110) using ARUPS, LEED and TDS. The ARUPS and TDS data indicated that there was hydride loss to form the PhNH species in the monolayer phases. The molecules coordinate to the surface via the π electrons of the ring and the nitrogen lone pair. The geometry adopted is of the ring plane in close proximity to the metal surface. The results did not rule out tilting, which would be expected on steric grounds. A tilt of ca. 20° was calculated. A schematic model of the aniline monolayer surface structure is shown below.

[001]

[110]
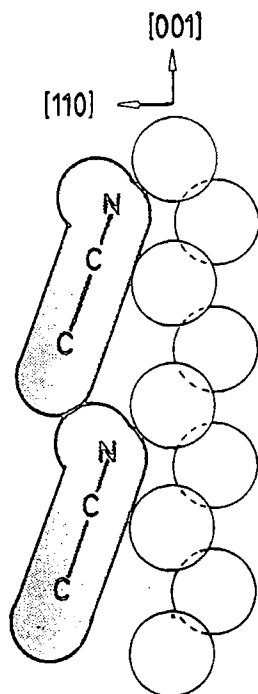
A NEXAFS and XPS study on the Ag(110) surface determined a ring tilt of 39±5° with respect to the plane of the surface [71]. The upward tilt was due to the bonding of the nitrogen lone pair to the surface (nitrogen is a good Lewis base).

On Rh(111) TPRS and XPS determined that N-H bond cleavage occurs to give PhNH and PhN species between 100 and 400K [72].

Schoofs and Benziger [73] used infra red spectroscopy to study adsorption on Ni(100). Aniline apparantly freezes in a multilayer configuration on the surface at 170K and the IR spectrum is similar to that of condensed aniline, indicating no strong ordering of orientation. After heating to 300K a monolayer remained on the surface and IR revealed the N-H bond to be intact and oriented with the dipole contribution normal to the surface (v(N-H) > 3100cm^{-1}). The ring is therefore parallel to the surface plane as it shows no IR activity. The N-H bonds must be almost normal to the surface. However, π bonding from the ring and contribution of the nitrogen lone pair were discounted because substantial amounts of hydrogen were evolved from the decomposition at 260K and because decomposition products were obtained at temperatures above 800K. An alternative view is that the surface acts as an electrophile and forms aniline cations. These initiate polymerization and form an extensive network structure like that of polyaniline. The ring would be parallel to the metal surface plane and the NH bond at an angle in this structure which agrees with the IR data.

Organometallic models for this system have not been

discussed in the literature.

2.5.3 Assignment of the FTIR spectrum of $HOs_3(CO)_{10}(NHC_6H_5)$

Experimental data for this complex is contained in Table 4.15 and Figure 4.14. ^1H NMR and IR data are consistent with the literature values for the isomer $HOs_3(CO)_{10}(HNPh)$ shown below.
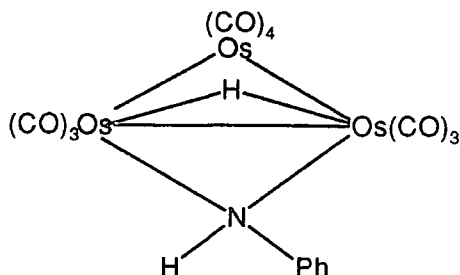
The vibrations of the cluster framework are expected to be similar to those discussed for the pyrrolyl, furyl and thienyl complexes above. The crystal space group of this complex is not known, but an assumption is made that, similar to the other triosmium clusters considered, it is monoclinic, leading to a site group C_1 [40]. The isolated molecule has a mirror plane if aniline bonding is as shown below
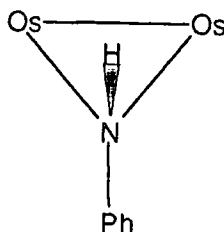
and thus the isolated molecule has symmetry C_s. This is reduced to C_1 if there is asymmetry of the PhNH ligand.

(i) Assignment of Os-C=O

Assuming C_s symmetry $\Gamma_{irred} = 6A' + 4A''$ for all the carbonyl vibrations and this leads to the expectation of 10 IR and 10 Raman active modes. In solution eight modes are visible in the IR spectrum. It was also assumed that for the osmium atoms bound to the PhNH ligand the CO groups could not be strictly termed axial or equatorial, and so further distinction in the assignment of Γ_{irred} was not made.

Applying site and factor group analysis:

Figure 4.14 The FTIR spectrum of $HOs_3(CO)_{10}(NHC_6H_5)$
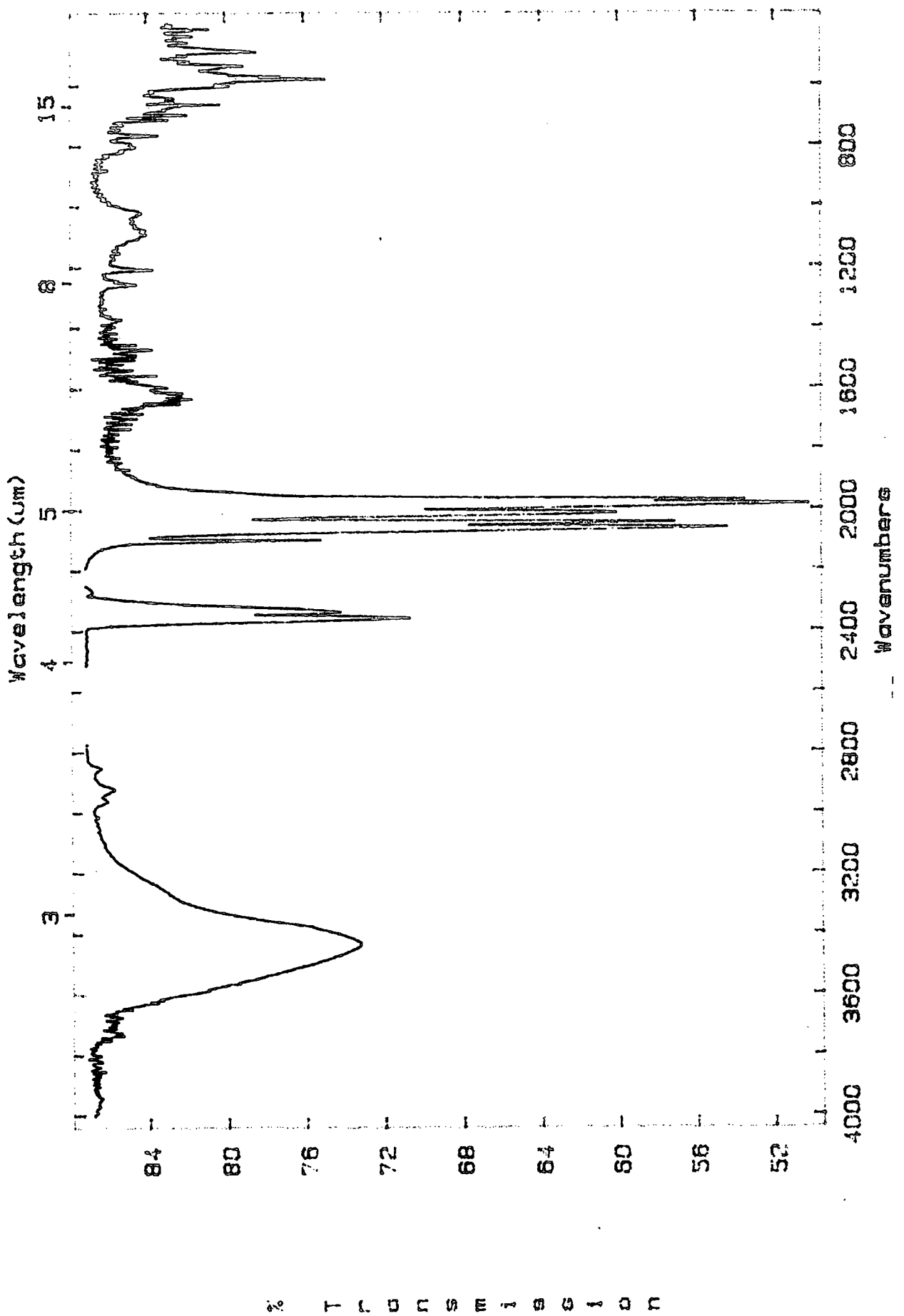
Table 4.15   *Vibrational frequencies of* $HOs_3(CO)_{10}(NHC_6H_5)$

FTIR	Low temp. FTIR
3055 w	
3031 w	
2965 w	2965 w
2925 w	2925 w
2854 w	2854 w
2103 m	2104 m
2065 s	2068 s
2046 s	2049 s
2016 s	2016 s
1991 sh	1993 sh
1987 vs	1989 vs
1974 s	1977 s
	1973 s
1637 w	
1600 w	
1262 w	1262 w
1252 vw	1252 sh
1214 w	1213 w
1096 w	1094 w
1083 w	
1023 w	1028 w
809 w	804 w
769 w	772 w
718 w	719 w
702 w	704 w
670 w	660 w
654 w	652 w
646 w	646 w
606 w	608 w
584 m	584 m
574 m	577 m
541 w	567 w
	542 w
528 vw	525 vw
509 vw	509 vw
496 m	498 m
	490 m
464 w	467 w
445 w	444 w
420 w	428 w
	472 w
	415 w
	407 w

All values in cm^{-1}

FTIR: KBr disc, $2cm^{-1}$ resolution
Low Temp. FTIR: KBr disc, $4cm^{-1}$ resolution

Molecular symmetry   Site symmetry   Factor group symmetry
        C_s C_1 C_{2h}^5 or C_{2h}^2

6A′ ────────────── A ═════════════ A_g (10)
4A″ ────────────── B_g (10)
                                   A_u (10)
                                   B_u (10)

    Thus 20 IR and 20 Raman active bands are expected. In this work the room temperature IR spectrum showed seven bands in the region 2103-1974cm^{-1}, and at -196°C eight bands (2104-1973cm^{-1}), (Table 4.15). The amount of π back donation to the CO ligands from the metal and its subsequent effect on frequency of both the CO stretching and Os-C-O stretching and deformation modes are as previously discussed for the heterocyclic complexes above. A number of weak bands are again observed in the region 702-420cm^{-1} (704-407cm^{-1}, -196°C), and they are assigned as deformation modes from 702 to 509cm^{-1} (704-509cm^{-1}, -196°C) and as stretching modes from 496-420cm^{-1} (498-407cm^{-1}, -196°C). Ring deformation modes may also be contained in this region (found at 691 and 618cm^{-1} in aniline [23]).

(ii) Ligand vibrations

    C-H stretching modes are assigned to five bands in the region 3088-3010cm^{-1} for aniline molecules [23] and in the complex the two weak bands at 3055 and 3031cm^{-1} arise from v(C-H) vibrations (table 4.15). Oil contamination was again present (2965-2854cm^{-1}), as seen in the spectra of the complexes discussed above.

    For the aromatic ring, bands are expected in the region 1620-1420cm^{-1} [11]. Two bands are observed at 1637 and 1600cm^{-1} and these are assigned to ring stretching modes. In aniline these modes appear at 1600, 1586, 1500, 1468 and 1330cm^{-1} [78]. N-H deformations also occur in this region in free amines (1650-1590cm^{-1} [11], 1618cm^{-1} in aniline).

    C-N stretching modes occur around 1340-1250cm^{-1} for aromatic amines [10] and three weak IR bands are found between 1267 and 1214cm^{-1} (Table 4.15). The bands at 1096, 1083 and 1023cm^{-1} are similar in frequency and intensity to those observed in other triosmium clusters in this series and they are assigned again to C-H deformation modes. Aromatic CH wagging modes are known to occur below 900cm^{-1}, down to 700cm^{-1} [11], and the bands observed in the spectrum at 809, 769 and 718cm^{-1} are assigned to these modes.

2.6 Complexes containing phenol ligands

2.6.1 Organometallic chemistry

The initial reaction of PhOH with $Os_3(CO)_{12}$ appears to be transfer of hydrogen from oxygen to osmium and formation of $Os_3(CO)_{10}H(OPh)$, (21) [24].
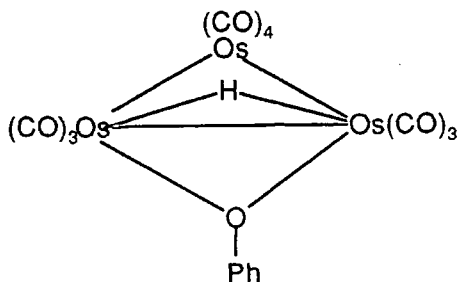
(21)

As with the aniline complex of similar structure, complex (21) readily loses a CO ligand in refluxing nonane to give the nonacarbonyl $Os_3(CO)_9H_2(OC_6H_4)$, initially assigned the structure (22).
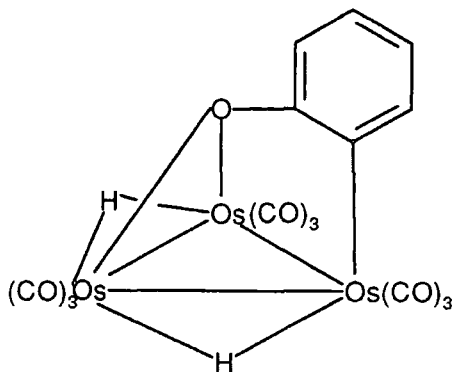
(22)

The removal of the *ortho* hydrogen is unambiguously confirmed by ^1H NMR data. However, structure (22) became doubtful because of very strong analogies with complexes derived from ketens and aldehydes [183]. The doubts were confirmed by X-ray structure of the related 2-benzylphenol derivative, which clearly showed that a carbon rather than an oxygen atom of the μ_3 ligand was bridging. The phenol molecule had been trapped in its dienone form (23) [22].
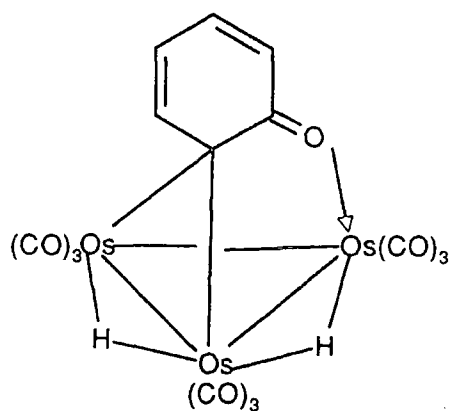
(23)

Complexes (24), (25) and (26) were considered as the structure of the dienone form, with (24) being ruled out immediately. It was not so clear whether (25) or (26) was the most appropriate. The possibility of an electron-deficient phenyl bridge as in (26) was indicated by the structure of $Os_3(CO)_8(PPh_2)(Ph)(PPhC_6H_4)$ for example [184]. However, bond length considerations fully support the structure (25). An alternation of bond lengths was found around the diene part of the ring, one C-C bond of the ring is essentially single (1.52A) and the C-O bond length (1.28A) indicates a multiple bond [22].
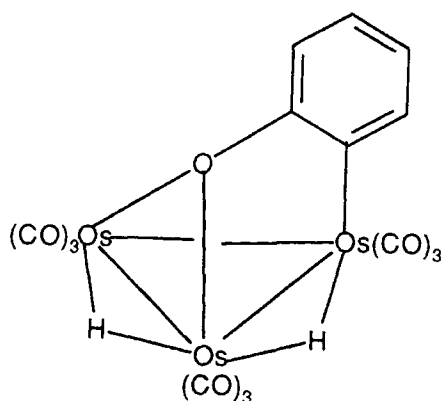
(24)
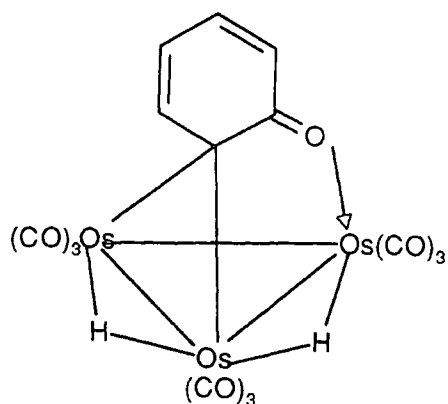
(25)
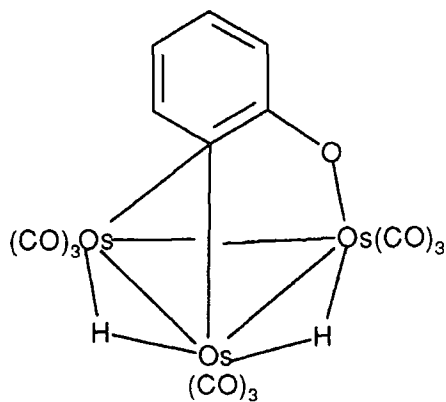
(26)

2.6.2 Surface studies of adsorbed phenol

Phenolic groups account for a substantial portion of the oxygen-containing species in liquid fuel feedstocks and undergo hydrodeoxygenation during catalytic hydrotreatment [185]. Adhesives containing phenolic groups are also important in metal bonding [186].

Phenol may interact with the metal surface by bonding through the oxygen lone pair as an electron donor or by interaction of the π ring system with the surface. Few studies have been carried out.

On Mo(110) the O-H bond cleaves at temperatures below 360K (after the desorption of weakly bound molecular species) to give a surface bound phenoxide. This is followed by C-H activation at 370K [74].

More than one intermediate was present on the surface upto 300K, one of which is phenoxide. The structures could not be identified by NEXAFS. By comparison with benzenethiol on the same surface, which gives benzyne bound perpendicular to the surface, it is suggested that not all the phenol intermediates can be bound parallel to the surface plane. On an oxygen precovered (0.33L) Mo(110) surface phenoxide was found to be remarkably stable, remaining intact until ca. 650K [75]. This kinetic stability was attributed in part to the nearly perpendicular geometry. The phenyl ring is directed away from the surface, with the ring plane making an angle of ca. 30° with respect to the surface normal. Mononuclear organometallic models for this bonding geometry include $(Et_4N)[W(OPh)_6]$ and $WH_3(OPh)(PMe_3)_4$ [187], where the bond angles correspond to ring inclinations of ca. 40°.

Netzer and co-workers' study of phenol on Pd(110) used ARUPS and TDS to show that phenoxide species are formed in the monolayer [70]. The molecules are coordinated to the surface via the π electrons of the ring and the oxygen lone pair electrons. The geometry adopted was with the ring plane in close proximity to the metal surface. Tilting would be expected on steric grounds and phenol may adopt the densely packed structure of aniline with the molecules aligned with their functional groups along the [001] azimuth.

TDS revealed that the phenol O-H bond in the monolayer phase was cleaved below 240K on the Ni(110) surface [76], and the use of d_1-phenol established convincingly the formation of phenoxide. ARUPS suggested that the molecular ring orientation is in close proximity to the metal surface plane, but not necessarily parallel. Surface coordination was via the ring π electrons and also possibly the oxygen lone pair. The bonding is with the phenoxide moiety tilting so that the O atom dips into the grooves of the surface to optimize the nickel coordination around oxygen. Nickel's

affinity for oxygen is high and this may be a favourable coordination and a driving force for this geometry. On palladium the affinity for oxygen is much lower and the molecular arrangement may be determined to a larger extent by packing density and adsorbate-adsorbate interactions. Bu et al [77] measured the angle of inclination for phenoxide on Ni(110) and found it to be 15°.

Based on packing densities measured by AES phenoxide was proposed to lie parallel to the Pt(111) surface [188]. On Ag(110), Madix and co-workers found the plane of the phenol ring orients with a maximum tilt of 40±5° with respect to the surface plane [71]. This arises from bonding of the oxygen lone pair to the surface and also from strong intermolecular interactions.

2.6.3 Assignment of the FTIR spectra of $HOs_3(CO)_{10}(OPh)$ and $H_2Os_3(CO)_9(OC_6H_4)$

Experimental data for the two complexes is contained in Tables 4.16 and 4.17, and Figures 4.15, 4.16 and 4.17. ^1H NMR and IR data were consistent with the literature values for the complexes $HOs_3(CO)_{10}(OPh)$ and $H_2Os_3(CO)_9(OC_6H_4)$ shown below.
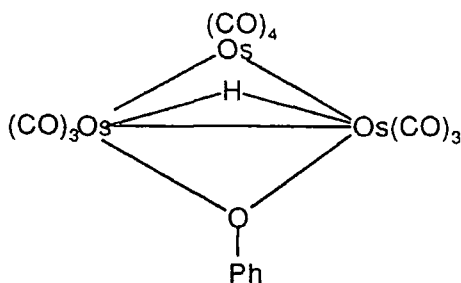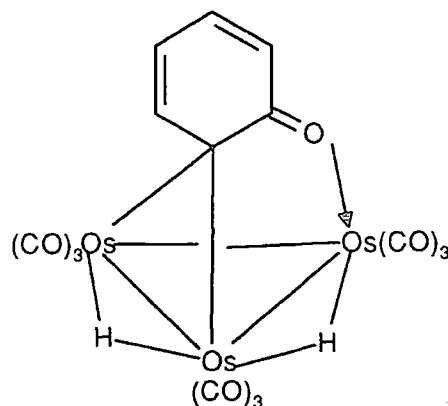
$HOs_3(CO)_{10}(OPh)$ $H_2Os_3(CO)_9(OC_6H_4)$

2.6.3a $HOs_3(CO)_{10}(OPh)$

(i) Assignment of Os-C=O modes

This complex is isostructural with the aniline complex and a fuller discussion of the spectral assignments is given in section 2.5.3 above. Nine CO stretching bands are observed in both the room temperature and low temperature IR spectra (2110-1977 and 2112-1979cm^{-1} respectively), with the

Figure 4.15 The FTIR spectrum of $HOs_3(CO)_{10}(OPh)$
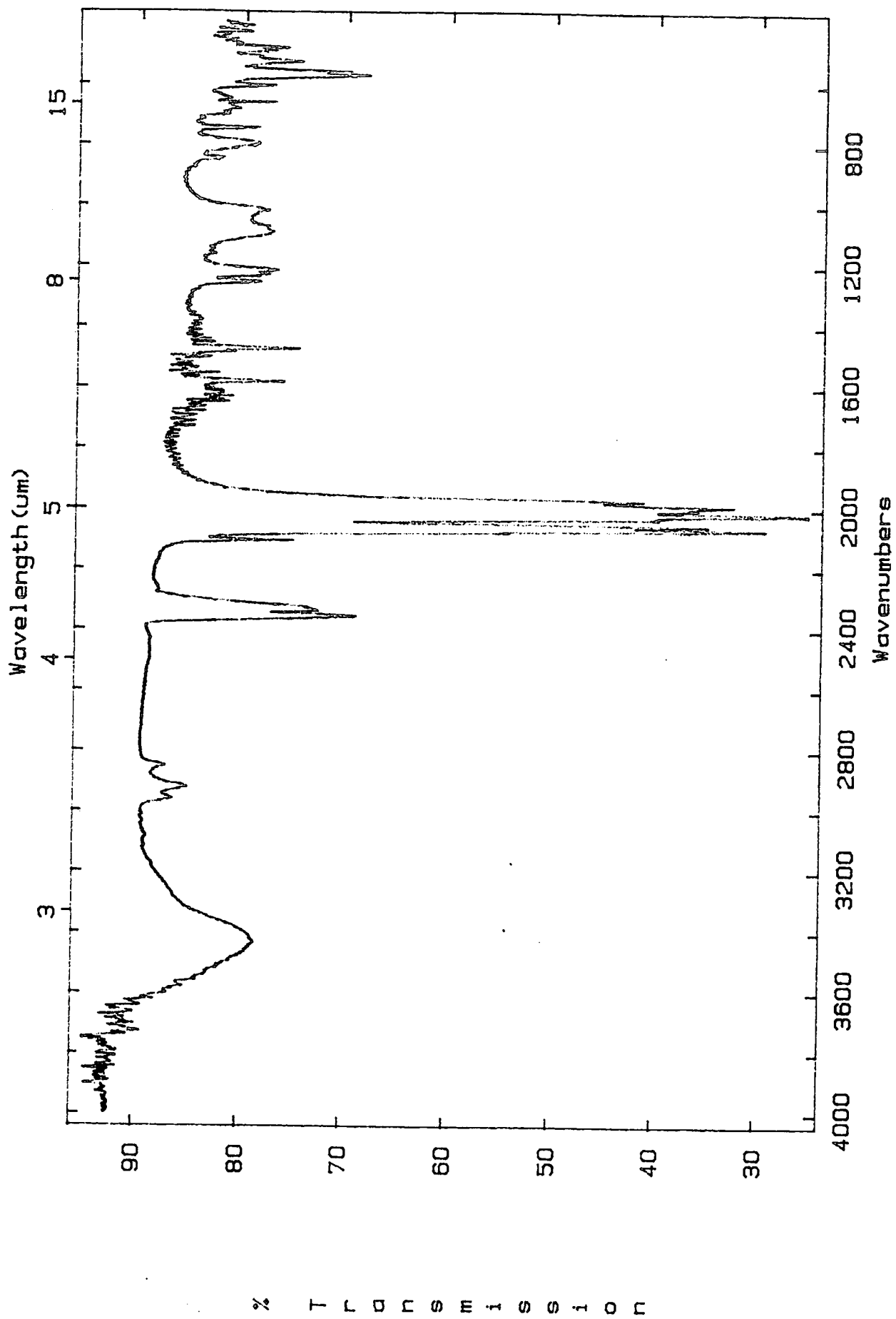
Figure 4.16 The Raman spectrum of $HOs_3(CO)_{10}(OPh)$
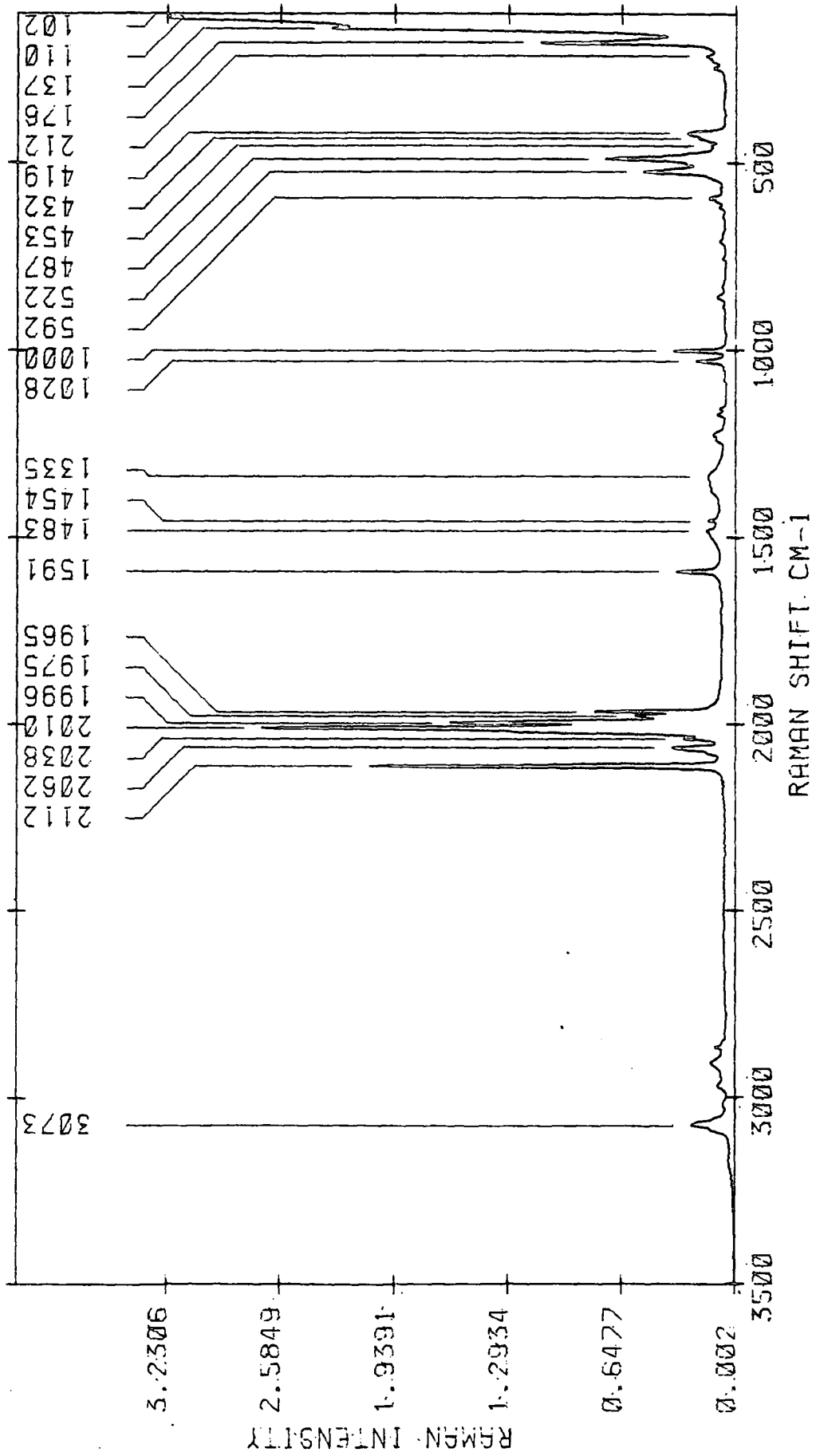
Table 4.16   _Vibrational frequencies of HOs$_3$(CO)$_{10}$(OPh)_

FTIR		Low temp. FTIR	
3067	w	3066	w
3064	w	3064	w
3058	w	3055	w
2962	w	2961	w
2923	w	2920	w
2856	w	2849	w
2113	m	2114	m
2083	s	2083	s
2058	s	2054	vs
2043	s	2043	s
2029	s	2029	s
2010	vs	2010	vs
2001	s	2002	s
1988	s	1989	s
1980	vs	1981	vs
1597	m		
1512	w		
1433	m		
1279	sh	1287	m
1260	m	1260	w
1223	w		
1200	vw		
1178	vw	1142	m
1154	vw	1142	m
1106	m	1103	w
1022	m	1049	w
		1036	w
963	w		
865	vw		
839	w		
810	m	810	m
780	w		
765	w		
733	w		
722	vw		
669	w		
656	w		
633	vw		
622	vw		
595	m		
584	m		
563	m		
539	w		
527	w		
497	w		
474	w		
468	w		
452	w		

All values in cm^{-1}

FTIR: KBr disc, 2cm^{-1} resolution
Low Temp. FTIR: KBr disc, 4cm^{-1} resolution

Os-C-O stretching and deformation modes occurring in the region 707-417cm^{-1} (698-417cm^{-1} -196°C). The stretching modes are in turn assigned to bands between 495 and 417cm^{-1}, the deformation modes to the higher frequency bands, as discussed by Anson and Jayasooria [45]. Ring deformation modes are also found in this region: 691, 618 and 415cm^{-1} for phenol [79].

(ii) Ligand vibrations

Bands at 3084, 3038 and 3009cm^{-1} (3079, 3036 and 3008cm^{-1} -196°C) are assigned to CH stretching modes and are in good agreement with values for the phenol molecule of 3070, 3043 and 3019cm^{-1}. Ring stretching modes occur at 1605, 1598, 1501, 1473 and 1370cm^{-1} for phenol, with bands being found at 1588 and 1479cm^{-1} for the triosmium cluster complex (Table 4.16).

OH deformation modes are found at 1370 and 1230cm^{-1} in phenol and the lower frequency band finds correspondence in the cluster which has medium intensity bands between 1261 and 1224cm^{-1}.

The CH bending modes are assigned to the bands in the region 1169-753cm^{-1}. For the phenol molecule CH deformations were assigned to bands in the region 1169-828cm^{-1}. Bands at 1093, 1076 and 1025cm^{-1} are of medium intensity and appear to be common to the set of cluster compounds studied here.

2.6.3b $H_2Os_3(CO)_9(OC_6H_4)$

(i) Assignment of Os-C=O modes

The crystal belongs to the space group P2$_1$/c (C$_{2h}^5$), with Z = 4, and this leads to a site group of C$_1$ [40]. The isolated molecule does not possess any symmetry and thus all the carbonyl stretching vibrations are allowed. In the solid state, each stretching vibration (of A representation) will give rise to two IR active (A$_u$ + B$_u$) and two Raman active (A$_g$ + B$_g$) vibrations. The exact frequency of each vibration is determined by the extent of π back donation of electrons from the metal atoms to the CO ligands as discussed previously. Nine bands are seen in the IR spectrum, 2113-1980cm^{-1} at room temperature and 2114-1981 cm^{-1} at 196°C (Table 4.17).

The Os-C-O stretching and deformation modes are observed in the region from ca. 733-423cm^{-1}. The deformation modes are at the higher frequencies (733-527cm^{-1}), the stretching modes from 497 to 423cm^{-1}. Again, metal-ligand π back donation of electrons determines the Os-C bond order and hence its vibrational frequencies.

Figure 4.17 The FTIR spectrum of $H_2Os_3(CO)_9(OC_6H_4)$
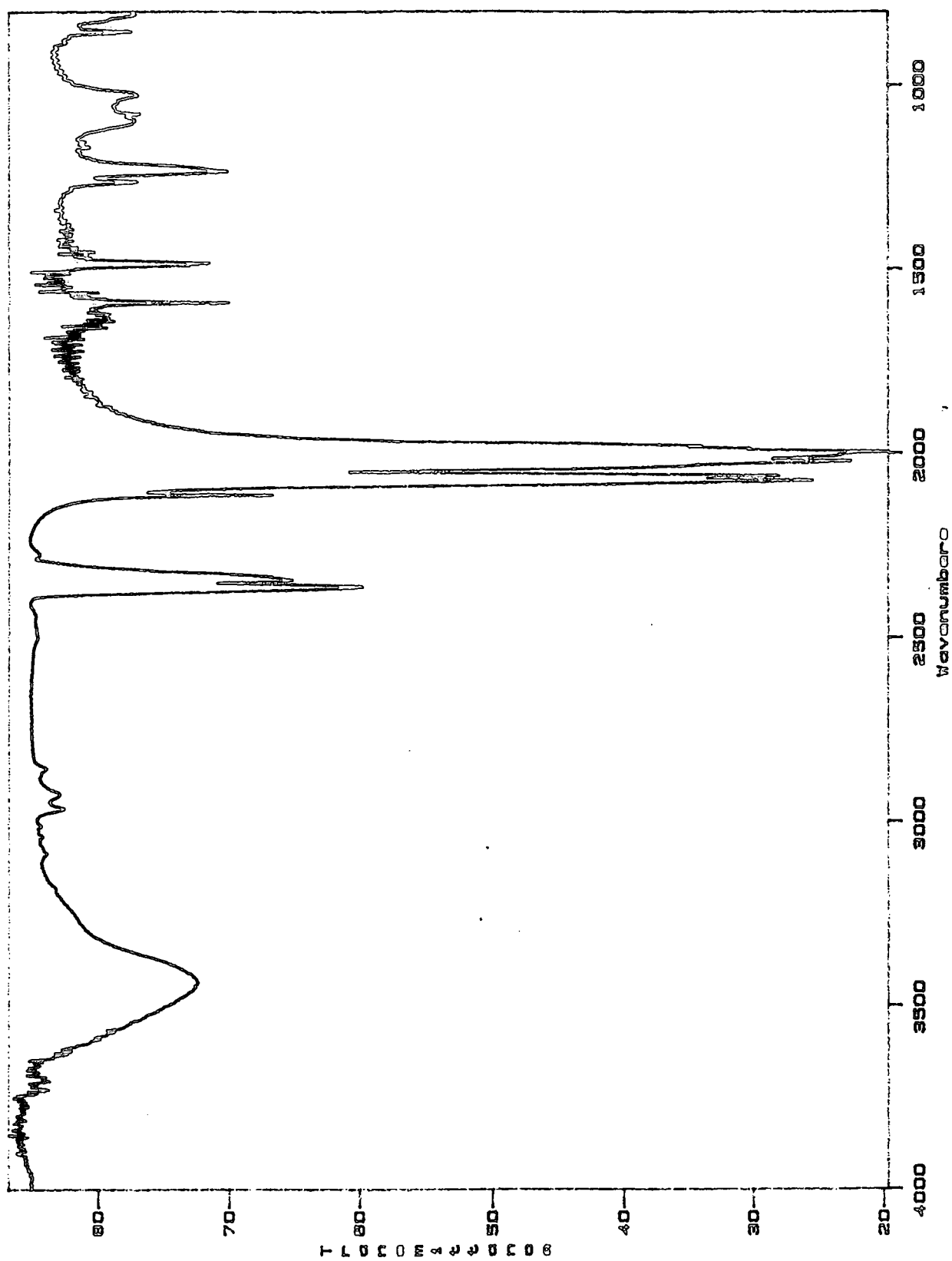
Table 4.17 _Vibrational frequencies of $H_2Os_3(CO)_9(OC_6H_4)$_

FTIR	Low temp. FTIR
3084 w	3079 w
3038 w	3036 w
3009 w	3008 w
2965 w	2961 w
2924 w	2918 w
2857 w	2851 w
2110 w	2112 w
2072 s	2074 vs
2060 s	2060 s
2031 sh	2032 m
2020 vs	2022 vs
2006 s	2008 s
1995 vs	1995 s
1985 m	1985 m
1977 w	1979 m
1588 m	1588 m
1479 m	1478 m
1261 m	1262 m
1234 m	1240 m
1224 m	1225 m
1169 vw	
1152 vw	
	1103 m
1093 m	1092 m
1076 m	1078 m
1025 m	1026 m
851 w	856 w
	853 w
804 m	802 m
753 m	754 m
707 w	
688 w	698 w
665 m	
655 w	
614 m	615 w
579 m	582 m
568 m	569 m
532 w	536 w
495 w	517 w
	498 w
489 w	490 w
438 w	440 w
430 w	432 w
417 w	417 w

All values in cm^{-1}
FTIR: KBr disc, $2cm^{-1}$ resolution
Low Temp. FTIR: KBr disc, $4cm^{-1}$ resolution

(ii) Ligand vibrations

The ligand is not aromatic, but is in the dienone form, and hence ring vibrational frequencies are expected to be higher, tending towards the aliphatic rather than aromatic regions. The three CH stretching modes are found in a narrow frequency range, 3067-3058cm^{-1} (3066-3055cm^{-1} - 196°C), (Table 4.17), cf. 3070-3019cm^{-1} for phenol.

The ring C=C stretching modes are assigned to the medium intensity bands at 1597, 1512 and 1433cm^{-1}, higher than the corresponding values for the complex containing the OPh ligand.

The bands in the region 1279-733cm^{-1} are assigned to C-H deformation modes. The medium intensity bands 1106 and 1022cm^{-1} are similar in frequency to those found in other clusters in this study.

2.7 Complexes containing benzene ligands

2.7.1 Organometallic chemistry

Benzene and other arenes form the most widely studied section of η^6 transistion metal chemistry [52], and η^6 bonding has also been structurally characterized in a variety of polynuclear metal complexes [26].

Bisbenzene complexes are known for many of the transition metals. η^6 arene chromium tricarbonyl complexes have either a staggered or eclipsed structure defined by the relative orientation of the Cr-CO bond vectors and ring carbon atoms [73].
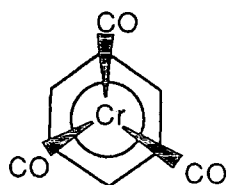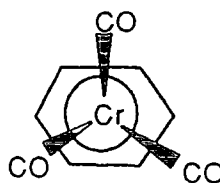
Eclipsed   Staggered

Low temperature structural determination revealed a staggered structure, where the C-C bonds located over each Cr-CO bond are slightly longer than the other three intra-ring C-C bonds. The six arene hydrogen atoms are displaced 0.021-0.038A out of the C$_6$ plane towards the chromium atom. η^{6}C$_6$H$_6$ is a stronger π donor and weaker π acid than CO,

reflected in the shorter Cr-CO distance than in $Cr(CO)_6$ [56,79]. The dominant $M-C_6H_6$ bonding occurs as $M(3d)-C_6H_6$ (2n,3n) π bonding, but significant $M(4s,4p)-C_6H_6$ σ bonding interactions are also observed.

Formal donation of six electrons is not mandatory and arenes may behave as pseudo-diene or olefinic ligands in η^4 and η^2 coordination modes respectively [26]. In these compounds arene ring parameters may diverge substantially from those of the free ligand, ring planarity is lost and there is extensive localization of single and double bonds. η^2 complexes have been proposed to be important intermediates in arene activation reactions [189,190]. Arenes can also act as bridging ligands between two metal atoms, occurring either *syn* or *anti* facial with respect to the C_6 ring [26,81].

The first synthesis of a molecular cluster complex containing an arene ligand bonded to three or more metal atoms was carried out by Lewis *et al* [82]. An octahedral Ru cluster was obtained, having one benzene ring bonded as a η^6 ligand to a ruthenium atom, the second takes a position parallel to a triangular face of the Ru_6 octahedron and interacts with three metal atoms. The structure is shown below.
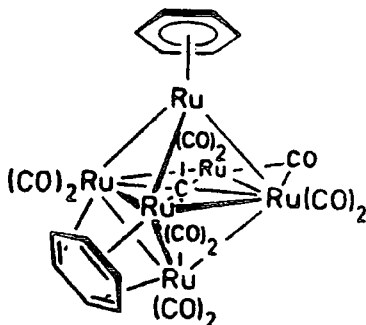
A similar "face capping" benzene ligand has been obtained in an triosmium cluster via the μ_3 cyclohexadienyl intermediate, as shown in Scheme 4.1.

273

$[H_2Os_3(CO)_{10}]$ $\xrightarrow[\text{- 2H}]{1,3\text{-}C_6H_8}$

1) Ph_3C^+
2) DBU

hv

$[Os_3(CO)_{10}(NCMe)_2]$ $\xrightarrow{C_6H_6}$
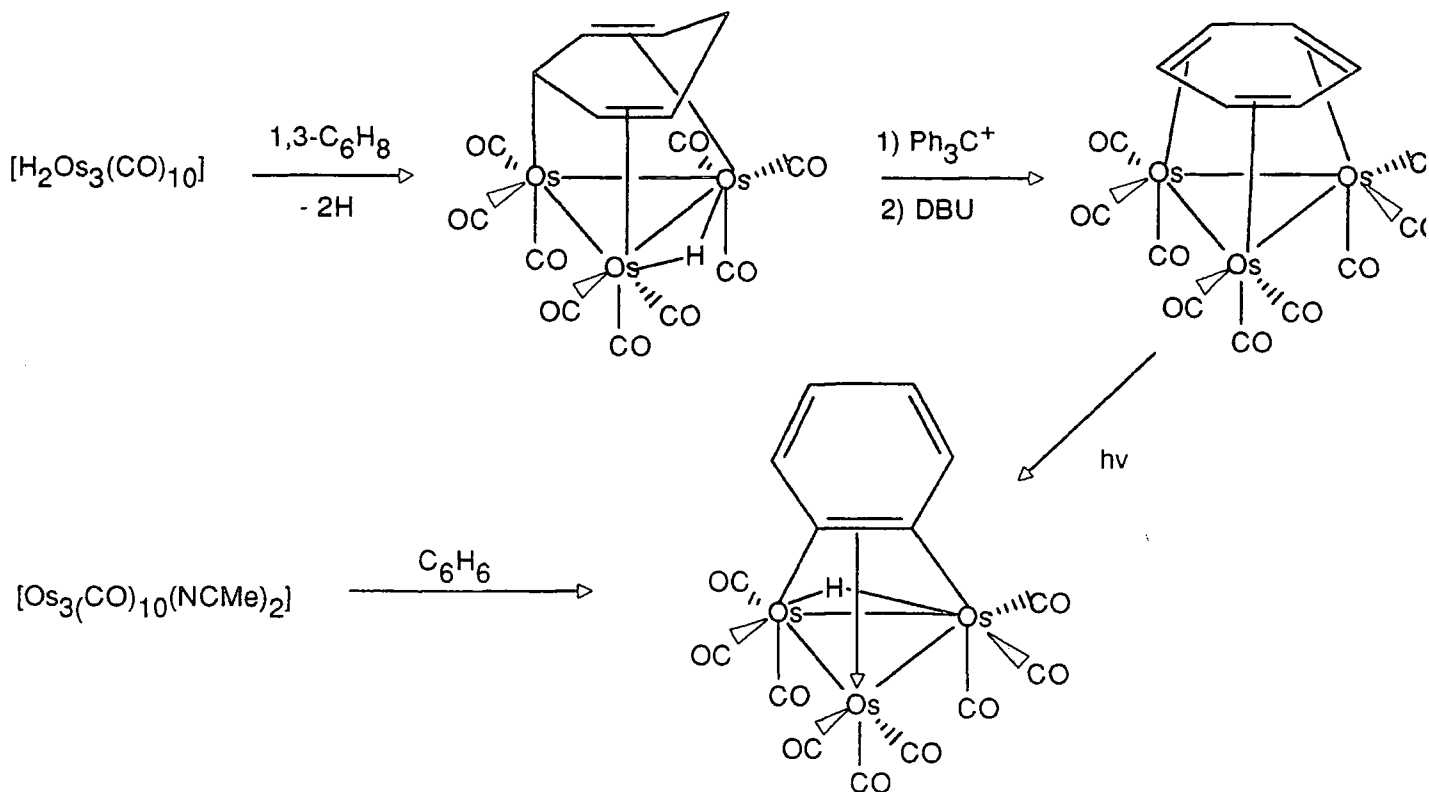
By reaction of the η^6 benzene complex with Me_3NO/MeCN the complex $Os_3(CO)_7(C_2H_4)(MeCN)(\mu_3\eta C_6H_6)$ is accessible, which reacts with alkynes C_2R_2 to give $Os_3(CO)_7(\eta^6C_6H_6)(\mu_3\eta^1\eta^2\eta^1C_2R_2)$. In this reaction the benzene ligand is transferred from the Os_3 face capping position into a η^6 coordination at only one osmium atom [83].

On irradiation (λ=290nm) the face capping benzene cluster $Os_3(CO)_9(\mu,\eta^2\eta^2\eta^2C_6H_6)$ isomeriszes quantitatively by oxidative addition of the μ_3 benzene to the Os_3 cluster to form the $\mu,\eta^1\eta^2\eta^1$dehydrobenzene cluster [84]. This conversion is irreversible and can be accomplished by prolonged heating. Thermal reaction of benzene with $Os_3(CO)_{12}$ gives a coordinated benzyne by oxidative addition, structure (27) shown below. Yields are normally poor, and some improvement can be obtained by reaction of the bisacetonitrile complex with benzene [80].
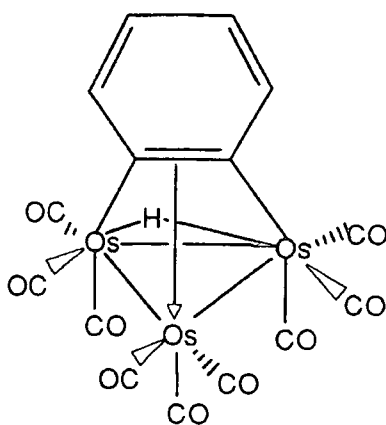
(27)

All these results indicate that the dehydrobenzene cluster is the thermodynamically more stable isomer. This experiment was carried out in an NMR tube in this study and the ^{1}H NMR spectrum reveals that the singlet resonance at δ 4.37 (C_6H_6) has not completely disappeared, but is joined by multiplet signals at δ 6.88 and 7.88 due to the two distinct hydrogen sites on the benzyne cluster. A signal at δ -18.99 confirms the bridging hydride ligand.

The complex $Os_3(CO)_9(C_6H_6)$ has been studied by X-ray crystallography [26]. These studies coupled with ^{1}H and ^{13}C NMR and IR data lead to the conclusion that the benzene ligand is coordinated to the metal triangle in a staggered orientation and is best viewed as a bond localised cyclohexa-1,3,5-triene [26]. The cluster has approximate C_{3v} symmetry and the metal-metal distances are comparable to those found in $Os_3(CO)_{12}$ (average Os-Os = 2.877A). The plane of the C_6H_6 ring makes an angle of only 1.1° with the plane defined by the Os atoms and the equatorial carbonyl ligands, indicating that the two units are essentially parallel. A pattern of alternating "long" and "short" bond lengths is observed, mean "coordinated" and "noncoordinated" C-C distances are 1.41 and 1.51A respectively, although the high estimated standard deviations associated with these distances renders this variation statisticaly insignificant at the 2σ level.

The trigonal distortion of μ_3 arenes towards a Kekule structure is induced by a mixing of HOMO and LUMO of the arene, according to theoretical analysis [191]. This occurs in such a way that the three C-C bonds which lie above the metal atoms are shortened, whereas the others are lengthened. This is made possible by the threefold symmetry enforced upon the arene by the metal cluster. There is an interesting parallel to the mononuclear complexes $(CO)_3M(\eta^6C_6H_6)$ (M = Cr, Mo, W), which also show a weak alternation of the C-C bond lengths in the benzene ligand

275

which can also be understood from MO theory.

Face capping coordination has been established for *trans*-β-methylstyrene in the cobalt cluster $(CpCo)_3(\mu^3\eta^2\eta^2\eta^2C_6H_5CH=CHMe)$ [81]. The C-C bond lengths in the aromatic ring here show almost negligible alternation (mean distances 1.420 and 1.446A) illustrating that pronounced Kekule distortion of an arene is not an intrinsic property of its coordination at a 3-fold metal site.

2.7.2 Surface studies of adsorbed benzene

The adsorption of benzene on transition metal surfaces has been well studied. Most investigations were carried out on single crystal surfaces with low Miller indices [81, and referenes therein]. In almost all cases benzene is adsorbed non-dissociatively and the ring lies parallel to the metal surface. However, different adsorption sites for different metals have been proposed. Benzene can be bonded to one or more surface atoms. For the simple case of benzene on a close packed, atomically flat metal surface, eg. the (111) face of a metal with cubic close packing, there are at least four different sites for the chemisorbed benzene: one with six fold local symmetry (highest symmetry C_{6v}), e.g. Rh(111), Pd(111); one with threefold local symmetry ($C_{3v}(o_v)$ or $C_{3v}(o_d)$) e.g. Os(0001), Rh(111)/Na, Pd(111)/2CO, Pt(111); and with two fold symmetry (C_{2v}), e.g. Pt(111)/4CO. A schematic representation of the different symmetries is shown in Figure 4.18 below.

Figure 4.18 Adsorption sites of benzene on a densely packed transition metal surface

$C_{3v}(\sigma_d)$ $C_{3v}(\sigma_v)$ C_{6v} C_{2v}
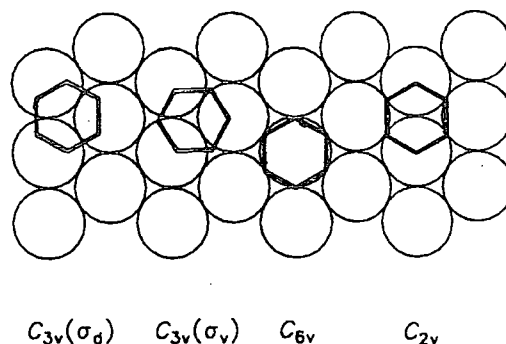
A summary of the adsorption studies of benzene on various transition metal single crystal faces is given in Table 4.18.

Table 4.18 _Summary of results for adsorption of benzene on transition metal single crystals_

Metal	Comments	Ref.
Mo(110)	Parallel to surface	[101]
W(001)	Dissociative chemisorption at 300K and low coverages, saturated layer sees molecular and dissociative adsorption	[192]
Re(0001)	Partial dissociation at 300K, C_{3v} symmetry	[193]
Ru(001)	Parallel to surface (120-240K), C_{6v} symmetry	[96]
Os(0001)	Parallel to metal surface, C_{3v} symmetry, high distortion at 300K	[99, 100]
Rh(111)	Molecular adsorption at 300K, parallel to surface, C_{6v} symmetry	[94]
Rh(111)	Parallel to metal surface 300K, C_{6v} symmetry (ARUPS), LEED -> C_{3v} symmetry, alternate single and double C-C bonds. Borderline between molecular and dissociative adsorption	[103 106]
Ir(111)	Parallel to metal surface, C_{3v} symmetry, high distortion	[102]
Ni(111)	Molecular adsorption, parallel to surface C_{3v} symmetry, bonding to 3 fold hollow site Ni-C_6H_6 2.2A, no ring distortion (2% expansion)	[86]
Ni(111)	Parallel to surface, C_{3v} symmetry	[89]
Ni(111)	Parallel to surface, 3 fold hollow site for adsorption	[93, 109]
Ni(110)	Compressed benzene Molecular adsorption to 300K parallel to surface, C_{2v} symmetry	[87]
Ni(110)	Parallel to surface, C_{2v} symmetry Saturated layer: benzene is parallel but C_1 symmetry due to azimuthal rotation induced by strong lateral interactions	[88]

Pd(111)   Monolayer, parallel to surface C_{6v} symmetry   [90,
          Dense overlayer, tilted, plane 30° to surface   97]

Pd(110)   Tilted, 10-20° to surface at 300K to minimize   [98]
          steric interactions, tilting is into grooves
          of surface toward [001] azimuth, symmetry C_s

Pt(100)   Parallel to surface, , EELS 840cm⁻¹ δCH   [95]
          o.o.p. very intense
          300K, parallel to surface, C_{3v} geometry   [108]

Pt(001)   Parallel to metal surface   [105]

Cu(110)   Parallel to surface   [194]

Cu(111)   Parallel to surface   [194]

Ag(110)   Submonolayer, most molecules parallel to   [91]
          surface, minority tilted 10-15°, associated
          with defect sites

Ag(111)   Parallel to surface, bound in 3 fold hollow   [92,
          site, C_{3v} symmetry   104]

Au(film) Parallel to surface   [107]

     Somorjai and Mate [111] have studied the CO ordering
effect on benzene adsorbed on Pt(111) and Rh(111) using
HREELS.

	Pt(111)	+0.5L CO (300K)	+ 1.0L CO	Rh(111)
vCH	3000	3000	3025	2970
δCC	1420	1420	1425	1430
vCC	1330	1330	1325	1330
δCH	1130	1135	1135	1115
γCH	830	835	845	805
vM-C	360	365	365	345
				545

     For adsorption on Pt(111) the in-plane modes (vCH, the
ring modes vCC, δCC, δCH) are weak and the out-of-plane C-H
bend (830cm⁻¹) intense, which if the surface dipole
selection rule is operating, indicates that the benzene
molecules are bound parallel with the surface. The
coadsorption of CO does not change this significantly, but
the CO molecules are seen to be adsorbed in three kinds of
site. LEED studies [112] showed the rings to be centred over
bridge sites with local C_{2v} symmetry for the coadsorption
system Pt(111)-(2√3x4) rect-2C_6H_6 + 4CO. A large ring

expansion was also observed.

For Rh(111) HREELS data indicates that the ring is bound parallel with the metal surface plane since the bands are weak with the exception of the out-of-plane C-H bending mode at 805cm^{-1} [111].

Vibrational spectra reveal two adsorption states for benzene on the Pd(110) surface. In one of these states the ring is nearly parallel with the surface plane, and this is predominant at low exposures. In the other the ring is tilted and is located in the c(4x2) domains. More tilted species are found at higher exposures, and this is the predominant state for saturated exposure. Evidence of the tilting is provided by the growth of intensity for the ring modes in the region of 1400cm^{-1}. The out-of-plane C-H bending mode occurs at 705cm^{-1} for the flat species but a band at 745cm^{-1} was assigned to the tilted species. This band is observed to increase with coverage, the former to decrease [113].

On Rh(111) benzene coadsorbs with CO in two stoichiometries to give the surface complexes Rh(111)-(3x3)C$_6$H$_6$ + 2CO (A) and Rh(111) c{2(3)$^{1/2}$x4}rect C$_6$H$_6$ + CO (B), whose coordination geometries are accurately modelled by the cluster Os$_3$(CO)$_9$($\mu_3\eta^2\eta^2\eta^2$C$_6$H$_6$) [26]. In both overlayers benzene chemisorbs intact at 3 fold hcp-type sites and lies parallel to the surface, with an expanded C$_6$ ring showing in-plane Kekule distortions. C-C bond distances alternate between 1.46 and 1.58A in (A) and between 1.31 and 1.81A in (B), the short bonds lying above single metal atoms while the long C-C bonds form bridges linking pairs of rhodium atoms. Metal-carbon bond distances also compare favourably between the surface and cluster complexes. Distortions are larger on the extended surface as there are more metal atoms to influence each benzene molecule. ARUPS studies on these Rh(111) systems found no evidence for ring distortions, although trigonal deformations are detected by this technique for benzene chemisorbed on Pt(111), Ir(111) and Os(0001) surfaces [106,195,196]. The degree of Kekule distortion apparantly increses from Pt through to Os and adsorption at 3-fold hollow sites is presumed. Theoretical studies also predict maximum stability for surface complexes having C$_{3v}$ symmetry [197].

Coadsorption of electropositive potassium with benzene on Pt(111) raises the metal s-d band in energy and, at high potassium coverage, promotes electron donation from the surface to the benzene LUMO [197,198]. This suggests that the cluster Os$_3$(CO)$_9$($\mu_3\eta^2\eta^2\eta^2$C$_6$H$_6$) may be better regarded as a model for a cathodically charged surface complex or for benzene chemisorption on an earlier transition metal having a higher-lying Fermi level. Anodic charging of the cluster complex may be simulated by protonation at the metal

triangle to give $[(\mu\text{-}H)Os_3(CO)_9(\mu_3\eta^2\eta^2\eta^2C_6H_6)]^+$.

It is difficult to distinguish between coadsorbed systems and those without the coadsorbates using cluster models since the cluster complexes all contain "coadsorbates", i.e. other ligands [110].

The decomposition chemistry of coordinated benzene is one further area in which formal analogies between the surface and cluster system are evident. C-H bond scission constitutes an important degradation pathway, and on atomically flat surfaces is particularly facile for earlier transition metals e.g., benzene is completely dissociated at low coverage on W(100) at ambient temperature [192]. Broad band visible irradiation of cluster $Os_3(CO)_9(\mu_3\eta^2\eta^2\eta^2C_6H_6)$ results in efficient isomerization to the dimetalated benzyne complex $[(uH)_2Os_3(CO)_9(\mu_3\eta^1\eta^2\eta^1C_6H_4)]$, offering a model for the interconversion of associatively and dissociatively chemisorbed states of benzene via C-H activation [84].

Graen *et al* [99] used HREELS spectra to identify two precursor states in the dissociative adsorption of benzene on Os(0001). Both phenyl and benzyne (C_6H_4) were detected, and both are tilted with respect to the metal surface, 15° for the phenyl ring, and 45° for benzyne. HREELS data was compared for a number of metal surfaces and the C-H out of plane bending mode ca. $810cm^{-1}$ is the most intense feature. This mode has its dipole perpendicular to the surface if the molecule is parallel to the metal surface plane. Changes in intensity observed as the temperature is increased from 130-382K are explained by tilting of the ring which allows the weak in plane modes to become active under the surface selection rule.

Muetterties suggested in 1982 that the dissociative chemisorption (C-H bond cleavage) observed for benzene on a stepped metal (111) surface is due to its η^6 coordination parallel to one terrace of the surface allowing a close approach of its hydrogens to the step atoms of a second terrace [199,200]. The five metal atoms of the complex $Ru_5(CO)_{13}(\mu_4PPh)(\mu_5\text{-}\eta^5\text{-}C_6H_4)$ are in the arrangement of a step site on a (111) surface and the complex can be viewed as a model for the aftermath of benzene C-H activation on such a surface [116].

When $Ru_3(CO)_{11}(PPh_3)$ is heated in toluene for 18 hours three complexes are formed: $Ru_3(CO)_7(\mu\text{-}PPh_2)(\mu_3\text{-}\eta^2\text{-}C_6H_4)$, $Ru_4(CO)_{11}(\mu_4PPh)(\mu_4\text{-}\eta^4\text{-}C_6H_4)$ and $Ru_5(CO)_{13}(\mu_4PPh)(\mu_5\text{-}\eta^5\text{-}C_6H_4)$. The five Ru atoms in the latter mimic a step-site on the (111) surface with three of the metal atoms in one terrace and two are step atoms in the first row of the next.. It can be envisaged that the approach of benzene on a metal (111) surface to exposed low coordinate step atoms

will result in the activation of two *ortho*-CH bonds to generate benzyne chemisorbed as in the Ru$_5$ cluster.

The Ru$_3$ and Ru$_4$ clusters can likewise be regarded as models for the dissociative chemisorption of benzene on metal (111) and (100) surfaces respectively.

2.7.3 Assignment of the FTIR spectrum of Os$_3$(CO)$_9$(C$_6$H$_6$)

Experimental data for complex is contained in Tables 4.19 and Figures 4.19 and 4.20. ^{1}H NMR and IR data were consistent with the literature values for the complex Os$_3$(CO)$_9$(μ,$\eta^2\eta^2\eta^2$C$_6$H$_6$).

The complex Os$_3$(CO)$_9$(μ,$\eta^2\eta^2\eta^2$C$_6$H$_6$) belongs to the molecular point group C$_{3v}$ and the crystal to space group Im (C$_s^3$), a non-standard setting of Cm, with 1.5 molecules per asymmetric unit and z = 6. The site symmetry is C$_1$.

(i) Assignment of Os-C≡O modes

X-ray crystallography revealed three radial and six axial CO ligands, and their irreducible representations are:

$$\Gamma_{CO\ axial} = A_1 + E$$
$$\Gamma_{CO\ radial} = A_1 + A_2 + 2E$$

The A$_2$ representation is inactive in the IR and Raman, but all other representations are active in both. Therefore a total of five IR and Raman bands are expected for the isolated molecule: in dichloromethane solution this is what is observed, with bands at 2077, 2031, 1998, 1991 and 1979 cm^{-1}.

Correlation of the molecular symmetry species with the factor group symmetry species via the site group is shown below.

Molecular symmetry C$_{3v}$	Site group C$_1$	Factor group C$_s^3$

axial A$_1$
       E
       A$_1$
                                    A
radial A$_2$
       2E
                                                A′(9)
                                                A″(9)

Both A′ and A″ representations are IR and Raman active and therefore the solid state spectra should contain 18 bands for the carbonyl stretching region. The high resolution IR spectrum has nine bands between 2076 and

281

Figure 4.19 The FTIR spectrum of $Os_3(CO)_9(u_3,n^2,n^2,n^2-C_6H_6)$
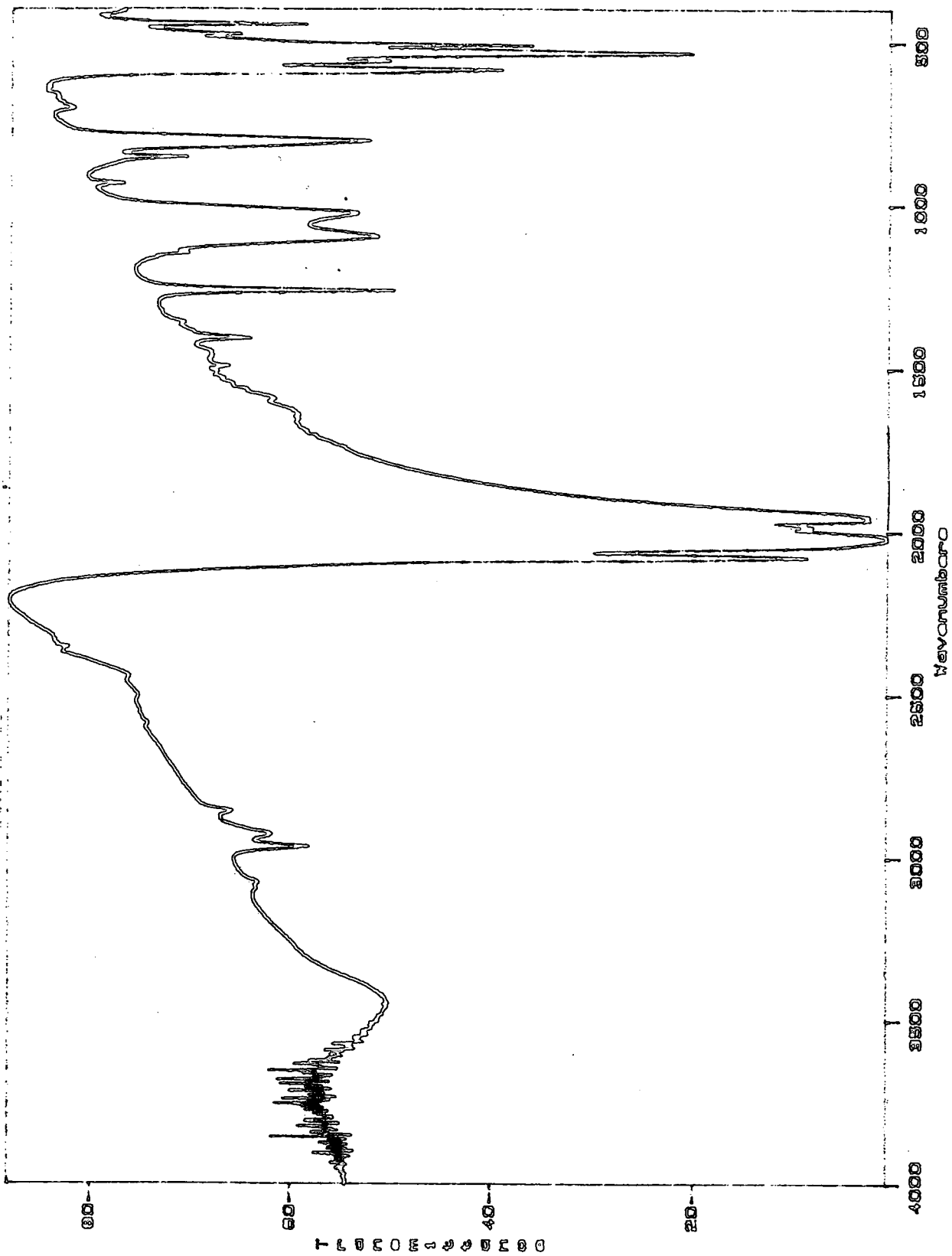
Figure 4.20 The Raman spectrum of $Os_3(CO)_9(u_3,n^2,n^2,n^2-C_6H_6)$
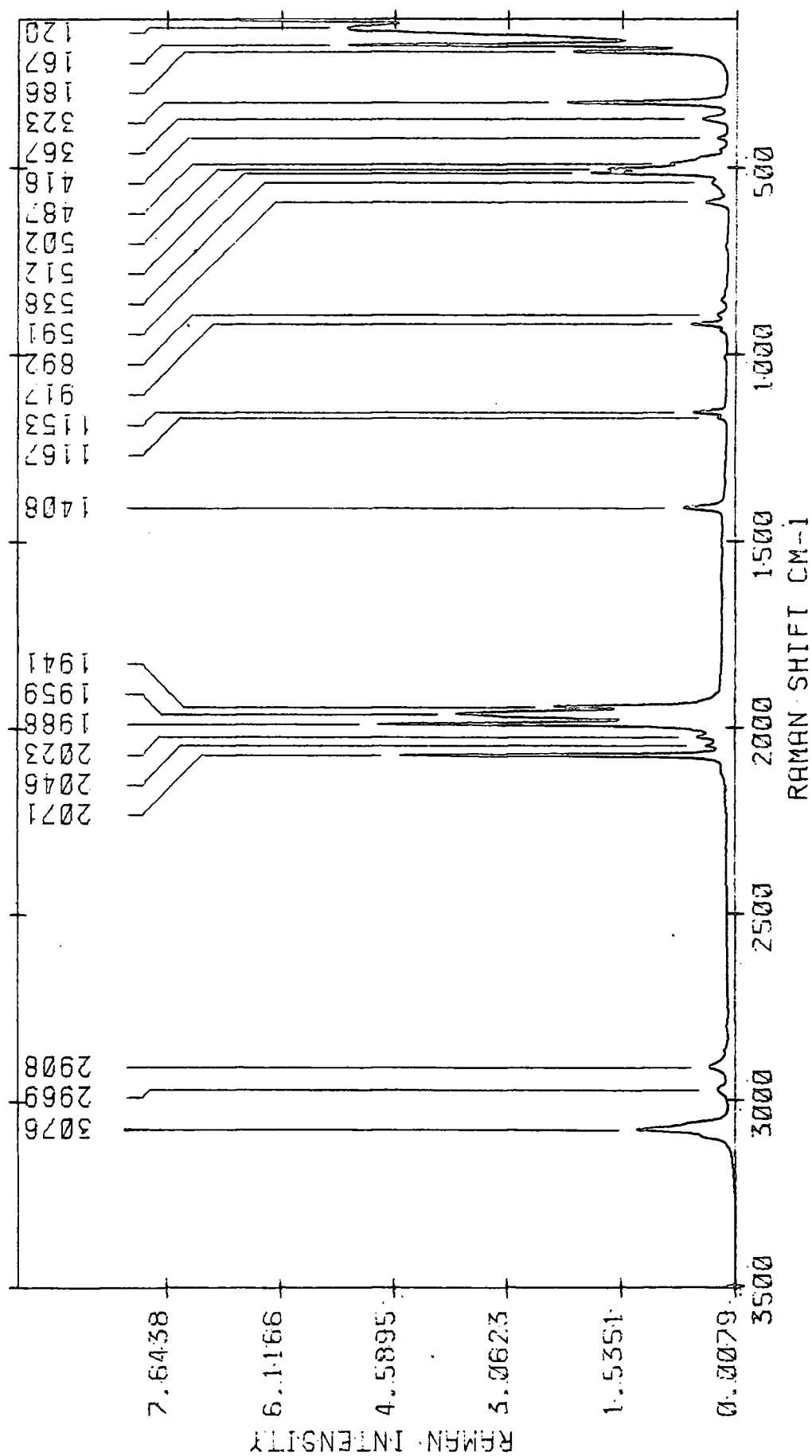
Table 4.19   Vibrational   frequencies   for
$Os_3(CO)_9(\mu_3,\eta^2,\eta^2,\eta^2-C_6H_6)$

FTIR	Low temp. FTIR	Raman
3090 w		3076 m
3073 w		2969 w
2963 w	2967 w	2908 w
	2960 w	
2924 w	2942 vw	
	2920 w	
2853 w	2851 w	
2076 m	2077 m	2071 vs
	2045 sh	2046 vs
2020 vs	2022 vs	2023 w
1983 w	1983 w	1988 w
1962 s	1964 s	1959 s
1952 s	1952 s	1941 m
	1942 s	
1591 w		
1495 w		
1410 w		1408 w
1265 m	1262 w	
1148 w		1167 w
		1153 w
1098 m	1098 w	
1026 m	1024 w	
936 vw		
		917 w
		892
856 w	856 vw	
804 m	802 w	
704 vw		
		591 w
	598 w	
586 m	584 w	
559 w	559 w	
534 m	536 m	538 w
511 m	511 m	512 m
478 w		502 m
478 w		487 w
		418 w
		367 w
		323 m
		186 s
		167 s
		120 s

All values in cm⁻¹
FTIR: KBr disc, 2cm⁻¹ resolution
Low Temp. FTIR: KBr disc, 4cm⁻¹ resolution

1943cm^{-1} and the Raman spectrum six bands between 2071 and 1941cm^{-1}. The assignment of bands to radial and axial CO stretches is dependent on the π donor abilities of benzene compared to Os. The axial CO groups are *trans* to the benzene ligand, which is a good π donor but a weaker π acceptor than CO. This results in an increased Os ⟶ CO back donation and a decrease of the bond order. These bands should therefore be at lower frequency than those of the radial CO ligands.

The region below 600cm^{-1} in the IR spectrum is assigned to Os-C-O stretching and deformation modes, (Table 4.19). As with $Os_3(CO)_{12}$ and the other cluster complexes considered here, the stretching vibrations are at lower frequency, 448 and 478cm^{-1}, with bands in the region 511-586cm^{-1} being assigned to deformation modes. The assignment to axial or radial CO ligands depends on the amount of π back donation from the osmium atoms: where the CO ligand receives π donation from the metal, the Os-C bond is strengthened and in this complex it will be the axial bonds. These bond stretches and deformations should thus generally be at higher frequency than those of the radial bonds. As with the parent carbonyl, there will be some mixing of radial and axial frequencies.

In the Raman spectrum bands at 538, 512 and 502cm^{-1} are assigned to deformation modes, and those in the region 487-367cm^{-1} are assigned to the Os-C-O stretching vibrations. The very low frequency bands at 120, 167 and 186cm^{-1} are dassigned to Os-Os stretching modes of the cluster framework.

(ii) Ligand vibrations

The solid state IR spectrum of benzene contains v(CH) vibrational modes at 3069, 3063, 3060 and 3040cm^{-1} [111,113]. By comparison, the solid state IR spectrum of $(CO)_3Cr(C_6H_6)$, which contains an η^6 benzene ligand, has bands at 3110, 3090 and 3023cm^{-1} [4]. Bands observed at 3090 and 3073cm^{-1} (3076cm^{-1} Raman) for the Os_3 complex are assigned to v(CH) modes (Table 4.19). Gallop *et al* [26] quote values of 3104 and 3071cm^{-1} for the IR spectrum of the triosmium complex, which was obtained in dichloromethane solution. In the Ru_6 carbonyl complex prepared by the same authors, which has μ_1 and μ_3-benzene ligands, the v(CH) modes were observed at 3125/3118 and 3100/3065cm^{-1} respectively. Gallop *et al* [26] suggested that the transition from η^6 apical-to-face capping coordination is accompanied by partial rehybridization (sp^2 ⟶ sp^3) of the ring carbon atoms (i.e. an out of plane distortion of the C-H bonds), perhaps a consequence of increased π acceptance from the cluster in the triply bridging mode.

Bands in the region 2963-2853cm^{-1} (2969 and 2908cm^{-1} Raman)

were assigned to contamination by aliphatic CH, thought to be oil contamination from the laboratory atmosphere.

The remaining bands between 1591 and 704cm^{-1} in the IR spectrum were assigned by comparison with the published spectra of benzene and the mononuclear π complex $(CO)_3Cr(C_6H_6)$. Ring stretching modes were observed in the IR at 1519, 1448 and 1316cm^{-1} in the chromium complex and 1596, 1478 and 1312cm^{-1} for solid state benzene. The IR spectrum of the triosmium complex contains weak bands at 1591, 1495 and 1410cm^{-1} and a more intense band at 1265cm^{-1}, all of which are assigned to the ring stretching modes.

The bands between 1148 and 704cm^{-1} (Table 4.19) are assigned to various C-H deformation modes. In the solid state benzene C-H in plane bending modes were observed at 1340, 1174 and 1147cm^{-1} and out of plane modes were at frequencies of 990, 864, 854 and 687cm^{-1}. For the chromium complex the values were 1161, 1150 and 965cm^{-1} and 1017, 904 and 790cm^{-1} respectively. In the triosmium complex in plane bending modes are assigned to the bands at 1148 and 1098cm^{-1} and out of plane bending modes to the bands at 936, 856 and 804cm^{-1}. The band of medium intensity at 1026cm^{-1} could be a C-H bending mode or a ring deformation (ring bending mode in benzene 1010cm^{-1}, CH deformation $(CO)_3Cr(C_6H_6)$ 1017 and 1036cm^{-1}). The band at 704cm^{-1} is assigned to a ring bending mode motion by comparison with the solid state IR spectrum of benzene (703cm^{-1}). Raman bands are matched to their ir counterparts as follows: 1408 ring stretch, 1167 and 1153 in plane CH bending, and 917 and 892cm^{-1} CH out of plane bending modes. In addition the Raman band at 323cm^{-1} was assigned to a symmetric metal-ring stretch by reference to the work of Gallop *et al* [26].

2.8 Assignment of the FTIR spectrum of $(CO)_3Cr(C_6H_6)$

The IR and Raman spectra for this complex are contained in Table 4.20 and Figure 4.21. Assignment of bands is made by direct comparison with the published spectra [4,118].

Table 4.20   *Assignment of the vibrational modes of $(CO)_3Cr(C_6H_6)$*

Frequency/cm^{-1} ref. [4,118]	Assignment	Frequency/cm-1 (this work)
3110	vCH	3116 w
3090	vCH	3107 w
3023	vCH	3071 w
1987	vCO	1985 s
1918	vCO	1915 vs

Figure 4.21 The FTIR spectrum of $(CO)_3Cr(C_6H_6)$
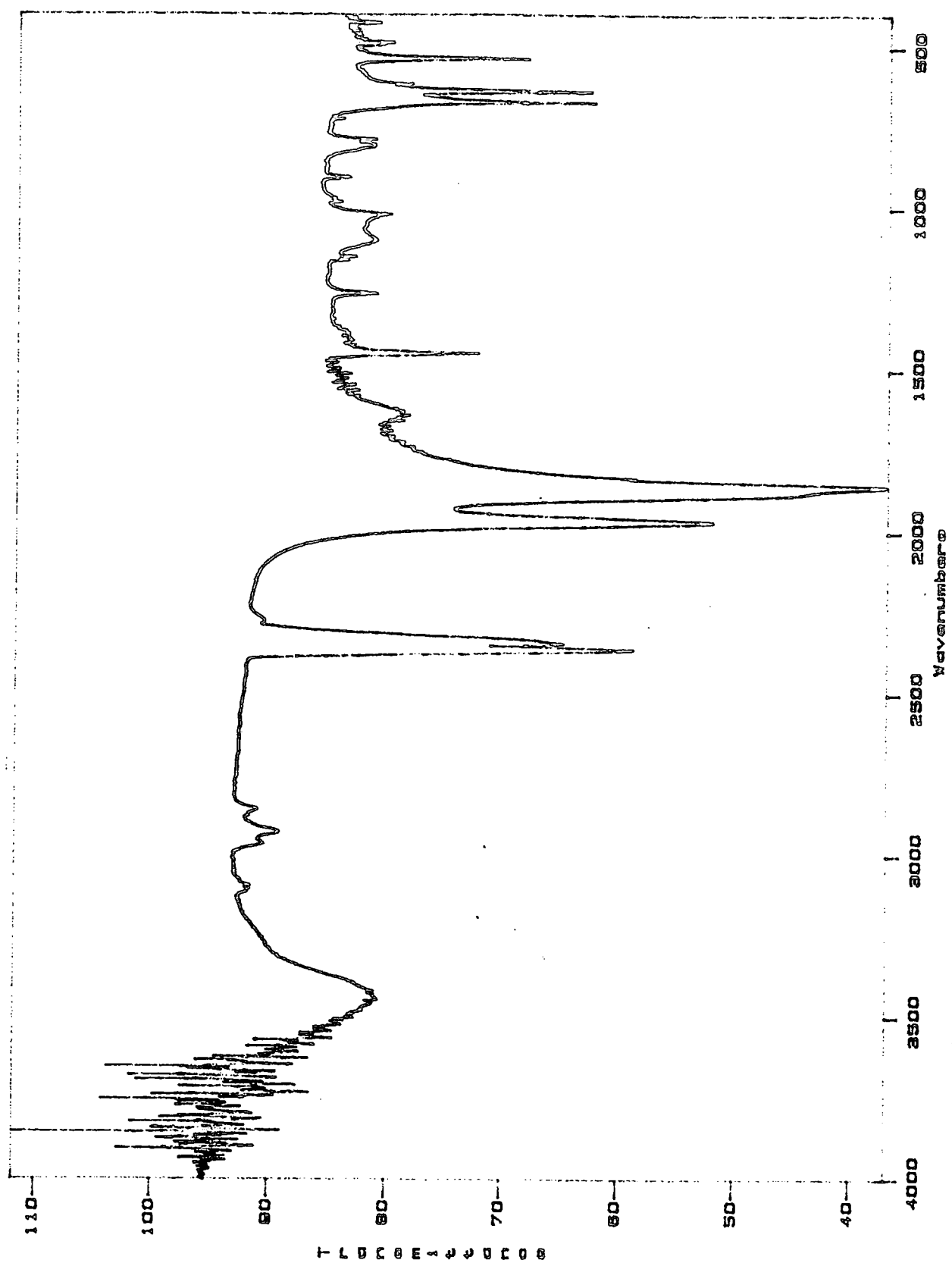
1519	νCC	
1448	νCC	1446 m
1361	νCC	1259 m
1161	βCH	1143 w
1150	βCH	1125 w
1017	γCH	1018 m
979	νCC	982 w
965	βCH	955 w
904	γCH	893 w
790	γCH	804/777 m
666	$\delta(CrCO)$	679 s
637	$\delta(CrCO)$	652 s
614	$\alpha(CCC)$	616 w
543	$\delta(CrO)$	536 s
490	$\tau(CCCC)$	491 w
484	$\nu(CrC)$ mixed mode	482 w
424	"	429 w
330	"	
298	"	

3 Discussion and Conclusions

It has been possible to assign the vibrational modes of the six prepared triosmium carbonyl complexes by comparison of their FTIR spectra with spectral data obtained for the free ligand molecules and the detailed analysis carried out by Anson and Jayasooria [45] on the parent carbonyl complex $Os_3(CO)_{12}$. It is necessary to take into account the changes in frequency which occur on binding the ligand to the triosmium cluster, with the resultant reduction in symmetry Indeed, the complexes prepared in this study, with the exception of $Os_3(CO)_9(\mu_3, \eta^2 \, \eta^2, \eta^2 \text{-} C_6H_6)$, lack any symmetry other than the identity element, and this further complicates the assignment, since IR bands which would otherwise be forbidden become allowed with the lowering of symmetry. A full normal coordinate analysis would be required to make more detailed assignments of the IR bands, but was beyond the scope of this study.

From the results in Section 2 above, it can be seen that similarities occur for all the triosmium complexes studied. The framework Os-C=O stretching and deformation modes occur at similar frequencies, and are not greatly shifted from the frequencies of the parent cluster $Os_3(CO)_{12}$. For the heterocycles pyrrole, furan and pyrrole the ligand modes occur at similar frequencies, in particular ring stretching and deformation modes found between 1400 and 1000cm^{-1}, which emphasises the structural similarities.

It was intended to make studies of aniline, phenol, pyrrole, furan, thiophene and benzene as adsorbates on metal single crystal surfaces using vibrational spectroscopies

such as EELS and RAIRS. The spectra of the fully characterized triosmium cluster complexes were then to be used to help assign the spectra of the metal-adsorbate systems. However, the surface work could not be carried out, and comparison has to be made with studies reported in the literature, where available.

Of the heterocyclic molecules of interest, thiophene is the most studied adsorbate, due to the industrial importance of its removal from petroleum feedstocks in the HDS reaction. On a number of metal surfaces thiophene is bound parallel to the surface plane (Table 4.12 above). A tilted bonding geometry has been observed on the Mo(100) [63], Mo(110) [64], Ru(0001) [62], Pt(100) [65] and Cu(100) [54] surfaces. The complex $HOs_3(CO)_9(\mu,\eta^2\text{-}C_4H_3S)$ prepared and characterized in this study is clearly not a suitable model for the "flat" surface geometry, but may be more useful in interpreting spectra from species which adopt the "tilted" geometry, since the thiophene molecule binds to the metal surface through the sulphur atom lone pairs when it is tilted. Table 4.21 below compares the assignments for thiophene adsorbed on the Ru(0001) and Mo(110) surfaces as multilayers at low temperature with those of the prepared complex.

Table 4.21   *Vibrational frequencies and assignments for thiophene adsorbed on Ru(0001) and Mo(110) compared with those for the cluster complex $HOs_3(CO)_9(\mu,\eta^2\text{-}C_4H_3S)$*

Assignment	Liquid C_4H_4S	Ru(0001)	Mo(110)	Os_3 cluster
χ C-H	714	760	735	710
ρ C-H	834	880	840	804
χ C-H	1084	1065	1090	1047
δ C-H	1256	1250	1265	1248/1261
v C-C	1409	1410	1435	1410
v C-H	3126	3125	3150	3124
	3098			3091
	3086			3084

For pyrrole and furan there are few available vibrational spectra to make comparisons. A ring tilt of 22° away from the surface plane has been observed for furan adsorbed on Ag(110) [59]. On heating, loss of α-H is known to occur for both adsorbates and the prepared complexes $H_2Os_3(CO)_9(\mu_3\text{-}C_4H_3N)$ and $HOs_3(CO)_{10}(\mu,\eta^2\text{-}C_4H_3O)$ may be suitable models for the intermediates and products of this cleavage.

There has been relatively little work published on the adsorption of aniline and phenol on metal single crystal surfaces, but evidence of PhNH and PhO species has been obtained on Pd(110) [70], Rh(111) [72] and Ni(100) [73], and Mo(110) [74,75], Ni(110) [76] and Pd(110) [70]

respectively. Again, the complexes prepared in this study may be suitable models for reactions on the surface involving N-H and O-H bond cleavage, or the C-H activation which has been reported to occur at 370K for phenol adsorbed on Mo(110) [74].

The role of the complex $Os_3(CO)_9(\mu_3,\eta^2,\eta^2,\eta^2-C_6H_6)$ as a model for benzene adsorption on metal single crystal surfaces has been discussed at length in Section 2.7.3 above. This is a good example of an organometallic complex providing a useful and faithful model of adsorbate-metal interaction, but it also reveals that the chosen cluster complex and surface system need to be matched with care. This particular cluster is a model for adsorption of benzene on metal surfaces with electropositive promoters, such as potassium, or on earlier transition metals which have a higher-lying Fermi level. For coadsorption of benzene and CO on the Rh(111) surface the $Os_3(CO)_9(\mu_3,\eta^2,\eta^2,\eta^2-C_6H_6)$ cluster models the benzene chemisorption on 3-fold hexagonal close packed sites, parallel to the surface, and reproduces the Kekule ring distortions and the metal-carbon distances [26].

The conversion of the complex $Os_3(CO)_9(\mu_3,\eta^2,\eta^2,\eta^2-C_6H_6)$ to the dimetalated benzyne complex $(\mu-H)_2Os_3(CO)_9(\mu_3,\eta^1,\eta^2,\eta^2-C_6H_4)$ by broad band visible irradiation offers a model of the interconversion of associatively and dissociatively chemisorbed states of benzyne via C-H activation [199]. C-H bond scission is an important decomposition pathway for chemisorbed states of benzene, and on atomically flat surfaces is particularly facile for earlier transition metals, for example W(100) [192].

To model similar reactions on stepped metal surfaces such as the (111) face, multinuclear complexes are required, as demonstrated by Knox et al [116]. These authors modelled C-H activation at step sites using the cluster $Ru_5(CO)_{13}(\mu_4PPh)(\mu_5,\eta^5C_6H_4)$, where three of the metal atoms are arranged as in one terrace and the other two represent the step atoms in the first row of the next terrace.

In conclusion, organometallic cluster complexes can be characterized successfully by IR spectroscopy and are good models for surface reactions, providing the model and system are carefully matched in terms of bonding geometries. For more complex adsorbate-surface bonding such as that occurring on a metal stepped surface, a larger, multinuclear cluster may be required to adequately represent the geometry.

REFERENCES

[1] a) C.A.L. Mahaffry and P.L. Pauson, *Inorg. Synth.*, 28, 136, 1990; B. Nicholls and M.C. Whiting, *J. Chem. Soc.*, 551, 1959
b) T.G. Traylor, K.J. Stewart and M.J. Goldberg, *J. Am. Chem. Soc.*, 106, 4445, 1984
[2] D.D. Perrin and W.L.F. Armarego, *Purification of Laboratory Chemicals*, Pergamon, Oxford, 3rd edn., 1988
[3] K. Nakamoto, *Infra Red and Raman Spectra of Inorganic and Coordination Compounds*, Wiley Interscience, New York, 4th edn.,1986
[4] D.M. Adams, R.E. Christopher and D.C. Stevens, *Inorg. Chem.*, 14, 1562, 1975
[5] E.M. Bisby, G. Davidson and D.A. Duce, *J. Mol. Structure*, 48, 93, 1978
[6] D.A. Lesch, J.W. Richardson, R.A. Jacobson and R.J. Angelici, *J. Am. Chem. Soc.*, 106, 2901, 1984
[7] W.C. Trogler, *J. Am. Chem. Soc.*, 101, 6459, 1979
[8] a) L-N. Ji, D.L. Kershner, M.E. Rerek and F. Basolo, *J. Organomet. Chem.*, 296, 83, 1985
b) N.I. Pyshnogrueva, A.S. Batsonov, Yu.T. Struchtov, A.G. Ginsberg and V.N. Setkina, *J. Organomet. Chem.*, 297, 69, 1985
c) D.L. Kershner and F. Basolo, *J. Am. Chem. Soc.*, 109, 7396, 1987
[9] K.K. Joshi and P.L.Pauson, *Proc. Chem. Soc.*, 326, 1962
[10] L.J. Bellamy, *The Infra Red Spectra of Complex Molecules*, Chapman and Hall, London, 3rd edn., 1986
[11] N.B. Colthup, L.H. Daly and S.E. Wiberley, *Introduction to Infra Red and Raman Spectroscopy*, Academic Press, London, 1990
[12] A.R. Katrizky, *Physical Methods in Heterocyclic Chemistry*, Academic Press, New York, 1963, vol. II
[13] A.R. Katrizky and C.W. Rees, *Comprehensive Heterocyclic Chemistry*, Pergamon Press, Oxford, 1984, vol. 4
[14] C. Choo Yin and A.J. Deeming, *J. Chem. Soc. Dalton Trans.*, 2563, 1982
[15] M.W. Day, K.I. Hardcastle, A.J. Deeming, A.J. Arce and Y. De Sanctis, *Organomet.*, 9, 6, 1990
[16] M.W. Day, K.I. Hardcastle, A.J. Deeming, A.J. Arce and Y. De Sanctis, *Organomet.*, 8, 1408, 1989
[17] A.J. Arce, J. Manzus, M. Marquez, Y. De Sanctis and A.J. Deeming, *J. Organomet. Chem.*, 412, 177, 1991
[18] D. Himmelreich and G Muller, *J. Organomet. Chem.*, 297, 341, 1985
[19] A.J. Arce, Y. De Sanctis and A.J. Deeming, *J. Organomet. Chem.*, 311, 371, 1986
[20] A.J. Arce, A.J. Deeming, Y. De Sanctis, R. Machado, J. Manzur and C. Rivas, *J. Chem. Soc. Chem. Commun.*, 1568, 1990
[21] C. Choo Yin and A.J. Deeming, *J. Chem. Soc. Dalton Trans.*, 1013, 1974
[22] K.A. Azam, A.J. Deeming, I.P. Rothwell, M.B. Hursthouse and J.D.J. Backer-Dirks, *J. Chem. Soc. Dalton*

Trans., 2039, 1981

[23] J.C. Evans, *Spectrochim. Acta.*, 16, 428, 1960

[24] K.A. Azam, A.J.Deeming, R.E.Kimber and P.R. Shukia, *J. Chem. Soc. Dalton Trans.*, 1853, 1976

[25] J.C. Evans, *Spectrochim. Acta*, 16, 1382, 1960

[26] M.A. Gallop, M.P. Gomez-Sal, C.E. Housecroft, B.F.G. Johnson, J.Lewis, S.M. Owen, P.R. Raithby and A.H. Wright, *J. Am. Chem. Soc.*, 114, 2502, 1992

[27] B.F.G.Johnson, *Colloquium*, University of Durham, 1991

[28] E.B. Wilson, J.C. Decius and P.C. Cross, *Molecular Vibrations*, McGraw-Hill, New York, 1955

[29] P.C. Painter and J.L. Koenig, *Spectrochim. Acta*, 33A, 1003, 1977

[30] R.D. Mair and D.F. Hornig, *J. Chem. Phys.*, 17, 1236, 1949

[31] B.F.G. Johnson, J. Lewis, P.R. Raithby and M.J. Rosales, *J. Chem. Soc. Dalton Trans.*, 2257, 1983

[32] A.J. Deeming and M. Underhill, *J. Chem. Soc. Dalton Trans.*, 1415, 1974

[33] C.R. Eady, B.F.G. Johnson and J.Lewis, *J. Organomet. Chem.*, 37, C39, 1972

[34] C.E. Anson and U.A. Jayasooria, *Spectrochim. Acta*, 46A, 967, 1990

[35] H.H. Willard, L.L. Merritt, J.A. Dean and F.A.Settle *Instrumental Methods of Analysis*, Wadsworth, California, 7th edn., 1988

[36] B. Schrader, *Molecular Spectroscopy*, Specialist Periodical Reports, The Chemical Society, London, 1978, vol. 5

[37] P.M.A. Sherwood, *Vibrational Spectroscopy of Solids*, Cambridge University Press, Cambridge, 1972

[38] E.A.V. Ebsworth, D.W.H. Rankin and S. Cradock, *Structural Methods in Inorganic Chemistry*, Blackwell, Oxford, 1987.

[39] G. Davidson, *Group Theory For Chemists*, Macmillan, London, 1991

[40] R.S. Halford, *J. Chem. Phys.*, 14, 8, 1946; W.G. Fateley, F.R. Dollish, N.T. McDevitt and F.F. Bentley, *Infrared and Raman Selection Rules For Molecular and Lattice Vibrations*, Wiley Science, New York, 1972

[41] M.R. Churchill, F.J. Hollander and J.P. Hutchinson, *Inorg. Chem.*, 16, 2655, 1977

[42] M.R. Churchill and B.G. De Boer, *Inorg. Chem.*, 16, 878, 1977

[43] D.K. Huggins, N. Flitcroft and H.D. Kaesz, *Inorg. Chem.*, 4, 166, 1965

[44] D. Reidel, *International Tables for Crystallography Vol. A*, Dordrecht, Holland, 1983

[45] C.E. Anson and U.A. Jayasooriya, *Spectrochim. Acta*, 46A, 861, 1990

[46] N. Sheppard, *Ann. Rev. Phys. Chem.*, 39, 589, 1988

[47] D.A. Adams and I.D. Taylor, *J. Chem. Soc. Faraday Trans. 2*, 78, 1561, 1982

[48] T.R. Gilson, *J. Chem. Soc. Dalton Trans.*, 149, 1984

[49]   C.O.   Quicksall and T.G.   Spiro, *Inorg.   Chem.*,   11,
2365, 1966
[50]   S.F.A. Kettle and P.L. Stanghellini, *Inorg. Chem.*, 18,
2749, 1979
[51]   S.   Kishner,   P.J.   Fitzpatrick, K.R. Plowman and I.S.
Butler, *J. Mol. Struct.*, 74, 29, 1981
[52]   A.   Yamamoto, *Organotransition Metal Chemistry*, Wiley-
Interscience, New York, 1986
[53]   F.P. Netzer, E. Bertel and A. Goldman, *Surf. Sci.*,
199, 87, 1988
[54]   B.A. Sexton, *Surf. Sci.*, 163, 99, 1985
[55]   G. Tourillon, S. Raaen, T.A. Skotheum, M. Sagurton, R.
Garrett and G.P. Williams, *Surf. Sci.*, 184, L345, 1987
[56]   Ch.   Elschenbroich and   A.   Salzer,   *Organometallics*,
V.C.H., Weinheim, Germany, 1989
[57]   D.H.   Williams and I.   Fleming, *Spectroscopic Methods
in Organic Chemistry*, McGraw-Hill, London, 3rd edn., 1980
[58]   W.W. Crew and R.J. Madix, *J. Am. Chem. Soc.*, 115, 729,
1993
[59] J.L.Solomon, R.J.   Madix and J. Stohr, *J. Chem. Phys.*,
94, 4012, 1991
[60]   G.R.   Schoofs and J.B. Benziger, *Surf. Sci.*, 192, 373,
1987
[61]   B.   Chaudret and   F.A.   Jalon,   *J.   Chem.   Soc.   Chem.
Commun.*, 711, 1988
[62]   W.H.   Heise and B.J.   Tatarchuk, *Surf. Sci.*, 207, 297,
1989
[63]   J.P.   Fulmer, F. Zaera and W.T. Tysoe, *J. Phys. Chem.*,
92, 4147, 1988
[64]   J.T.   Roberts,and C.M.   Friend, *Surf. Sci.*, 186, 201,
1987
[65]   J.F. Lang and R.I. Masel, *Surf. Sci.*, 183, 44, 1987
[66]   F.Zaera, E.B. Kollin and J.L. Gland, *Surf. Sci.*, 184,
75, 1987
[67]   F.P.   Netzer,   E.   Bertel and A.   Goldman, *Surf. Sci.*,
201, 257, 1988
[68]   M-G.   Choi and R.J.   Angelici,   *Organomet.*,   10, 2436,
1991
[69]   G.N.   Glavee,   L.M.   Daniels   and   R.J.   Angelici,
Organomet, 8, 1856, 1989
[70]   M.G. Ramsey, G. Rosina, D. Steinmuller, H.H. Graen and
F.P. Netzer, *Surf. Sci.*, 232, 266, 1990
[71]   J.L.   Solomon,   R.J.   Madix and J.   Stohr, *Surf. Sci.*,
255, 12, 1991
[72]   X.Xu and C.M.   Friend,   *J. Vac. Sci. Tech. A*, 9, 1599,
1991
[73]   G.R.   Schoofs and J.B.   Benziger,   *J. Phys. Chem.*, 92,
741, 1988
[74]   J.G.   Serafin and C.M.   Friend, *Surf. Sci.*, 209, L163,
1989
[75]   A.C.   Liu,   C.M. Friend and J. Stohr, *Surf. Sci.*, 236,
L349, 1990
[76]   D.   Steinmuller,   M.G.   Ramsey,   F.P.   Netzer and   M.
Neuber, *Surf. Sci.*, 271, 567, 1992

[77] H. Bu, P. Bertrand and J.W. Rabelais, *J. Chem. Phys.*, 98, 5855, 1993

[78] T. Ohta, T. Fujikawa and J. Kuroda, *Bull. Chem. Soc. Jpn.*, 48, 2017, 1975

[79] C.M. Lukehart, *Fundamental Transition Metal Organometallic Chemistry*, Brooks/Cole, California, 1985

[80] K. Burgess, *Polyhedron*, 3, 1175, 1984

[81] H. Wadepohl, *Angew. Chem. Int. Edn. Engl.*, 31, 247, 1992

[82] M.P. Gomez-Sal, B.F.G. Johnson, J. Lewis, P.R. Raithby and A.H. Wright, *J. Chem. Soc. Chem. Commun.*, 1682, 1985

[83] D. Braga, F. Grepioni, B.F.G. Johnson, J. Lewis, M. Martinelli and M. A. Gallop, *J. Chem. Soc. Chem. Commun.*, 53, 1990

[84] M. A. Gallop, B.F.G. Johnson, J. Lewis, A. McCamley and R.N. Perutz, *J. Chem. Soc. Chem. Commun.*, 1071, 1988

[85] B.F.G. Johnson, J. Lewis, C.E. Housecroft, M.A. Gallop, M. Martinelli, D. Braga and F. Grepioni, *J. Mol. Catal.*, 74, 61, 1992

[86] Z. Jing and J.L. Whitten, *Surf. Sci.*, 250, 147, 1991

[87] M.G. Ramsey, D. Steinmuller, F.P. Netzer, T. Schedel, A. Santaniello and D.R. Lloyd, *Surf. Sci.*, 250/251, 979, 1991

[88] W. Huber, M. Weinelt, P. Zebisch and H.P. Steinruck, *Surf. Sci.*, 253, 72, 1991

[89] W. Huber, P. Zebisch, T. Bornemann and H.P. Steinruck, *Surf. Sci.*, 258, 16, 1991

[90] H. Hoffmann, F. Zaera, R.M. Ormerod, R.M. Lambert, L.P.Wong and W.T. Tysoe, *Surf. Sci.*, 232, 259, 1990

[91] A.C. Liu, J. Stohr, C.M. Friend and R.J.Madix, *Surf. Sci.*, 235, 107, 1990

[92] X.L. Zhou, M.E. Castro and J.M. White, *Surf. Sci.*, 238, 215, 1990

[93] H.P. Steinbruck, W. Huber, T. Pache and D. Menzel, *Surf. Sci.*, 218, 293, 1989

[94] M. Neuman, J.U. Mack, E. Bertel and F.P. Netzer, *Surf. Sci.*, 155, 629, 1985

[95] M. Abon, J.C. Bertolini, J. Billy, J. Massardier and B. Tardy, *Surf. Sci.*, 162, 395, 1985

[96] P. Jakob and D. Menzel, *Surf. Sci.*, 201, 503, 1988

[97] J.F.M. Aarts and N.R.M. Sassen, *Surf. Sci.*, 214, 257, 1989

[98] F.P. Netzer, G. Rangelov, G. Rosina, H.B. Saalfeld, M. Newmann and D.R. Lloyd, *Phys. Rev. B*, 37, 10399, 1988

[99] H.H. Graen, M. Neuber, J. Nawbach and H.J. Freund, *Chem. Phys. Lett.*, 165, 137, 1990

[100] H.H. Graen, M. Neuber, M. Neumann, G. Illing and H.J. Freund, *Surf. Sci.*, 223, 33, 1989

[101] A.C. Liu and C.M. Friend, *J. Chem. Phys.*, 89, 4396, 1988

[102] J.U. Mack, E. Bertel and F.P. Netzer, *Surf. Sci.*, 159, 265, 1985

[103] F.P. Netzer, G. Rosina, E. Bertel and H. Saalfeld, *Surf. Sci.*, 184, L397, 1987

[104] R. Dudde, R-H. Frank and E.E. Koch, *Surf. Sci.*, 225, 267, 1990

[105] N.V. Richardson and N.R. Palmer, *Surf. Sci.*, 114, Ll, 1982

[106] R.F. Lin, R.J. Koestner, M. A. van Hove and G.A. Somorjai, *Surf. Sci.*, 134, 161, 1983

[107] X. Gao, J.P. Davies and M.J. Weaver, *J. Phys. Chem.*, 94, 6858, 1990

[108] J.S. Somers, M.E. Bridge and D.R. Lloyd, *Spectrochim. Acta*, 43A, 1549, 1987

[109] A.K. Myers, G.R. Schoofs and J.B. Benziger, *J. Phys. Chem.*, 91, 2230, 1987

[110] A. Wander, G. Held, R.Q. Hwang, G.S. Blackman, M.L. Xu, P. de Andres, M.A. van Hove and G.A. Somorjai, *Surf. Sci.*, 249, 21, 1991

[111] C.M. Mate and G.A. Somorjai, *Surf. Sci.*, 160, 542, 1985

[112] D.F. Ogletree, M.A. van Hove and G. A. Somorjai, *Surf. Sci.*, 183, 1, 1987

[113] M. Fujisawa, T. Sekitani, Y. Morikawa and M. Nishijima, *J. Phys. Chem.*, 95, 7415, 1991

[114] N.G. Dongre, B.P. Asthana and P.C. Mishra, *Spectrochim. Acta*, 47A, 673, 1991

[115] R. D. Mair and D.F. Hornig, *J. Chem. Phys.*, 17, 1236, 1949

[116] S.A.R. Knox, B.R. Lloyd, A.G.Orpen, J.M. Vinas and M. Weber, *J. Chem. Soc. Chem. Commun.*, 1498, 1987

[117] M.A. Gallop, B.F.G. Johnson, J. Lewis and P.R. Raithby, *J. Chem. Soc. Chem. Commun.*, 1809, 1987

[118] K. Chhor and G. Lucazeau, *J. Raman Spectrosc.*, 13, 235, 1982

[119] E.L. Muetterties, T.N. Rhodin, E. Band, C.F. Bruckes and W.R. Pretzer, *Chem. Rev.*, 79, 91, 1979 and refs. therein.

[120] P. Skinner, M.R. Howard, I.A. Hoxton, S.F.A. Kettle, D.B. Powell and N. Sheppard, a) *J. Chem. Soc. Faraday Trans.*, 77, 1203, 1981; b) *J. Chem. Soc. Faraday Trans.*, 77, 397, 1981

[121] L.L. Kesmodel, L.H. Dubois and G.A. Somorjai, *J. Chem. Phys.*, 70, 2180, 1979

[122] M. Rashidi and R.J. Puddephat, *Organomet.*, 7, 1636, 1988

[123] B.A. Sexton and R.J. Madix, *Surf. Sci.*, 105, 177, 1981

[124] B. A. Sexton, *Surf. Sci.*, 88, 299, 1979

[125] N. Sheppard and T.T. Nguyen, in *Advances in Infrared and Raman Spectroscopy*, eds. R.J. Clark and R.E. Hester, Heyden, London, 1978, vol.5, p. 67

[126] E.L. Muetterties, *Angew. Chem. Int. Edn. Engl.*, 17, 845, 1978

[127] N.D.S. Canning and R.J. Madix, *J. Phys. Chem.*, 88,2437, 1984

[128] V. H. Grassian and E.L. Muetterties, *J. Phys. Chem.*, 90, 5900, 1986

[129] G. Bell, *Report*, University of Durham, 1989

[130] M. Barker and R.J. Madix, *Surf. Sci.*, 116, 549, 1982

[131] R.J. Madix, S.B. Lee and M. Thornbery, *J. Vac. Sci. Tech. A*, 1, 1254, 1983

[132] B.A. Sexton, *Surf. Sci.*, 102, 271, 1981

[133] J. B. Benziger and R.J. Madix, *J. Catal.*, 65, 36, 1980

[134] E.I. Ko and R.J. Madix, *Surf. Sci.*, 112, 373, 1981

[135] M Tachikawa and R.J. Shapley, *J. Organomet. Chem.*, 124, C19, 1977

[136] K.A. Azam, C.C. Yiri and A.J. Deeming, *J.Chem. Soc. Dalton Trans.*, 1201, 1978

[137] R.J. Madix, *Adv. Catal.*, 29, 1, 1980

[138] J.R. Shapley, G.M. St. George, M.R. Churchill and F.J. Hollander, *Inorg. Chem.*, 21, 3295, 1982

[139] B.A. Sexton, *Surf. Sci.*, 88, 319, 1979

[140] J.E. Demuth, P.N. Sanda, J. M. Waulamont, J.C. Tsang and K. Christmann, in *Vibrations at Surfaces*, eds. R. Caudana, J-M, Giles and A.A. Lucas, Plenum, New York, 1982, p. 391

[141] R.M. Wexler, M-C. Tsai, C.M. Friend and E.L. Muetterties, *J. Am. Chem. Soc.*, 104, 2034, 1982

[142] J. Durig, B.R. Mitchell, D.W. Sink and J.N. Willis, *Spectrochim. Acta*, 23A, 1121, 1976

[143] A.L. Johnson, E.L. Muetterties, J. Stohr and F. Sette, *J. Phys. Chem.*, 89, 4071, 1985

[144] K.A. Azam and A.J. Deeming and I.P.Rothwell, *J. Organomet. Chem.*, 178, C20, 1979

[145] A.J. Deeming, *Adv. Organomet. Chem.*, 26, 1, 1986

[146] K.H. Pannell, B.L. Kalsotra and C. Parkanyi, *J. Heterocycl. Chem.*,15, 1057, 1978

[147] G. Huttner and O.S. Mills, *Chem. Ber.*, 105, 301, 1972

[148] K. Azam and A.J. Deeming, *J. Mol. Catal.*, 3, 207, 1977; K. Azam, A.J. Deeming and I.P. Rothwell, *J. Chem. Soc. Dalton Trans.*, 91, 1981

[149] K.K. Joshi, P.L. Pausen, A.R. Quazi and W.H. Stubbs, *J. Organomet. Chem.*, 1, 471, 1964

[150] F. Seel and V. Sperber, *J. Organo met. Chem.*, 14, 405, 1968

[151] K. Ofele and E. Dotzauer, *J. Organomet. Chem.*, 30, 211, 1971

[152] N. Kuhn, E-M. Horn, E. Zauder, D. Blazer and R. Boese, *Angew. Chem. Int. Ed. Engl.*, 27, 579, 1988

[153] P. Pfluger and G.B. Street, *J. Chem. Phys.*, 80, 544, 1984

[154] K. Jacobi, M. Sheffler, K. Kambe and F. Forstmann, *Solid State Commun.*, 22, 17, 1977

[155] M. Connolly, J. Somers, M.E. Bridge and D.R. Lloyd, *Surf. Sci.*, 185, 559, 1987

[156] H. Ibach and D.L. Mills, *Electron Energy Loss Spectroscopy and Surface Vibrations*, Academic Press, New York, 1982

[157] M.R. Churchill and J.R. Missert, *J. Organomet. Chem.*, 256, 349, 1983

[158] A.J. Deeming, S. Hasso and M. Underhill, *J. Chem. Soc. Dalton Trans.*, 1614, 1975

[159] E. Sappa, A. Tiripicchio and A.M. Manotti Lanfredi, *J. Organomet. Chem.*, 249, 391, 1988

[160] A.J. Orpen, D. Pippard, G.M. Sheldrick and K.D. Rouse, *Acta Crystallogr. B*, 34, 2466, 1978

[161] A.J. Deeming, S. Hasso and M. Underhill, *J. Organomet. Chem.*, 80, C33, 1974

[162] A.D. Clauss, M. Tachikawa, J.R. Shapley and C.G. Pierpont, *Inorg. Chem.*, 20, 1528, 1981

[163] J.J. Guy, B.E. Reichert and G.M. Sheldrick, *Acta Crystallogr. B*, 32, 3319, 1976

[164] M. Rico, M. Barrachina and J.M. Orza, *J. Mol. Spectrosc.*, 24, 133 1967

[165] M-G. Choi and R.J. Angelici, *J. Am. Chem. Soc.*, 111, 8753, 1989 and refs. therein

[166] H.D. Kaesz, R.B. King, T.A. Manuel, L.D. Nichols and F.G.A. Stone, *J. Am. Chem, Soc.*, 82, 4749, 1960

[167] A.E. Ogilvy and M. Draganjac, T.B. Rauchfuss and S.R. Wilson, *Organomet.*, 7, 1171, 1988

[168] A. Mayr, Y.C. Lin, N.M. Boag and H.D. Kaesz, *Inorg. Chem.*, 21, 1704, 1982

[169] B.F.G. Johnson, J.Lewis, T.I. Odiaka and P.R. Raithby, *J. Organomet. Chem.*, 216, C56, 1981

[170] A.J. Arce, Y. De Sanctis and A.J. Deeming, *J. Organomet. Chem.*, 295, 365, 1985

[171] C.G. Kuehn and H. Taube, *J. Am. Chem. Soc.*, 98, 689, 1976

[172] G.H.Spies and R.J. Angelici, *J. Am. Chem. Soc.*, 107, 5569, 1985

[173] N.J. Di Nardo, Ph. Avouris and J.E. Demuth, *J. Chem. Phys.*, 81, 2169, 1984

[174] Ph. Avouris and J.E. Demuth, *J. Chem. Phys.*, 75, 5953, 1981

[175] A. L. Johnson, E.L. Muetterties, J. Stohr and F. Sette, *J. Phys. Chem.*, 89, 4071, 1985

[176] M. Bader, J. Haase, K.H. Frank, A. Puschmann and A. Otto, *Phys. Rev. Lett.*, 56, 1921, 1986

[177] J, Stohr, J.L. Gland, E.B. Kollin, R,J, Koestner, A.L. Johnson, E.L. Muetterties and F. Sette, *Phys. Rev. Lett.*, 53, 2161, 1984

[178] N.V. Richardson and J.C. Campuzano, *Vacuum*, 31, 449, 1981

[179] A.J. Deeming and M. Underhill, *J. Organomet. Chem.*, 42, C60, 1972

[180] A.J. Deeming and M. Underhill, *J. Chem. Soc. Chem. Commun.*, 277, 1973

[181] J.L. Gland and G.A. Somorjai, *Surf. Sci.*, 41, 387, 1974

[182] K. Kishi, K. Chinomi, Y. Inou and S. Ikeda, *J. Catal.*, 60, 228, 1979

[183] K.A. Azam, A. J. Deeming, I.P. Rothwell, M.B. Hursthouse and L. New, *J. Chem. Soc. Chem. Commun.*, 1086, 1978

297

[184] C.W. Bradford, R.S. Nyholm, G.J. Gainsford, J.M. Guss, P.R. Ireland and R. Mason, *J. Chem. Soc. Chem. Commun.*, 87,1972

[185] E. Furimsky, *Catal. Rev. Sci. Eng.*, 25, 421, 1983

[186] J. Robins, in *Structural Adhesives, Chemistry and Technology*, Plenum, New York, 1986

[187] K.W. Chiu, R.A. Jones, G. Wilkinson, A.M.R. Galas, M.B. Hursthouse and K.M.A. Malik, *J. Chem. Soc. Dalton Trans.*, 1204, 1981

[188] F. Lu, G.N. Salaita, L. Laguren-Davidson, D.A. Stern, E. Wellner, D.G. Frank, N. Batina, D.C. Zapien, N.Walton and A.T. Hubbard, *Langmuir*, 4, 637, 1988

[189] J.R. Sweet and W.A.G. Graham, *Organomet.*, 2, 135, 1983

[190] W.D. Jones and F.J. Feher, *J. Am. Chem. Soc.*, 106, 1650, 1984

[191] H. Wadepohl and L. Zhu, *J. Organomet. Chem.*, 376, 115, 1989

[192] A.K. Bhattacharya, *J. Chem. Soc. Faraday Trans. 1*, 76, 126, 1980

[193] S. Tartarenko and R. Ducros, *J. Chem. Physique*, 79, 409, 1982

[194] M. Bader,J. Haase, K-H. Frank, C. Oral and A. Puschmann, *J. Phys. (Paris)*, 47, C8-491, 1986

[195] S. Somers, M.E. Bridge, D.R. Lloyd and T. McCabe, *Surf. Sci.*, 181, L167, 1987

[196] F.P. Netzer, H.H. Graes, H. Kuhlenbeck and M. Neumann, *Chem. Phys. Lett.*, 133, 49, 1987

[197] E.L. Garfunkel, C. Minot, A. Gavezzotti and M. Simonetta, *Surf. Sci.*, 167, 1986; A.B. Anderson, M.R. McDevitt and F.L. Urbach, *Surf. Sci.*, 146, 80, 1984

[198] E.L. Garfunkel, J.J. May, J.C. Frost, M.H. Farias and G.A. Somorjai, *J. Phys. Chem.*, 87, 3629, 1983

[199] E.L. Muetterties, *Pure Appl. Chem.*, 54, 83, 1982

[200] C.M. Friend and E.L. Muetterties, *J. Am. Chem. Soc.*, 103, 773, 1981

APPENDIX

ʢ

ʢ

<u>Appendix</u>

The Board of Studies in Chemistry requires that each postgraduate research thesis contains an appendix listing:-
(1) all research colloquia, seminars and lectures arranged by the Department of Chemistry during the period of the author's residence as a postgraduate student;
(2) lectures organised by Durham University Chemical Society;
(3) all research conferences attended and papers presented by the author during the period when research for the thesis was carried out;
(4) details of the postgraduate induction course.

COLLOQUIA, LECTURES AND SEMINARS GIVEN BY INVITED SPEAKERS.

OCTOBER 1988 - SEPTEMBER 1992

(Those attended are marked *)

18.10.88	Dr. J. Dingwall (Ciba Geigy) Phosphorous Containing Amino Acids: Biologically Active Natural and Unnatural Products
24.11.88	Drs. R.R. Baldwin and R.W. Walker (University of Hull) Combustion: Some Burning Problems
12.11.88	Dr. G. Hardgrove (St. Olaf College, USA) Polymers in the Physical Chemistry Laboratory
25.1.89	Dr. L. Harwood (University of Oxford) Synthetic Approaches to Phorbols Via Intramolecular Furan Diels-Alder Reactions: Chemistry Under Pressure
2.2.89	Prof. L.D. Hall (Addenbrooke's Hospital, Cambridge) NMR - A Window to the Human Body
9.2.89	Prof. J.E. Baldwin (University of Oxford) Recent Advances in the Bioorganic Chemistry of Penicillin Biosynthesis

15.2.89   Dr. A.R. Butler (University of St. Andrews)
             Cancer in Linxiam: The Chemical Dimension

16.2.89   Prof. B.J. Aylett (Queen Mary College, London)
             Silicon Based Chips: The Chemist's Contribution

1.3.89   Dr. R.J. Errington (University of Newcastle)
             Polymetalate Assembly in Organic Solvents

15.3.89   Dr. R. Aveyard (University of Hull)
*   Surfactants at your Surface

20.4.89   Dr. M. Casey (University of Salford)
             Sulphoxides in Stereoselective Synthesis

27.4.89   Dr. D. Crich (University College, London)
             Some Novel Uses of Free Radicals in Organic Synthesis

11.5.89   Dr. J. Frey (University of Southampton)
             Spectroscopy of the Reaction Path: Photodissociation Raman
             Spectra of NOCl

10.11.89   Prof. J.I.G. Cadogan (B.P. Research Centre)
*   From Pure Science to Profit

17.10.89   Dr. F. Palmer (University of Nottingham)
*   Thunder and Lightning

25.10.89   Prof. C. Floriani (Lausanne University)
             Molecular Aggregates - A Bridge Between Homogeneous and
             Heterogeneous Systems

1.11.89   Dr. J.P.S. Badyal (University of Durham)
*   Breakthroughs in Heterogeneous Catalysis

9.11.89   Prof. N.N. Greenwood (University of Leeds)
*   Novel Cluster Geometries in Metalloborane Chemistry

10.11.89   Prof. J.E. Bercaw (California Institute of Technology)
*   Polymerisation of Olefins.

13.11.89   Dr. J. Becher (Odense University)
            Synthesis of New Macrocyclic Systems using Heterocyclic
            Building Blocks

16.11.89   Dr. D. Parker (University of Durham)
            Macrocycles, Drugs and Rock 'n' Roll

29.11.89   Prof. D.J. Cole-Hamilton (University of St. Andrews)
*   New Polymers from Homogeneous Catalysis

30.11.89   Dr. M.N. Hughes (King's College, London)
*   A Bug's Eye View of the Periodic Table

4.12.89   Dr. D. Graham (B.P. Research Centre)
            How Proteins Absorb on Interfaces

6.12.89   Dr. R.L. Powell (ICI)
*   The Development of CFC Replacements

7.12.89   Dr. A. Butler (University of St. Andrews)
            The Discovery of Penicillin: Facts and Fancies

13.12.89   Dr. J. Klinowski (University of Cambridge)
*   Solid State NMR Studies of Zeolite Cages

15.12.89   Prof. R. Huisgen (Universitat Munchen)
            Recent Mechanistic Studies of [2+2] Additions

24.1.90   Dr. R.N. Perutz (University of York)
*   Plotting the Course of C-H Activations with Organometallics

31.1.90   Dr. U. Dyer (Glaxo)
            Synthesis and Conformation of C-Glycosides

1.2.90   Prof. J.H. Holloway (University of Leicester)
            Noble Gas Chemistry

7.2.90   Dr. D.P. Thompson (University of Newcastle)
The role of Nitrogen in Extending Silicate Crystal Chemistry

8.2.90   Rev. R. Lancaster (Kimbolton Fireworks)
*   Fireworks - Principles and Practice

12.2.90   Prof. L. Lunazzi (University of Bologna)
Application of Dynamic NMR to the Study of Conformational
Isomerism

14.2.90   Prof. D. Sutton (Simon Fraser University, Vancouver B.C.)
Synthesis and Applications of Dinitrogen and Diazo
Compounds of Rhenium and Iridium

15.2.90   Prof. L. Crombie (University of Nottingham)
*   The Chemistry of Cannabis and Khat

21.2.90   Dr. C. Bleasdale (University of Newcastle)
The Mode of Action of some Anti-tumour Agents

22.2.90   Prof. D.T. Clark (ICI Wilton)
*   Spatially Resolved Chemistry using Nature's Paradigm in the
Advanced Materials Area

28.2.90   Dr. R.K. Thomas (University of Oxford)
*   Neutron Reflectometry from Surfaces

1.3.90   Dr. J.F. Stoddart (University of Sheffield)
*   Molecular Lego

8.3.90   Dr. A.K. Cheetham (University of Oxford)
*   Chemistry of Zeolite Cages

21.3.90   Dr. I. Powis (University of Nottingham)
Spinning off in a huff: Photodissociation of Methyl Iodide

23.3.90   Prof. J.M. Bowman (Emory University)
Fitting Experiment with Theory in Ar-OH

9.7.90	Prof. L.S. German (USSR Academy of Sciences - Moscow) New Syntheses in Fluoroaliphatic Chemistry: Recent Advances in the Chemistry of Fluorinated Oxiranes
9.7.90	Prof. V.E. Platonov (USSR Academy of Sciences - Novosibirsk) Polyfluoroindanes: Synthesis and Transformation
9.7.90	Prof. I.N. Rozhkov (USSR Academy of Sciences - Moscow) Reactivity of Perfluoroalkyl Bromides
11.10.90	Dr. W.A. MacDonald (ICI Wilton) Materials for the Space Age
24.10.90 *	Dr. M. Bochmann (University of East Anglia) Synthesis, Reactions and Catalytic Activity of Cationic Titanium Alkyls
26.10.90 *	Prof. R. Soulen (South Western University, Texas) Chemistry of some Fluorinated Cyclobutenes
31.10.90	Dr. R. Jackson (University of Newcastle) New Synthetic Methods: a-aminoacids and Small Rings
1.11.90	Dr. N. Logan (University of Nottingham) Rocket Propellants
6.11.90 *	Dr. P. Kocovsky (Uppsala University) Stereo-controlled Reactions Mediated by Transition and Non-Transition Metals
7.11.90 *	Dr. D. Gerrard (B.P. Research Centre) Raman Spectroscopy for Industrial Analysis
7.11.90	Dr. W. Dolbier (Gainsville, Florida) Rearrangements of bis CF_3 Vinyl Aromatics: a Route to 1,3,5-Hexatrienes
8.11.91	Dr. S.K. Scott (University of Leeds) Clocks, Oscillations and Chaos

14.11.90 *	Prof. T. Bell (SUNY, Stony Brook) Functional Molecular Architicture and Molecular Recognition
21.11.90 *	Prof. J. Pritchard (Queen Mary and Westfield College, London) Copper Surfaces and Catalysts
28.11.90 *	Dr. B.J. Whitaker (University of Leeds) Two-dimensional Velocity Imaging of State-selected Reaction Products
29.11.90	Prof. D. Crout (University of Warwick) Enzymes in Organic Synthesis
5.12.90 *	Dr. P.G. Pringle (University of Bristol) Metal Complexes with Functionalised Phosphines
13.12.90	Prof. A.H. Cowley (University of Texas) New Organometallic Routes to Electronic Materials
15.1.91	Dr. B.J. Alder (Lawrence Livermore Labs., California) Hydrogen in all its Glory
17.1.91 *	Dr. P. Sarre (University of Nottingham) Comet Chemistry
23.1.91	Prof. J.S. Higgins (Imperial College, London) Rheology and Molecular Structure of Ionomer Solutions
24.1.91	Dr. P.J. Sadler (Birkbeck College, London) Design of Inorganic Drugs: Precious Metals, Hypertension and HIV
30.1.91	Prof. E. Sinn (University of Hull) New Results in High T_C Superconductivity
31.1.91	Dr. D. Lacey (University of Hull) Liquid Crystals

6.2.91   Dr. R. Bushby (University of Leeds)
                Biradicals and Organic Magnets

14.2.91   Dr. M.C. Petty (University of Durham)
                Molecular Electronics

20.2.91   Prof. B.L. Shaw (University of Leeds)
*   New Chemistry with Transition Metal Multihydrides

28.2.91   Dr. J. Brown (University of Oxford)
                Can Chemistry Provide Catalysts Superior to Enzymes?

6.3.91   Dr. C.M. Dobson (University of Oxford)
*   NMR Studies of Dynamics in Molecular Crystals

7.3.91   Dr. J. Markam (ICI Pharmaceuticals)
                DNA Fingerprinting

24.4.91   Prof. R.R. Schrock (MIT)
*   Metal-ligand Multiple Bonds and Metathesis Initiators

25.4.91   Prof. T. Hudlicky (Virginia Polytechnic Institute)
                Biocatalysis and Symmetry Based Approaches to the Efficient
                Synthesis of Complex Natural Products

20.6.91   Prof. M.S. Brookhart (University of North Carolina)
                Olefin Polymerisations, Oligomerisations and Dimerisations
                Using Electrophilic Late Transition Metal Catalysts

29.7.91   Dr. M.A. Brimble (Massey University, New Zealand)
                Synthetic Studies Towards the Antibiotic Griseusin-A

17.10.91   Dr. J.A. Salthouse (University of Manchester)
                Son et Lumiere - a demonstration lecture

6.11.91   Prof. B.F.G. Johnson (University of Edinburgh)
*   Cluster-Surface Analogies

7.11.91   Dr. A.R. Butler (University of St. Andrews)
               Traditional Chinese Herbal Drugs: A Different Way of Treating
               Disease

13.11.91   Prof. D. Gani (University of St. Andrews)
               The chemistry of PLP-Dependent Enzymes

20.11.91   Dr. R. More O'Ferrall (University College Dublin)
*   Some Acid-Catalyzed Rearrangements in Organic Chemistry

28.11.91   Prof. I.M. Ward (University of Leeds)
               The SCI Lecture: The Science and Technology of Oriented
               Polymers

4.12.91   Prof. R. Grigg (University of Leeds)
*   Palladium-Catalysed Cyclisation and Ion-Capture Processes

5.12.91   Prof. A.L. Smith (ex Unilever)
               Soaps, Detergents and Black Puddings

11.12.91   Dr. W.D. Cooper (Shell Research)
               Colloid Science: Theory and Practice

22.1.92   Dr. K.D.M. Harris (University of St. Andrews)
               Understanding the Properties of Solid Inclusion Compounds

29.1.92   Dr. A. Holmes (University of Cambridge)
*   Cycloaddition Reactions in the Service of the Synthesis of
               Piperidine and Indolizidine Natural Products

30.1.92   Dr. M. Anderson (Shell Research)
               Recent Advances in the Safe and Selective Chemical Control of
               Insect Pests

12.2.92   Prof. D.E. Fenton (University of Sheffield)
               Polynuclear Complexes of Molecular Clefts as Models for
               Copper Biosites

307

13.2.92	Dr. J. Saunders (Glaxo Group Research Ltd.) Molecular Modelling in Drug Discovery
19.2.92 *	Prof. E.J. Thomas (University of Manchester) Applications of Organostannanes to Organic Synthesis
20.2.92	Prof. E. Vogel (University of Cologne) The Musgrave Lecture: Porphyrins: Molecules of Interdisciplinary Interest
25.2.92	Prof. J.F. Nixon (University of Sussex) The Tilden Lecture: Phosphaalkynes: New Building Blocks in Inorganic and Organometallic Chemistry
26.2.92 *	Prof. M.L. Hitchman (University of Strathclyde) Chemical Vapour Deposition
5.3.92	Dr. N.C. Billingham (University of Sussex) Degradable Plastics - Myth or Magic?
11.3.92 *	Dr. S.E. Thomas (Imperial College, London) Recent Advances in Organoiron Chemistry
12.3.92	Dr. R.A. Hann (ICI Imagedata) Electronic Photography - An Image of the Future
18.3.92 *	Dr. M. Maskill (University of Newcastle) Concerted or Stepwise Fragmentation in a Deamination-Type Reaction
7.4.92	Prof. D.M. Knight (University of Durham) Interpreting Experiments: The Beginning of Electrochemistry
13.5.92	Dr. J-C. Gehret (Ciba Geigy, Basel) Some Aspects of Industrial Agrochemical Research

RESEARCH CONFERENCES ATTENDED

Sept. 1989   Cambridge Surface Science Summer School
April 1990   North East Graduate Symposium, Newcastle University
April 1991   North East Graduate Symposium, Newcastle University

FIRST YEAR INDUCTION COURSE

This course consists of a series of one hour lectures on the services available in the department.

Departmental Organisation - Dr. E.J.F. Ross
Safety Matters - Dr. M.R. Crampton
Electrical Appliances - Mr. B.T. Barker
Chromatography and Microanalysis - Mr. T.F. Holmes
Atomic Absorptiometry and Inorganic Analysis - Mr. R. Coult
Library Facilities - Mr. R.B. Woodward
Mass Spectroscopy - Dr. M. Jones
Nuclear Magnetic Resonance Spectroscopy - Dr. R.S. Matthews
Glass-blowing Techniques - Mr. R. Hart and Mr. G. Haswell